2014

A path towards adaptive proton pencil beam scanning therapy

Nicolas Depauw
University of Wollongong

A PATH TOWARDS ADAPTIVE PROTON PENCIL BEAM SCANNING THERAPY

A thesis submitted in fulfilment of the
requirements for the award of the degree

Doctor of Philosophy

from

University of Wollongong

by

Nicolas Depauw
Masters of General Engineering
E.S.E.O. (France), 2008

Masters of Medical Radiation Physics,
University of Wollongong, 2007

School of Physics, Faculty of Engineering and Information Sciences
2014

A PATH TOWARDS ADAPTIVE PROTON PENCIL BEAM SCANNING THERAPY

Nicolas Depauw

A Thesis for Doctor of Philosophy
Centre for Medical Radiation Physics
University of Wollongong

Abstract

As technology advances, so does the quality of treatment offered to cancer patients. Proton therapy, and more specifically proton pencil beam scanning, is currently at the forefront of radiation therapy. Pencil beam scanning offers excellent tumor dose control as well as surrounding organs at risk sparing. Current treatment planning, however, is performed on a static image acquired before treatment. Naturally, this is not a proper representation of the actual patient on a daily basis. Thus, there is a need for adaptive radiation therapy, such as readjusting a given treatment plan based on the patient's daily setup or a moving tumor location. In order to perform adaptive treatment delivery, appropriate imaging as well as an extremely fast, yet accurate, dose computation engine is needed.

GEANT4 Monte Carlo simulations were performed in order to assess the imaging capabilities and limitations of a proton radiography detector, comparing them to conventional X-ray imaging. In parallel, a small form factor proton radiography system was designed based on available technologies. Thus, photonic bandgap fibers, a CMOS active pixel sensor, and Bicron scintillating fibers were evaluated for proton imaging purposes.

The requisites and limitations of treatment planning for proton pencil beam scanning were further defined, from the acquisition of the treatment planning software's beam model to the methodologies and treatment robustness. Based on this work, a simplified Monte Carlo algorithm was designed and implemented on the CPU architecture. This computation engine, GMC, was validated against physical observables and then compared to the treatment plan-

ning software dose calculation, as well as a "full" Monte Carlo recomputation.

Proton radiography showed poor spatial resolution but excellent density resolution when compared to X-ray radiography. This density resolution can be of importance when attempting to perform tumor tracking. The lower imaging dose associated with proton radiography is also of interest, especially in pediatric patients. Moreover, the use of a unique beam's eye view could slightly improve the accuracy of treatment delivery. Photonic bangap fibers, as well as the specific CMOS active pixel sensor used in this work, did not yield promising results for proton imaging. Conversely, Bicron scintillating fibers proved to be suitable for the design of a proton radiography system, as both the individual particle's position and energy could be acquired.

The treatment planning software's beam model is very simple, as compared to other modalities. However, the planning stage presented a few limitations, such as a lack of robustness analysis and issues related to spot placement. It was shown that both of these issues could be addressed with the use of a fast, yet accurate, dose computation engine. GMC was successfully implemented on the CPU architecture, and compared extremely well against actual pre-treatment QA measurements. The comparisons against the current algorithm of the treatment planning software and the full Monte Carlo engine matched the expectations for such an algorithm.

The complementing work on proton imaging and fast dose computation algorithm lays a solid foundation to materializing pencil beam scanning adaptive radiotherapy. Future work will focus on generating the necessary synergy between the two systems in order to implement the tools in the clinical setting.

Statement of Originality

This is to certify that the work described in this thesis is entirely my own, except where due reference is made in the text.

No work in this thesis has been submitted for a degree to any other university or institution.

Signed

Nicolas Depauw

January 21, 2015

Publications

[1] N. Depauw, J. Daartz, E. Batin, A. Rosenfeld, H. Kooy, S. MacDonald, and H. Lu, "A novel approach to post-mastectomy radiation therapy using scanned proton beam." *International Journal of Radiation Oncology* Biology* Physics* **91**, no. 2, 427–434, (2015).

[2] M. F. Spadea, A. Fassi, P. Zaffino, M. Riboldi, G. Baroni, N. Depauw, and J. Seco, "Contrast-enhanced proton radiography for patient set-up by using x-ray ct prior knowledge," *International Journal of Radiation Oncology* Biology* Physics* **90**, no. 3, 628–636, (2014).

[3] N. Depauw, B. Clasie, T. Madden, A. Rosenfeld, and H. Kooy, "GMC ['gimik]: algorithm for proton therapy." *Journal of Physics: Conference Series* **489**, (2014).

[4] T. F. DeLaney, N. J. Liebsch, F. X. Pedlow, J. Adams, E. A. Weyman, B. Y. Yeap, N. Depauw, G. P. Nielsen, D. C. Harmon, S. S. Yoon **et al.**, "Long-term results of phase ii study of high dose photon/proton radiotherapy in the management of spine chordomas, chondrosarcomas, and other sarcomas," *Journal of surgical oncology*," (2014).

[5] M. D. Cheney, Y.-L. Chen, R. Lim, B. K. Winrich, A. L. Grosu, A. V. Trofimov, N. Depauw, H. A. Shih, J. H. Schwab, F. J. Hornicek **et al.**, "[18f]-fluoromisonidazole positron emission tomography/computed tomography visualization of tumor hypoxia in patients with chordoma of the mobile and sacrococcygeal spine," *International Journal of Radiation Oncology* Biology* Physics* **90**, no. 5, 1030–1036, (2014).

[6] Y. D. Tseng, J. Y. Wo, M. Ancukiewicz, J. Adams, N. Depauw, H. J. Mamon, and T. S. Hong, "Dosimetric predictors of nausea and vomiting: an exploratory analysis of a prospective phase I/II trial with neoadjuvant accelerated short-course radiotherapy and capecitabine for resectable pancreatic cancer," *Journal of Radiation Oncology*," 1–8, (2013).

[7] J. C. Polf, N. Depauw, and J. Seco, "Monte carlo studies of prompt gamma emission and of proton radiography/proton-CT," in *Monte Carlo Techniques in Radiation Therapy*, J. Seco and F. Verhaegen, Eds., CRC Press, 2013, 263–272.

[8] J. Seco, M. Oumano, N. Depauw, M. F. Dias, R. P. Teixeira, and M. F. Spadea, "Characterizing the modulation transfer function (MTF) of proton/carbon radiography using monte carlo simulations," *Medical physics* **40**, 091717, (2013).

[9] R. B. Jimenez, R. Sethi, N. Depauw, M. B. Pulsifer, J. Adams, S. M. McBride, D. Ebb, B. C. Fullerton, N. J. Tarbell, T. I. Yock **et al.**, "Proton radiation therapy for pediatric medulloblastoma and supratentorial primitive neuroectodermal tumors: Outcomes for very young children treated with upfront chemotherapy," *International Journal of Radiation Oncology* Biology* Physics*," (2013).

[10] N. Depauw, M. Dias, A. Rosenfeld, and J. Seco, "Ion radiography as a tool for patient set-up and image guided particle therapy: A monte carlo study." *Technology in cancer research & treatment*" (2013).

[11] S. J. Dowdell, B. Clasie, N. Depauw, P. Metcalfe, A. B. Rosenfeld, H. M. Kooy, J. B. Flanz, and H. Paganetti, "Monte carlo study of the potential reduction in out-of-field dose using a patient-specific aperture in pencil beam scanning proton therapy," *Physics in Medicine and Biology* **57**, no. 10, 2829, (2012).

[12] B. Clasie, N. Depauw, M. Fransen, C. Gomà, H. R. Panahandeh, J. Seco, J. B. Flanz, and H. M. Kooy, "Golden beam data for proton pencil-beam scanning," *Physics in medicine and biology* **57**, no. 5, 1147, (2012).

[13] A. Carabe, M. Moteabbed, N. Depauw, J. Schuemann, and H. Paganetti, "Range uncertainty in proton therapy due to variable biological effectiveness," *Physics in Medicine and Biology* **57**, no. 5, 1159, (2012).

[14] K. T. Butterworth, C. K. McGarry, B. Clasie, A. Carabe-Fernandez, J. Schuemann, N. Depauw, S. Tang, S. J. McMahon, G. Schettino, J. M. O'Sullivan **et al.**, "Relative biological effectiveness (RBE) and out-of-field cell survival responses to passive scattering and pencil beam scanning proton beam deliveries," *Physics in Medicine and Biology* **57**, no. 20, 6671, (2012).

[15] J. Seco, N. Depauw, S. Danto, H. Paganeti, and Y. Fink, "Qualitative evaluation of proton radiography for viewing density differences in lung tumors: A monte carlo study," *Nuclear technology* **175**, no. 1, 27–31, (2011).

[16] J. Seco and N. Depauw, "Proof of principle study of the use of a CMOS active pixel sensor for proton radiography," *Medical Physics* **38**, 622, (2011).

[17] N. Depauw and J. Seco, "Sensitivity study of proton radiography and comparison with kV and MV x-ray imaging using GEANT4 monte carlo simulations," *Physics in Medicine and Biology* **56**, no. 8, 2407, (2011).

[18] N. Depauw, S. Danto, B. Bednarz, H. Paganetti, Y. Fink, and J. Seco, "Preliminary study of proton radiography imaging qualities using GEANT4 monte carlo simulations," *Nuclear technology* **175**, no. 1, 6–10, (2011).

[19] H. M. Kooy, B. M. Clasie, H.-M. Lu, T. M. Madden, H. Bentefour, N. Depauw, J. A. Adams, A. V. Trofimov, D. Demaret, T. F. Delaney **et al.**, "A case study in proton pencil-beam scanning delivery," *International Journal of Radiation Oncology* Biology* Physics* **76**, no. 2, 624–630, (2010).

[20] B. Clasie, A. Wroe, H. Kooy, N. Depauw, J. Flanz, H. Paganetti, and A. Rosenfeld, "Assessment of out-of-field absorbed dose and equivalent dose in proton fields," *Medical physics* **37**, no. 1, 311, (2010).

Presentations

[1] J. Wo, N. Depauw, J. Symonifka, H. Kooy, and T. Hong, "Dosimetric analysis of proton pencil beam scanning radiation therapy versus dose painted intensity modulated radiation therapy for squamous cell carcinoma of the anal canal," *International Journal of Radiation Oncology• Biology• Physics* **90**, no. 1, S398, (2014).

[2] N. Depauw, E. Batin, J. Daartz, S. MacDonald, H. Kooy, and H. Lu, "A novel proton pencil beam scanning technique for postmastectomy chest wall irradiation," *International Journal of Radiation Oncology• Biology• Physics* **90**, no. 1, S932, (2014).

[3] M. Cheney, Y. Chen, R. Lim, B. Winrich, A. Grosu, A. Trofimov, N. Depauw, H. Shih, J. Schwab, F. Hornicek **et al.**, "18f-fmiso pet/ct visualization of tumor hypoxia in patients with chordoma of the mobile and sacrococcygeal spine," *International Journal of Radiation Oncology• Biology• Physics* **90**, no. 1, S753, (2014).

[4] N. Rochet, E. Batin, N. Depauw, K. Jee, H. Kooy, F. Khan, P. Paetzold, A. Russell, T. Bortfeld, and D. Craft, "Advances in whole abdominal irradiation: What protons, VMAT, and IMRT using multicriteria optimization can offer," *International Journal of Radiation Oncology* Biology* Physics* **87**, no. 2, S748–S749, (2013).

[5] N. Depauw, B. Clasie, T. Madden, A. Rosenfeld, and H. Kooy, "GMC ['gimik]: a one-variable monte carlo dose algorithm for proton therapy, ," (2013).

[6] Y. Tseng, J. Wo, M. Ancukiewicz, J. Adams, H. Panahandeh, N. Depauw, and T. Hong, "Dosimetric and clinical predictors of nausea and vomiting: An exploratory analysis of a prospective phase I/II trial with neoadjuvant accelerated short course radiation therapy with capecitabine for resectable pancreatic cancer," *International Journal of Radiation Oncology* Biology* Physics* **84**, no. 3, S321–S322, (2012).

[7] M. Spadea, A. Fassi, N. Depauw, M. Riboldi, G. Baroni, and J. Seco, "TH-E-BRA-05: Improving the contrast of proton and carbon radiography by using CT prior knowledge." *Medical physics* **39**, no. 6, 4012, (2012).

[8] M. Spadea, A. Fassi, N. Depauw, M. Riboldi, G. Baroni, and J. Seco, "Contrast enhanced proton radiography for in-room soft tissue-based setup," *International Journal of Radiation Oncology* Biology* Physics* **84**, no. 3, S53, (2012).

[9] J. Seco, M. Oumano, N. Depauw, M. Dias, and R. Teixeira, "SU-EI-97: Characterizing the modulation transfer function (MTF) of proton radiography." *Medical physics* **39**, no. 6, 3647, (2012).

[10] C. McGarry, K. Butterworth, B. Clasie, S. A. Carabe-Fernandez, N. Depauw, H. Kooy, H. Ming, S. Tang, J. O'Sullivan, G. Schettino **et al.**, "EP-1587 cell survival responses to modulated proton beams delivered by passive scattering and pencil beam scanning," *Radiotherapy and Oncology* **103**, S608–S609, (2012).

[11] O. Koybasi, M. Goulet, N. Depauw, L. Gingras, L. Archambault, L. Beaulieu, and J. Seco, "Development of a 2D scintillating fiber detector for proton radiography," in *Nuclear Science Symposium and Medical Imaging Conference (NSS/MIC), 2012 IEEE*, IEEE, 2012, 4318–4323.

[12] R. Jimenez, T. Yock, N. Depauw, J. Adams, D. Ebb, B. Fullerton, N. Tarbell, and S. MacDonald, "Proton radiation therapy for high-risk pediatric medulloblastoma: Outcomes for very young children treated with upfront chemotherapy," *International Journal of Radiation Oncology* Biology* Physics* **84**, no. 3, S65–S66, (2012).

[13] M. Goulet, L. Gingras, N. Depauw, L. Archambault, J. Seco, and L. Beaulieu, "WE-G-BRB-06: Real-time radiation field tracking using long scintillating fibers." *Medical physics* **39**, no. 6, 3968, (2012).

[14] S. Dowdell, B. Clasie, N. Depauw, P. Metcalfe, A. Rosenfeld, H. Kooy, J. Flanz, and H. Paganetti, "MO-F-213AB-03: Potential reduction in out-of-field dose in pencil beam scanning proton therapy through use of a patient-specific aperture." *Medical physics* **39**, no. 6, 3872, (2012).

[15] N. Depauw and J. Seco, "TH-A-213CD-09: The use of scintillating fibers for proton imaging purposes." *Medical physics* **39**, no. 6, 3988, (2012).

[16] N. Depauw and J. Seco, "Preliminary results of a scintillating fibers detector for proton radiography, ," (2012).

[17] J. Seco, M. Dias, N. Depauw, and S. MacDonald, "SU-EJ-168: Proton radiography for pediatric, t-spine and lung malignancies; development and enhancement of a proton imaging technique," *Medical Physics* **38**, 3482, (2011).

[18] M. Dias, N. Depauw, and J. Seco, "TU-C-214-02: Proton radiography gui interface, PR-Creator, for in-room patient setup and real-time tumor tracking in proton beam therapy," *Medical Physics* **38**, 3756, (2011).

[19] N. Depauw, M. Dias, and J. Seco, "TH-E-220-04: IGPT using proton radiography: A monte carlo study," *Medical Physics* **38**, 3879, (2011).

[20] N. Depauw, J. Seco, J. Adams, H. Panahandeh, H. Paganetti, and H. Kooy, "SU-ET-694: Evaluating pencil beam dose algorithm in lung with monte carlo," *Medical Physics* **38**, 3650, (2011).

[21] B. Clasie, H. Kooy, N. Depauw, C. Goma, A. Carabe-Fernandez, H. Panahandeh, J. Seco, S. Tang, and J. Flanz, "SU-ET-723: Pencil beam depth-dose distributions in the astroid TPS," *Medical Physics* **38**, 3657, (2011).

[22] A. Carabe-Fernandez, M. Moteabbed, N. Depauw, and H. Paganetti, "SU-E-T-648: Range uncertainty in proton therapy due to variable biological effectiveness," *Medical Physics* **38**, 3639, (2011).

[23] J. Seco and N. Depauw, "WE-E-201C-04: Development of the first MGH proton range telescope (PRaT) prototype using scintillating fibers," *Medical Physics* **37**, 3440, (2010).

[24] N. Depauw, V. Taranenko, S. Danto, F. Sorin, Y. Fink, and J. Seco, "TH-D-201B-03: A comparison of protons versus gamma x-rays in producing patient radiographs: A monte carlo study," *Medical Physics* **37**, 3472, (2010).

[25] B. Clasie, H. Bentefour, P. Boisseau, Y. Claereboudt, D. Demaret, N. Depauw, D. Herrup, H. Lu, W. Nett, H. Kooy **et al.**, "TH-C-BRD-01: Technical and practical considerations in implementing proton pencil beam scanning," *Medical Physics* **36**, 2794, (2009).

Acknowledgments

My deepest gratitude goes to my supervisors, **Prof. Anatoly Rosenfeld** of the University of Wollongong, and **Dr. Hanne Kooy** of the Massachusetts General Hospital (MGH), without whom this dissertation would not have been possible. They both have been tremendous mentors over the years, and their insight and ideas have shaped the work presented in this Thesis.

I further wish to acknowledge **Ben Clasie** for all the hard exchange of work, laughters, and Balvenie. He, too, has been a wonderful mentor and supporter over the years. Joao Seco is also to be thanked for all his great ideas and support, as well as his supervision and push for a proton imaging system at MGH.

A special thanks goes to my wife, Stephanie, for not only her great support but also her wonderful proof-reading skills. Thanks also to Jule Daartz for helping with the final revisions of this dissertation, Jan Schuemann for generating last minute TOPAS/GEANT4 dose computations, and, naturally, Tom Madden for his genius and the various debugging sessions.

I cannot be thankful enough to many employees of the Department of Radiation Oncology at MGH for the continuous help and support they provided me along the way; particularly, I would like to thank Greg, Julie, Estelle, Shannon, Norm, Joe, Bob, Hsiao-Ming, Peter, Judy, Al, and, of course, Little Buddy for his greatness and the countless meetings even though he abandoned me halfway through it all.

Finally, thanks to my family and friends, and all those who bore my silliness along the way yet supported me.

Contents

List of Abbreviations

ADC	Analog-to-digital converter
APS	Active pixel sensor
BEV	Beam's eye view
BIS	Beam imaging device
CMOS	Complementary metal-oxide semiconductors
CMRP	Centre for Medical Radiation Physics
CNR	Contrast-to-noise ratio
CPC	Conductive polycarbonate
CsI	Cesium-iodine
CT	Computed tomography
CW	Chest wall
DAQ	Data acquisition system
DRR	Digitally reconstructed radiograph
DS	Double scattering
DVH	Dose volume histogram
GEM	Gas electron multipliers
Gp	Gigaprotons (10^9 protons)
GPU	Graphical processing unit
HCL	Harvard cyclotron laboratory
HU	Hounsfield unit
IC	Ionization chamber
ICRP	International Commission on Radiobiological Protection
ICRU	International Commission on Radiation Units and Measurements
IGIT	Image guided ion therapy
IGPT	Image guided proton therapy

IGRT	Image guided radiation therapy
IMPT	Intensity modulated proton therapy
IMRT	Intensity modulated radiation therapy
LET_∞	Linear energy transfer
MC	Monte Carlo
MCS	Multiple Coulomb scattering
MGH	Massachusetts General Hospital
MIT	Massachusetts Institute of Technology
MLP	Most likely path
NSCLC	Non-small cell lung cancer
NIST	National Institute of Standards and Technology
OAR	Organ(s) at risk
PBA	Pencil beam algorithm
PBG	Photonic bandgap
PBS	Pencil beam scanning
PC	PolyCarbonate
PCB	Printed circuit boards
pCT	proton computed tomography
PES	Polyethersulfone
PID	Portal imaging device
PMRT	Post-mastectomy radiation therapy
PMT	Photomultiplier tube
PR	Proton radiography
QA	Quality assurance
RBE	Relative biological effectiveness
ROI	Region of interest
RSP	Relative stopping power ratio
SAD	Source-to-axis distance
SEM	Scanning electron microscope
SiPM	Silicon photomultiplier
SNR	Signal-to-noise ratio
SOBP	Spread-out Bragg peak

STV	Scanning target volume
TLD	Thermoluminescent dosimeter
TPS	Treatment planning software
VMAT	Volumetric modulated arc therapy

List of Figures

List of Tables

Chapter 1

Introduction

External beam radiation therapy generally aims at controlling tumor tissue growth using high-energy rays. Diverse modalities are available but all have the same intent: maximizing the amount of dose received by the tumor while minimizing the dose to the surrounding healthy tissue. Through the use of its finite range in tissue, proton radiotherapy offers excellent opportunities at fulfilling this goal. As costs decrease and technology advances, so does the quality of radiation treatments. One such example is proton pencil beam scanning (PBS).// Proton therapy treatments in a clinical setting began in the U.K. in 1989 at the Clatterbridge Cancer Centre. At the time, cost and technology only permitted the treatment of eye patients due to the relatively low energy of the beam (62 MeV). As time passed, it became possible to treat deep/large tumors using double-scattering technology, a 3D conformal proton therapy technique with results comparable to photon IMRT treatments (*St Clair et al., Mock et al., Trofimov et al. [14, 15, 16]*). The first treatment of a patient with PBS followed in 1996 at the Paul Sherrer Institute in Switzerland; however, it was not until 2008 that PBS become truly available in a clinical setting. Through the use of intensity modulation, PBS offers excellent tumor dose conformality along with notable organs at risk sparing. Thus, PBS is quickly becoming a modality of choice for new radiotherapy centers.

In spite of the fact that PBS is at the forefront of radiotherapy, numerous challenges remain. One challenge is the adaptation of a radiation therapy treatment plan. This adaptation could occur based on a patient's daily setup position or "online" through the use of tumor tracking. The continuous expansion of computing power and speed plays a key factor in the achievement of this skill. PBS adaptive radiotherapy requires novel imaging capabilities, such as

proton imaging, in order to efficiently position the patient and recompute the intended treatment plan dose. This recalculation must be practically instantaneous yet accurate, so the treatment can be adapted without any delay.
This thesis aims to build the basis for proton pencil beam scanning adaptive radiotherapy. Proton therapy mechanism and current workflows are presented in chapter 2. Chapters 3 and 4 investigate the possibilities and limitations of a clinically viable proton radiography imaging system. PBS treatment planning requisites and the development of a simplified Monte Carlo dose algorithm are the focus of the work presented in chapters 5 and 6.

1.1 Aims and objectives

1.1.1 Proton imaging characteristics, limitations, and feasibility

Current proton centers mostly rely on orthogonal X-ray imaging for patient setup verifications. This imaging modality may result in a relatively large, undesired dose to the patient, especially in pediatric patients (*Miglioretti et al. [17]*). As this thesis will show, X-ray imaging is quite possibly not the optimal modality for certain tumor sites. Because of this, there is a need for proton imaging which could be used at the time of patient setup. Additionally, the possibility of using tumor tracking with proton imaging could result in the online adaptation of the treatment plan, hence ensure the treatment is truly delivered as intended.
Research question:

> *What are the imaging capabilities of a small form factor, clinically viable proton radiography detector?*

Chapter 3 presents various work using Monte Carlo simulations in order to demonstrate the theoretical possibilities of a clinically viable proton radiography system.

1.1.2 Design of a proton radiography detector

All current solutions for proton radiography detectors rely on a range telescope-like device in order to acquire the proton range/energy information (*Schneider and Pedroni [18]*, *Schneider and Pedroni [19]*, *Schneider et al. [3]*, *Sauli [20]*, *Pemler et al. [4]*, *Johnson et al. [21]*, *Talamonti et al. [22]*, *Sipala et al. [23]*). While such systems could be used to produce proton images,

the range telescope is impractical for clinical use due to its rather bulky design.

Research question:

> *What technologies are available in order to build a small form factor, clinically viable proton radiography detector?*

Subsequent to the simulation work realized on proton radiography imaging, chapter 4 shows the different designs and empirical work performed in order to build a clinically viable proton radiography system.

1.1.3 Proton pencil beam scanning planning

Proton pencil beam scanning is currently the most promising radiation treatment modality. The use of intensity modulation as well as the finite range provided by the individual Bragg peaks can result in highly conformal target coverage, along with great organs at risk sparing. It is, however, a new modality, and as such, there is still limited experience or proper guidelines for treatment planning.

Research question:

> *What are the current methodologies and limitations of proton pencil beam scanning treatment planning?*

Chapter 5 presents the requisites as well as the current treatment planning methodologies used at Massachusetts General Hospital for proton pencil beam scanning delivery. The limitations and uncertainties of these methodologies are also discussed.

1.1.4 Fast MC dose algorithm

The current clinical practice for proton treatment planning relies on dose computations using a pencil beam algorithm (PBA). PBA are analytical dose computation engines that presents the advantage of speed and relatively good accuracy. In the presence of large heterogeneities, however, these PBA engines tend to fall apart and large discrepancies may be observed (*Schaffner et al., Grassberger et al. [13, 24]*). Conversely, full Monte Carlo dose computations engine are far more accurate but present a large overhead and result in clinically unacceptable computation time. Not only does PBA suffer from these inaccuracies but, when it comes to

adaptive radiotherapy, its dose calculation speed remains inadequate as the whole process must occur within seconds.

Research question:

> *Could the current clinical PBA dose computation engine for proton therapy be replaced with a faster yet more accurate MC algorithm?*

Chapter 6 presents the implementation of a fast yet accurate Monte Carlo dose algorithm for proton therapy treatment planning.

1.2 Contributions and Publications

The principal contributions discussed in this thesis resulted in the following publications and presentations:

- **Chapter 3:** *Proton Radiography: feasibility studies.*

  The work presented in chapter 3 has been published in numerous articles (*Depauw et al. [25]*, *Depauw and Seco [26]*, *Depauw et al. [27]*), and presented at multiples conferences (*Depauw et al. [28]*, *Depauw et al. [29]*).

  Additionally, co-authored work has been published (*Seco and Depauw [30]*, *Seco et al. [31]*, *Polf et al. [32]*, **?** *[***?** *]*), and presented at various conferences (*Seco and Depauw [33]*, *Dias et al. [34]*, *Seco et al. [35]*, *Seco et al. [36]*, *Spadea et al. [37]*, *Spadea et al. [38]*).

- **Chapter 4:** *Proton Radiography: experimental realization.*

  The experimental work described in chapter 4 resulted in a couple of papers (*Polf et al. [32]* and *Seco and Depauw [30]*), as well as presented at various conferences (*Depauw and Seco [39]*, *Depauw and Seco [40]*, *Seco and Depauw [33]*, *Goulet et al. [41]*, *Koybasi et al. [42]*). An invited talk was also given at the University of Wollongong (*Depauw [43]*).

- **Chapter 5:** *Proton pencil beam scanning planning.*

  The PBS planning methodologies presented in chapter 5, as well as their results, have been published and presented in numerous places. Multiple manuscripts were also awaiting submission at the time of writing. Specifically, the PMRT example was recently

accepted for publication in the *Red Journal* (*Depauw et al. [44]*).

Co-authored work has been published in *Kooy et al. [45]*, *Clasie et al. [11]*, *Dowdell et al. [46]*, *Carabe et al. [47]*, and *Butterworth et al. [48]*, as well as presented at various conferences (*Clasie et al. [49]*, *Clasie et al. [50]*, *Dowdell et al. [51]*, *Rochet et al. [52]*, *Carabe-Fernandez et al. [53]*, *McGarry et al. [54]*).

- **Chapter 6:** *Fast MC dose algorithm.*

  The work in chapter 6 is yet to be published, but was partially presented at the International Conference on the Use of Computers in Radiation Therapy (*Depauw et al. [55]*), and published in their proceedings (*Depauw et al. [56]*).

  Numerous submissions shall follow this thesis work, including future work on the algorithm's validation and speed improvements.

Chapter 2

Contemporary proton pencil beam scanning

2.1 Introduction

Proton beams were first suggested for medical use by *Wilson [57]*, leading to the treatment of the first cancer patient in 1954 at Lawrence Berkley Laboratory (*Lawrence [58]*). The first patients were treated using a cross-firing technique utilizing the plateau region of the beam. The advantages of the Bragg peak (figure 2.9) over conventional radiotherapy, however, quickly became clear. Thus, the Harvard Cyclotron Laboratory (HCL), together with the Massachusetts General Hospital (MGH), focused on the use of the Bragg peak for cancer therapy in the 1960s (*Lawrence [59]*). Early on, proton therapy was only administered through such collaboration efforts in physics research facility. The first hospital-based proton therapy center was initiated at the Clatterbridge Centre for Oncology in the U,K., followed in 1990 by the first U.S.-based center in Loma Linda (*Slater et al. [60]*). Only two additional U.S.-based centers were opened over the course of the following decade, including MGH's Francis H Burr proton center (*Particle Therapy Co-Operative Group [61]*). Since 2001, however, eleven additional centers have treated patients, and ten more are under-construction, solely in the U.S. (*Particle Therapy Co-Operative Group, Particle Therapy Co-Operative Group [61, 62]*). Largely assisted through recent improvements in accelerators and delivery techniques, this increase in treating proton centers highlights the great interest in proton therapy due to protons' promising physical characteristics. Historically, only passive scattering delivery techniques were available. Such techniques present intrinsic limitations which prohibit the full use of pro-

ton therapy's theoretical benefits over conventional radiotherapy. More recently, pencil beam scanning (PBS) delivery techniques have emerged in hospital environments. Thus, both MGH and M.D. Anderson treated their first patients using this technique in 2008. PBS allows for high tumor conformality along with great organs at risk (OAR) sparing.
The physical properties of proton pencil beam scanning are described below, as well as the current state-of-the-art in PBS technology. The current workflow and limitations of PBS adaptive radiotherapy are further highlighted.

2.2 Proton therapy

Unless specified, the information presented in this section was derived from *De Laney and Kooy [63]*, *Attix [64]*, or *Paganetti [2]*.

2.2.1 Physical interactions

Protons mainly interact with matter in two distinct ways: electromagnetic interactions and nuclear interactions. All protons undergo many electromagnetic interactions which are mostly nonelastic (kinetic energy loss and particles' states unchanged). These electromagnetic interactions occur with either atomic electrons or atom nuclei. Conversely, only a fraction of the incident protons will undergo nuclear interactions.
In the case of electromagnetic interactions with atomic electrons (figure 2.1(a)), the proton transfers part of its momentum to the electron. The electron gets ejected and becomes a so-called δ-electron that will ionize the medium. As the proton loses momentum, it transfers more and more energy during each interaction with an electron as it remains for a longer period of time within the electron's vicinity. As later discussed, this gives rise to the characteristic Bragg peak (figure 2.2). Although the proton transfers only very little energy during these collisions, it will come to a rest due to the large number of interactions. The proton scattering is negligible during such interactions.
A proton generally loses negligible energy during an electromagnetic interaction with an atomic nucleus (elastic interactions) but scatters with a small angle. This interaction is presented in figure 2.1(b). Although the proton's local deflection is small, an increasing angular spread of the protons is observed at depth due to the large number of these interactions (figure 2.4). This angular spread phenomenon is commonly referred to as "multiple Coulomb scattering"

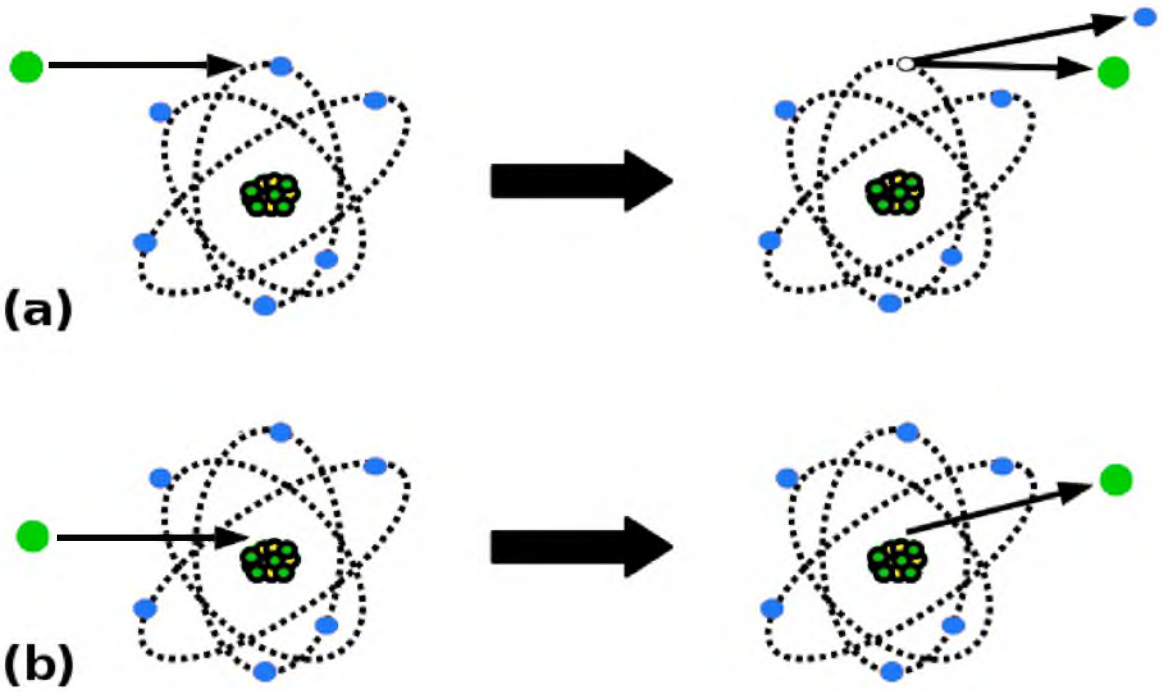

Figure 2.1: *Electromagnetic interactions between an incident proton (green) and (a) an atomic electron (blue) or (b) an atomic nucleus (yellow and green). These interactions result in either a transfer of momentum (energy loss) to the electron (a), or a slight scatter (b).*

(MCS).

As previously discussed, the energy of the incident proton decreases as the energy locally deposited ($\frac{dE}{dx}$) increases due to the increasing time the proton remains within the electron's vicinity. As a consequence, a proton of a given incident energy comes to rest at a known depth that depends on the medium's density. This depth is known as its "range". A monoenergetic proton beam is thus characterized by its depth dose distribution, the so-called "Bragg peak". An example of a pristine Bragg peak is given in figure 2.2 for an incident proton beam with an energy of 170 MeV. Although not a fully understood process, there is a very small build-up observed at the entrance of the peak which is believed to arise from in-air nuclear interactions prior to the water. The curve highlights the initial slight increase in dose deposited ($\frac{dE}{dx}$), called the "plateau region", followed by the peak as $\frac{dE}{dx}$ increases as a power law function [65]. The physical range R_{80} of a monoenergetic beam corresponds to the depth at which 50 % of the incident protons have stopped, and is defined as the distal 80 % mark on the depth dose curve. The range of each proton varies slightly due to statistical fluctuations in the number of interactions the proton undergoes. This phenomenon is known as range straggling and results in an increase in the width of the peak. Within the clinical therapeutic range (30 MeV

to 250 MeV), range straggling equates to ≈ 1.2 % of the nominal range across materials of various densities.

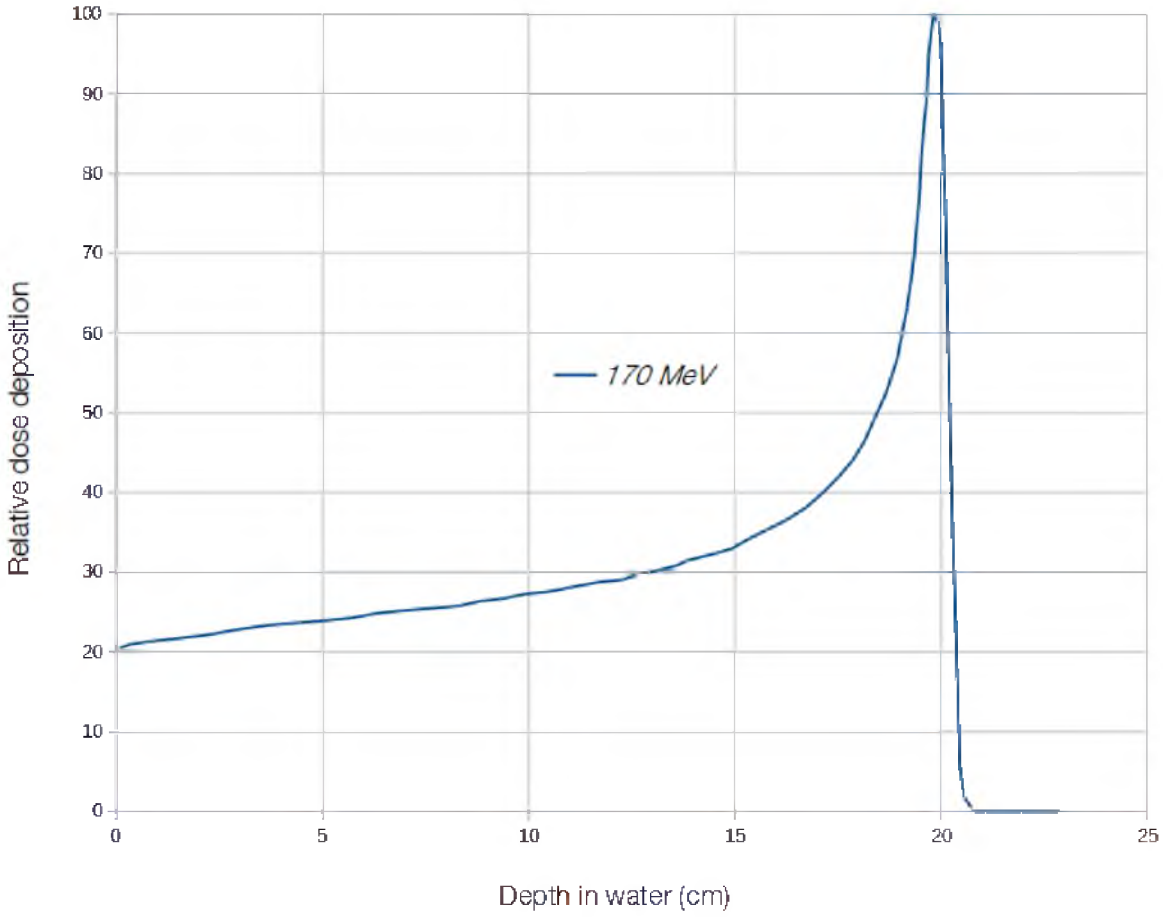

Figure 2.2: *Depth dose distribution of a 170 MeV proton beam known as the "Bragg peak".*

A Spread-Out Bragg peak (SOBP) can be generated by overlapping Bragg peaks from protons of various energies. A SOBP is characterized by its range R_{90} (defined as the distal 90 % mark on the depth dose curve) and its modulation (defined as the proximal 98 % mark on the depth dose curve). Figure 2.3 shows an example of an SOBP along with the weighted individual Bragg peaks that it is composed of. Although the SOBP is a very important concept in a scattered proton delivery system, it is less relevant to PBS delivery techniques due to the three dimensional intensity modulation feature, as later discussed.

Laterally, the MCS component of the beam results in a near-Gaussian angular distribution. The numerous atomic interactions that occur within a medium result in a small displacement of the protons which slowly increases the width of the cross section of a unidirectional beam

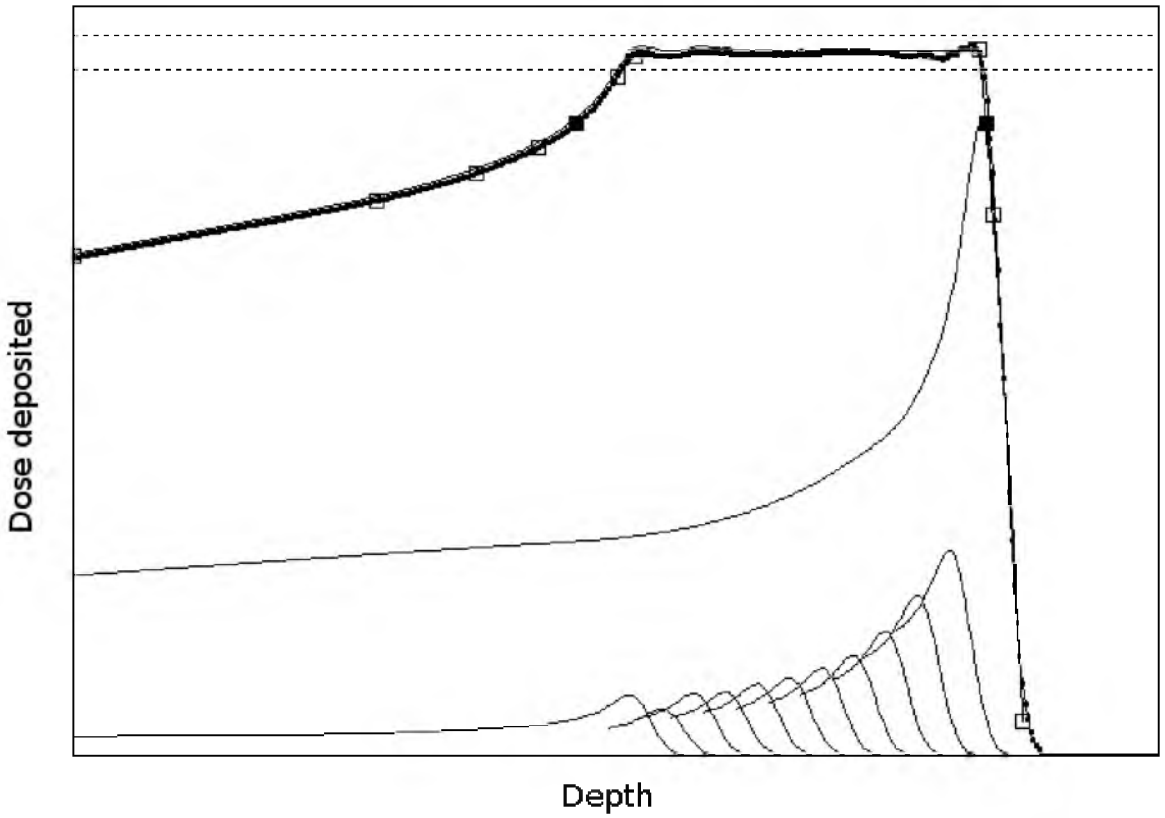

Figure 2.3: *A spread-Out Bragg peak (thick line) generated from a composition of individual pristine Bragg peaks (thin lines). The solid squares represent the proximal and distal 90 % of the curve, determining the range and modulation of the beam; the empty square highlights different points along the curve between the proximal 70 % and distal 10 %. This figure was produced using Gottschalk [1]*

at the macroscopic level. This angle can be measured at a given depth as highlighted in figure 2.4(a). Furthermore, this scattering angle rapidly increases as the momentum of the protons rapidly diminishes at the end of range. This is illustrated in figure 2.4(b), which shows the relative increase in MCS as a function of depth over range.

Additionally, a fraction of the incident protons undergo head-on collisions with the nucleus of an atom. Although these nuclear interactions may be elestic, they are generally nonelastic and result in the generation of two secondary particles as illustrated in figure 2.5. One of these secondaries is the original incident proton, while the other is a fragment of the nucleus. This nuclear fragment can consist of a simple nucleon (proton or neutron), or could be a larger particle such as an alpha particle. It was shown through Monte Carlo simulations that, in 57 % of nuclear interactions, the nuclear fragment was a proton. In such an instance it is then impossible to tell which secondary particle is the original proton. The energy of these secondary particles greatly varies and is dictated by the amount of momentum transfered during the collision between the proton and the atomic nucleus. These secondaries present a

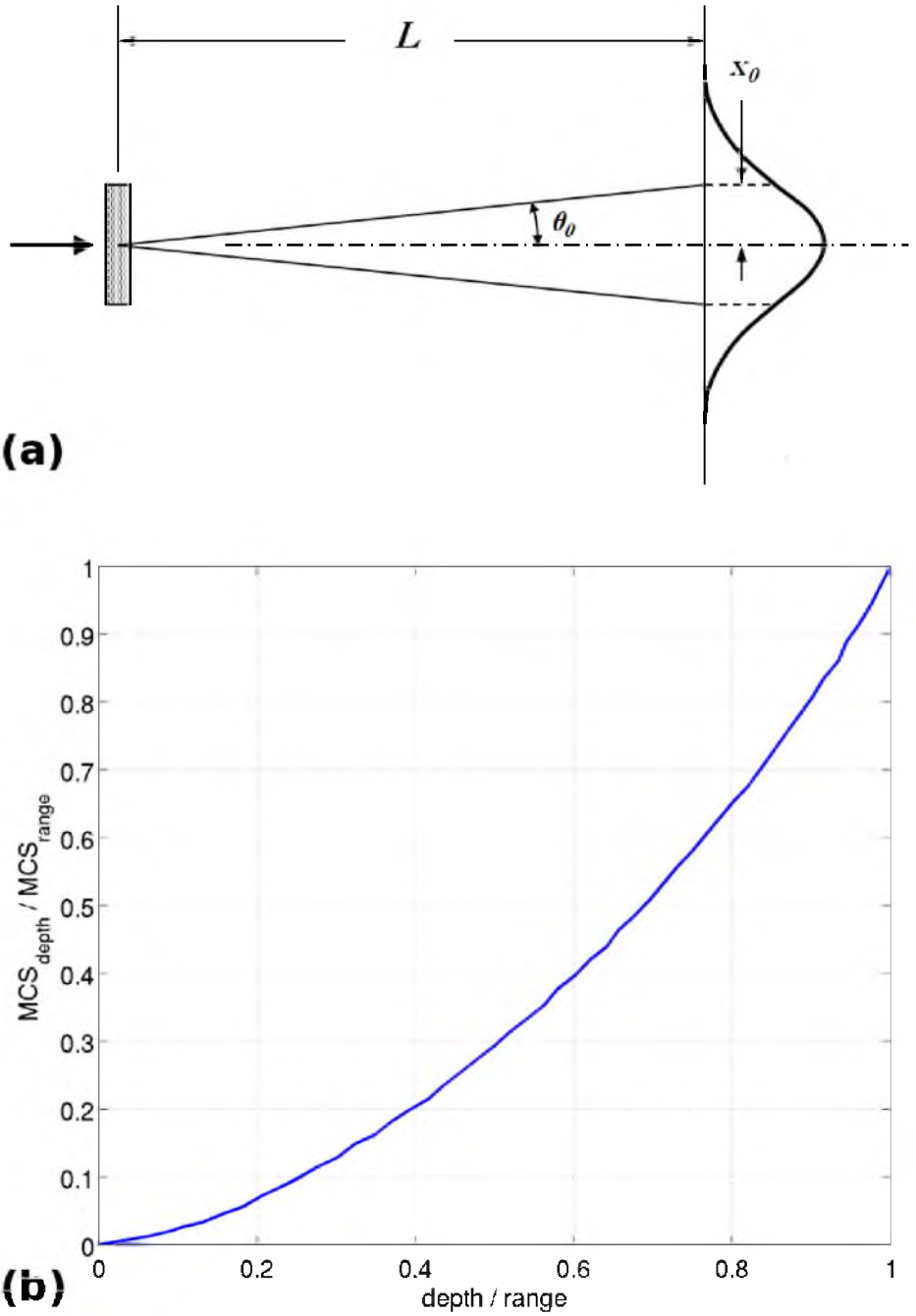

Figure 2.4: *(a) Scattering angle θ_0 due to the multiple Coulomb scattering of the protons; θ_0 is ruled by a normal distribution which can be measured as a displacement x_0 (sigma) at an arbitrary distance T; (b) Multiple Coulomb scattering as a function of depth over incident range.*

relatively high energy compared to δ-electrons, and their dose therefore cannot be considered locally deposited. The range of these secondaries is typically within 1 to 2 cm. Furthermore, these interactions typically result in large angle scattering ranging anywhere between 0 and 90 °.

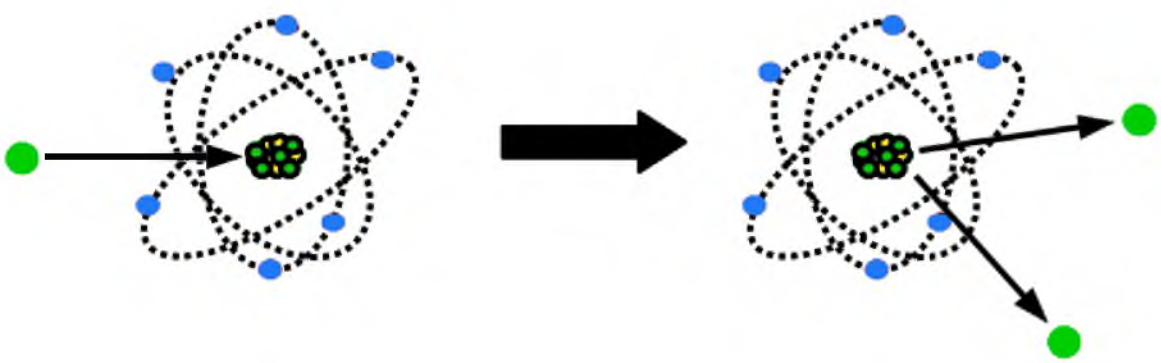

Figure 2.5: *Nuclear interactions of an incident proton (green) with an atomic nucleus (yellow and green). In this instance, the incident proton transfered some of its momentum to a nuclear proton which got ejected.*

Figure 2.6 shows the probability of nonelastic nuclear interactions in water based on incident proton range in water (i.e energy). The probability of a nuclear interaction for a particle with a given proton range (energy) is 1 %/g.cm^2 (*Janni [66]*).

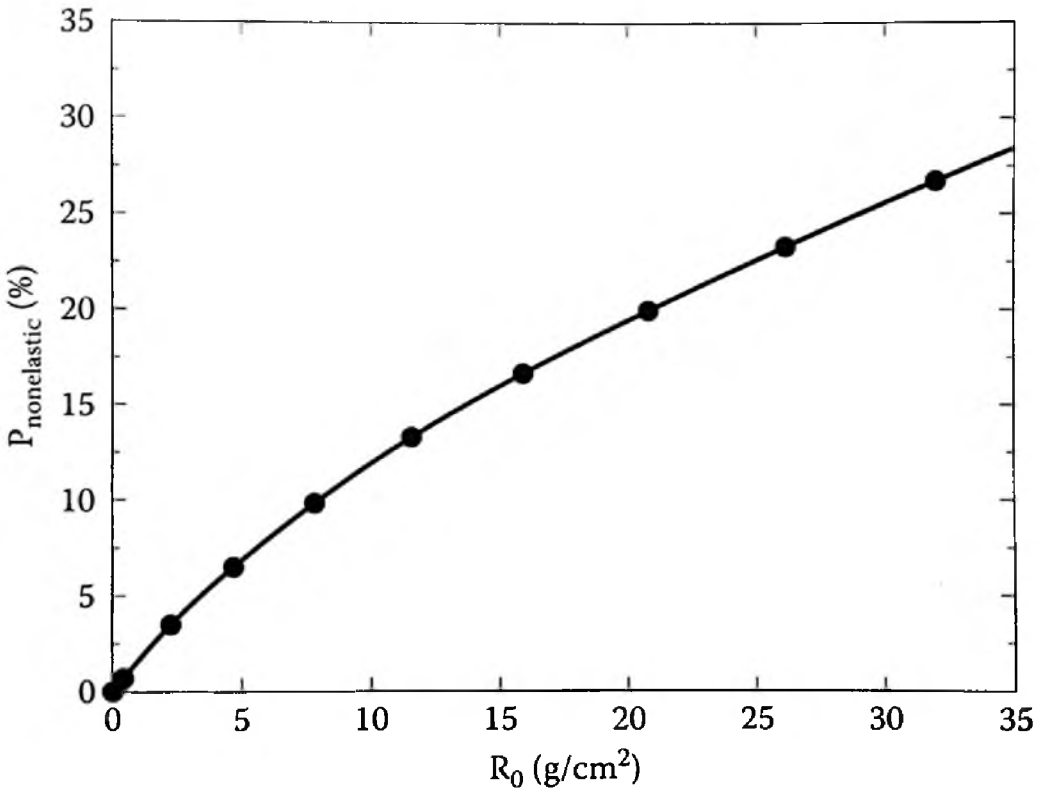

Figure 2.6: *Nonelastic nuclear interaction probability as a function of incident proton range in water, courtesy of Paganetti [2].*

2.2.2 Beam delivery

2.2.2.1 Scattering

A narrow beam is broadened through a range modulator wheel and scattering foils in order to generate a broad Gaussian distribution. In the case of double scattering, the Gaussian distribution is flattened through the use of a bell-shaped second scatterer which results in a larger area of uniform fluence. A collimator, generally an aperture made of high-Z material, is then tailored to eliminate the undesired dose outside of the target. The incident energy of the narrow beam is simultaneously modified through a modulation wheel. The modulation wheel presents steps of various thicknesses and rotates at a high speed. This results in the generation of a SOBP which is delivered multiple times per second. Downstream of the collimation device, a range compensator is used in order to conform the distal dose distribution to the target volume. While this results in good distal conformality, this also results in larger proximal dose as the full modulation of the SOBP must be delivered throughout the entire target volume. A schematic of a double scattering system is given in figure 2.7.

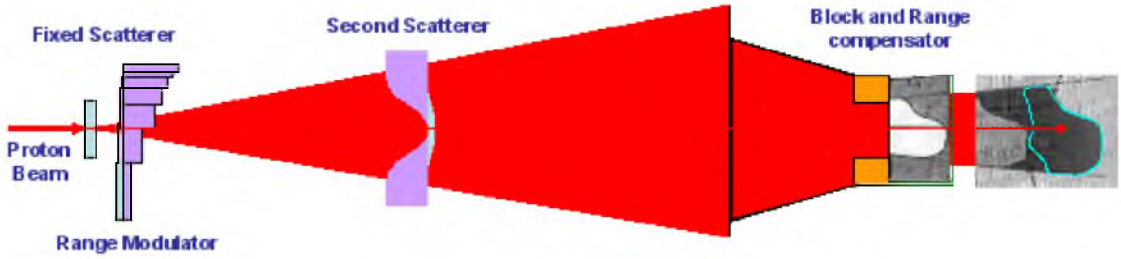

Figure 2.7: *Schematic of a double scattering delivery system: a narrow incident proton beam is scattered twice while the energy of the beam is modulated through a range modulator; the resultant uniform central dose distribution is then collimated and compensated in order to deliver a uniform SOBP that will conform laterally and distally to the target volume.*

2.2.2.2 Scanning

In scanning systems, the narrow incident proton beam is magnetically scanned throughout the target volume using dipoles. In the case of uniform scanning, a single scatterer is used to first broaden the field and deliver a uniform dose that is then collimated similarly to a scattered delivery system. In pencil beam scanning (PBS) mode, the narrow field is displaced laterally such that it conformally shapes to the tumor at each depth. The beam's energy is then modulated directly at the output of the accelerator in order to deliver layers (slices) at depth

throughout the target volume. Additionally, the beam's intensity is modulated throughout the delivery resulting in fully conformal three dimensional dose distributions. The quality of the dose distribution is characterized by the machine parameters such as the range of available energies and the size of the beam. While collimators and range compensators are not required in PBS to obtain good target conformality, they still might be relevant with a machine presenting a larger spot size. A machine with a smaller incident beam, on the other hand, would directly achieve optimal lateral and distal tumor conformality. A smaller spot also permits highly discreet intensity modulation within the target volume, thus allowing for efficient sparing of OAR abutting the target volume. For instance, a hole can be generated within the dose distribution in order to spare the spinal cord in the case that it is located in the middle of the target volume. One solution to reduce the beam size is to utilize a pair of quadrupoles positioned upstream of the scanning magnets, followed by a vacuum chamber. In order to ensure that the delivery is correctly performed, the beam's position, size, and intensity are checked online using ionization chambers (IC). The schematic of a PBS delivery system is presented in figure 2.8.

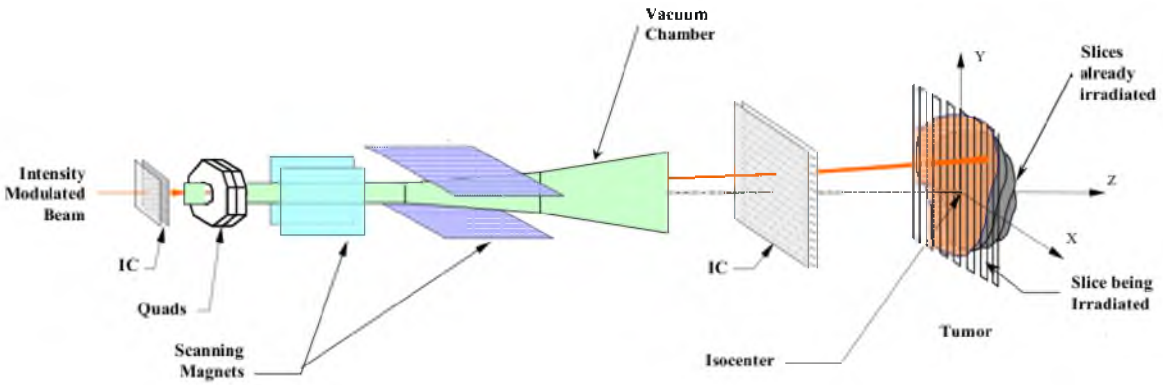

Figure 2.8: *Schematic of a pencil beam scanning delivery system: a narrow incident beam with a given energy is magnetically scanned laterally to conform to the target volume; the energy of the beam is then altered upstream in order to deliver subsequent layers. This technique results in high target conformality laterally, distally, proximally, as well as within the target volume through the use of intensity modulation.*

2.2.3 Clinical advantages

Figure 2.9 compares a 15 MV dose distribution versus a proton SOBP field. The theoretical advantages of protons are quite obvious. The lower entrance dose as well as the lack of exit dose with protons can result in a much greater target conformality along with better OAR spar-

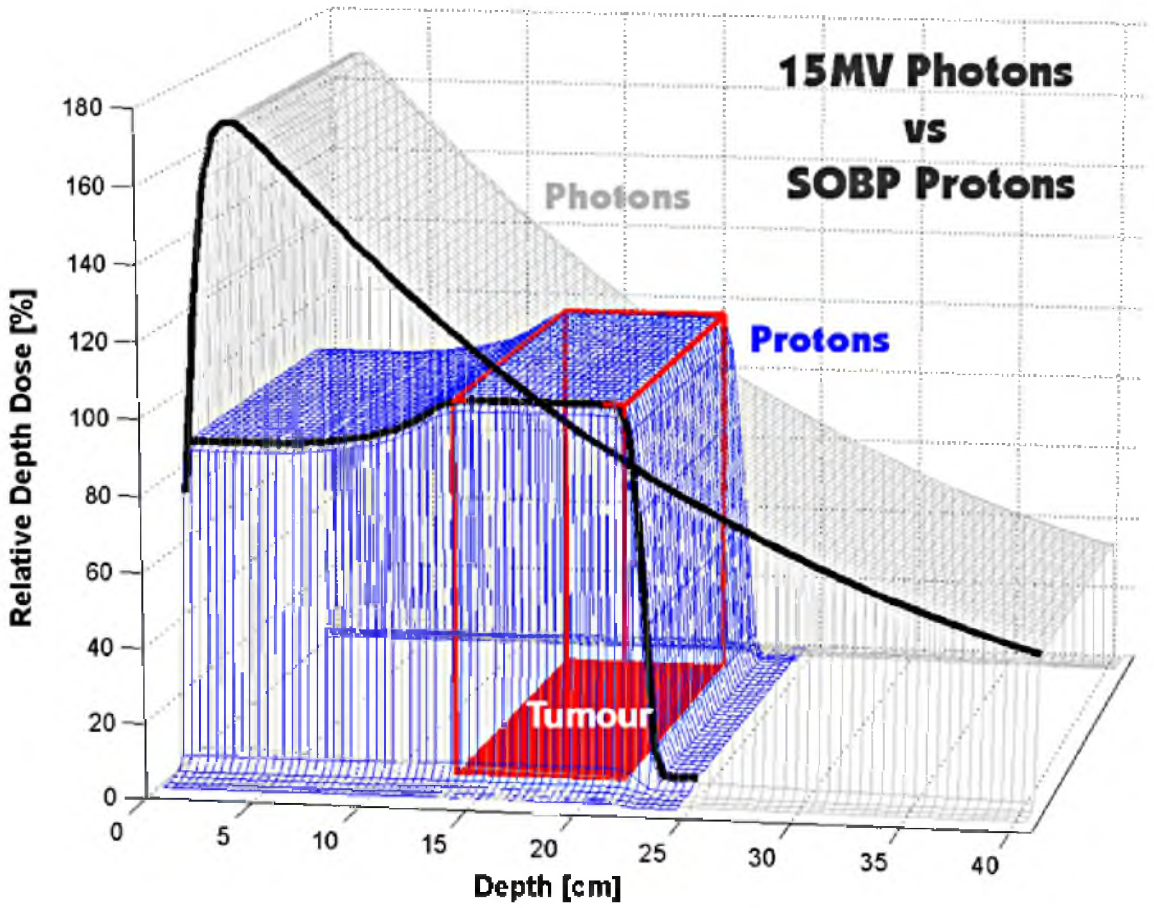

Figure 2.9: *Depth dose distributions of a SOBP proton beam, as compared to a 15 MV photon beam, both adequately covering the tumor.*

ing. Thus, the main benefit of proton therapy usually resides in the significantly lower integral dose as compared to photons (*Purdy [67]*).

Intensity modulated radiation therapy (IMRT) or volumetric modulated arc therapy (VMAT) also offers high target conformality using photons. In some cases, these techniques offer similar treatment quality as passively scattered protons (*Trofimov et al. [16]*). This highlights the limitation of the clinical advantages of proton therapy over conventional therapy. These are, however, invalid comparisons. Indeed, IMRT and VMAT techniques are state-of-the-art in photon therapy, whereas passively scattered proton techniques represent the basics of proton therapy. Conversely, proton PBS techniques allow for far greater conformality of the dose around as well as within the target volume. Recent studies by *Zhang et al. [68]* and *Van de Water et al. [69]* highlight the greater treatment quality expected from PBS as compared to IMRT and VMAT.

2.3 Setup Imaging

2.3.1 Current clinical workflow

A CT scan of the patient is acquired prior to treatment for planning purposes. Digitally reconstructed radiographs (DRR) are then generated for setup purposes based on the CT and the beam isocenter(s) used for treatment planning. The patient is subsequently setup and treated based on these images.
The conventional proton setup process at MGH and most other proton facilities consists of the following steps:

1. The patient is positioned based on tattoos priorly inked at the time of CT.
2. Orthogonal X-rays are taken at a specified cardinal angle.
3. The couch is moved in accordance to the DRR priorly submitted, resulting in a precise placement of the patient at the treatment isocenter.
4. A final "beamline" X-ray is acquired at the treatment gantry angle in order to confirm the accuracy of the treatment position.

This aforementioned workflow presents a number of pitfalls. The CT scan is a map of Hounsfield units (HU) corresponding to the difference in X-rays absorption of the different tissues throughout the body. This HU map must then be converted to proton relative stopping power ratios (RSP) for appropriate dose computation using protons [70]. This conversion carries a certain error due to the quality of the CT reconstruction; this, in turn, contributes to range uncertainties in the proton treatment (*España and Paganetti, Paganetti [71, 72]*). Furthermore, the in-room setup process currently relies on the use of an X-ray unit that is independent to the therapeutic proton beam. Since the imaging and therapeutic beams do not share the exact same isocenter, a systematic shift could potentially exist between the two unit's beam's eye view (BEV).
A proton computed tomography (pCT) imaging system, on the other hand, would directly generate RSP maps. The range uncertainties associated with the pCT scan would therefore be significantly smaller compared to the current CT scan. Additionally, an in-room proton radiography setup system would suppress the aforementioned potential BEV discrepancy. Other

potential advantages of proton imaging technology are the reduced imaging dose and the tumor tracking capabilities.

2.3.2 Proton radiography and computed tomography

The advantages of proton imaging, both radiography (PR) and computed tomography (pCT), were explored in the late 1970s (*Hanson, Hanson, Steward, Kramer et al. [73, 74, 75, 76]*). Their work highlighted the dose reduction with regards to conventional photon imaging as well as the intrinsic problem of limited spatial resolution due to proton scattering (MCS). Nevertheless, this intrinsic spatial resolution limitation was only quantified in the 1990s by a group at the Paul-Scherrer-Institute (PSI) (*Schneider and Pedroni [18]*). The group further developed the idea of proton radiography as a tool for quality control in proton therapy (*Schneider and Pedroni [19]*) and, eventually, produced the first actual proton radiograph of an animal (a dog) (*Schneider et al. [3]*). This first animal radiograph is shown in figure 2.10.

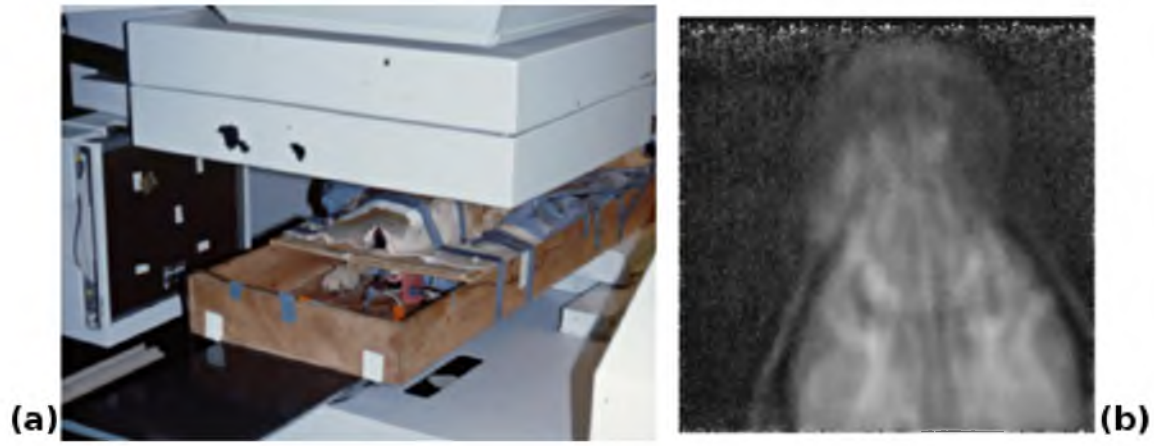

Figure 2.10: *First actual proton radiograph of an animal patient (dog) by Schneider et al. [3]: (a) setup, (b) reconstructed radiograph based on a backprojection algorithm after 100 iterations.*

The poor spatial resolution of proton imaging in comparison to conventional X-ray radiography is quite obvious in this first radiograph. Although, not truly identifiable in this radiograph, the density resolution is higher for proton radiography than photon imaging. This greater density resolution is a strength of proton imaging as it can result in clearer edge detection in certain tumor sites (*Schulte et al. [77]*). The detector used to produce this radiograph was based on the work by *Pemler et al. [4]*. This radiography detector consisted of two scintillating fibers's hodoscopes and a range telescope. The hodoscopes, placed in the front and back of the patient, were used in order to track the position of individual particles. The range telescope

is a large water equivalent column in which the residual Bragg peak is recorded, and the residual range R_{80} beyond the patient computed. This range telescope, not easily discernible in the setup photograph of the experiment (figure 2.10(a)), is bulky and not ideal. A schematic of the design of Pemler's detector is presented in figure 2.11. The computed R_{80} can then be subtracted to the incident beam range in order to obtain a map of water-equivalent path length.

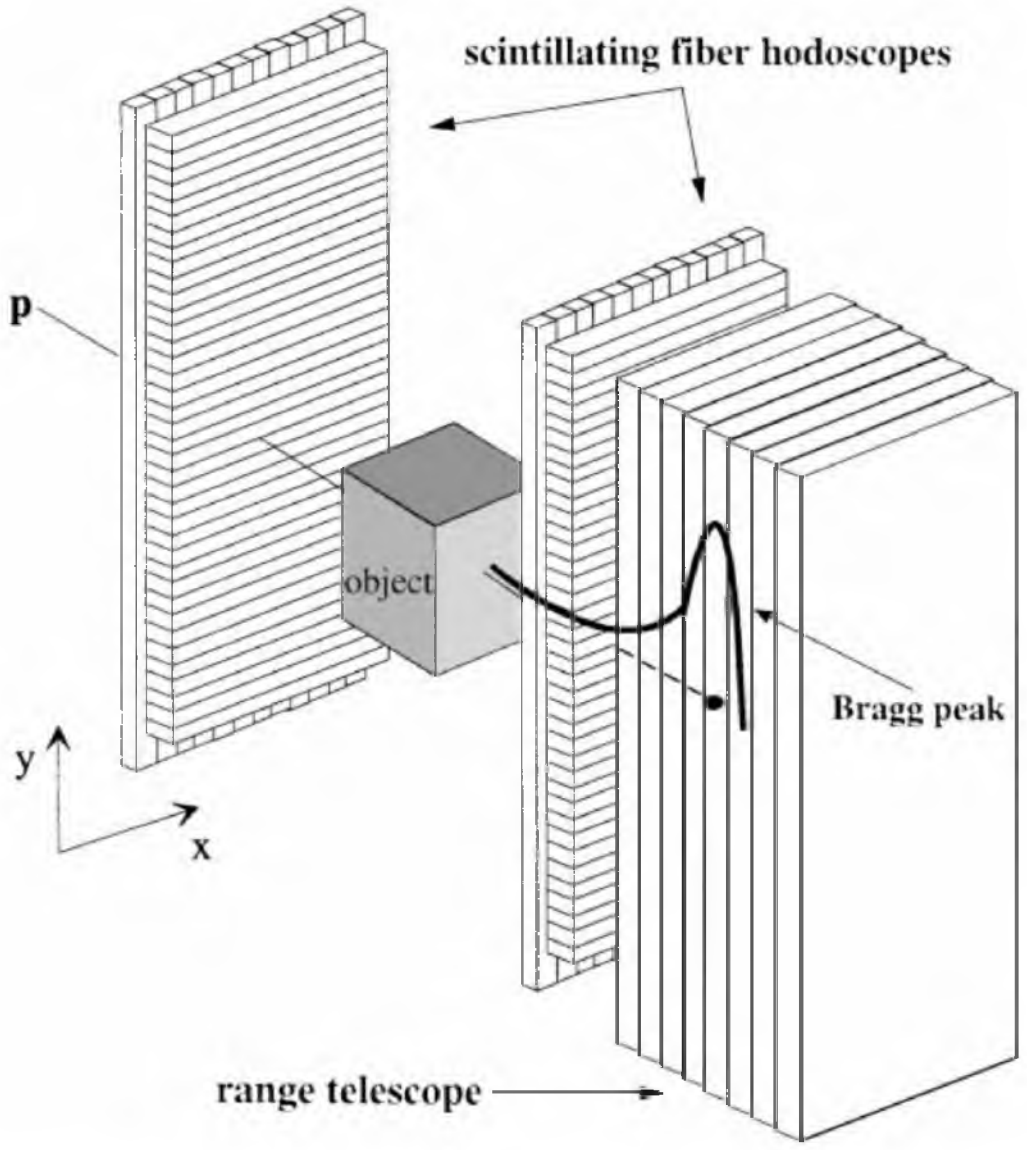

Figure 2.11: *The original design of the proton radiography detector system built at PSI, courtesy of (Pemler et al. [4]).*

The incident proton energy is much higher for proton imaging (ideally maximal) compared to

the typical therapeutic range. The extended energy permits the placement of the Bragg peak beyond the patient and therefore produces images using only the plateau region of the beam. This results in a significant reduction of the amount of dose delivered to the patient.
The protons do not travel in a straight line due to MCS within the patient. Thus, the simple acquisition of the individual particle's position is not enough to ensure an acceptable image quality. The directional information for each particle would also need to be acquired in order to obtain greater image quality. One solution would be to pair the position acquisition devices with a second set (such as the hodoscopes); the direction vectors could then be reconstructed from the two positional information. This was also proposed by *Coutrakon et al. [78]*. The added information could therefore be used to implement more advanced reconstruction techniques such as the most likely path formalism (MLP), proposed by *Schneider and Pedroni [18]*. The MLP technique intends to estimate the proton trajectory in a patient, and therefore more accurately estimate the range degradation. This technique was later improved by *Li et al. [5]* and *Schulte et al. [79]*. Nevertheless, one important limitation to the MLP technique is that it considers the patient as a uniform medium.
The generation of pCT images would also be possible by rotating a proton imaging device mounted on a treatment gantry, such as the one proposed by *Pemler et al. [4]*. It was later shown that an appropriate pCT image quality could be obtained using a conventional back projection reconstruction algorithm along with MLP techniques (*Li et al., Ryu et al. [5, 80]*). Figure 2.12 shows various reconstruction techniques that were investigated through Monte Carlo simulations by *Li et al. [5]*: straight line path (SLP), most-likely path (MLP), and cubic spline path (CSP).

Various improvements have been proposed for either PR or pCT devices based on the original design at PSI. Thus, more recent imaging devices used different technologies such as scintillating tiles (hodoscopes), gas electron multipliers (GEM) detectors, and silicon strip detectors (*Sauli, Johnson et al., Talamonti et al., Sipala et al. [20, 21, 22, 23]*). Whether they are intended for radiography or for pCT purpose, all of these detectors present a range telescope of some sort in order to acquire the energy information of the individual particles. The range telescope-like device renders the entire system bulkier and less practical for clinical use. Thus, a simpler device, in a smaller form factor, would be valuable. A more compact proton radiography system would also open the door to a therapeutic pCT system. Such a device could

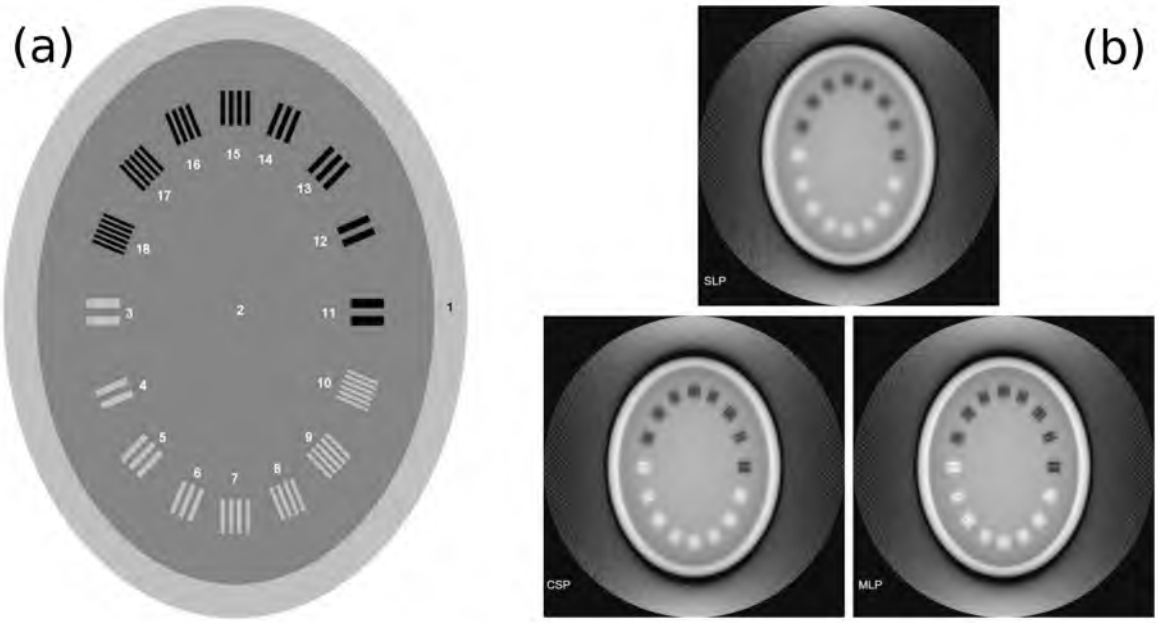

Figure 2.12: *a) Phantom used for pCT reconstruction algorithm consisting of an outer shell with bone density (1), a water inner filling (2), and strips of either air (black) or bone (white) at different densities; b) Monte Carlo simulation of pCT reconstruction of the phantom using different reconstruction algorithm, courtesy of Li et al. [5].*

then be used to obtain accurate proton RSP maps of the patient, which would ensure proper dose calculation accuracy.

A clinical proton imaging system would reduce uncertainties linked to possible discrepancies between the imaging BEV and the therapeutic BEV, while offering a largely reduced imaging dose to the patient. Moreover, proton imaging could be used for online tracking of the tumor during dose delivery by modulating the energy of the beam at the output of the accelerator at a very high speed. With the continuously improving technologies and speed, the system could also update the trajectory of the protons automatically to follow the target, hence reducing the treatment margins.

2.4 Adaptive radiotherapy

2.4.1 Current clinical workflow & TPS

The word "adaptive" presents various meanings as related to radiotherapy. People commonly consider a specific subset of ideas or tools when referring to adaptive treatment. The general definition, however, refers to the overall processes used to alter a given patient treatment

based on an unexpected situation. This situation may arise from a plethora of causes. For instance, anatomical changes in the patient may be detected over the course of treatment during setup imaging; these changes in anatomy might grant the need for replanning. Such a situation arises relatively frequently for certain tumor sites, in head & neck patients for example for which the tumor might initially be present in an anatomical cavity and later recede out of it due to radiotherapy. Another unexpected situation may be the early termination of a patient's treatment for medical or personal reasons. There is only little work associated in this latter situation from a physics or dosimetric's point of view. Typically, only the paperwork and patient record would have to be modified in order to reflect the treatment received. Such a situation is therefore not of real interest in this work. On the other hand, there are various steps associated with adapting a patient's treatment in the case that replanning seems necessary due to anatomical changes:

1. A new CT scan must be promptly acquired, which involves finding space in the CT room schedule.
2. Contours might have to be transfered from the original planning CT to the newly acquired CT through deformable registration.
3. Fixing the transfered contours and/or recontouring would be necessary.
4. If the difference in tumor tissues and soft tissues surrounding the tumor is small between the two registered CT, it might be useful to proceed to a deformable registration of the original dose and assess the discrepancies. This step would be performed for time saving purposes only; the ideal situation would be to recompute the original plan based on the field(s)'s fluences onto the new scan.
5. The quality of the original plan recomputed onto the new CT must then be assessed in order to confirm or rebut the need for replanning.
6. If replanning was deemed necessary, an entire treatment plan, including the paperwork and QA steps, would have to be generated in haste.

The patient might have to be put on a treatment break in order to correctly complete these steps and ensure the planned treatment is delivered. The aforementioned replanning process

must be hurried due to the quick turn around required to ensure the appropriate biological response is received. Thus, mistakes can easily occur.

Although not all cases of adaptive radiotherapy are this work intensive, replanning is regularly necessary. Thus, the adaptive radiotherapy workflow should optimally be seamless. In the ideal situation, the patient would be setup using an advanced setup imaging system, such as cone-beam CT, with some additional software features. The imaging system could automatically recompute the intended treatment plan onto the daily image and decide, based on parameters set by the physician, whether the daily treatment is appropriate or not. If the treatment was deemed inappropriate, the system would automatically adjust the fluence maps from the original plan so that the correct treatment was to be delivered. This process would have to be performed within a few minutes in order to not delay the machine schedule nor compromise the patient's comfort who would be laying on the table.

Such a system is currently unavailable due to the present state-of-the-art in proton algorithm computation speed and the lack of advanced imaging. The current version of Astroid, the TPS at MGH, can only be used for simple treatment planning purposes. Each treatment plan is uncorrelated from one another, and there is no direct link to the actual patient's treatment. In the case of replanning, individual plans must be re-weighted (currently in an external software) so that the actual delivered treatment appears in the patient's record. In the aforementioned optimal scenario, the treatment received would automatically match the initial intended treatment, as the imaging system would automatically recompute/adapt the daily treatment.

The adaptation of the treatment based on the tumor motion is another form of adaptive radiotherapy. Such adaptability would only be possible through online imaging and tumor tracking. A proton imaging system with fast energy switching in combination with a fast recompuation software could then adjust the fluence map on the fly, so that the beam coincides with the target at all times. In the current workflow, this issue must be mitigated through added margins and robustness analysis; this is viable for a passively scattered beam, but might be problematic in PBS due to interplay effects arising from the motion of both the beam and the tumor.

2.4.2 Monte Carlo Verification

Proton radiotherapy centers currently use a pencil beam algorithm (PBA) for dose calculations. At MGH, the PBA is based on the work by *Hong et al. [81]*. The advantages of such algorithms

are their high computation speed capabilities and relatively good accuracy. In the presence of large heterogeneities, however, the lack of lateral equilibrium results in calculation errors as high as 10 % (*Grassberger et al. [24]*). The uncertainties can be partially mitigated through the use of added range and modulation margins based on the planner's experience.

In order to obtain accurate dose distributions, it is thus necessary to turn towards Monte Carlo computations. Figure 2.13 shows the model of MGH's proton double scattering nozzle generated in GEANT4, a Monte Carlo toolkit (*Agostinelli et al., Allison et al. [82, 83]*), based on the constructor's blueprint. This simulation setup permits the accurate recomputation of patient treatment plans at MGH (*Paganetti et al., Paganetti et al. [6, 84]*). Unfortunately, single particle tracking is very lengthy and such GEANT4 calculations present a large overhead. Furthermore, such implementation is difficult to put in place, with not all proton centers having the ability to obtain such resources.

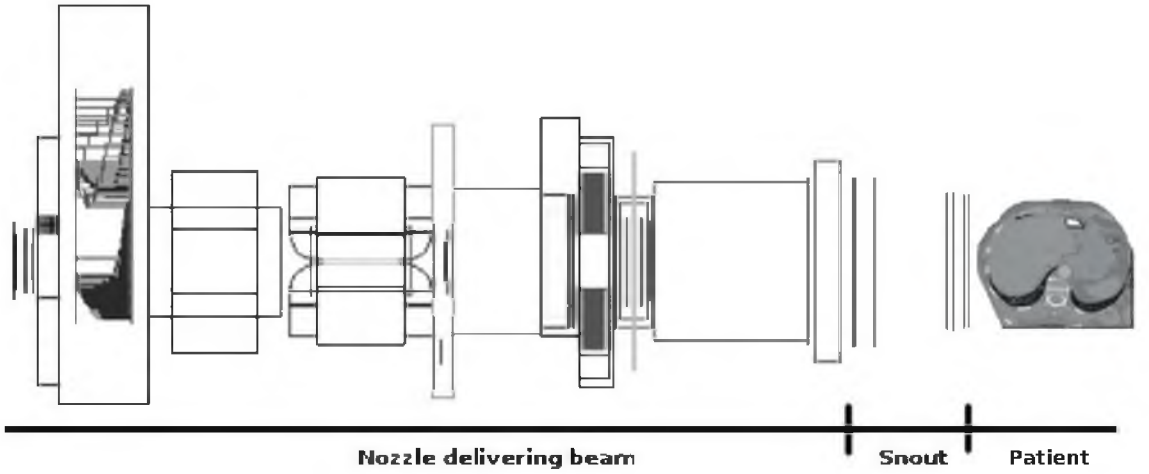

Figure 2.13: *MGH's proton double scattering nozzle model in GEANT4 Monte Carlo toolkit (Paganetti et al. [6]).*

A clinical treatment plan is usually generated through multiple optimizations and at times through multiple beam calculations (change in gantry angle or range shifter). Thus, computation speed is key and Monte Carlo algorithms such as the one presented here are not appropriate for clinical use. The relatively good accuracy of the PBA is thus the trade off for speed. In specific cases, such as patients with large anatomic heterogeneities or large heterogeneities in beam fluence, the patient's intended treatment plan can be recomputed with the Monte Carlo algorithm as a verification step. In the unlikely case that the discrepancies between the Monte Carlo and the PBA calculations are too large, a new plan must be gener-

ated from the outset which might result in a delay in the start of the patient's treatment.
A fast yet accurate dose computation engine, possibly based on Monte Carlo kernels or simplified Monte Carlo calculations, would be useful in order to optimize time and plan quality in the clinical setting.

2.5 Conclusion

Proton pencil beam scanning is at the forefront of the radio therapeutic treatments that can currently be offered. Nevertheless, the technology is in its infancy, with substantial room for improvement. More advanced daily imaging is needed in order to ensure better treatment delivery. More specifically, proton imaging could not only limit the issues linked to uncorrelated imaging and therapeutic beam's eye views, but also result in a significant reduction in imaging dose. Proton computed tomography would also permit the reduction of uncertainties in proton dose calculations. Drastically faster proton dose computation engines are also required in order to significantly improve the current treatment planning workflow and accuracy. The combination of both features, advanced imaging and fast computation engine, would lead to optimal proton PBS adaptive radiotherapy. Daily treatment plan adaptation to account for setup errors and anatomical changes, as well as an online adaptation of the beam position to follow the target, would then become possible. The following work therefore suggests a solution for proton radiography using meshes of scintillating fibers without a range telescope, as well as a fast oversimplified Monte Carlo dose engine for proton dose calculations. The small size of the radiography system would render it more suitable for clinical use, with further development possibly resulting in pCT. The suggested dose engine would track individual particles, thus making it drastically more accurate against tissue heterogeneities than the current pencil beam algorithms. Moreover, the highly parallelizable properties of the dose algorithm would make it suitable for portage to the GPU architecture, thus opening the door to online recomputations.

Chapter 3

Proton Radiography: feasibility studies

3.1 Introduction

Proton radiography was first investigated as a radiologic tool in the late 1970's and early 1980's (*Steward and Koehler, Hanson et al. [85, 86]*), but was unsuccessful to keep up with the growth of its cheaper alternative, X-ray radiography. The latter is now the common diagnostic and setup imaging tool in the clinic. Nevertheless, the recent rise in the number of proton therapy centers around the world is leading to a renewed interest in proton imaging. The use of proton radiography in the clinic for daily set-up could present several advantages: a lesser imaging dose to the patient than with conventional imaging (*Depauw and Seco [26]*), a single beam's eye view (BEV) for both patient imaging and treatment, and a reduced amount of hardware required in the treatment head. The use of a single beam's eye view ensures that there is no possible discrepancy between the imaging isocenter and the therapeutic beam isocenter, and in turn reduce the amount of quality assurance (QA) needed for the machine.
Moreover, the use of more advanced proton imaging such as proton computed tomography (pCT), would result in a significantly more accurate knowledge of the proton stopping power ratios in patient. This could further lead to a reduction in range uncertainties which would translate into smaller treatment margins. It should be noted that, unlike conventional X-ray radiographs which are simple fluence maps, proton radiographs carry some information about the absorbed range in the patient and could potentially help reduce the range uncertainties as well.

The main disadvantage of proton radiography, compared to X-ray radiography, is its poor intrinsic spatial resolution, as shown by *Schneider and Pedroni [18]*. Nevertheless, its higher sensitivity to density variations would possibly present tumor localization advantages in specific tumor sites (*Depauw et al., Depauw and Seco [25, 26]*). The sensitivity of proton radiography to small density variations, as well as its theoretical use in the clinic, are being studied in this work using Monte Carlo simulations. It should be noted that this work is based on "perfect" detectors so that results do not suffer from any bias due to the current detector technology. [1]

3.2 Proton radiography versus X-ray radiography

3.2.1 Simulations setup

This study was performed using the Monte Carlo toolkit GEANT4 version 9.2.p01 (*Agostinelli et al. [82]*) with the physics settings described by *Jarlskog and Paganetti [87]*. Scanned proton pencil beams (monochromatic and unidirectional) (PBS) were considered for this study and set to different energies: 200, 300, 400, and 490 MeV. A double scattered beam (*MGH DS*) at MGH's highest deliverable energy (235 MeV) was also evaluated. The latter was generated using the work by *Paganetti et al. [6]* in which the entire MGH nozzle was implemented, including scatterers and the rotating range modulating wheel. In this case, the wheel was positioned at its thinnest step, resulting in the narrowest energy spectrum at nozzle exit, with a peak at 220 MeV. Furthermore, monoenergetic and unidirectional gamma X-ray beams were simulated for comparison purposes. These consisted of 50 and 100 keV beams, as well as 1 and 2 MeV beams, imitating non-divergent planar sources of kV diagnostic X-rays and MV therapeutic X-rays, respectively.

All beams were simulated covering a homogeneous 40 cm wide square area. It should be noted that due to the absence of multiple Coulomb scattering in the X-ray beams, simulating non-divergent fields slightly bias the results in favors of the X-ray beams. Likewise, the absence of energy spectra (monoenergetic beams) causes a bias towards the X-ray results.

For each primary particle, energy, Cartesian coordinates, and direction cosines were then recorded 1 cm in front of the phantom. Similar information was gathered for both primary and

[1] This work was published in numerous articles (*Depauw et al. [25], Depauw and Seco [26], Seco and Depauw [30], Seco et al. [31], Depauw et al. [27], Polf et al. [32], ? [?]*), and presented at various conferences (*Depauw et al. [28], Seco and Depauw [33], Depauw et al. [29], Dias et al. [34], Seco et al. [35], Seco et al. [36], Spadea et al. [37], Spadea et al. [38]*).

secondary particles in a plane 1 cm behind the phantom. In order to associate the particles in the rear plane and their incident parent in the fore plane, a track-ID number was assigned. This process is shown in figure 3.1(a).

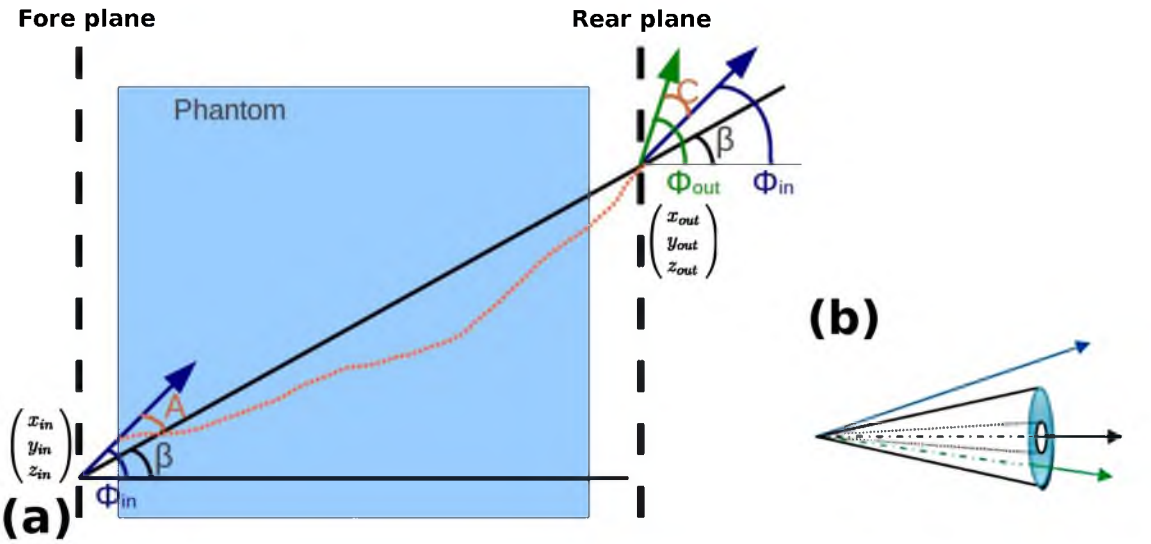

Figure 3.1: *(a) Depiction of data required for radiographs reconstruction: incident particle position (x_{in}, y_{in}, z_{in}) and direction (Φ_{in}), and exit particle position (x_{out}, y_{out}, z_{out}) and direction (Φ_{out}); β shows the angle between the entrance and exit positions, A the angle between the entrance direction and β, and C the one between the exit direction and the entrance direction. (b) Example of a cut in the output data; in this case the green particle would be kept, the blue would be discarded.*

As previously stated, this study does not take into account detector resolution in the image quality in order to avoid any bias from the state of the art in detector technology.

A phantom was specifically designed for this study in order to compare the sensitivity of protons versus X-rays for radiography purpose. The phantom, as seen in figure 3.2, was implemented as a water tank ($30 \times 30 \times 8$ cm^3 or $30 \times 30 \times 15$ cm^3) with cylindrical inserts of various sizes and material compositions. The composition data from the National Institute of Standards and Technology (NIST) (*Berger [88]*) was used to implement air (0.001 g/cm^3), lung type tissue (0.1-0.2-0.3-0.4-0.5-0.6-0.7-and 0.8 g/cm^3), adipose tissue (0.9 g/cm^3), and soft tissue (1 g/cm^3) inserts. The composition data for higher density bony-material (1.1-1.2-1.29-1.39-1.49-1.58-1.67-1.77-1.86-and-1.92 g/cm^3) was implemented based on former data compiled from EGSnrc (*Kawrakow and Rogers [89]*). For each material, a total of 10 cylindrical inserts with similar thickness were modeled with increasing diameter, from 0.88 mm to 20 mm. The simulations were performed a total of 6 times per beam, for 2 water tank

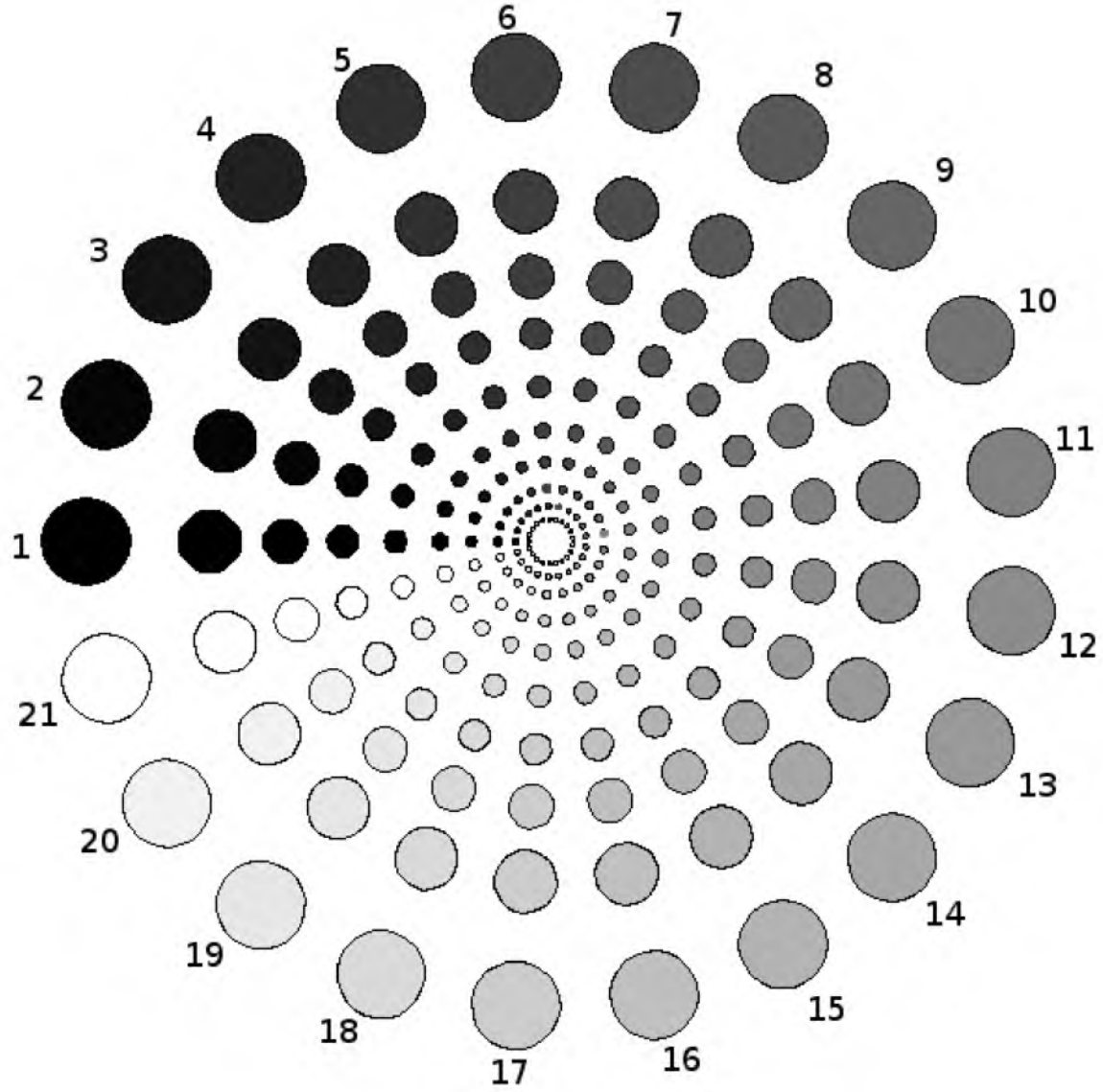

Figure 3.2: *Designed phantom:* $30 \times 30 \times 8$ cm^3 *or* $30 \times 30 \times 15$ cm^3 *water volume filled with rows of 21 different materials with densities ranging from 0.001 g/cm*^{3} *(Air - #1) to 1.92 g/cm*^{3} *(Bony material - #21). This figure was obtained using the GEANT4 visualization driver WIRED (Donszelmann [7]), and then colorized with GIMP (GIMP [8]).*

thicknesses (8 *or* 15 cm^3) and 3 insert thicknesses (2, 4, and 6 cm).

3.2.2 Image reconstruction

Radiographic images in this work were generated using the Matlab™ 2008b commercial software (*MathWorks [90]*). The 40 cm^2 area was reconstructed as 1024x1024-pixel images, roughly corresponding to a 0.4 mm/px resolution. It should be noted that each radiograph's

quality was improved by the proper handling of their window and level, i.e. scaling of the gray values in the images to efficiently use the color map (256 shades of gray).

X-ray radiographs are simple "fluence maps": in each pixel, the imaged value is the number of particles going through that specific pixel. The fore plane particle information was therefore not used during this reconstruction process; instead, radiographs were generated from a pixelated histogram of the output data (rear plane). A 2° angular cut in the output data was performed in order to improved the image quality, mimicking an anti-scatter grid on an actual X-ray system. The actual anti-scatter grid consists of a plate with narrow parallel slits. These slits stop the bulk of the scattered component of the primary X-ray beam, only allowing for the parallel component to pass through and reach the imaging panel.
Conversely, proton radiographs carry more information; they are "range/energy maps": in each pixel, the imaged value is the mean absorbed range R_{abs}, which corresponds to the range in water of the mean energy loss E_{abs} of all the particles going through that pixel. For each particle, the energy loss is computed as the subtraction of the exiting energy (rear plane) to the entering energy (fore plane), with the help of the track-ID number. The report 49 from the International Commission on Radiation Units and Measurements (ICRU) (*Allisy et al. [10]*) was used to determined R_{abs} from E_{abs}.
It should be noted that not all types of proton imaging detectors would be able to perform such reconstruction since they do not all present the capacity to either get the incident particles' data or link this incident data to the output data. This study, however, was supporting a project using a proton stopping power ($\frac{dE}{dx}$) detector which would have such capabilities.
As discussed in Chapter 2, different reconstruction techniques exist for proton imaging. Complex algorithms such as "the most likely path" tend to be more accurate since the protons do not travel in a straight line within the patient. These techniques, however, rely on a homogeneous medium which have yet to be validated in the patient. For this reason, this work considered the reconstruction in the middle of a virtual straight line between the entrance coordinates and the exit coordinates.

In order to reasonably compare the proton to the X-ray radiographs, it was necessary to have both modalities on a similar ground. It was therefore decided to produce images based on an approximate equivalent imaging dose, i.e. absorbed dose to the phantom. An estimation of the absorbed dose was thence performed for each modality. Five million protons and fifty

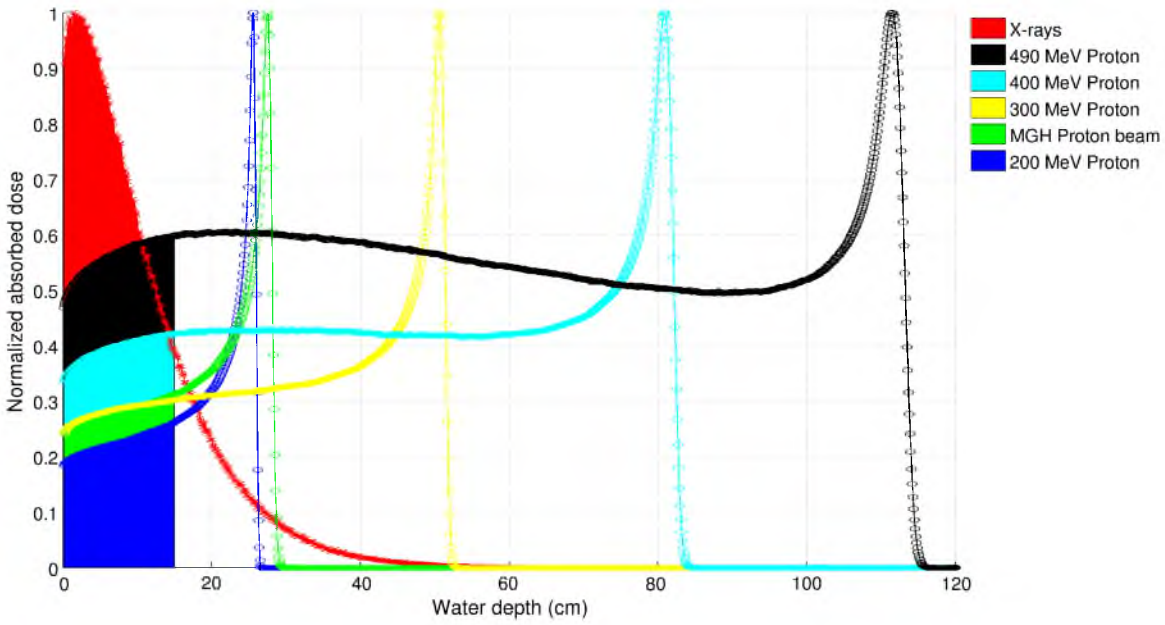

Figure 3.3: *Normalized dose distributions for 100 keV X-rays and various proton energies. The filled area under the curve corresponds to the normalized dose delivered during radiography for a 15 cm thick phantom.*

million X-rays were simulated through $30 \times 30 \times 8$ cm^3 or $30 \times 30 \times 15$ cm^3 water tanks, with the integral energy deposited recorded. It was then possible to derive a relationship between modalities to obtain equivalent simulations for different energies. For instance, fifty million 100 keV photons deliver the same absorbed dose to the 15 cm thick phantom as approximately thirty thousand 200 MeV protons, or fifty-five thousand 490 MeV protons. As seen in figure 3.3, the large difference in the number of particles needed for protons vs X-rays is mainly due to their respective dose deposition curve; in fact, the protons exit the phantom within the plateau region, hence depositing most of their energy beyond it. The radiographic simulations, based on twenty million histories, represent an absorbed dose of approximately 0.002 mGy for a 200 MeV proton beam.

3.2.3 Effect of secondary protons

As previously discussed, protons sometimes undergo a head-on collision with an atomic nucleus in the medium they traverse (see section 2.2.1). These nuclear interactions result in the primary particle transferring a large portion of its energy to a proton in the nucleus. This results in the ejection of both particles with a large scattering angle. The energy of these particles is unpredictable and does not carry the range information desired in proton imaging. Thus, this

represents noise in the output image. In order to study the effect of such noise and how to mitigate it, multiple radiographs were generated for each phantom set-up condition: one for the raw data, one with a cut in the angular spread distribution, one with a cut in the output energy spectrum, and one with both aforementioned cuts. The angular cut was set to different values ranging from 0.1° to 2°, and, for each reconstruction, the best result was kept for analyses. The energetic cut was set so that the lowest 1% of the cumulative energies of the output spectrum was suppressed. These cuts corresponded to enhancements that could easily be implemented in the reconstruction algorithm of an actual proton radiography detector. An example of this is shown in figure 3.1(b).

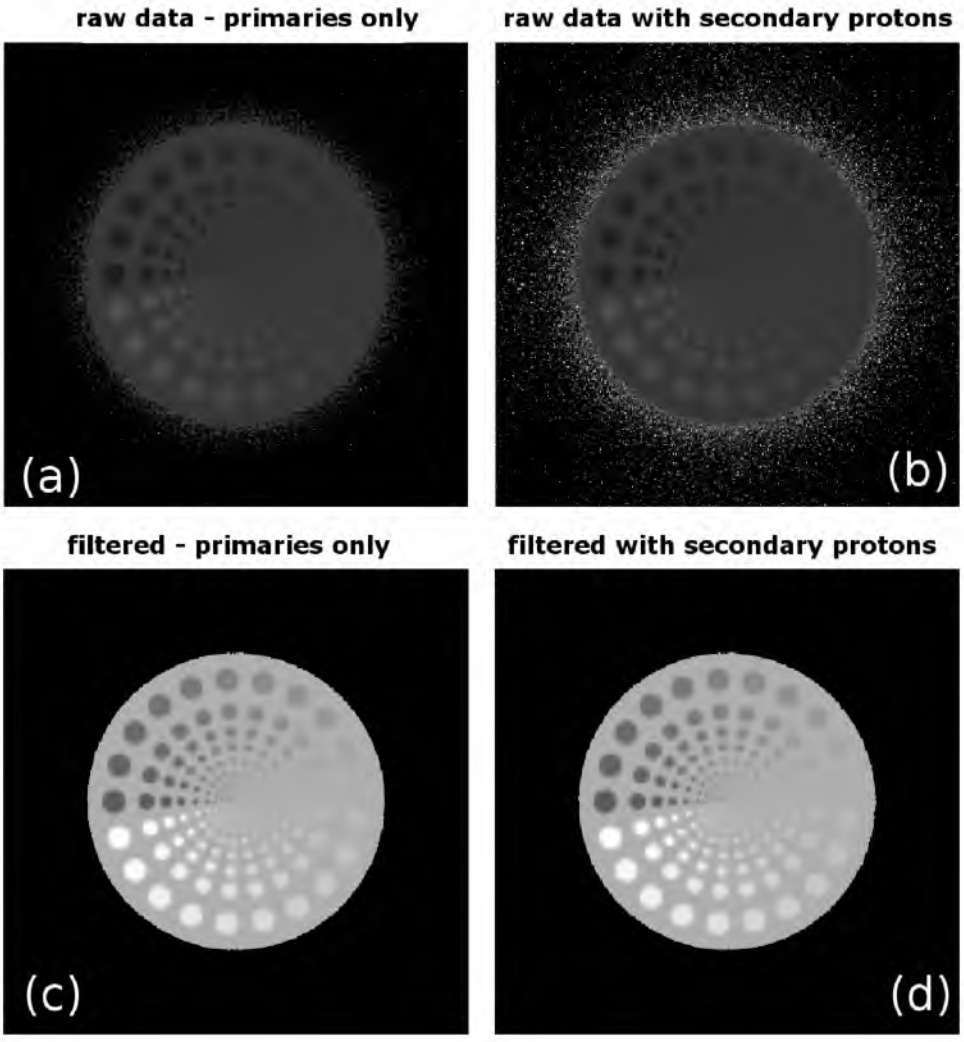

Figure 3.4: *Reconstructed 490 MeV proton radiographs for (a) primary protons only, (b) primary and secondary protons, (c) primary protons with angular and energetic cuts, and (d) primary and secondary protons with angular and energetic cuts. All images were optimized to use the full gray scale, hence resulting in significant contrast difference.*

Figure 3.4 shows a set of four radiographs generated for a 200 MeV proton PBS beam simulated through a 15 cm thick phantom with 4 cm thick inserts. These radiographs were reconstructed using the raw data as well as after both energetic and angular cuts; they also took into account either only primary particles or both primary and secondary particles. Figures 3.4(a) and (b) clearly illustrate the noise created by the secondary protons. Furthermore, figures 3.4(c) and (d) highlight the possibility to mitigate this significant affect by using the proposed cuts. Indeed, the difference image between figure 3.4 (c) and (d) (not shown here by lack of interest) is close to null in every pixel.
Given this result, it was decided to proceed with realistic radiographs for all analyses thereafter, i.e. considering both primary and secondary particles, and using both proposed cuts.

3.2.4 Spatial and density resolution

The spatial resolution can be defined as the minimum size (in mm) a region of interest (ROI) must be in order to be resolved. In this study, the spatial resolution was obtained manually by plotting profiles through the center of each material row (see figure 3.2) and determining the smallest observable insert. An example is shown in figure 3.5. This process was performed using the ImageJ software (*Rasband [9]*) version 1.42q on a Linux system; no automated batch script was used, consequently, the entire analysis was performed by a single person in order to avoid inter-user discrepancies. Additionally, the analyses were ran separately to avoid bias from previous results. This was done to ensure integrity among results and allowing for fair comparisons.
It should be noted that the spatial resolution could have been obtained through the determination of modulation transfer functions. Although it would have been theoretically feasible, such an analysis would have been difficult to perform due to the presence of multiple densities per image. If performed, each line of inserts with a given density would need to be sliced out of the image, leaving very limited information for the smaller elements, and thus jeopardizing the accuracy of the analysis.

The result of this analysis for different beam energies and types is shown in figure 3.6. It can be noted that a more energetic proton beam results in slightly improved spatial resolution. This is explained by the relative reduction in multiple Coulomb scattering as the protons travel through a phantom of similar thickness. Although this result is not clinically significant, there are other

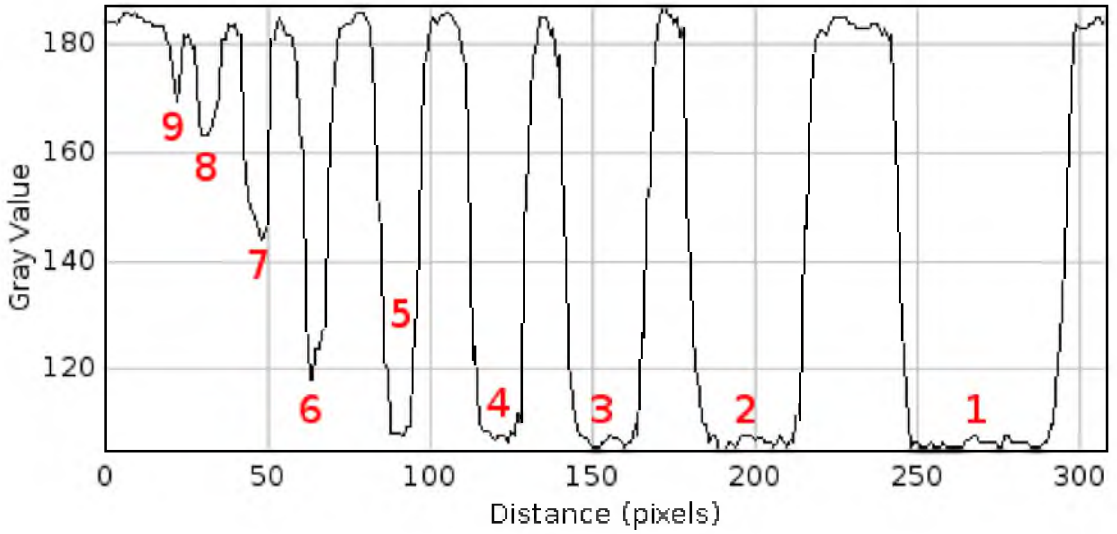

Figure 3.5: *Plotted profile through the air insert row (ρ =0.001 g/cm^3) of a 490 MeV PBS proton beam radiograph using the ImageJ software (Rasband [9]) version 1.42q. The spatial resolution can be determined as the smallest visible insert, # 9 in this instance, hence corresponding to a 1.25mm spatial resolution.*

benefits of using a more energetic beam such as a significant reduction in imaging dose, as well as the possibility to image larger patients due to the deeper penetration properties of the beam.

While the MGH double scattered beam (*MGH DS*) and the 200 MeV proton pencil beam (*PBS 200 MeV*) present similar initial energies, the latter offers far better spatial resolution. This can be explained from the the beam generation. Indeed, the *MGH DS* field was produced through scattering processes in the nozzle which resulted in a large initial energetic and angular spreads of the beam at the phantom entrance; the *PBS 200 MeV* field, on the other hand, was simulated as purely monochromatic and unidirectional. It should be noted that an actual PBS beam would present a certain initial angular spread due to its virtual point source. However, since the location and size of this virtual source are known machine parameters, the presented results are appropriate. Furthermore, this large initial energetic and angular spread in the *MGH DS* beam merely results in a considerably larger number of particles being cut during the radiograph generation. Considering a much larger number of initial particles would certainly result in a spatial resolution close to the one observed for the *PBS 200 MeV* beams.

The spatial resolution for all protons beams is very stable against density, $\approx$ 2-3 mm for any densities greater than 0.1 g/cm^3 to water (background). In order to further assess how far

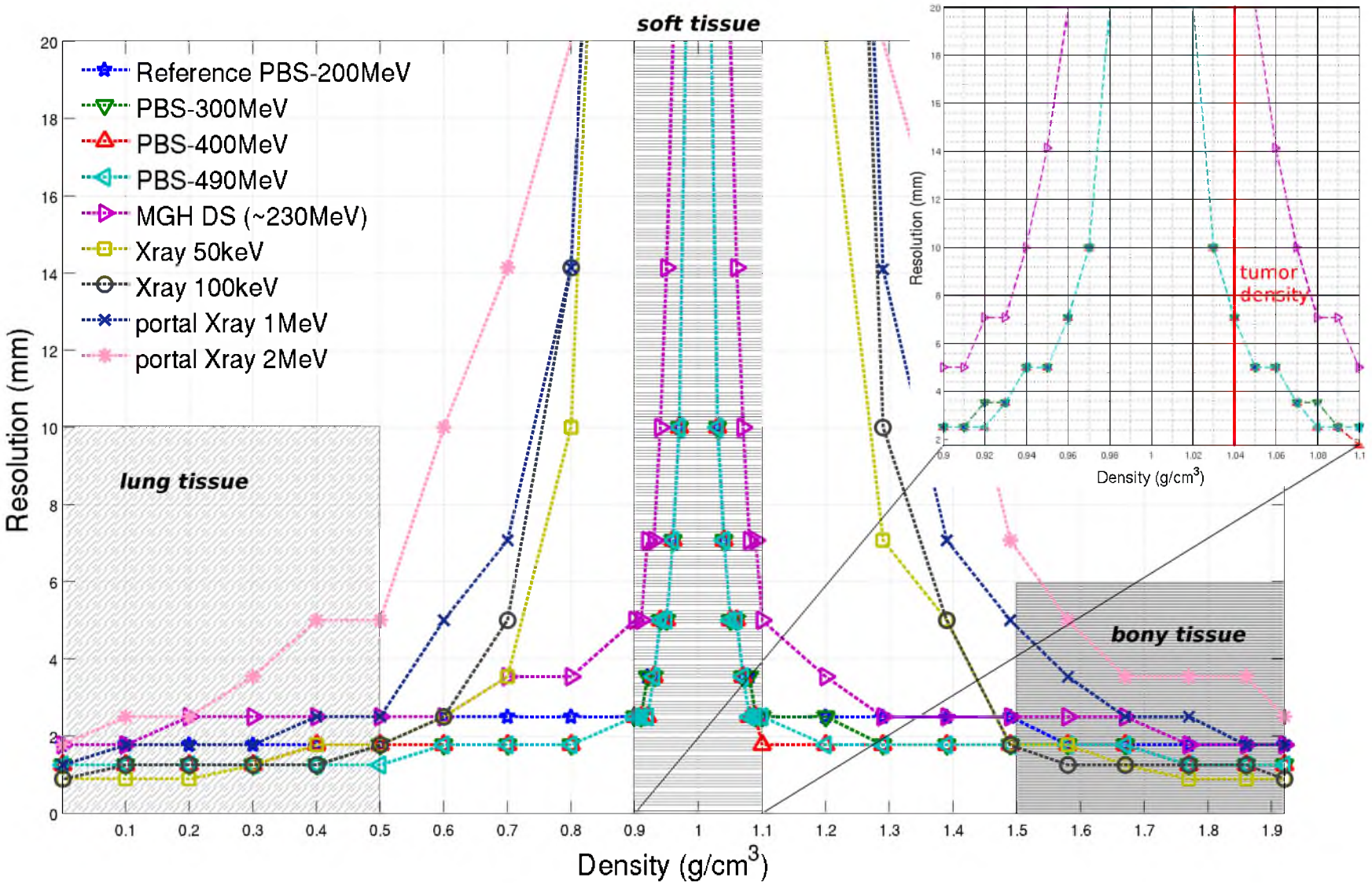

Figure 3.6: *Spatial resolution for radiographs generated with different beams: 200, 300, 400, and 490 MeV scanned proton pencil beams, the MGH double scattered proton beam (~230 MeV), and 50 keV, 100 keV, 1 MeV, and 2 MeV X-ray beams. These were obtained using comparable absorbed dose in a 15 cm thick phantom and 4 cm thick inserts.*

materials could be resolved using proton beams, a modified phantom with similar geometry was ran, but with 21 materials of densities ranging from 0.9 to 1.1 g/cm^3. These materials presented identical composition based on the striated muscle data published in the ICRU-49 report (*Allisy et al. [10]*); only their density was modulated. The striated muscle material was chosen for its density of ρ =1.04 g/cm^3, similar to the density of most tumors.

The close-up in figure 3.6 highlights the results obtained for this modified phantom. It was thus found that, in the best case scenario (i.e. the most energetic pencil beam – 490 MeV), the largest insert (2 cm) could be resolved for any densities greater than 0.02 g/cm^3 to that of the background. For insert with densities significantly different than that of their background (in the given case, $\rho \leq$ 0.6 g/cm^3 or $\rho \geq$1.5 g/cm^3, i.e. lung and bony tissues versus water), conventional X-ray radiography shows better spatial resolution (sub-millimeter) than proton radiography for equivalent imaging dose. This is to be expected due to the intrinsically poor spatial resolution of proton radiography caused by multiple Coulomb scattering (MCS), as stated by *Schneider and Pedroni [18]*. For water density equivalent materials, X-ray operates poorly, emphasizing the poor density resolution of X-rays versus protons. There is no substantial difference in spatial resolution from using a 50 keV beam versus a 100 keV beam. On the other hand, switching to a 1 or 2 MeV beam, i.e. similar to a therapeutic beam on a portal imaging device (PID), translates to a drastic loss in spatial resolution for similar imaging dose. It is worthy to mention that in a clinical context, both kV and MV X-ray radiography would present a remarkably better performance (sub-millimeter resolution for kV) for a much broader range of densities. This discrepancy is explained by the relatively low number of particles simulated in order to preserve the consistency in imaging dose; an actual imaging X-ray source would deliver a significantly higher dose, hence a larger number of particles (see section 3.2.2).

The spatial resolution was also studied as a function of the thickness of both the phantom and material inserts. The results for a 200 MeV proton PBS beam are shown in figure 3.7. The spatial resolution greatly improves as the material insert's relative thickness increases. This is expected due to the increase in interactions with a relatively larger insert. Thus, the best spatial resolution, 0.9 mm, is observed for an 8 cm thick phantom and 6 cm thick inserts. This further emphasizes the protons' sensitivity to density variations.

It might be expected to observe similar spatial resolutions for equivalent phantom/insert thicknesses ratio. This, however, did not occur; for example an 8 cm thick phantom with 2 cm

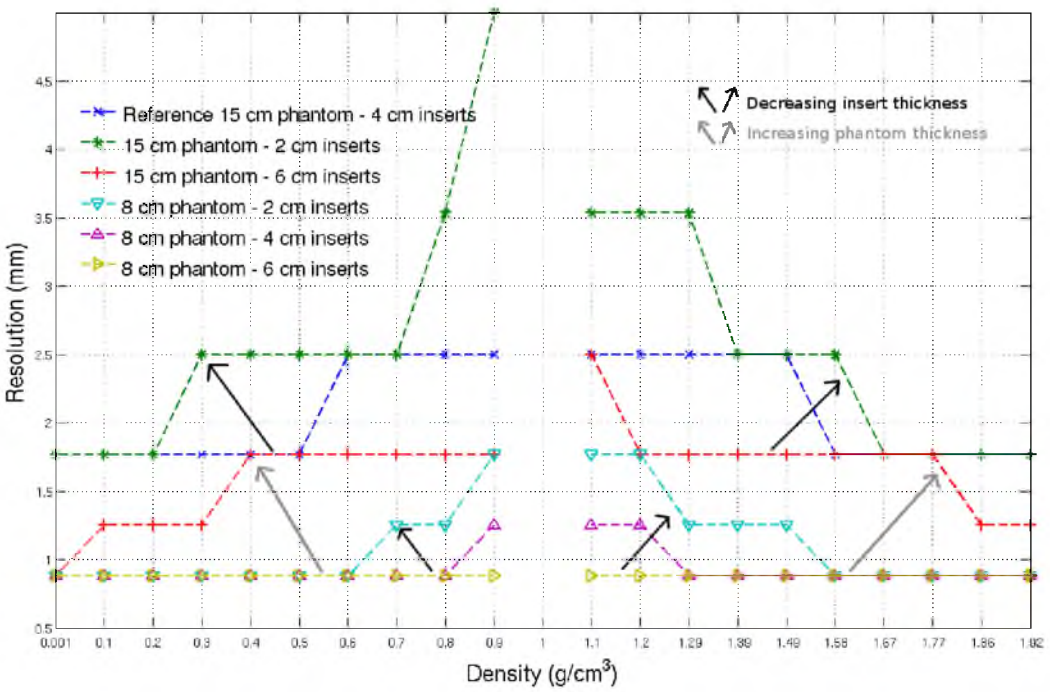

Figure 3.7: *Spatial resolution as a function of material density for various thicknesses of phantom and material inserts: a 8 or 15 cm thick phantom with 2, 4, or 6 cm thick material inserts. The results shown are for a 200 MeV proton PBS beam. Similarly to the previous results, these were obtained considering a similar absorbed dose for a given phantom thickness.*

thick inserts versus a 15 cm thick phantom with 4 cm thick inserts yielded 0.9-1.8 mm versus 1.8-2.5 mm, respectively. This disparity is due to the difference in MCS contribution while traveling through the phantom. Indeed, the geometrical aspect of the MCS's Gaussian distribution (see section 2.2.1) will result in a larger spread of the beam while traveling through a relatively larger medium (as defined in water equivalent depth). For a given relative insert thickness, an 8 cm thick phantom therefore results in a smaller spread of the beam than a 15 cm thick phantom, hence deteriorating the spatial resolution. Similarly, a more energetic beam, i.e. greater velocity of the protons, results in a smaller spread in the exit plane compared to a less energetic beam. This further translates to better spatial resolution. This is illustrated in figure 3.6 with the results for a 490 MeV beam compared to a 200 MeV beam.

The spatial resolution for proton radiography observed in this work was in the order of 1 to 2 mm. This is slightly larger than the 1 mm spatial resolution observed in the literature for studies that used MLP techniques during radiograph reconstruction (*Schneider and Pedroni, Li et al., Schulte et al. [18, 5, 79]*). As previously discussed, these MLP techniques were developed for homogeneous phantoms. In largely heterogeneous mediums, such as a patient,

the accuracy of those techniques have not yet been demonstrated, especially for radiography (single projection) purpose. For this reason, it was decided to only consider simpler reconstruction techniques. This, however, means that more complex reconstruction algorithms taking heterogeneities into account – possibly using the diagnostic X-ray planning CT scan – could show an improvement in the presented results.

3.2.5 Contrast-to-noise ratio

The contrast-to-noise ratio (CNR) is the most important parameter in radiotherapy imaging. It essentially represents the difference in signal-to-noise ratio (SNR) between a region of interest (ROI) and its surrounding background. In other words, clinically, the CNR quantifies the ability to distinguish a tumor from its surrounding healthy tissue. The CNR is defined below in equation 3.1.

$$CNR = 20 * \log\left(\frac{|f-b|}{\sqrt{\sigma_f^2+\sigma_b^2}}\right) \; dB \tag{3.1}$$

Where *f* is the mean signal value in the region of interest, *b* is the average background noise, and $\sigma_{f,b}$ their respective standard deviations. Due to the low statistics in smaller ROI, the standard deviation in the ROI σ_f was substituted by the standard deviation of the background signal σ_b; this is appropriate as the latter is a surrogate for the noise in the system as a whole. CNR was therefore evaluated for each visible cylinder (as defined by the results in the previous section) for various beam energies and type for all studied densities. For consistency purposes, the ROI size for the first insert (2 cm diameter) was set to a circle of 45 pixels in diameter. Each following insert's ROI was then divided by two (diameter divided by $\sqrt{2}$), hence matching the trend of the insert's size themselves.

Due to the excessive amount of data, it was not feasible to report CNR values for each material in all phantom/insert thickness configurations. Thus, we chose to focus on three materials of distinct densities: air (ρ =0.001 g/cm^3), a soft tissue with density close to water (ρ =0.9 g/cm^3), and a higher density bony material (ρ =1.58 g/cm^3). The analysis was performed for proton radiographs using all available PBS beams (200 to 490 MeV) for the different phantom/insert thickness ratios. The results for a 15 cm thick phantom with 4 cm thick inserts are shown in figure 3.8. Additionally, the theoretical local contrasts between those three materials and their water background was computed based on the mass stopping powers of these monoenergetic proton beam as $\frac{|(1/\rho\ dE/dx)_{material}-(1/\rho\ dE/dx)_{background}|}{(1/\rho\ dE/dx)_{background}}$, as seen in table

3.1. The mass stopping power data was obtained from NIST (*Berger [88]*). This table highlights the fact that local contrasts are almost independent of proton energy. Nevertheless, figure 3.8 shows an improvement in CNR as a function of energy for those tissue equivalent materials. This is due to 1) the greater number of particles simulated for a higher energetic beam in order to obtain similar imaging dose, and 2) the larger spreading angle through the medium of the lesser energetic beam due to MCS, as previously discussed. A more energetic beam and/or less material to travel through then translates into less spreading of the output signal, hence better CNR. Thus, following expectations, CNR increases with a thinner phantom and/or thicker inserts; this result is not shown here. For any material densities, the signal in the smaller inserts ($\leq$ 3 mm) becomes too close to that of the water background and the CNR rapidly deteriorates. Similarly, CNR are better for densities greatly different than 1 (background).

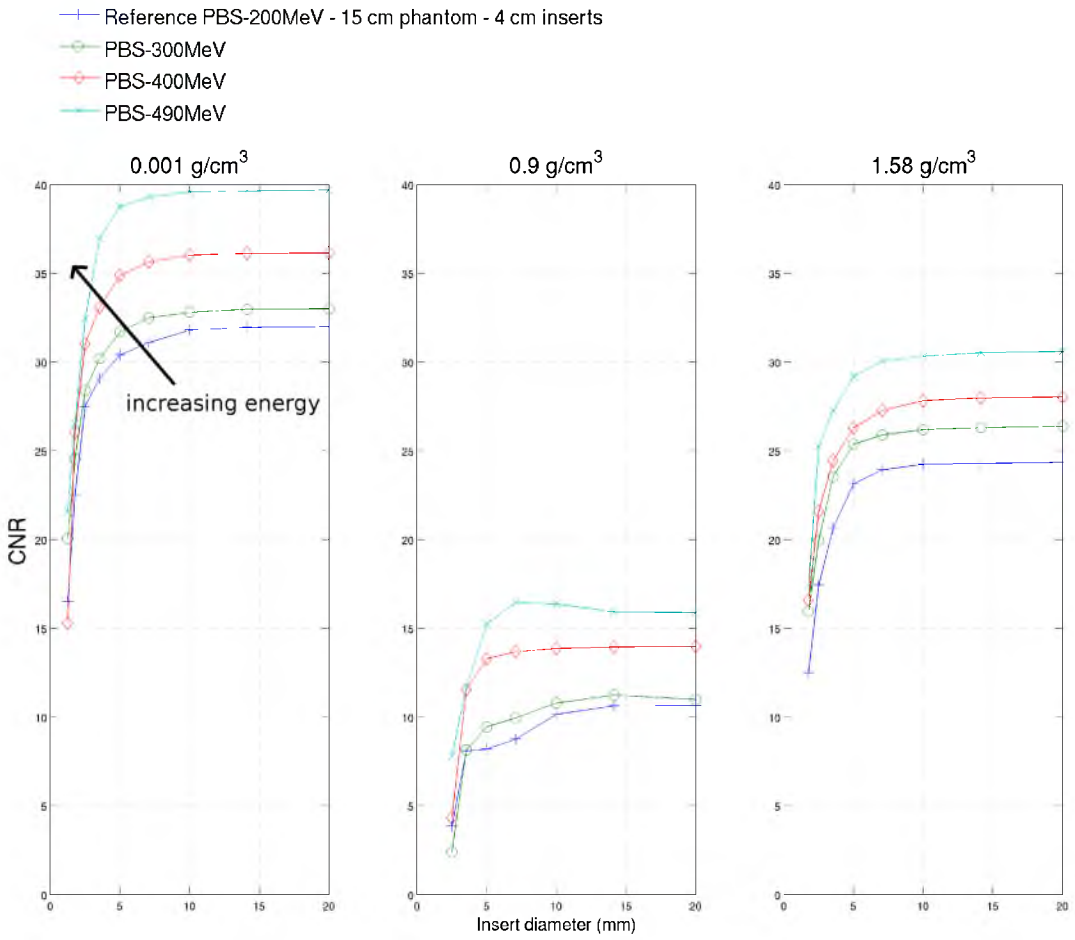

Figure 3.8: *Contrast-to-noise ratio (CNR) of proton radiographs for 3 different densities (0.001, 0.9, and 1.58 g/cm^3) using various scanned pencil beam energies.*

Tissue	200 MeV		300 MeV		400 MeV		490 MeV	
	$^1/_\rho \times {}^{dE}/_{dx}$ (MeV.cm^2.g^{-1})	contrast	$^1/_\rho \times {}^{dE}/_{dx}$ (MeV.cm^2.g^{-1})	contrast	$^1/_\rho \times {}^{dE}/_{dx}$ (MeV.cm^2.g^{-1})	contrast	$^1/_\rho \times {}^{dE}/_{dx}$ (MeV.cm^2.g^{-1})	contrast
Air (0.01 g.cm^{-3})	3.98	0.11	3.12	0.11	2.69	0.11	2.45	0.11
Adipose tissue (0.9 g.cm^{-3})	4.61	0.03	3.61	0.03	3.11	0.03	2.84	0.02
Bony tissue (1.58 g.cm^{-3})	4.20	0.07	3.29	0.06	2.84	0.06	2.59	0.06
Water background (1.0 g.cm^{-3})	4.49	–	3.52	–	3.03	–	2.77	–

Table 3.1: *Theoretical local contrasts between different materials and water (background) for four proton beam energies (200, 300, 400, and 490 MeV).*

A comparison of CNR between a 200 MeV proton PBS radiograph, a kV X-ray radiograph, and an MV X-ray portal image is shown in figure 3.9. These radiographs were generated with similar imaging dose. CNR values are very good for protons for low and high density regions ($\rho \leq 0.6$ g/cm^3 or $\rho \geq 1.5$ g/cm^3), better than conventional X-rays. Nevertheless, as previously discussed, clinical X-ray images would present significantly higher CNR values due to the higher imaging dose (number of particles). The medium density region (0.6 g/cm^3 $\leq$ $\rho \leq$1.5 g/cm^3) could not be resolved using X-rays, whereas protons present acceptable CNR values. This further supports the greater density resolution of proton radiography as compared to conventional X-ray radiography for a similar absorbed dose. Protons offer better visualization of density variations and could therefore provide more distinct delimitation of specific tumors' edges. Analogous to the spatial resolution results, an MV X-ray therapeutic beam results in far worse CNR than a diagnostic kV unit. Thus, reducing tumor localization compared to kV imaging.

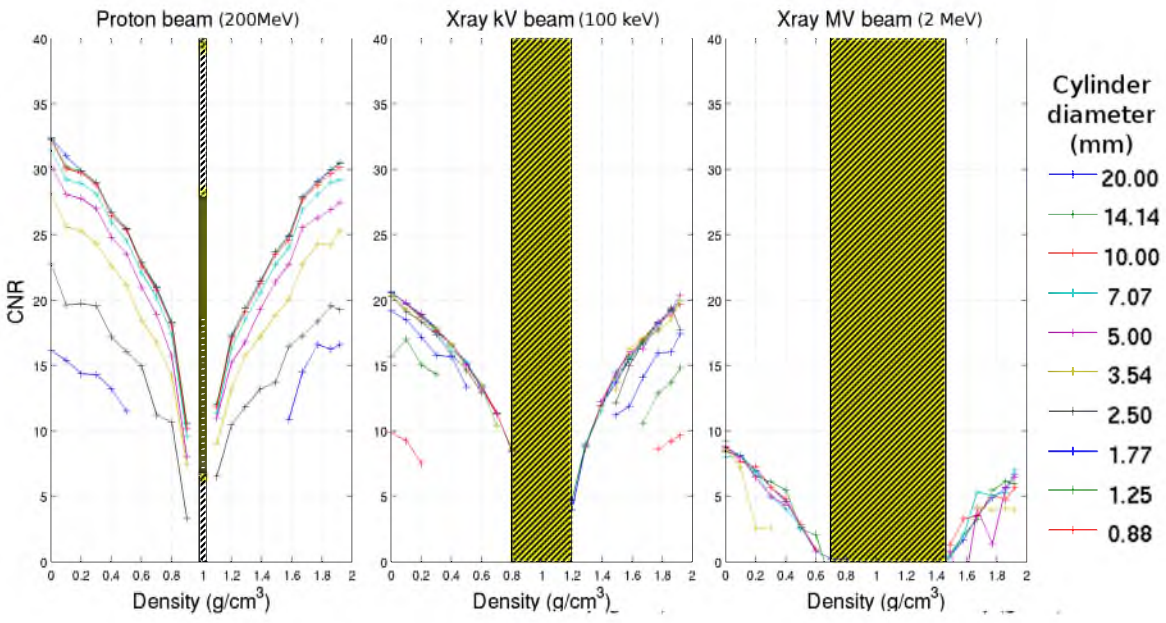

Figure 3.9: *Contrast-to-noise ratio as a function of material density and insert size for radiographs generated with a 200 MeV proton PBS beam, a pure 100 keV X-ray beam and a pure 2 MeV X-ray beam, for similar absorbed dose. The hatched area reflects the range of densities for which no insert could be resolved for the specific modality.*

3.3 Patient studies

Proton radiography, compared to conventional radiography, is promising for clinical use due to its lower imaging dose and greater density resolution. Indeed, higher imaging dose in pediatric patients undergoing conventional X-ray radiography can result in dramatic effects for the patient, such as abnormal growth or the risk of future malignancies [17]. The use of proton imaging, however, could help mitigate these effects due to the lower imaging dose. Furthermore, for patients with moving tumors, proton treatment delivery could be enhanced using proton radiography as a tool for tumor tracking.

Thus, the following work focuses on patient cases in order to confirm the imaging capabilities of proton radiography, as well as to look into image guided proton radiation therapy (IGPT) based on lung and liver cases. This work was complemented by evaluating the use of carbon ions for patient imaging due to their similar physical properties and further intrinsic imaging qualities (reduced MCS component compared to protons).

3.3.1 Simulations setup

A stage IIIA non-small cell lung cancer (NSCLC) patient was sought out in order to confirm the previous results on imaging quality. Additionally, a pediatric case consisting of a 3 $^1/_2$ year old patient who had a whole body CT scan was considered. In order to assess the possibility of IGPT using direct tumor tracking, the patient cohort was comprised of two adult cases with lung cancer: a female patient presenting a tumor in the lower region of the right lung with significant motion amplitude ($\approx$1 cm), and a male patient with a tumor in the upper region of the right lung with smaller motion amplitude ($\approx$0.5 cm). Finally, a third adult liver case with fiducial markers was considered in order to investigate IGPT using indirect tumor tracking.

Similarly to the previous phantom study, the Monte Carlo toolkit GEANT4 version 9.2.p01 (*Agostinelli et al. [82]*) was used with the physics settings described by *Jarlskog and Paganetti [87]*. Except for the initial NSCLC patient study, scanned pencil beams (monochromatic and unidirectional) of 230 and 330 MeV protons, as well as 500 MeV/nucleon carbon ions, were simulated covering a 40 cm^2 homogeneous area. For the former NSCLC study, proton radiographs were simulated with 230 and 490 MeV beams in a 30 cm circular field. On average, twenty million histories (primary particles) were simulated to produce proton and carbon ion radiographs. For each patient, CT scans were acquired on a GE LightSpeed QX/i

with 2.5 mm slices made of 512 × 512 pixels. In the case of the lung and liver patients, 4D CT data sets comprised of the 10 breathing phases were each considered in order to evaluate the effect of tumor motion. The CT data was imported into the GEANT4 code through a Hounsfield unit (HU) to material conversion based on the work first described by *Paganetti et al. [84]*. Although this original method described a conversion using 24 distinct tissue definitions with 24 densities, the implementation utilized in this work was based on an improved conversion using the same 24 tissue definitions but with a total of 4,071 distinct densities. This conversion therefore allows for accurate computations of particle interactions within the patient.

The energy, Cartesian coordinates, and direction cosines were recorded for each primary particle crossing a plane 1 cm before the patient, as well as for each primary and secondary ion crossing a plane 1 cm behind the patient. A track-ID registration parameter was used in order to correctly associate output and input particles. This patient simulation setup is presented in figure 3.10.

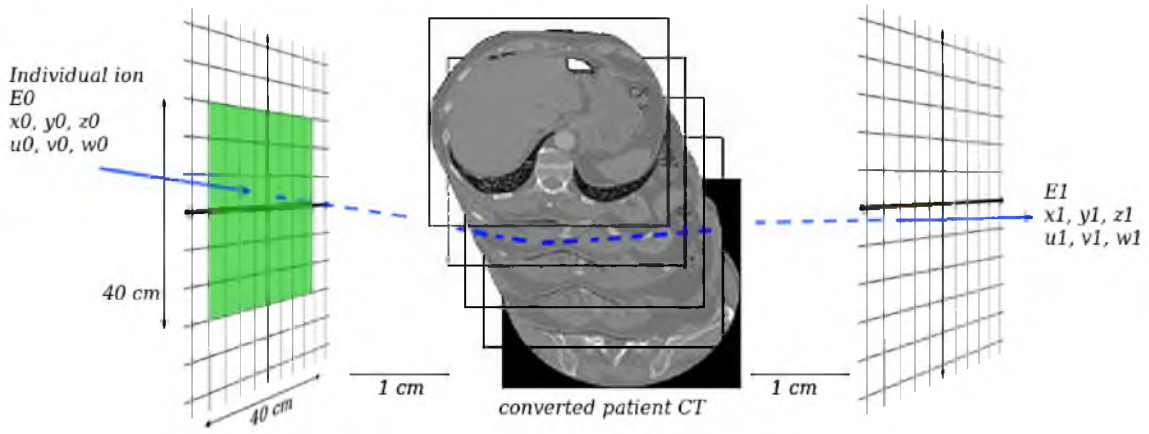

Figure 3.10: *Proton radiography patient simulation setup designed in the GEANT4 MC toolkit based on the patient CT scan converted to material definitions. E_0, (x_0, y_0, z_0), and (u_0, v_0, w_0) represent the initial particle's energy, position, and directions respectively, while E_1, (x_1, y_1, z_1), and (u_1, v_1, w_1) represent similar parameters for the exiting particle.*

Ion radiographs in this study were reconstructed with an algorithm similar to the one presented in section 3.2.2. Apart for the initial NSCLC case, pictures in this study were reconstructed as 1024 x 1024 pixel images corresponding to a 0.4 mm/pixel resolution. Energetic and angular cuts were also applied in order to obtain the most visually appealing images in which tumor location could be appreciated at its best. For patients with 4D CT data (lung and liver), an ion

radiograph was produced for each phase of the breathing cycle, and an animated sequence was subsequently generated in order to fully evaluate the tumor tracking capabilities.
CNR values were computed between the tumor and various surrounding tissues based on equation 3.1, in order to evaluate the tumor visualization quality. These analyses were performed using the ImageJ software (*Rasband [9]*) version 1.46a, except for the earlier NSCLC study for which version 1.42q was used.

3.3.2 Lung patients

3.3.2.1 Image quality

A side by side comparison of an actual kV X-ray CT scout and the simulated proton radiographs for the selected NSCLC patient is shown in figure 3.11. It should be noted that, unlike the previously presented phantom study, no absorbed dose equivalency between X-ray and protons was performed. The Health Physics Society's recommendations, as well as independent studies, suggest that a conventional chest X-ray delivers approximately 0.02 mSv to a patient (*Society, Walter et al. [91, 92]*), an order of magnitude larger in comparison with the simulated radiograph. Thus, this translates into a bias toward the X-ray quality due to the significantly larger imaging dose. It does not, however, impair these results from drawing appropriate clinical judgments.

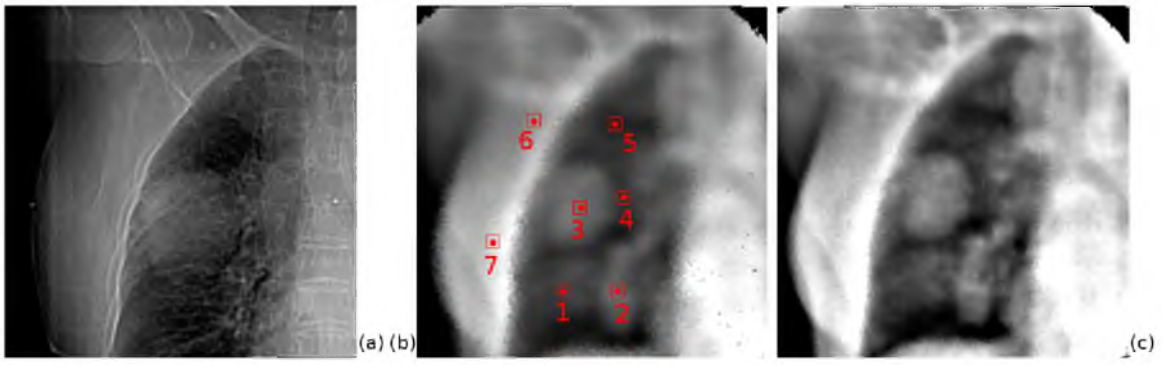

Figure 3.11: *(a) Actual kV X-ray scout and simulated (b) 230 MeV and (c) 490 MeV proton PBS beam radiographs for a selected patient with NSCLC. The numbered squares in b) correspond to the selected areas for which CNR versus the tumor (region 3) were compared.*

Spatial resolution is difficult to quantify in images generated from highly heterogeneous medium such as patients; it was thus decided to evaluate the spatial resolution only through visual inspection. The X-ray scout offers a noticeably better spatial resolution, as highlighted by the

superior edge detection in certain tissues such as the vertebraes and the clavicular bones. As previously discussed in section 3.2.4, the poor spatial resolution is an intrinsic limitation of proton radiography due to the MCS component of the beam. Matching expectations, a more energetic proton beam (490 MeV radiograph compared to 230 MeV image) results in a higher spatial resolution due to the smaller scattering angle of the beam.

Figure 3.11(b) shows 7 ROI within the lung and bony tissues surrounding the tumor (ROI #3). CNR between these various background ROI and the tumor were computed. The results are presented in table 3.2.

ROI #	actual kV X-ray scout			200 MeV proton radiograph			490 MeV proton radiograph		
	Signal Mean	Std Dev	CNR	Signal Mean	Std Dev	CNR	Signal Mean	Std Dev	CNR
1	42.1	8.2	12.0	69.5	2.2	19.3	64.3	3.7	20.8
2	41.4	7.5	12.6	90.9	4.3	10.6	85.3	8.2	12.6
3	82.1	5.9	-	110.6	3.9	-	124.2	4.0	-
4	58.4	8.0	7.6	57.3	3.1	20.6	52.1	3.8	22.3
5	30.6	4.8	16.6	50.4	2.4	22.4	44.3	3.9	23.1
6	120.0	2.6	15.4	141.2	3.2	15.7	169.9	4.5	17.6
7	133.0	5.8	15.8	214.6	6.1	23.2	231.4	4.7	24.8

Table 3.2: *CNR values between different ROI and a tumor background (ROI #3).*

The use of protons for lung tumor imaging results in higher CNR than using conventional X-ray radiography due to their higher density resolution, and furthermore, at a fraction of the patient absorbed dose. This confirms our previous findings and signifies a clearer tumor edge definition in proton radiographs, despite the greater spatial resolution in the X-ray scout image. This further emphasizes the possibility for using proton imaging for lung patient setup. An additional benefit, as further discussed in the pediatric case study (see section 3.3.4), is the use of a unique beam's eye view for both the imaging beam and the therapeutic beam.
These results led us to further look into the possibility of using proton imaging for direct tumor tracking in lung cancer patients.

3.3.2.2 Direct tumor tracking capabilities

Figure 3.12 shows reconstructed sequences of the male lung tumor case for 230 MeV and 330 MeV proton beams, as well as for a 500 MeV/nucleon carbon ion beam.

CNR were also evaluated between the tumor and its direct surrounding tissues, as previously

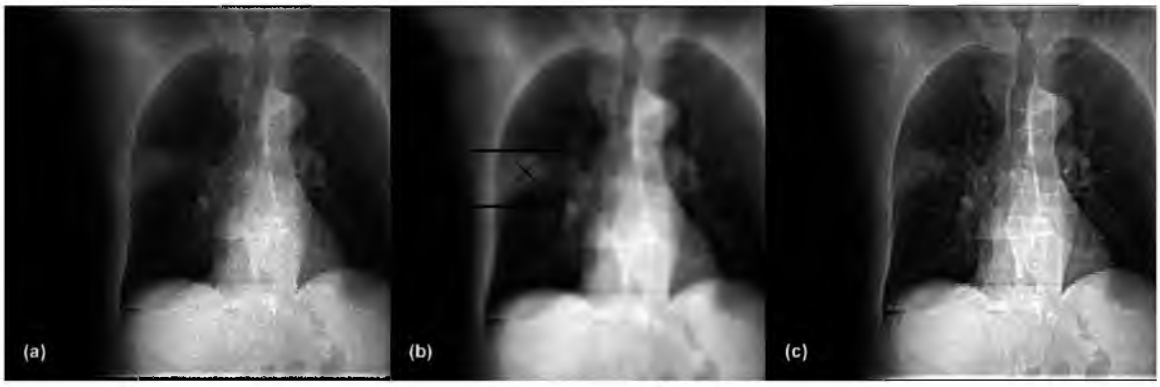

Figure 3.12: *Reconstructed 4D radiograph sequences through a lung tumor patient breathing cycle for radiograph with (a) a 230 MeV proton pencil beam, (b) a 330 MeV proton pencil beam, and (c) a 500 MeV/nucleon carbon ion pencil beam. Please note: These sequences must be visualized using a PDF reader software with sequence display capabilities such as Adobe Acrobat™ in order to fully appreciate the motion.*

described in the static lung study. In this case, the average of values in ROI similar to square 4 and 5 in figure 3.11 was chosen, corresponding to surrounding lung tissue. CNR values were 4.7 dB, 6.1 dB, and 9.3 dB for figure 3.12(a), 3.12(b), and 3.12(c), respectively.

As predicted, the tumor edges are clearly defined on each of these radiographs. Higher proton energies not only result in higher spatial resolution due to the relatively lower MCS effect of the beam, but also result in higher CNR which translates into significant improvement of tumor edge detectability. Imaging of the tumor could therefore be performed concurrently to the radiation treatment as long as the accelerator's output energy can quickly be modulated accordingly. While this would not apply to current cyclotron-based ion centers, this would be feasible with a synchrotron-based delivery system. Such system would therefore result in a proton "gated" delivery based on direct tumor tracking. The greater tumor edges' sensitivity of the more energetic beam transcribes to greater IGPT capabilities, while delivering lower imaging dose to the patient, and offering the possibility for imaging thicker patients.

A carbon ion beam undergoes much smaller deflection than a proton beam, hence resulting in drastic imaging improvement. This highlights the excellent opportunity offered by ion beams for IGPT with direct tumor tracking.

A comparison of 330 MeV proton radiograph sequences generated for both aforementioned lung patients is shown in figure 3.13.

Computed CNR are 4.9 and 6.1 for radiograph 3.13(a) and 3.13(b), respectively. The differ-

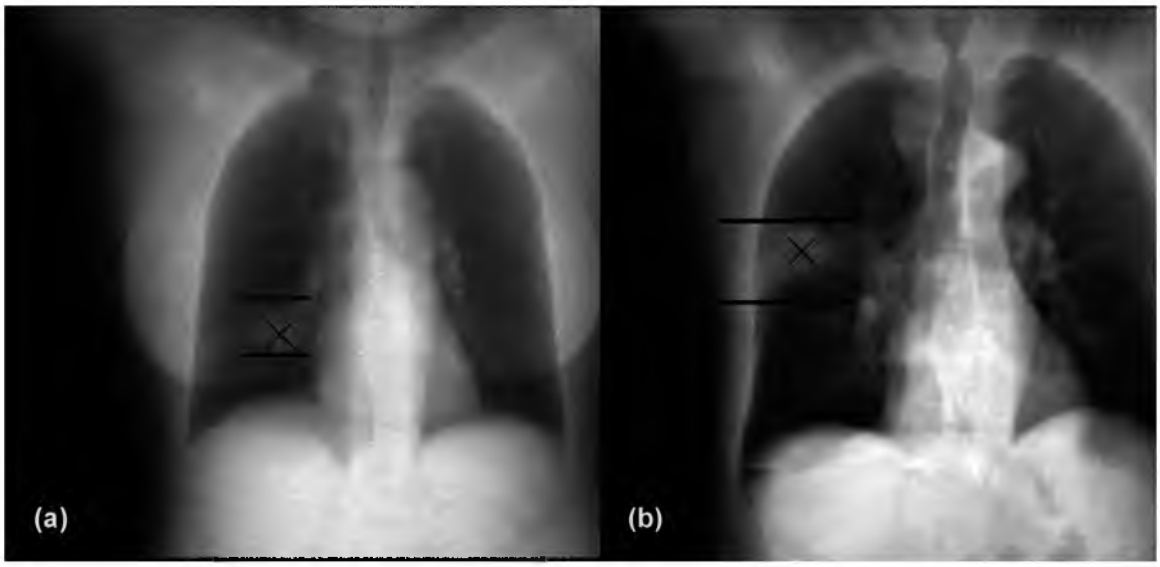

Figure 3.13: *Reconstructed 4D radiograph sequences for two lung cancer patients: (a) a female case and (b) a male case. These radiographs were generated based on 330 MeV proton beam simulations. The tumor edges are clearly defined, and the tumor center position is shown by an "X" mark. The tumor motion amplitude is further highlighted with the lines. Please note: These sequences must be visualized using a PDF reader software with sequence display capabilities such as Adobe Acrobat™ in order to fully appreciate the motion.*

ence in CNR, as well as overall visual quality, is easily explained by the differences in patient anatomy. Patient (a) is a large female presenting a large breast which contributes to a significant deterioration in the proton beam; conversely, patient (b) is a slender male which translates to greater imaging capabilities due to MCS. This discrepancy further highlights the advantage of using a more energetic beam which would not deteriorate through various patient anatomy as significantly as observed in this study. Although the tumor's amplitude of motion, size, and location varies greatly among these two cases, both images result in clear tumor delineation and clear appreciation of tumor motion (≈0.5 cm in the female case and ≈1 cm in the male case). Thus, direct tumor tracking could be used for IGPT in a large cohort of lung cancer patients with distinct tumor specifications. The large difference in tissue density between the tumor and its surrounding tissues in the case of lung patients is an important factor in these results. In order to further assess the limit of IGPT possibilities, we further looked at a liver case for which the tumor and its surrounding tissue present very similar densities.

3.3.3 Liver patients - indirect tumor tracking

Tumor delineation is significantly more complex in liver patients than it is in some other sites due to the close proximity in densities between the tumor (≈1.04 g/cm^3) and its surrounding

tissues ($\approx$1.06 g/cm^3). For this reason, it is common practice to surgically add fiducial markers (gold seeds) in predefined locations around the tumor for delineation and setup purposes. When visually resolvable, these markers can further be used for indirect tumor tracking in ion therapy.

Figure 3.14 shows a side by side comparison between radiographic sequences generated with a 330 MeV proton beam and a 500 MeV/nucleon carbon ion beam through a liver patient 4D CT. The fiducial markers were 1.2 mm in diameter and 5 mm in length. The 230 MeV proton radiography sequence is not displayed here by lack of interest, as further discussed. The CNR between the tumor and its surrounding tissue were evaluated at 0.06 dB, 0.09 dB, and 0.44 dB for the 3 beams, respectively. These very low values further highlights the difficulty in detecting the tumor's edges.

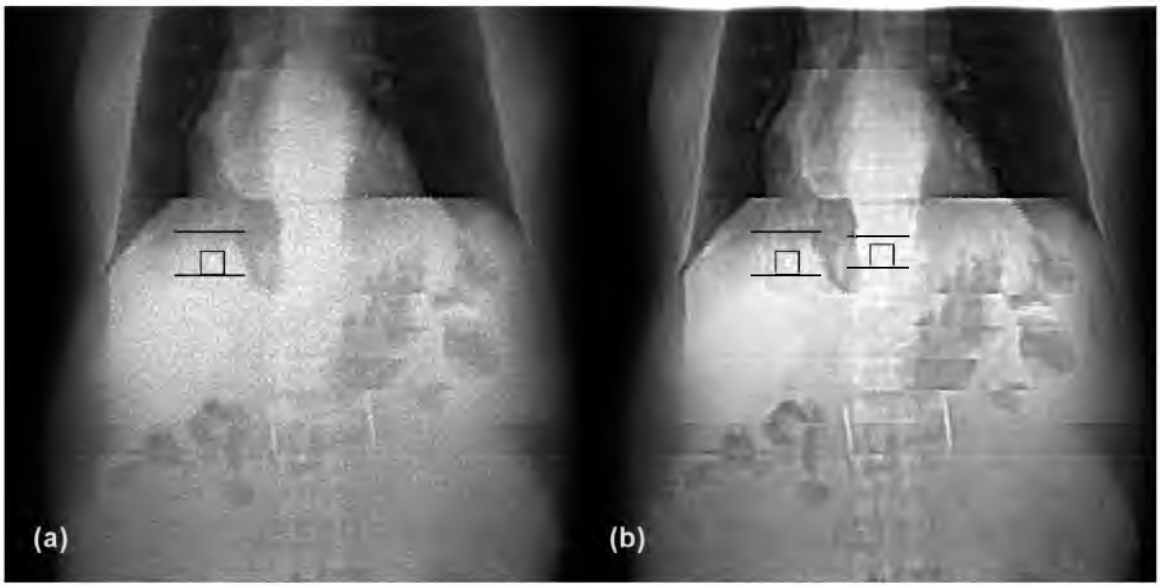

Figure 3.14: *Reconstructed 4D radiograph sequences through a liver tumor patient breathing cycle using (a) a 230 MeV proton pencil beam, (b) a 330 MeV proton pencil beam, and (c) a 500 MeV/nucleon carbon ion pencil beam. Please note: These sequences must be visualized using a PDF reader software with sequence display capabilities such as Adobe Acrobat™ in order to fully appreciate the motion.*

In the presented case, two fiducial markers were surgically inserted before CT. These markers are not visible on a 230 MeV proton radiograph, which makes such beam irrelevant for liver imaging. A 330 MeV radiograph, however, allows visualization of a single seed that is not located in-line with the spine (large bony anatomy). On the other hand, both seeds are clearly visible on the carbon ion radiograph. These markers have been contoured on the radiographs in figure 3.14, with their amplitude of motion characterized between the lines. The difference

in marker visibility followed the expectations based on the difference in MCS component between these beams. Thus, a lower energy proton beam ($\leq$ 250 MeV) would not be suitable for liver patients setup and/or indirect tumor tracking. On the other hand, depending on the location of the seeds, a higher energy beam ($\geq$ 300 MeV) would be appropriate for marker tracking. In such a case, the fiducial markers could specifically be surgically inserted away from the spine. Nonetheless, image guided ion therapy using indirect tumor tracking would only be feasible by using heavier ions, such as carbon. The intrinsically greater spatial resolution of heavy ions compared to protons, truly allows for a visualization of the gold seeds, as well as accurate tracking of the tumor position.

3.3.4 Pediatric patients

An actual kV X-ray scout (120 kV - 10 mA - 0.597 mm $\times$ 0.545 mm voxel size), as well as a reconstructed 230 MeV proton radiograph for the 3 $^1/_2$ year old pediatric patient are shown in figure 3.15. Computed CNR for the scout and the radiograph were 4.2 dB and 2.0 dB, respectively. As previously observed in the lung case, the X-ray scout results in a higher spatial resolution than the proton radiograph. In spite of this quality difference, bony anatomy is still clearly visible in the ion radiograph. Proton imaging could therefore allow for accurate daily patient setup, along with a drastic diminution in imaging dose as previously discussed (order of magnitude versus X-ray imaging). This is of particular importance in pediatric patients for whom a small dose of radiation can lead to irreversible damages. Moreover, it is not believed that significantly increasing the number of incident particles (hence the imaging dose), for ion radiographs would result in a dramatic improvement in image quality.

Furthermore, the use of a single BEV for both imaging and therapeutic purpose would reduce systematic shifts due to uncertainties in BEV positions. This is not necessarily relevant in passive scattering irradiation for which the whole volume is treated at once given well-defined aperture edges which can be visualized on prior setup X-ray radiography. Conversely, this can be more problematic during PBS irradiation for which the dose is deposited one layer at a time, with a beam position that potentially changes.
Similarly to the previously presented lung case , these findings can be extended to heavy ion therapy, such as carbon ions, due to their intrinsically similar physical properties.

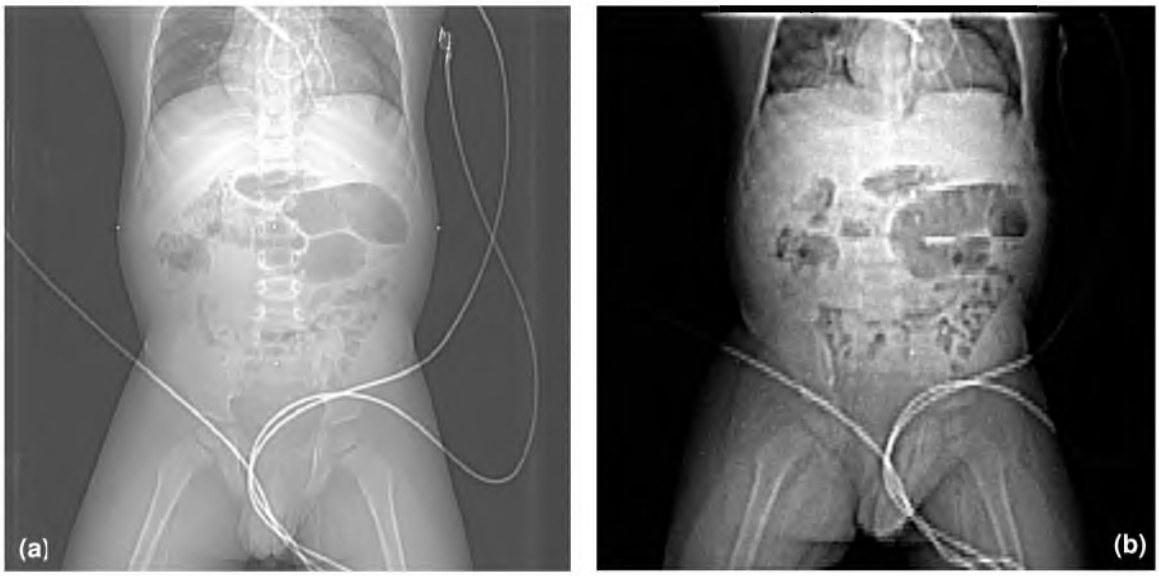

Figure 3.15: *(a) Actual kV X-ray scout, and (b) 230 MeV proton radiograph of a 3 $^1/_2$ year old pediatric patient.*

3.3.5 Study limitations

It is important to note that these patient studies suffer from a few limitations. Reconstructed patient radiographs present an advantage over actual proton imaging system due to the current state-of-the-art in detector technology. In this sense, this work presents the best achievable results. On the other hand, the number of imaging particles could be increased in order to improve the signal statistics in an actual detector. Of course, such tweak would come at the cost of extra imaging dose, but, in that sense, the results presented in this work are clinically viable.

Furthermore, the use of an actual X-ray CT scan vastly impacts the quality of the simulated ion radiographs. Not only are there small uncertainties in the Hounsfield unit values obtained from a CT scanner (≈2%) as well as in the material conversion in the GEANT4 MC code (≈2%), but the CT produces a discrete data set, in this case 2.5 mm slices, which greatly impacts the optimal output quality. An ion radiography system used on actual subjects could very well yield different results than the ones observed in this work. This is of particular importance in the liver cancer patient case for which the small fiducial markers might become visible at lower proton energies, with potentially greater edge detection.

Concerning the 4D studies, the patient was considered instantaneously imaged through each single phase of their breathing cycle. While this is believable from a technology stand point, as

the delivery of a single high energy pencil beam layer is in the order of a ms (machine specific), one can foresee interplay effects between the beam motion and the patient internal motion. Nonetheless, these effects have yet to be characterized even from a therapeutic dose delivery point of view, and were therefore ignored.

Some readers might also see a limitation in this work in regards to using higher energy proton beams ($\geq$ 250 MeV) compared to the commercial availability at the time of redaction. Nevertheless, none of the current systems offer ion imaging capabilities; this work was based on the prospective use of near-future systems that will offer both higher energy beams and imaging capabilities , such as Protom™'s Radiance 330 system.

3.4 Conclusion

The emergence of proton and heavy ion therapy centers has spurred a renewed interest in ion imaging. In this work, the imaging properties of proton radiography have been characterized and compared against conventional kV and MV X-ray imaging through MC simulations using a specific phantom. This study confirmed the known intrinsic limitations in spatial resolution of proton radiography due to the large contribution of multiple Coulomb scattering. It was shown in figure 3.9, however, that proton radiography offers significant improvement in density resolution over X-ray imaging, giving the ability to detect inserts with densities closely related to the density of their background (up to 0.02 g/cm^3 density difference).

Such theoretical results were further analyzed in a clinical framework by comparing actual patient X-ray images with simulated ion radiographs. The large difference in density of the tumor and its surrounding tissues in lung cancer patients proved to be of greatest interest for proton imaging. Not only does the clear delineation of patient anatomy and tumor position allow for accurate setup, but it also results in the possible use of image guided proton therapy through direct tumor tracking. Furthermore, the use of a single beam for both imaging and treatment significantly reduces the potential discrepancies in BEV position.

The use of ion imaging would also significantly reduce the amount of imaging dose. This is of particular relevance for pediatric patients, as even a small amount of imaging dose can be detrimental. As a rather low energy proton beam for imaging (230 MeV) already offers bony anatomy detection, this modality would be suitable for patient setup.

Proton radiography somewhat finds its limitation in a more homogeneous tumor location, such

as the liver. In such a case, the use of proton imaging for patient setup and/or tumor tracking is questionable. Conversely, heavy ion beams present a lower MCS component resulting in greater imaging quality. This further translates to the possible use of heavy ion radiography for patient setup and IGRT with direct or indirect tumor tracking, even in homogeneous patient anatomy such as the liver.

Additionally, it is believed that ion radiography, despite its unique projection angle, carries range information that could be further used to reduce range uncertainties and treatment margins. More investigative work, however, is needed to accurately answer this hypothesis. Withal, such findings on ion imaging seem fruitless without an actual radiography detector. As a consequence, the conception of a clinically viable proton imaging system was proposed.

Chapter 4

Proton Radiography: experimental realization

4.1 Introduction

Ion imaging could improve patient's daily setup prior to proton therapy as well as potentially offer some IGPT properties, as previously demonstrated in chapter 3. Based on those theoretical results, the investigation of a clinical proton radiography system was initiated. As introduced in section 2.3, prior experimental realizations of a proton radiography system have been carried out using either (a) scintillating tiles (hodoscopes), (b) gas electron multipliers (GEM) detectors, or (c) silicon strip detectors (*Schneider and Pedroni [18]*, *Schneider and Pedroni [19]*, *Schneider et al. [3]*, *Sauli [20]*, *Pemler et al. [4]*, *Johnson et al. [21]*, *Talamonti et al. [22]*, *Sipala et al. [23]*). A first breakthrough was performed in 2004 by *Schneider et al. [3]*, in which the world's first actual proton radiograph of an animal patient was presented. In this experiment, the detector consisted of hodoscopes and a range telescope to acquire the position and the remaining energy. The system was so inefficient that it took hours to obtain the radiograph (the dog was anesthetized), therefore resulting in a dramatically large amount of imaging dose as compared to our theoretical results. Thus, this system was totally inviable for clinical use with patients due to both its inefficiency and its bulkiness.

This work was intended to design a clinical proton imaging system that would present both a small form factor and adequate accuracy in position and energy resolution. Three distinct approaches were therefore considered in order to acquire both particle position and energy on a particle-by-particle basis: photonic bandgap fibers (PBG fibers), complementary metal-oxide

semiconductors (CMOS), and scintillating fibers. [1]

4.2 A novel approach

Current proton imaging systems are unable to acquire both positioning and energy information simultaneously, resulting in larger systems. The system could therefore be reduced by acquiring particle-by-particle information in simple planes in front and beyond the patient. The reconstruction of such radiographs would then be performed as described in section 3.2.2. Such novel approach is represented in figure 4.1.

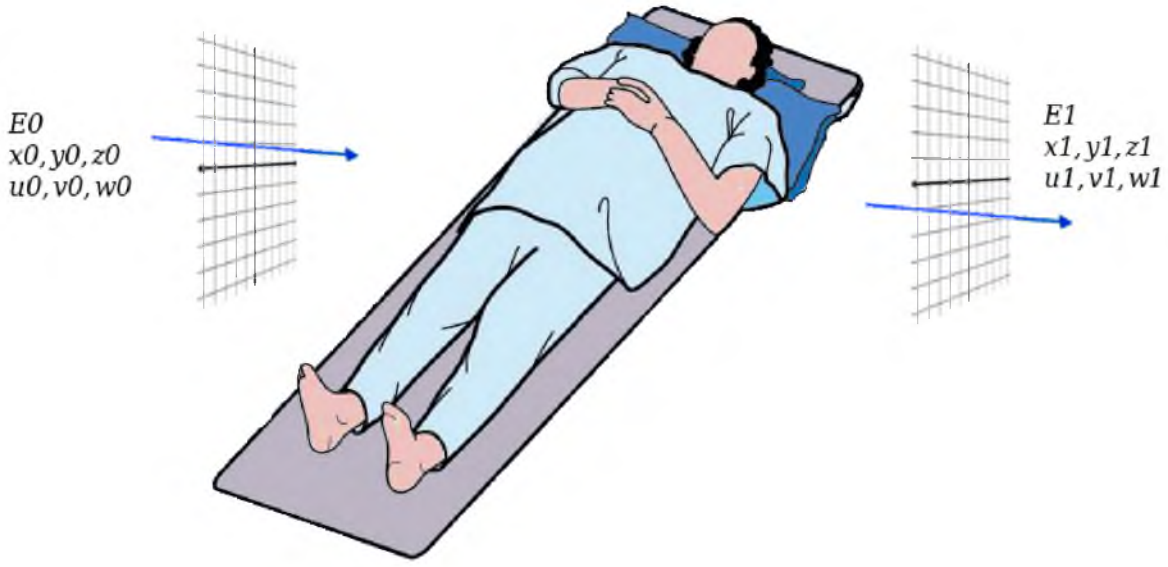

Figure 4.1: *Depiction of a clinical proton radiography system, small and functioning on a particle-by-particle basis. E_0, (x_0, y_0, z_0), and (u_0, v_0, w_0) represent the initial particle's energy, position, and directions, respectively Similarly, E_1, (x_1, y_1, z_1), and (u_1, v_1, w_1) represent the energy, position, and directions of the exiting particle.*

The main challenges of such a system are speed, efficiency, and resolution (both spatial and energetic). In order to optimize the imaging system's efficiency, the read-out system would have to match the output current of the machine, thus operating on a particle-by-particle basis. Unfortunately, the typical therapeutic output of a proton accelerator is in the order of thousands of gigaprotons per seconds. For imaging purposes, this rate should be limited as much as possible, but usually remains extremely high due to machine output capabilities. At MGH, for

[1] This work was published in *Polf et al. [32]* and *Seco and Depauw [30]*, as well as presented at various conferences (*Depauw and Seco [39]*, *Depauw and Seco [40]*, *Seco and Depauw [33]*, *Goulet et al. [41]*, *Koybasi et al. [42]*).

instance, the lowest available beam rate would correspond to a couple of gigaprotons per second. Given the cyclotron's duty cycle ($\approx$ 10 ns), this represents a couple of protons in each cyclotron pulse ($\approx$ 3 ns) every 10 ns. This further translates into the need for a read-out system presenting Gigahertz bandwidth and capable of Gigasamples/s sampling rate. This is a major consideration for the system design since this type of electronics presents a remarkable cost. Conversely, a synchrotron-based center could offer far smaller beam rates. The efficiency of the system would therefore be largely based on its speed capabilities, and dictate the improvement in imaging dose compared to current clinical systems.

The accuracy of the imaging system will be based on its spatial and energetic resolution. Depending on the system's design, these specifications could either be independent or closely tied one to another. In this sense, protons' intrinsic limited spatial resolution (due to MCS) would actually be helpful since spatial resolution could be slightly compromised at the benefit of a higher energetic resolution.

Based on these considerations, the three aforementioned routes were pursued. The following section describes the detector technology as well as the necessary read-out electronics that was utilized for experimental testing.

4.2.1 Photonic bandgap fibers

Extensive knowledge in fiber design and manufacturing exists at the Massachusetts Institute of Technology (MIT), which resulted in their development of fibers that confine light into a hollow core, the so-called Photonic Bandgap (PBG) fibers (*Kuriki et al. [93]*). These fibers have previously been made from arrays of air holes in a solid dielectric, as well as from pairs of solid materials forming multilayer structures (*Yeh et al., Cregan et al., Allan et al., Eggleton et al. [94, 95, 96, 97]*). PBG fibers were then improved with the integration of distinct functional elements and the development of intelligent self-monitoring optical fibers(*Bayindir et al. [98]*). Metal-insulator-semiconductor photo-detecting fiber devices were further produced based on these previous improvements. Such fiber consisted of an inner polymer tube made of polyethersulfone (PES) or polycarbonate (PC), supporting a thin film of photo-conducting element contacted with four metallic tin conduits. The inner tube is encapsulated by polymer cladding which leaves its strength and flexibility to the fiber (*Sorin et al. [99]*). Figure 4.2 shows a schematic drawing as well as a scanning electron microscope (SEM) micrograph of both the cross and longitudinal sections of the PBG fiber.

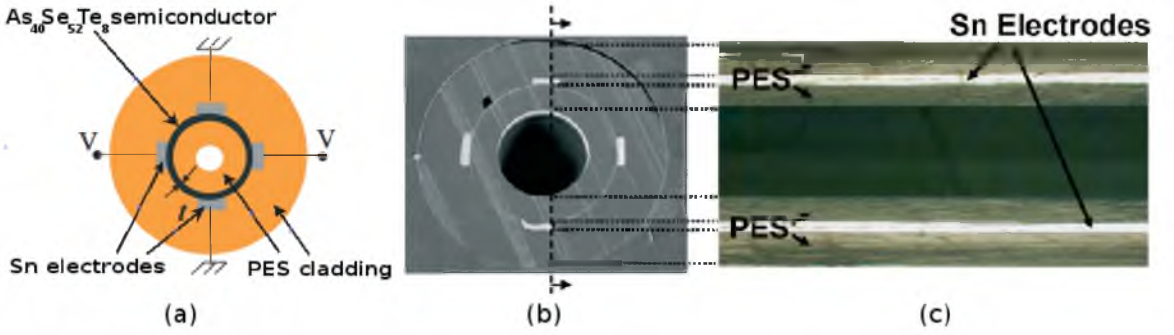

Figure 4.2: *(a) Schematic cross-section of a thin-film fiber device showing the electrical connections to an external circuit; SEM images of (b) cross section and (c) longitudinal section of the thin-film fiber device (the thin film is not visible in the longitudinal section).*

The original assumption behind the consideration of such fiber for proton imaging was that, by irradiating the fibers, the creation of electron-pair holes in the electrodes would generate a local current that could be recorded. Such scenario would then permit the acquisition of a signal for individual protons crossing the fiber. After initial experiments and subsequent brainstorming, it was decided that it would be more appropriate and effective to fill the fiber's hollow-core with signal-enhancing material ("dope"). It was therefore suggested to add scintillating material inside the fiber. The photo-electrons would then generate a stronger signal in the electrodes that would be readable with an appropriate electrometer. In this work, the scintillating materials considered were cesium-iodine (CsI), an inorganic scintillator known for its relatively high light yield ($\approx$ 50,000 photons/MeV), and BC-517 (Saint-Gobain Crystals™), an organic scintillator known for its extremely fast decay time ($\approx$ 2 ns). Both these scintillating materials produce light in the violet to green range, making the $Ar_{40}Se_{52}Te_8$ model of the MIT PBG fibers highly suitable for doping, as they are specifically tailored to transmitting visible light. Both the diameter of the hollow core and the concentration of scintillating material were varied in order to assess the optimal configuration. The manufacturing process for these doped fibers is described in figure 4.3.

In parallel to experimenting with these scintillating PBG fibers, an attempt was made to replace both the conductive glass and the scintillating material with layers of conductive material. Such alternative design would result in a fiber operating in a similar way as an ionization chamber (IC): protons interact in the medium and collide with electrons, with the ejected electron and the residual positive ion constituting an ion pair. Each ion pair produced in air results in an

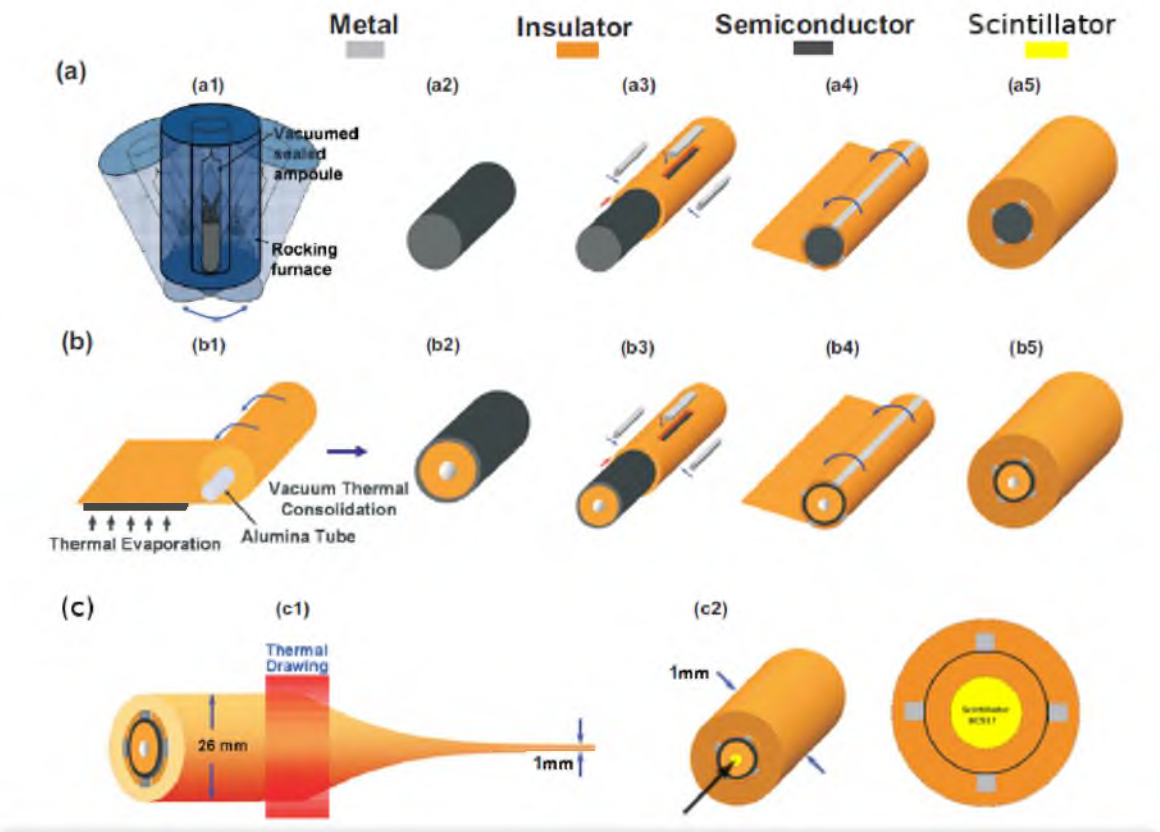

Figure 4.3: *Fabrication steps of a scintillating thin-film fiber device: a) production of the solid-core fiber device; b) production of the thin-film fiber device; c) finalization of the scintillating fiber through doping. In details, a chalcogenide rod (a2) is slid into a polymer tube where rectangular spaces have been cut to place the tin (Sn) electrodes (a3); the structure is then encapsulated in a polymer cladding (a4) and consolidated to obtain a macroscopic preform (a5); chalcogenide glass is then thermally evaporated on a polymer sheet (b1) that is rolled and consolidated to obtain a polymer tube with an outer layer of controlled thickness of glass (b2); the structure is then encapsulated in a polymer cladding (b4) and consolidated to obtain a macroscopic preform (b5); afterward the macroscopic preform is thermally drawn to yield a thin-film fiber device (c1) which is finally doped with the scintillating material (c2).*

average expended energy of 33.85 eV, also known as the W-quantity.

The linear energy transfer (LET_∞) corresponds to the average loss in energy per unit length of path of the incident radiation. LET_∞ can be obtained from the range-energy relationship of the incident energy in the medium. The number of ion pairs produced in a given medium per unit length of path of the incident radiation, called the specific ionization, can therefore be obtained from equation 4.1.

$$SI = \frac{LET_\infty}{W} = \frac{E}{R \times W} \tag{4.1}$$

where, SI is the specific ionization, W the W-quantity, E the incident particle energy, and R the corresponding incident particle range in the medium.

The theoretical ion pair production for a 230 MeV proton was therefore evaluated for various materials, based on equation 4.1, in order to produce the most theoretically efficient fiber design. The choice of 230 MeV for the energy evaluation was based on MGH's accelerator capabilities, since proton radiography would be performed with the highest available energy. Different ratios for the anode and cathodes radii were computed for aluminum, graphite, iron, lead, tin, tungsten, and conductive polycarbonate (CPC), based on a 1 mm diameter fiber design. Figure 4.4 presents the theoretical ion pair production from protons as a function of energy, along with the optimal theoretical design for a PBG fiber using a CPC conductor, for which the specific ionization is $\approx$ 21.5 ion pairs/μm.

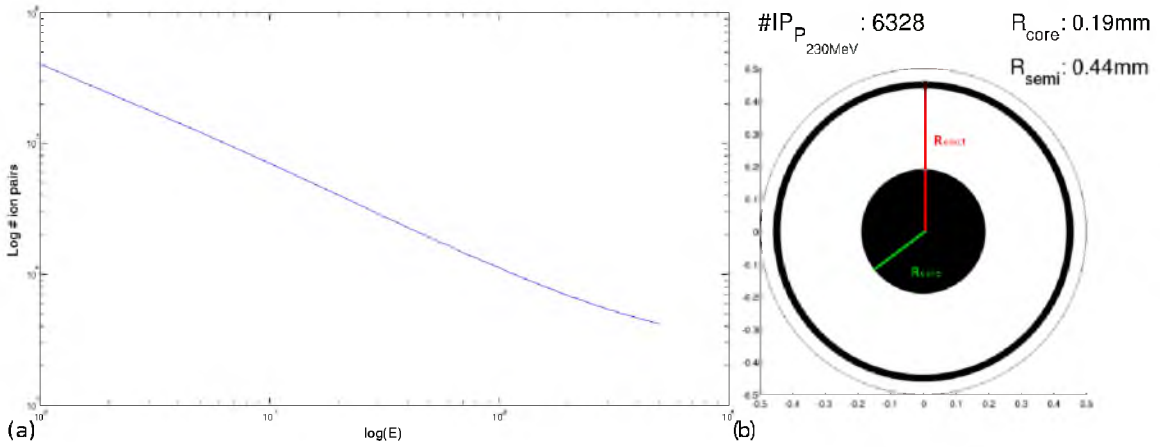

Figure 4.4: *(a) Number of ion pair produced in a 1 mm diameter IC-simile fiber as a function of proton energy on a log-log scale; (b) Optimal theoretical anode and cathode radii for a fiber using a CPC conductor, $\#IP_{P_{230MeV}}$ is the theoretical number of ion pairs collected using the given radii when a 230 MeV proton traverses the fiber.*

In this work, regardless of the model of PBG fibers considered (scintillating thin-film device or IC-simile device), the signal produced in a given fiber was acquired using a LeCroy™ electrometer with a very basic LabView (*LabVIEW [100]*) software. This software was provided by the MIT team, hence not described here.

4.2.2 Scintillating fibers

Subsequent to the suggestion of scintillating PBG fibers, it was further proposed to consider pure scintillating fibers. As individual protons traverse a fiber, they will lose energy based on their initial energy and the effective path length. This energy deposition, $\frac{dE}{dx}$, corresponds to the LET_∞ previously introduced. The interactions of the protons inside the fiber result in the

creation of photo-electrons, generating a luminescent signal throughout the fiber whose integral is relative to the energy deposited, hence LET_{∞}. The charge collected can therefore be interpreted such that one can obtain the particle's incident energy.

By perpendicularly aligning two sets of fibers in tight meshes, each particle would traverse two fibers. Not only can the particle's position be retrieved based on the coincident signals in these two fibers, but the dual $\frac{dE}{dx}$ readings would also result in a reduction of the uncertainties in the interpretation of the particle's incident energy. Additionally, the signal slowly attenuates throughout the fiber as a function of distance between the interaction point and the read-out system location. The $\frac{dE}{dx}$ reading could therefore be corrected based on the interaction position, thus further reducing the uncertainties in the interpreted incident energy. This coincidence mechanism is later depicted in the experiments section in figure 4.14.

As previously demonstrated in the Monte Carlo simulations (see chapter 3), the information required for proton radiograph reconstruction solely consists of the energy and position of individual particles before and after the patient. However, the difficulty resides in the fact that energy and position information present competing requirements from a fiber design specification point of view. A thicker scintillating fiber would result in a longer proton path and therefore, greater energy deposition. This greater energy deposition further translates into a brighter luminescent output signal from the fiber. This therefore results in a more accurate $\frac{dE}{dx}$ reading and better incident energy interpretation. Conversely, a thinner and narrower set of fibers would result in smaller "coincidence pixels" and thus, a more accurate acquisition in position information. Due to the poor intrinsic resolution of proton radiography, as evaluated in section 3.2.4, and in order to optimize the compromise between energy and position accuracy, this work considered 2 mm square scintillating fibers. These fibers' square cross-section, as opposed to the more conventional circular cross-section (e.g. PBG fibers), allows the design of gapless meshes of fibers. This improves both the accuracy (quasi constant 2 mm path length through the fiber would result in stable $\frac{dE}{dx}$ readings) and efficiency of the system.

As previously discussed, the MGH cyclotron operation is such that an $\approx$ 3 ns proton bunch is emitted approximately every 10 ns. The intensity of the beam in the room, i.e. the number of particles coming through in each bunch, is highly correlated to both the requested output current at the exit of the accelerator and the requested proton energy. The higher the beam's energy, i.e. greater individual proton's velocity, the smaller the spatial spread. A smaller spa-

tial spread further results in more particles able to exit the cyclotron. For particle radiography purposes, it is ideal to minimize the number of particles through the system, yet using the highest available energy which is the most efficient one. Thus, by reducing the output current at the accelerator level, at MGH it is possible to produce, on average, 1 particle per 3 ns burst at the nozzle exit, i.e. 1 particle in the room every 10 ns. Although this rate is extremely low from a proton accelerator output point of view, this is an extremely high rate of signals from a read-out system standpoint. Thus, this is an important consideration for the entire system's design and configuration.

Furthermore, due to read-out electronics availability and efficiency, it was preferable to consider scintillating fibers with output signals in the visible spectrum, especially blue or green.

Given these various considerations, it was decided to use BCF-20 plastic scintillating fibers from Saint-Gobain Crystals™. BCF-20 fibers emit light in the green spectrum with a peak at 492 nm and present a decay time of 2.7 ns. The decay time means that each particle interaction would result in a 2.7 ns pulse which would match the speed requirements set by the machine at MGH. The BCF-20 fibers' characteristics are such that an average of 8,000 photo-electrons were expected per 1 MeV energy deposition. The fibers present an acceptance angle of $\approx 21°$ which translates to $\approx 10\%$ efficiency of the system. These specifications can be found on the manufacturers' brochure (*Saint-Gobain Crystals™ [101]*). A few limitations in using these BCF-20 fibers were purposefully ignored during the initial phase of the project: the crosstalk between adjacent fibers (clear adjacent fibers in meshes); a 50 % efficiency loss based on signal acquisition at only one end of the fiber; and a small residual signal reflecting at the end of the fiber on the opposite side from the electronic read-out. A schematic of a round BCF-20 fiber from Saint-Gobain Crystals™ is depicted in figure 4.5, along with an actual photograph of the square fibers used in this work.

The read out process for signals coming from optical fibers is fairly well documented. The most common approach is to use photomultiplier tubes (PMT). The mechanism of a PMT is as follows: light photons are received on a thin photo cathode window and generate electrons through photoelectric interactions; these electrons are accelerated to an electrode (first dynode) through a high voltage (-1000 V in our case) which generates more secondary electrons; these secondary electrons are then accelerated to the next dynode which further generates more electrons; this patterns continue until the last dynode (the anode) where the signal is

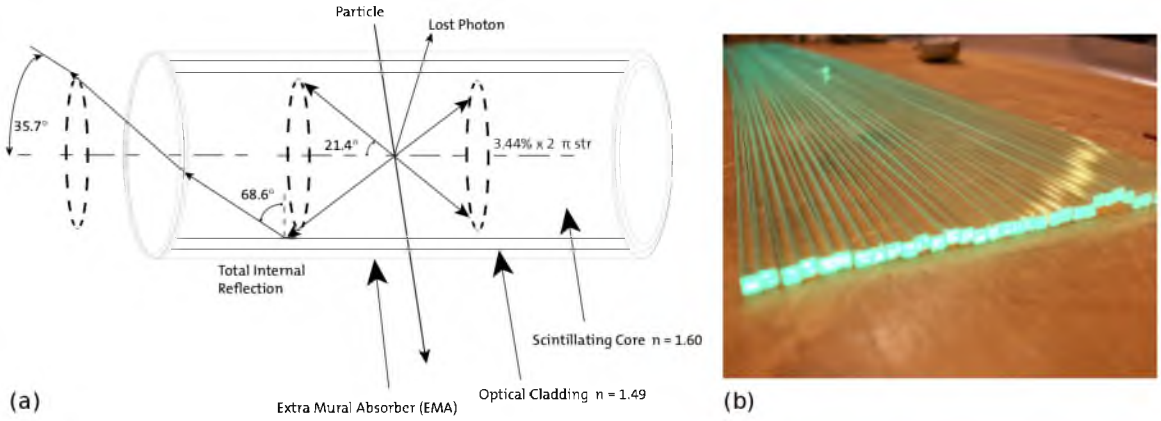

Figure 4.5: *(a) Schematic of a cylindrical BCF-20 fiber from Saint-Gobain Crystals™ depicting its main physical properties; (b) actual photograph of the square BCF-20 fibers used in this work.*

collected. This dynode cascade results in a tremendous signal gain (up to 100 millions times the original signal). It is then possible to perform individual photon counting depending on the setup and PMT specifications. The schematic of a PMT's way of functioning is depicted in figure 4.6.

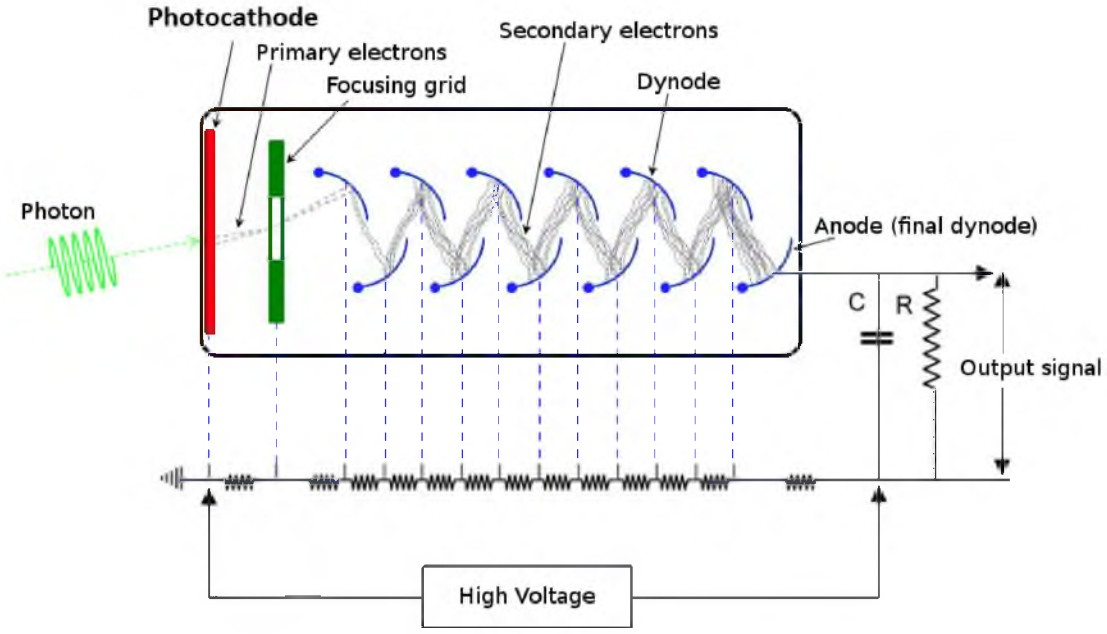

Figure 4.6: *Schematic of a photomultiplier tube (PMT). The light signal is received on the thin photo cathode and multiplied through a dynode chain to the anode.*

In order to match the speed requirements of the system, this work considered Hamamatsu™ 8-channel PMT arrays, model H9530-01. These arrays present 8 distinct 2 mm × 2.5 mm

sensitive areas allowing the light acquisition from 8 scintillating fibers side-by-side with a minimal gap in between (< 1 mm). An interaction in any fiber would result in the generation of a 3 ns output pulse with a ≈350 ps rise time at the exit of the PMT. The charge (integral) of the output pulse would then be relative to the amount of light transmitted from the interaction. Additionally, the charge of that pulse would also be linked to the gain of the PMT channel. This gain is directly related to both the channel's high voltage and the spectrum (energy) of the light transmitted through the fiber. Thus, a -1000 V high voltage unit, model C4900-01 from Hamamatsu™, was chosen on the manufacturer's recommendation to match the PMT assembly. For the given -1000 V high voltage and the previously described fiber's output spectrum peak of 492 nm, the manufacturer quotes a 3 $\times 10^6$ gain and an $\approx$ 12% quantum efficiency. This H9530-01 PMT array further offers minimal crosstalk between its 8 channels (< 0.1%) as well as minimal dark current. It should be noted that beyond the characteristics of the PMT or fiber model, the quality of the output signal is highly correlated to the quality of the fiber-PMT interface. Careful attention must be paid in smoothing the end of each fiber in order to avoid air gaps that could result in the reflexion of the luminescent signal instead of its absorption into the PMT. The fiber-PMT contact can also be improved through the use of optical gel (*cf.* measurements section). Nevertheless, no matter what is chosen for the final design, each individual fiber's response must be carefully characterized. Once the entire system has been fully calibrated, accurate data can be collected which can then be used for proton radiography purpose.

It is also crucial to minimize the light contamination in the system. This contamination comes from both stray light photons and cosmic rays, and is virtually impossible to completely suppress it. A tight black enclosure is a minimal requirement to mitigate the issue of stray photons. On the other hand, nothing can be done concerning cosmic rays which would result in false positive signals in the system. The original solution to assemble PMT arrays and fibers is presented in figure 4.7(a). The latter consisted of an in-house black acrylic holder allowing tight fiber-PMT coupling. The holder was then wrapped in a light cardboard box (minimal beam perturbation) and duck-taped over a couple of layers. Although rough on the edges, this solution permitted initial data acquisition that served as a proof of principle. Subsequent to promising initial results, a cleaner solution was sought. That solution, far more onerous, came directly from Hamamatsu™. Hamamatsu™ terminated the scintillating fibers with F-connectors and created a custom assembly that encapsulated the PMT array and matched our needs. This

advanced solution is shown in figure 4.7(b).

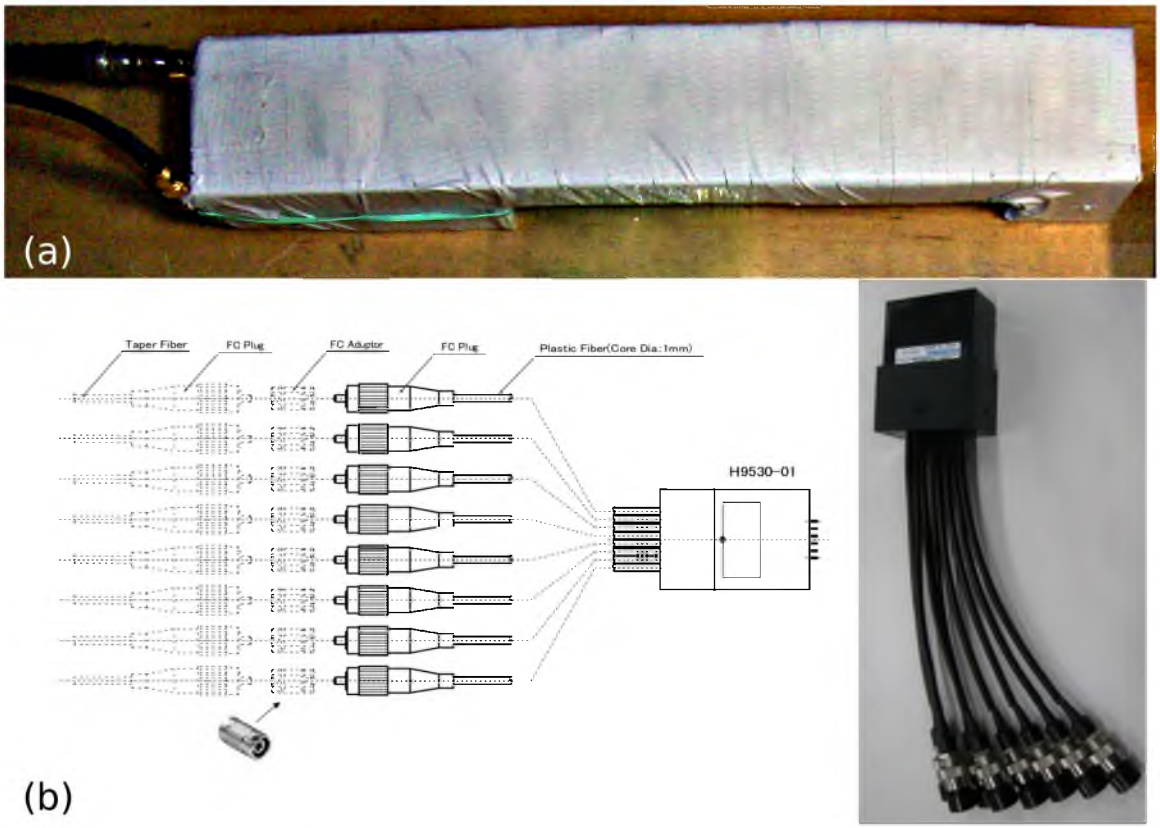

Figure 4.7: *(a) Original in-house fiber-PMT holder made of black Lucite, wrapped into light cardboard, and sealed with duck tape; (b) schematic representation and actual photograph of the subsequent onerous solution offered by Hamamatsu™.*

In parallel to the PMT solution, silicon photomultiplier (SiPM) were purchased from Hamamatsu™ for investigation. Due to a lack of budget and resources, only the PMT-based design could be pursued. The novelty of SiPM and their relatively unrecorded capabilities were in direct contrast with the well-documented PMT specifications and understanding. It is believed, however, that the minimal cost, stability, and ease of replacement of the SiPM would present an interesting alternative to the PMT-based system. It would thus be adequate to pursue such route once SiPM have reached a higher level of maturity.

Two distinct data acquisition systems (DAQ) were necessary for these scintillating fiber devices: a powerful oscilloscope (limited number of channels) and a more substantial system that would be scalable for clinical use. The oscilloscope could be used for proof of principle measurements, energy-output relationship characterization, and accurate characterization of single fibers. Conversely, the clinical system must be able to offer both coincidence (position)

and charge ($\frac{dE}{dx}$) acquisition on numerous channels with a reasonable efficiency.

The oscilloscope used in this work was a WavePro 715Zi-A from LeCroy™ with the WPZi-A-L-128 (extended memory) and WPZi-1.5GHz-4X20GS (advanced sampling rate) modules. The impressive characteristics of the oscilloscope made it a perfect match for the designed system. The 1.5 GHz bandwidth allowed the acquisition of an input signal approximately every 0.7 ns exceeding the requirements of 1 or 2 particles per 3 ns. Furthermore, in order to obtain an appropriate signal shape, i.e. accurately compute the signal's charge (integral), it was necessary to be able to acquire enough points along the signal curve. The WavePro 715Zi-A offers 40 GS/s on a single channel resulting in over a hundred points on a given 3 ns pulse. Such sampling speed is more than appropriate as highlighted in the measurements section. Moreover, since the oscilloscope runs directly on a Windows™ operating system, it offers a multitude of ultrafast signal processing analyses tool and export options. It also present the capability to run automated scripts for data analysis. The latter would be particularly useful in the future process of individual fiber characterization. This oscilloscope model actually presented far more advanced mathematical signal analysis options than that required by the project. The WavePro 715Zi-A was therefore very adequate for single fiber signal analyses.

In the context of the clinic however, a 10×10 cm^2 imaging panel size would represent a minimum requirement. Such panel size corresponds to a couple of meshes made of 50 adjacent scintillating fibers each based on the chosen design. The second DAQ system, intended for clinical use, therefore presented different requirements. It had to offer an appropriate bandwidth for the evaluation of a 100 channels, while offering a sampling resolution sufficiently high enough to accurately evaluate the timing (for coincidences) and charge of the signals coming from various fibers simultaneously. Unfortunately, such system was not readily available at the time of the work, nor was it feasible to build our own system due to a lack of resources. As a consequence, two DAQ devices were considered in this work. Although these DAQ system represented the state-of-the-art in acquisition systems, they did not meet the requirements set by the designed system. The first system, the Pixie-16 from XiA™, presented 64 channels split into 4 modules of 16 channels with 12-bit analog-to-digital converters (ADC) capable of a data sampling rate of 100 MS/s. The Pixie-16 came with a generic software from XiA™ which, for each channel, generated charge measurements as well as time stamps (75 MHz, 13 ns resolution). The time stamps could be used for coincidences measurements (*XiA™ [102]*). Alternatively, a more promising DAQ, the SIS3305 digitizer from Struck™, offered a 2 GHz

bandwidth with a 1.25 GS/s sampling rate on 8 channels in parallel (*Struck™ [103]*). Although the SIS3305 was a better fit given the design requirements of the proton radiography detector, it was not fully released at the time of the work (2011); only a single 8-channel module was available with no proprietary software. At the time of redaction, it is believed that the SIS3305 was successfully scaled to a 128 channel system and implemented off-site by Struck™.

4.2.3 CMOS APS

The use of CMOS technology for radiotherapy detection purposes has been previously investigated for proton and photon beam visualization and dosimetry (*Sipos et al., Sanchez-Crespo et al. [104, 105]*), as well as for imaging purposes in newer digital X-ray radiographic systems (*Yorkston [106]*).

The investigation of CMOS detectors for proton radiographic imaging use was not part of the initial project. Nevertheless, due to a collaborative project, we gained access to a CMOS active pixel sensor (APS). This CMOS APS was developed as part of the MI3 Consortium at the Science and Technology Facility Councils Rutherford Appleton Laboratory, UK (*Allinson et al., Turchetta et al. [107, 108]*); it presented a 42×42 mm^2 detection area made of of 40×40 μ m^2 pixels. The data acquisition was performed using the given read out system which operated at a frame rate of 1-100 frame/s. Because our group was not involved in the development process of this CMOS APS system, please refer to *Osmond et al. [109]* for more details.

4.3 Experimental results

Rarely expressed in published work, it seemed important here to report inconclusive/poor results obtained during our experimental process. Although these measurements mostly resulted in stopping points rather than advancements for the project, they must be described in order to highlight the inadequacy of certain technologies for proton radiography purposes.

4.3.1 CMOS APS: inconclusive results

CMOS detectors could potentially be used for proton radiography purposes. The CMOS APS system used in this work, however, did not present the required characteristics. Measurements were performed using the MGH proton beam line in double-scattering mode, with the

first scatterer, range modulator wheel, and second scatterer set in such a way that the delivered beam was monochromatic with an energy of 117 MeV. This energy is comparable to the energy of particles that would be exiting a patient during actual proton radiography. The CMOS APS, as well as commercial Gaphcromic™ EBT 2 films and Kodak™ X-Omat V films, were alternately placed at isocenter using two different configurations: a ball point pen with two metal screws (one in the beam direction, one perpendicular to it), and a phantom made of 5 alternated slabs of water, lung and bone equivalent materials.

For both aforementioned commercial films, the configurations were placed at various distances prior to the film, namely 0, 2, 5, and 10 cm. These measurements, displayed in figure 4.8 for the pen and screws configuration, were performed in order to assess the effect of proton beam scatter on the image formation.

During the CMOS APS experiments, both configurations were located 5 cm antecedent to the detector. The energy deposited by the protons ($\frac{dE}{dx}$) in the CMOS layer of the CMOS APS detector was recorded as a voltage amplitude, with the corresponding residual energy of the exiting protons computed. For comparison purpose, conventional photon X-ray radiographs were also performed in similar conditions at 70 kVp using a Varian™ PaxScan flat panel detector. Figure 4.9 highlights the comparison between the film X-ray irradiations and the CMOS APS proton irradiations.

The resemblance between the proton irradiated films at 5 cm (figure 4.8) and the CMOS APS images (figure 4.9) highlights the imaging capabilities of the CMOS technology. *Film* is considered a gold standard in the imaging practice regarding spatial resolution, which emphasizes the high capabilities of this CMOS APS system.

As expected, X-ray irradiated films have an apparent higher spatial resolution than CMOS APS acquired images (figure 4.9). The CMOS APS system, however, display higher density resolution as demonstrated by the visualization of the pen's edges in the proton images.

Despite the fact that these proton images represent the best reconstruction that were acquired throughout the entire project, these are not proton radiographs per se. Indeed, due to its integration time (10 ms), the system produces so-called scatter radiographs rather than the desired range radiographs. As highlighted in figure 4.8, scatter imaging is highly dependent on the distance between the setup and the detector (focus). As such, there is clearly an optimal distance (here 2 cm) which would depend on the proton beam energy as well as the

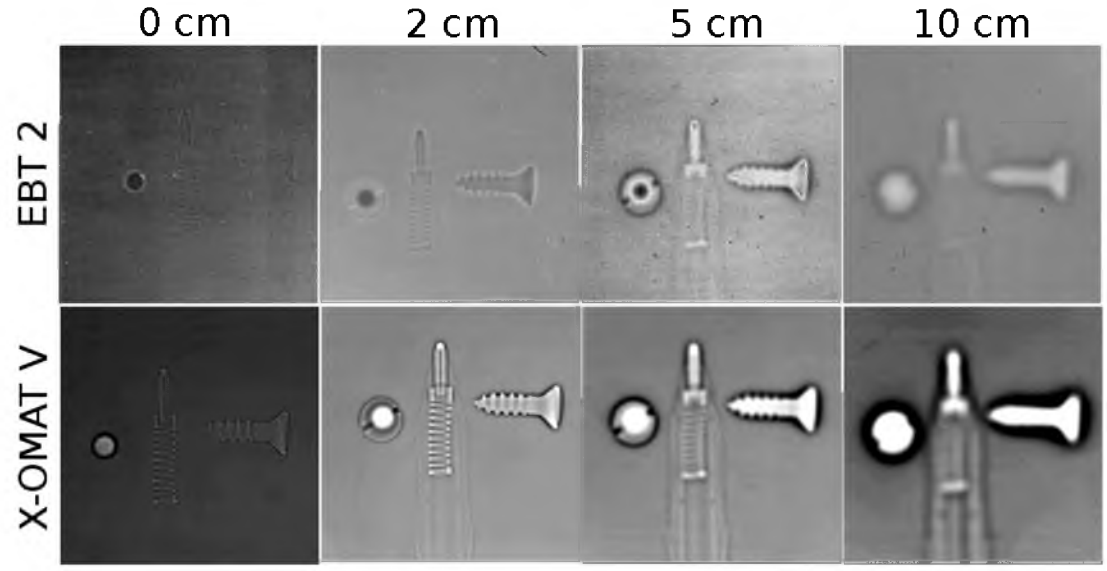

Figure 4.8: *117 MeV proton beam irradiation of the pen and metal screws configuration (one screw is in the beam direction while the other is perpendicular to it) using commercial Gafchromic™ EBT 2 and Kodak™ X-Omat V films placed at 0 cm, 2 cm, 5 cm, and 10 cm beyond the configuration. The difference in contrast between images is explained by the difference in dynamic range between the films, as well as the windowing and leveling used during the film scanning process.*

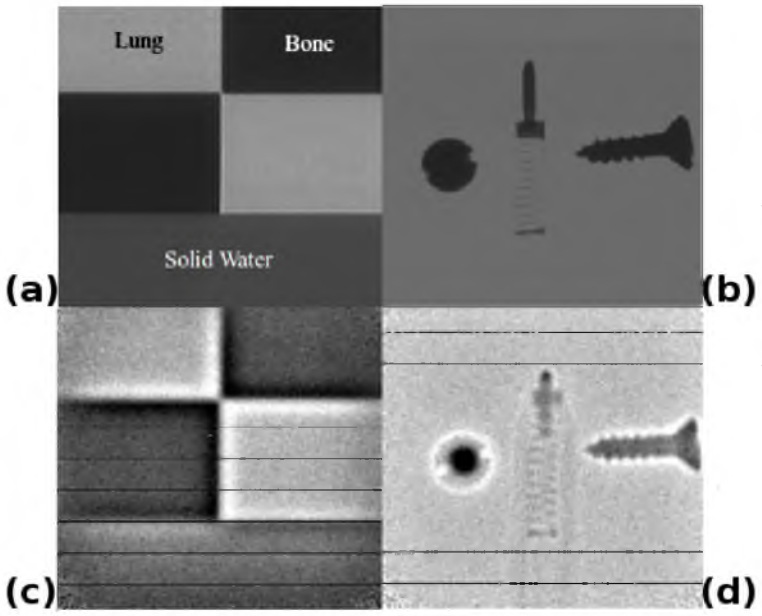

Figure 4.9: *70 kVp X-ray radiographs of (a) the water, lung, and bone phantom, and (b) the pen and metal screws configuration set-up using a Varian™ PaxScan flat panel detector; proton radiographs of (c) the water, lung, and bone phantom, and (d) the pen and metal screws configuration using the CMOS APS.*

thickness/composition of the traversed subject due to the amount of scatter. This high scatter dependency of the presented CMOS APS system does not make it a good alternative to conventional X-ray radiography. Conversely, should the system be rebuilt in such a way that individual channels offer on-line data acquisition rather than an integrated signal, range maps could be reconstructed. Such a system would present a true potential for proton imaging.

Unfortunately, this route could not be pursued as part of this work due to a lack of resources.

4.3.2 PBG fibers: poor results

The initial concept of a small proton radiography detector for this work was based on the PBG fibers. The experimental results obtained with such fibers, however, turned out to be inconclusive.

First, the PBG fibers were characterized outside of the proton radiation field in order to assess their stability. The characteristic curves, also known as intensity-voltage (IV) curves, correspond to the acquisition of output intensity (nA) as a function of input voltage (V) for a given light stimuli. IV curves were therefore acquired for various light stimuli (absence of light, red light, green light, ambient light) at different times (immediately after fiber drawing, and 2 to 4 weeks later), and at multiple voltages ranging from -100 V to 100 V. These curves were also acquired for different PBG fibers: with or without scintillating material; annealed or not annealed. Due to the large amount of data and the relative lack of interest, these IV curves are not shown here. The absence of change in IV curves versus time of acquisition highlighted the initial stability of those PBG devices outside of the radiation field.

Thus, the various PBG fiber "models" were taken for irradiation at MGH with a monochromatic beam which was produced with a double scattering field, similarly to the CMOS APS experiments. The most significant results are shown in figure 4.10.

Surprisingly, the presence or absence of scintillating material in the hollow core of the fibers had no visible effect (not displayed here). Furthermore, it appeared that the less conductive the glass was, the better the signal. Additionally, a modification of the beam location along the fiber resulted in different responses: the closer the beam was to the output contacts, the larger the response. This unexpected behavior from the system uncovered the non homogeneity of the electric field within the fibers which was believed to come from the manufacturing process. As seen in figure 4.10(b), the input voltage applied to the fibers had surprisingly no effect on the output response. In fact, only the dose rate dependency of these PBG fibers, illustrated in figure 4.10(a), followed expectations: the higher the intensity of the beam, the larger the response. The response of the fibers appeared to be quasi constant as a function of beam energy, as depicted in figure 4.10(c). This result was almost at the opposite of the expected behavior, the output signal should increase linearly versus the amount of energy deposited in

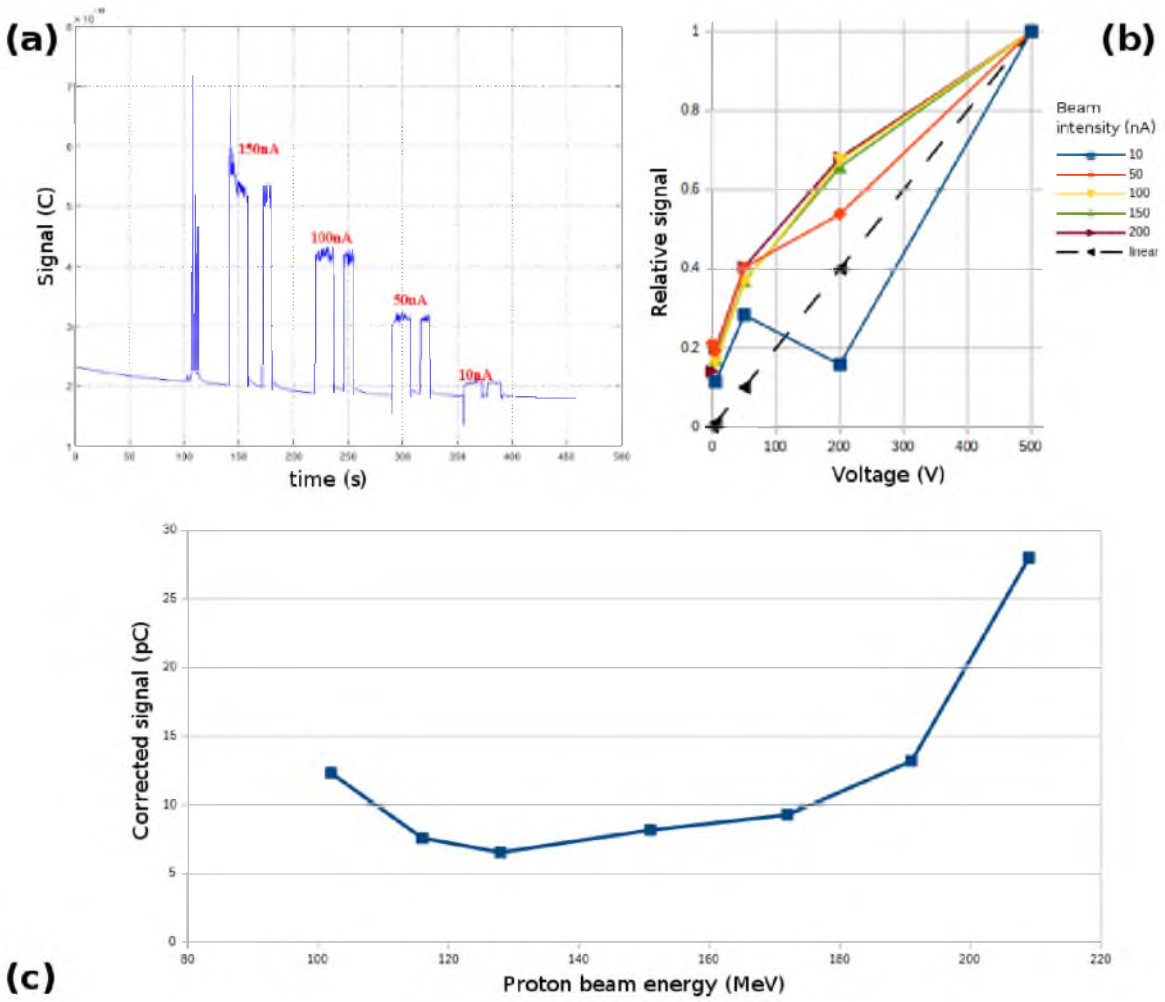

Figure 4.10: *Experimental results from proton irradiation of PBG fiber devices: (a) response curve versus beam intensity (dose rate) with two irradiations for each intensity; (b) relative response versus applied voltage as a function of dose rate; (c) response versus beam energy (signal corrected for dose rate).*

the fibers ($\frac{dE}{dx}$), hence decrease as a function of beam energy.

These inconclusive results stressed the inadequacy of the PBG fibers in their current form for proton radiography purposes, and therefore ended this approach.

4.3.3 Scintillating fibers: a novel path towards PR

The first measurements performed with the Saint-Gobain Crystals™ Bicron BCF-20 fibers served as a simple proof of principle. Two scintillating fibers were placed inside a homemade apparatus, as seen in figure 4.7(a). One fiber was set with optical grease at the PMT-fiber interface, the other without. The apparatus was then irradiated in pencil beam scanning (PBS)

mode using a 230 MeV beam. In order to optimize the chance of single event recordings, the beam's intensity was kept at a minimum, $\approx$ 1 nA at accelerator exit, which on average corresponds to a single proton per $\approx$ 3 ns being delivered inside the treatment room. For these experiments, the PMT array output channels for both fibers were connected to the LeCroy™ WavePro 715Zi-A oscilloscope. Figure 4.11 provides an example of an output trace obtained in the aforementioned setup when a proton traversed the fiber. The second smaller peak in the output trace was believe to come from ringing within the system. The ringing effect arose from the relatively poor quality of the cables and connections which resulted in a slight mismatch in impedance.

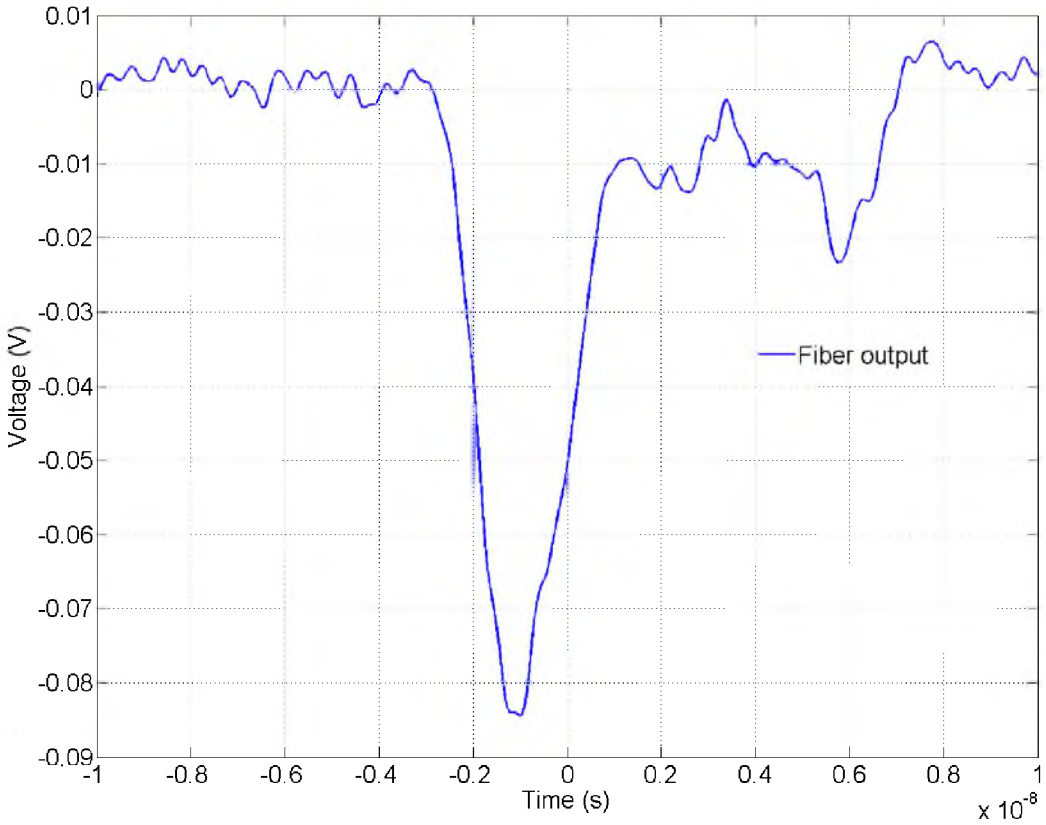

Figure 4.11: *Single event pulse produced by the PMT-BCF-20 scintillating fiber assembly and recorded with a LeCroy™ WavePro 715Zi-A oscilloscope.*

The output signals acquired in the aforementioned conditions, such as the trace shown in 4.11, proved the capabilities of the system to resolve individual interactions in the fibers. The comparison between traces obtained with and without optical grease at the fiber-PMT interface showed no apparent difference. This lack of difference highlighted the lack of benefit from using optical grease. Thus, the overall manufacturing requirements of a larger scale system

were simplified.

4.3.3.1 dE/dX measurements

Based on the knowledge acquired from the oscilloscope measurements, the homemade apparatus was subsequently connected to the full XiA™ Pixie-16 DAQ system. The assembly was then irradiated with a narrow proton beam using a 2 cm aperture. Measurements were performed at multiple energies, namely 191, 177, 151, 131, 116, 103, 93, and 77 MeV. The output spectra from these measurements were acquired with the Pixie-16 software. The output spectra corresponded to the raw light output from each fiber which could then be compared to the expected energy deposition ($\frac{dE}{dx}$) based on the incident proton beam energy. Figure 4.12 shows an example of output spectra obtained with a 151 MeV beam.

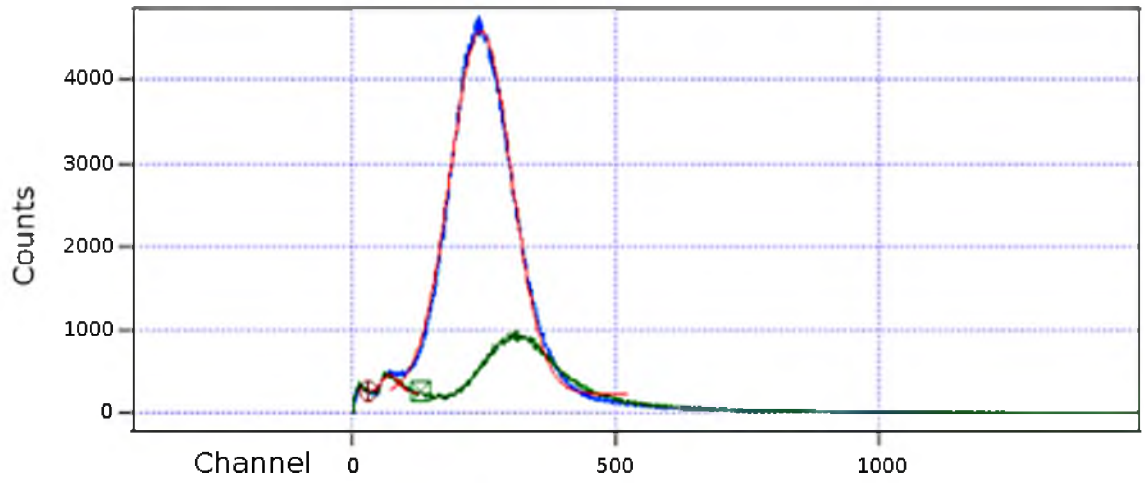

Figure 4.12: *Output spectra obtained from the irradiation of two scintillating fibers with a narrow 151 MeV monoenergetic proton beam and recorded with the XiA™ Pixie-16 DAQ system.*

The output spectra shown in figure 4.13 presented similar Gaussian profiles but with different characteristics (center and standard deviation). The center of a Gaussian fit of these curves corresponds to the relative signal, i.e. energy deposited ($\frac{dE}{dx}$) in the given fiber, while the width of the Gaussian (standard deviation) is representative of the noise. The discrepancy between the two signals can be explained by multiple causes. The narrow proton beam might not have been equally distributed over the 2 channels, resulting in more statistics/signal amplitude in one of the channels. Additionally, the difference in the signal's height could have risen from a significant difference in gain between the 2 channels due to the quality of the fiber/PMT interface. The shift in spectrum center, which translates to a discrepancy in energy deposited,

could be due to many things within the system; this discrepancy, however, would not be an issue as it would disappear once proper calibration of the individual fibers in the system has been performed.

The response of each channel as a function of both incident energy and expected energy deposited ($\frac{dE}{dx}$) is given in figure 4.13. The relationship used between incident energy and $\frac{dE}{dx}$ was based on the PSTAR data (*Berger [88]*) (based on ICRU-49 report data (*Allisy et al. [10]*)).

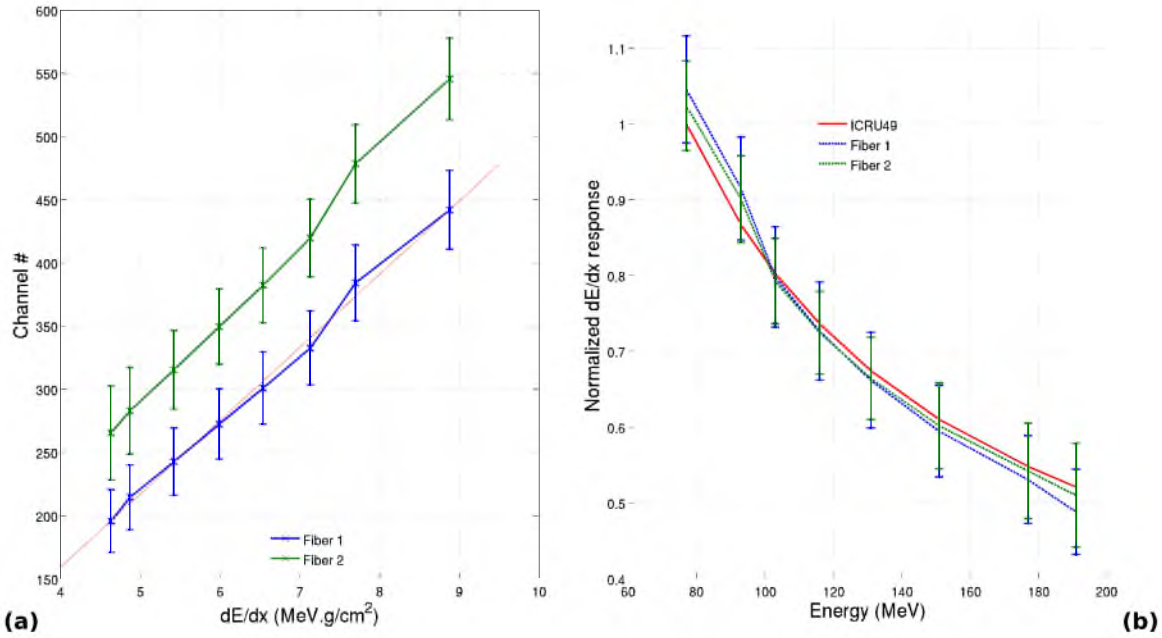

Figure 4.13: *BCF-20 fiber response to proton beam interactions as a function of (a) expected energy deposited ($\frac{dE}{dx}$) and (b) incident beam energy. The relationship between $\frac{dE}{dx}$ and incident energy was based on the ICRU-49 data (Allisy et al. [10]).*

These results highlight the appropriate agreement between fiber response and expected dose deposition. This further proves the possibilities of using a small factor detector made of scintillating fibers for proton imaging purpose. The relatively large error bars seen in 4.13 showed the limitations of the system used for these experiments. This large noise is believed to be due to the non-optimal connections throughout the system as well as the relatively low resolution speed of the DAQ system. Thus, the noise of the system could have been reduced through various improvements in the overall quality of the system.

It is noteworthy to point out that a 2 mm fiber design presents some limitations in accuracy. In practice, the inherent fluctuation in $\frac{dE}{dx}$ from each particle would result in an uncertainty in energy resolution. These fluctuations would translate into a spectral width in the acquired output signal, such as the one visualized in figure 4.12. These uncertainties in energy resolution

would grow larger with the incident beam's energy due to the inversely exponential shape of the $\frac{dE}{dx}$ curve as a function of energy. Although these uncertainties may be acceptable for proton imaging purpose, they are also expected to be slightly larger than a system using a range telescope, resulting in slightly poorer image quality. In figure 4.12, however, the large width of the acquired output spectra ($\approx$ 10 to 30 %) is mostly explained by the overall build quality of the prototype.

4.3.3.2 Coincidence measurements

For these experiments, a second homemade apparatus (figure 4.7(a)) was used. The apparatus contained two fibers each, and were positioned perpendicularly one to another, leaving the perpendicular fibers separated only by the slim encasing carton boxes and tape. Thus, this setup represented X and Y axes of a grid through which each particle interaction's position could be resolved. This concept is illustrated in figure 4.14. The coincidence area of two fibers (out of the four) was then irradiated with a narrow 151 MeV proton beam produced through a 2 cm aperture, similarly to the $\frac{dE}{dx}$ experiments. The coincidence area of the two other fibers, located outside yet at the edge of the irradiation field, could therefore be used to assess the noise in the system. Such experiments required the system to have a "coincidence window". As a proton would "simultaneously" traverse two fibers at a given intersection, two signals should be "simultaneously" acquired by the DAQ system. This is, in practice, not true, as the fibers are not infinitesimally thin, and the interactions would occur at a slightly different time. The system's coincidence window corresponds to how large this aforementioned time difference is allowed to be in order for multiple signals to be considered as pertaining to the same interaction. For these experiments, the coincidence window was set to 5 ns.

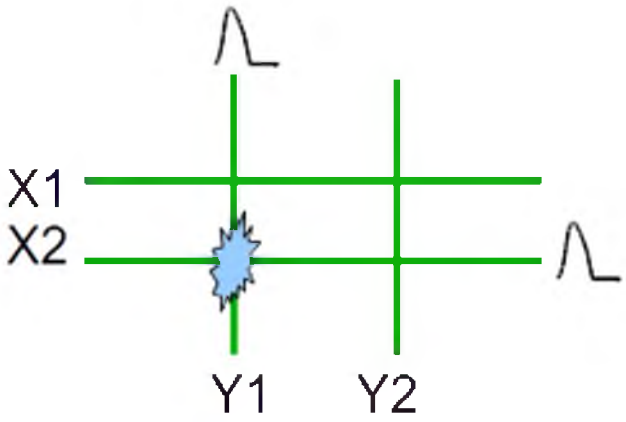

Figure 4.14: *Coincidence measurement concept: four fibers, perpendicularly positioned in pairs, were irradiated with a narrow proton beam; each coincidental interaction then resulted in a signal in both fibers which in turn gave the position of the interaction.*

In order to ensure the functionality of the system, a first measurement was performed with the Pixie-16 in spectral mode (similar to $\frac{dE}{dx}$ measurements) and was then repeated with the coincidence mode enabled. An example of output spectra is given in figure 4.15. As expected from the $\frac{dE}{dx}$ measurements, the characteristics (center and standard deviation) of the curves differed. This discrepancy would not have shown should the calibration of the individual fibers had been performed. Once enabled, the coincidence mode resulted in a duty cycle of $\approx$10 %. This means that 90 % of the interactions were not considered to be coincidental. Although this was true for many of these interactions, many others were not "caught" due to the large internal dead-time of the Pixie-16. Once the number of channels increases this issue would greatly worsen, for instance in a larger scale detector. This further highlights the need for a faster system such as the SIS3305 digitizer from Struck™. Additionally, although the channels outside the field resulted in counts without the coincidence mode enabled (mainly due to large scatter nuclear interactions), there was no significant signal/noise once the coincidence mode was enabled.

In a following experiment, various thicknesses of Lucite, namely 0, 1.25, 3.75, and 6.25 cm, were placed atop the apparatuses. The aim of this experiment was to assess the effects of scatter and small energy change. The coincidence spectra with and without the 6.25 cm Lucite buildup are shown in figure 4.15. It is believed that the first low energy peak in the output spectra corresponds to pile-up effects in the system. These pile-up effects could potentially be mitigated through smarter hardware and software, but this solution could not be pursued at the time of the project because of a limitation in available resources. As previously observed, there is a difference in the Gaussian characteristics of the curves for a given irradiation due to the lack of inter fiber calibration. The ratio of the centers from each channel, however, remain constant as a function of Lucite thickness. This shows that, after proper calibration of the individual channels in the system, both fibers in a coincidental interaction would yield similar signals. This information could be helpful in order to reduce the uncertainties in the computed $\frac{dE}{dx}$ value for the given interaction. Furthermore, the thicker the buildup was, the larger the standard deviation of the spectral distribution was. This is due to the energy spread created through the scattering process in the buildup material.

These experiments highlighted the position tracking capabilities of a scintillating fiber system through on-line channel coincidence analysis. Since such a detector would be able to resolve

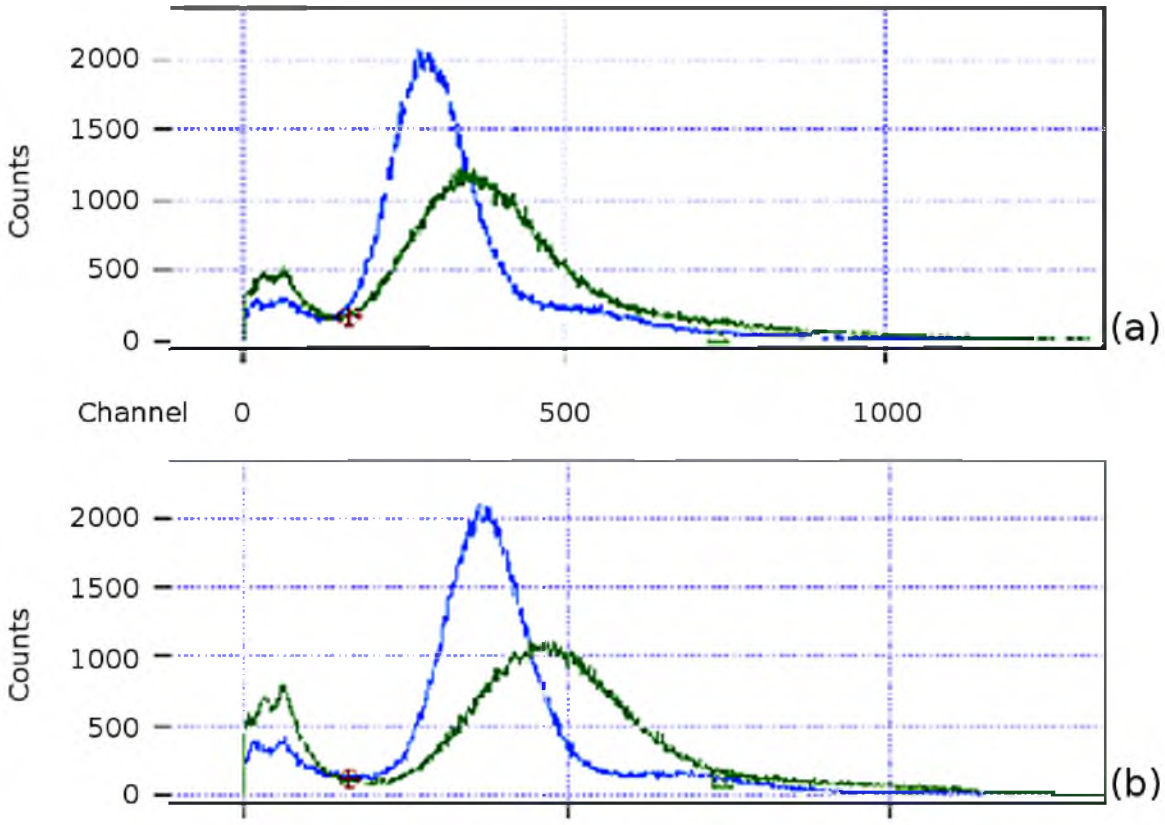

Figure 4.15: *Energy spectra from coincidence measurements of scintillating fibers irradiation with (a) no buildup, (b) a 6.25 cm Lucite buildup.*

both the position and energy information of each interaction on a particle-by-particle basis, a larger scale model would be suitable for proton radiography purpose.

4.3.3.3 Individual fiber calibration

Following these preliminary results, a homemade larger scale system was assembled. The final homemade assembly is shown in figure 4.16. The new system consisted of 64 BCF-20 scintillating fibers split into two two sets of 32 parallel fibers with a negligible small gap. The two sets of fibers were set perpendicular one to another, resulting in an X/Y mesh with a total detecting area of approximately 6.4 $\times$ 6.4 cm^2. The fibers' holders were made of black acrylic board in order to limit light contamination and cross talk between fibers. The scintillating fibers were then connected eight at a time to PMT arrays using custom assemblies made by Hamamatsu™, as previously described in figure 4.7(b). Note that additional light shielding was provided using light tight radiographic film sleeves that enclosed the whole fibers/PMT areas, this is not shown in figure 4.16. Printed circuit boards (PCB) were specifically designed

to provide HV power to the PMT arrays as well as optimal quality of connections throughout the system. For instance, each PMT array's output was connected directly to the Pixie-16 DAQ system through large D-connectors and BNC cables. This ensured a drastically higher quality of signals traveling throughout the system.

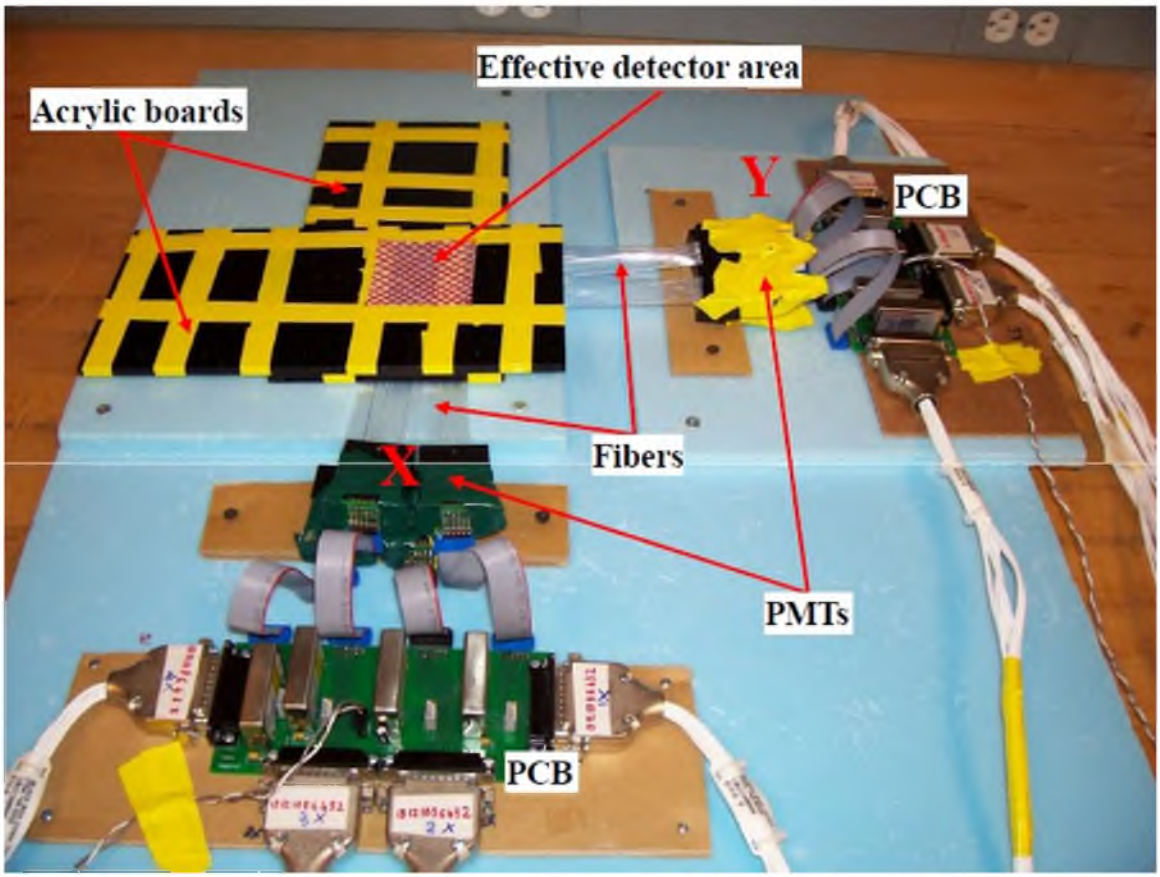

Figure 4.16: *Final homemade assembly of a proton imaging detector using 64 BCF-20 scintillating fibers set into an X/Y grid detecting area. The fibers were connected to PMT whose output was recorded by the Pixie-16 DAQ system.*

Individual pulses from each channel were first recorded using the LeCroy™ WavePro 715Zi-A oscilloscope in order to ensure the overall well functioning of the newly designed detector. The quality of the signals were far better than the ones previously acquired (figure PRPRtrace), which is explained by the significantly greater quality of the connections throughout the system. On the other hand, the new signals showed surprisingly lower gains compared to the original curves acquired ($\approx$ 30 % the size). After careful investigation, it was discovered that the Hamamatsu™'s custom PMT assemblies largely reduced the cross section of the terminated fibers (1 mm instead of 2 mm), resulting in a tremendous signal loss. This issue must be taken

into consideration for the design of a finished product as the efficiency of the whole system would greatly suffer.

Due to the small attenuation of the light transmitted through the scintillating fiber, it was first necessary to perform a position calibration in each channel. For this measurement, a small portion of the parallel fibers in a given set were simultaneously irradiated with a narrow beam (1 cm). The signal S_i collected at the PMT for a given fiber i was then given by equation 4.2 (*Koybasi et al. [42]*).

$$S_i(x) = A_i(x) \times C_i \times \Phi \times f(E) \tag{4.2}$$

where, x is the position within the fibers (cm) based on $x_0 = 0$ cm being the closest position to the PMT within the sensitive area; $Ai(x)$ is the unitless relative attenuation of the signal at the distance x compared to x_0; C_i represents the coupling efficiency of the fiber-PMT interface in %; Φ is the fluence of incident particles (protons/m^2); and $f(E)$ represents the relationship between light output and proton energy.

Thus, for a given fiber i, the values of C_i and $f(E)$ are constants which must be determined as a function of incident beam energy. For a known beam intensity (particle fluence), the position calibration could therefore be performed based on the ratio of signals $\frac{S_i(x)}{S_i(x_0)}$ at different positions x. Figure 4.17 shows the measured position calibration for two fibers. Note that modifying a specific channel's gain would not have helped harmonize the calibration between fibers. Instead, the software would need to compensate the attenuation of the acquired signal based on the estimated origin of the interaction. As previously discussed, the interaction's position would be obtained from the coincidental interaction that simultaneously occurred in a perpendicular fiber.

In order to inter-calibrate the scintillating fibers, the narrow irradiation field was kept at a known position, x_0, and a known energy, 151 MeV. The beam intensity (fluence rate) was modulated and the response from the fibers were acquired two at a time with the WavePro 715Zi-A oscilloscope. Figure 4.18 shows the responses for two fibers. The hardware gain for each channel could then be individually adjusted based on one arbitrarily chosen channel. As a consequence, similar absolute signal response can be acquired from any fiber subject to the interaction of a proton with a given energy and position within the fiber.

Subsequent to the successful calibration of the whole system using the WavePro 715Zi-A oscilloscope, the detector was connected to the Pixie-16 DAQ system and a broader irradiation

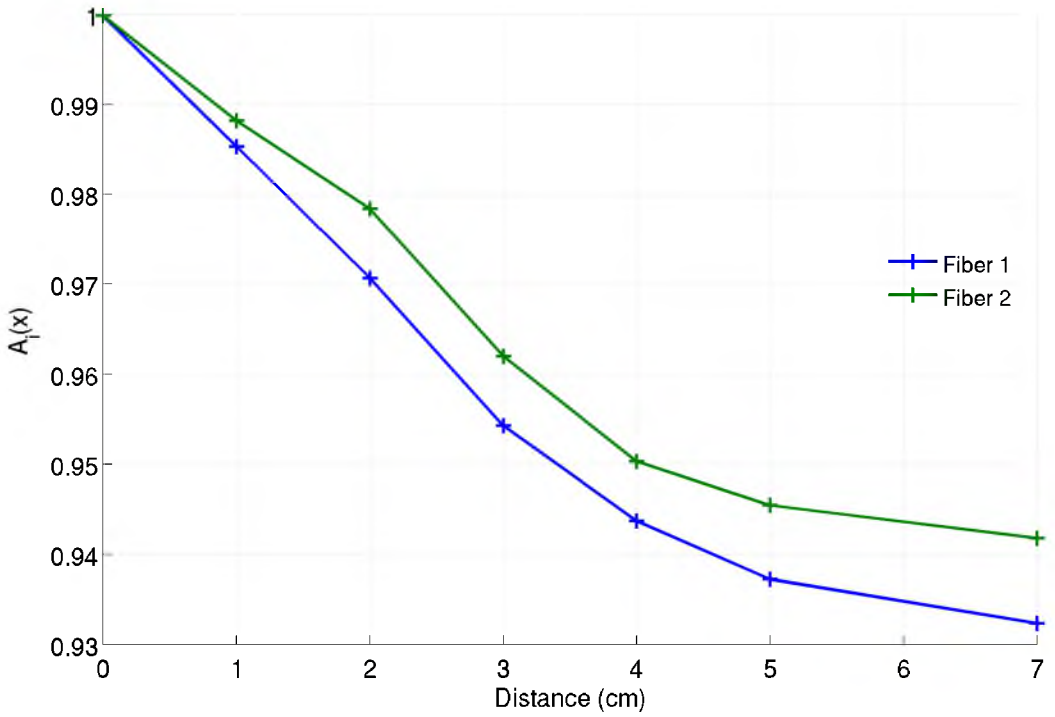

Figure 4.17: *Relative attenuation of the PMT output signal as a function of proton beam irradiation position along the sensitive area measured for two BCF-20 scintillating fibers with the WavePro 715Zi-A oscilloscope. The positive abscissa corresponds to an increasing distance from the PMT with* $x_0 = 0$ *cm being the closest position to the PMT within the system's sensitive area (see figure 4.16).*

of the sensitive area was performed. Unfortunately, neither the Pixie-16 was able to handle the processing of so many input signals, nor could the beam intensity be further decreased. The only solution would have been to move towards a significantly faster DAQ system such as the SIS3305 digitizer from Struck™. However, this route could not be pursued due to a lack of financial resources.

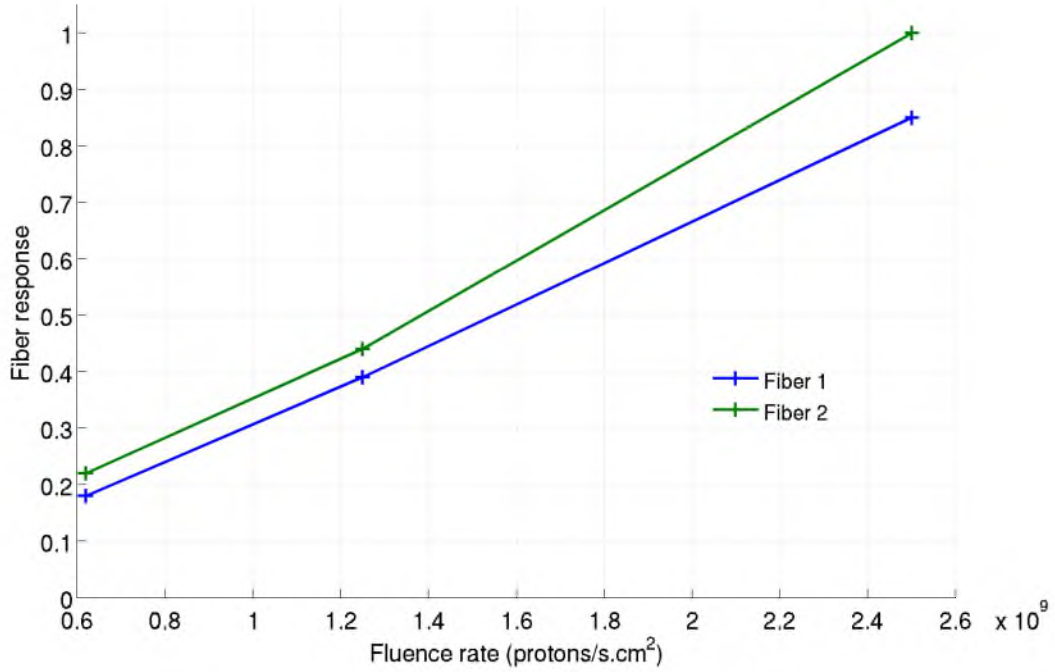

Figure 4.18: *PMT output signal as a function of incident proton beam fluence rate for two fibers, measured with the WavePro 715Zi-A oscilloscope. The proton beam energy and position were kept constant, at 151 MeV and x_0, respectively.*

4.4 Conclusion

Three different routes were explored in order to create a novel proton radiography system that would be reasonably compact for clinical use: photonic bandgap fibers, a CMOS active pixel sensor, and Bicron BCF-20 scintillating fibers. Unfortunately, the PBG fibers appeared to be fully inadequate for proton imaging purpose. Likewise, despite promising results from the CMOS technology, the specific CMOS APS system used in this work did not present capabilities for single event processing. Such a deficiency prevents the system from generating viable proton radiographs that would carry proton range information, therefore making the system unsuitable for the desired goals. Nevertheless, the redesign of a similar CMOS APS system would be worth exploring as it is believed the system's speed could greatly be improved as needed. The use of scintillating fibers, on the other hand, proved to be very fruitful. The acquisition of both a particle's energy and position of interaction are retrievable from the BCF-20 fibers. Each fiber could be calibrated in such a way that for a given position and proton energy, any fiber would result in a similar signal. Additionally, the layout of two sets of parallel fibers into a 2-dimensional X/Y mesh resulted in the capability to accurately

resolve the position of an interaction based on coincidental signals in the system. Theoretically, one could then reconstruct radiographs by recording both the positional and energetic information behind a patient given a known incident proton beam. It would be more sensible, however, to acquire this information twice, both upstream and downstream of the patient, in order to additionally gather directional information. Based on this additional information, the system could therefore benefit from better reconstruction algorithms using angular cuts (see Chapter 2). Unfortunately, in order not to suffer from the high duty cycle of the proton machine, yet preserve the theoretical dosimetric advantages of proton imaging, a considerably faster data acquisition system than the one used in this work would be needed. At the time of writing, such read-out electronics was not readily available, nor financially attainable. Based on the seemingly never-ending Moore's law (*Schaller [110]*), however, this type of electronics should become increasingly accessible over the next few years, thus making proton imaging a realistic project.

Chapter 5

Proton pencil beam scanning planning

5.1 Introduction

Pencil beam scanning (PBS), also known as intensity modulated proton therapy (IMPT), is a novel treatment technique for proton therapy. PBS refers to a narrow unscattered proton beam whose properties are modified as needed in order to offer optimal tumor conformality and organs at risk sparing. The beam properties mainly consist of beam position, energy (depth), charge (intensity modulation), and size. The lateral position of the beam is controlled through 'bending magnets' whose magnetic field is adjusted. The depth of the beam (third positional dimension) is adjusted by the incident beam energy in a layering fashion (*cf* figure 2.8). The beam's energy is governed by the output characteristics of the accelerator. The size of the beam (spot sigma) is a fixed parameter as a function of beam energy (layer) and is mainly determined by the quality of the beam transport line. At the present state of existing accelerator/beam line controls, it is not possible to adjust the beam transport line parameters, hence the beam size, on the fly. Nevertheless, the spot sigma could ultimately be adjusted within the treatment volume for speed purpose. Although the intensity of the beam itself is not modified on a per layer basis, the intensity modulation within the treatment volume comes from the length of time that the beam lingers in a given spot. There are two common ways to perform this intensity modulation: dose driven (spot scanning) or time driven (continuous scanning). In spot scanning, the beam is turned off while its position is being adjusted, then turned on for a defined period of time in order to obtain the desired dose in the target at

that spot; this is the way the MGH's system is configured. Conversely, in continuous scanning mode the beam is never turned off, but the traveling speed is modulated throughout the target to obtain the desired dose in a given spot.

The work presented here focuses on the treatment planning aspect of PBS and its current limitations based on Astroid, the current treatment planning software (TPS) at MGH. Other PBS considerations such as rescanning – the method for which each layer (depth) is being delivered multiple times in order to mitigate tumor motion issues – were not evaluated here because they are not currently implemented at MGH. [1]

5.2 PBS TPS beam model

Conventionally, the commissioning process of the TPS requires the acquisition of a large amount of data, the so-called "beam model", in order to ensure the accuracy of dose calculations (*Das et al. [111]*). For PBS planning, however, the amount of required data is quite manageable from the TPS point of view. Information such as magnet speeds, deliverable charges, etc, are not required for computations; they are subsequently applied to a computed plan in order to obtain a deliverable plan on a given accelerator. Thus, this simplistic PBS beam data set consists of measured Bragg peak curves in water as well as measured beam size at isocenter in air, both as a function of deliverable energy. All other parameters, such as source-to-axis distance (SAD) effects or off-axis ratio, are directly taken into account within the pencil beam algorithm's (PBA) computational model.

In order to further simplify this work, a set of a priori information named the *Golden* beam data set was compiled. The latter quantifies a set of absolute pristine Bragg peak depth-dose distribution in terms of multiple Coulomb scattering (primary) and nuclear scattering (secondary). A combination of this *Golden* beam data set and minimal measurements then suffices to describe the entire TPS beam data.

The *Golden* beam data set was generated using the Monte Carlo toolkit GEANT4 version 8.1.p01 (*Agostinelli et al. [82]*) with the physics settings described by *Jarlskog and Paganetti [87]*. Protons, electrons, neutrons, and photons were tracked with a cut off value of 0.05 mm. This set was comprised of Bragg peaks computed in water in a $300 \times 300 \times 0.2$ mm^3 geome-

[1] Co-authored work has been published in *Depauw et al. [44]*, *Kooy et al. [45]*, *Clasie et al. [11]*, *Dowdell et al. [46]*, *Carabe et al. [47]*, and *Butterworth et al. [48]*, as well as presented at various conferences (*Clasie et al. [49]*, *Clasie et al. [50]*, *Dowdell et al. [51]*, *Rochet et al. [52]*, *Carabe-Fernandez et al. [53]*, *McGarry et al. [54]*).

try for ranges every 5 mm between 2 cm and 35 cm. The peaks were generated with zero incident energy spread ($\frac{\Delta E}{E} = 0$) and zero emittance. These peaks were expressed in unit of Gy(RBE).mm^2.Gp^{-1} in accordance with the convention set by *Pedroni et al. [112]*(Gp = gigaprotons = 10^9 protons). The peaks were then normalized based on actual measurements of similar peaks acquired at a few specific energies. The normalization was performed at a combination of a 1 cm depth and $R_{80}/2$ due to the fact that the small energy spread of the actual beam presented a negligible effect at these points. The final *Golden* beam data set is presented in figure 5.1. The latter is considered universal as it represents the physical characteristics of a proton beam; any institution could therefore use this data in order to further limit the amount of measurements required to implement their TPS beam data.

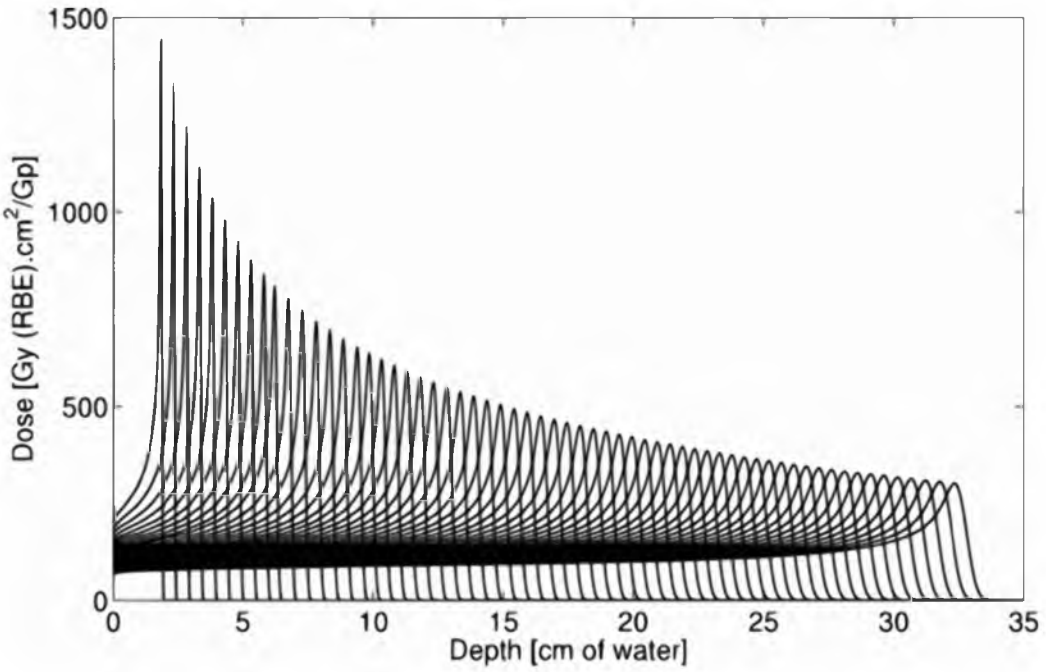

Figure 5.1: *Golden Bragg peaks data set generated in Monte Carlo and corrected through actual measurement. This Golden data set can simplify any institution's process to generate their TPS beam model for PBS planning.*

Once the *Golden* beam data set is acquired, only the range of deliverable energies with their corresponding energy spread ($\frac{\Delta E}{E}$) and beam size are needed to fully specify the delivery system. There are two approaches in order to obtain the $\frac{\Delta E}{E}$, either from theoretical models for a given accelerator, such as in the work by *Cascio et al. [113]*, or through measurements. At MGH, the measurement's approach was chosen for its higher accuracy. Thus, a few Bragg peak curves were measured with a PTW™ Bragg peak chamber ranging from the lowest (93

MeV) to the highest (225 MeV) available energies. Based on Monte Carlo calculations, it was shown that the diameter of the PTW™Bragg peak chamber (8 cm) was not large enough to fully characterize a Bragg peak curve. This is due to the small but non-negligible contribution of nuclear interactions (halo effect). The setup for the Monte Carlo comparison is highlighted in figure 5.2. The measurements therefore had to be corrected accordingly using the *Benhananik* formula displayed in equation 5.1.

$$C_X = 110 \times max(0, p35X^{35} + p4X^4 + p3X^3 + p2X^2 + p0) \qquad \text{Gy(RBE).mm}^2\text{.Gp}^{-1} \tag{5.1}$$

Where C_X is the correction factor, $X = \frac{d}{R_{80}}$ the relative depth along the Bragg peak, R_{80} the physical range of the given peak in cm, and $p35$, $p4$, $p3$, $p2$, $p0$ are factors given by:

$$p35(R_{80}) = min(0, 1.585 \times 10^{-5} R_{80}^2 - 0.004559 R_{80} + 0.04214)$$

$$p4(R_{80}) = 0.002133 R_{80}^2 - 0.04721 R_{80} + 0.195$$

$$p3(R_{80}) = -0.003363 R_{80}^2 + 0.0668 R_{80} - 0.3058$$

$$p2(R_{80}) = 0.001297 R_{80}^2 - 0.0174 R_{80} + 0.08441$$

$$p0(R_{80}) = 10^{-6} \times (0.4087 R_{80}^3 - 21.25 R_{80}^2 + 326 R_{80} + 215.6)$$

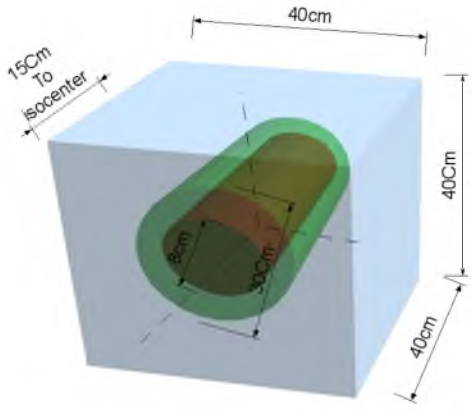

Figure 5.2: *GEANT4 Monte Carlo phantom geometry used for verification of the PTW™ Bragg peak chamber measurements. The energy deposited was recorded in a 8 cm diameter cylinder corresponding to the detector, as well as a 30 cm diameter cylinder which captured the full extent of the beam.*

The corresponding peaks from the *Golden* peak set at the measured energies were subsequently convolved using a Gaussian function. The Gaussian function parameters consisted of R_{80} and $\frac{\Delta E}{E}$ which were adjusted until the peak matched the corresponding corrected PTW™ Bragg peak chamber measurement. A fit of the energy spread as a function of the beam energy could then be derived. This process is shown in figure 5.3.
The full set of the MGH depth dose curves were finally created by convolving the entire *Golden* data set with the $\frac{\Delta E}{E}$ fit.

In addition to the Bragg peak set, the spot size as a function of beam energy was needed to

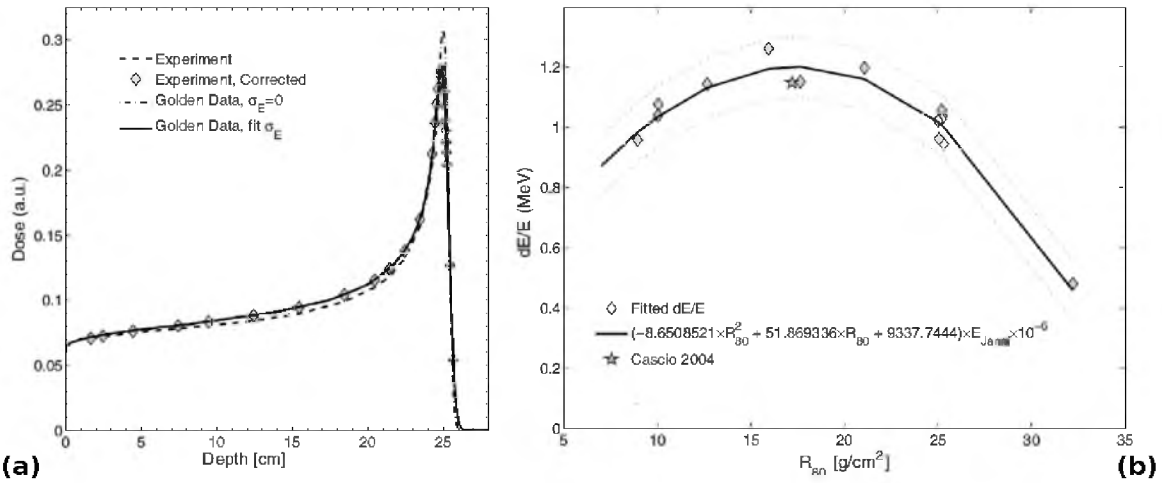

Figure 5.3: *(a) Fitting of a Bragg peak from the Golden data set to its corresponding measured peak. The measured peak was first corrected for the Halo effect component. The energy spread for that specific peak could then be determined. (b) Derived fit of* $\frac{\Delta E}{E}$ *as a function of beam range (energy) which can be used to conveniently generate the TPS beam model's depth dose curves. Modified from Clasie et al. [11].*

complete the TPS beam model. The spot size data was acquired as straightforward measurements using the Beam Imaging Device (BIS) from IBA™. The BIS consists of a high resolution scintillating screen and a readout CCD camera system. A single irradiation was performed with a single central spot at 26 distinct energies (layers). The energies ranged from the lowest to the highest available. The BIS was placed in air at the isocenter and a single snapshot was acquired for each layer. A simple Matlab™ routine was utilized to fit each spot with a Gaussian function from which the spot size value (Gaussian's σ parameter) could be obtained. A fit of the spot size as a function of beam energy was then derived. Figure 5.4 shows a single spot analysis with its Gaussian fit as well as the derived fit of spot sigma as a function of beam energy.

Once the entire beam model was acquired, Astroid was able to compute dose using a pencil beam algorithm (PBA). Thus, treatment plans could be generated following a defined prescription. A single or multiple beam approach may be utilized. Either way, each beam used in a plan presents a specific target that is segmented into a fixed-size grid on which spots are placed (*e.g.* figure 5.5). The dose delivered to this target by the given beam is then computed in water using a nominal 1 Gp fluence per spot. The contribution to each voxel j, from each spot i, gets recorded as bixels in a D_{ij} matrix, or bixel. The fluence in each of these bixels is then optimized by the system in order to meet a set of user-defined constraints. The

multi-criteria optimization process then results in the generation of anchor plans located on a Pareto-optimal surface based on objectives set by the user. These anchor plans are subsequently navigated by the user in order to obtain a desired treatment plan. This navigation process and the limitations of the specified constraints and objectives are further discussed below.

Solely these succinct descriptions of the PBA model and the optimization/navigation algorithm are provided here because original work was not performed on either of them. Instead, for further information the reader is invited to refer to the work by *Hong et al. [81]* concerning the PBA model, and the work by *Craft et al. [114]*, *Craft et al. [115]*, and *Chen et al. [116]* concerning the generation and navigation processes of Pareto-optimal surfaces for multi-criteria optimization purposes.

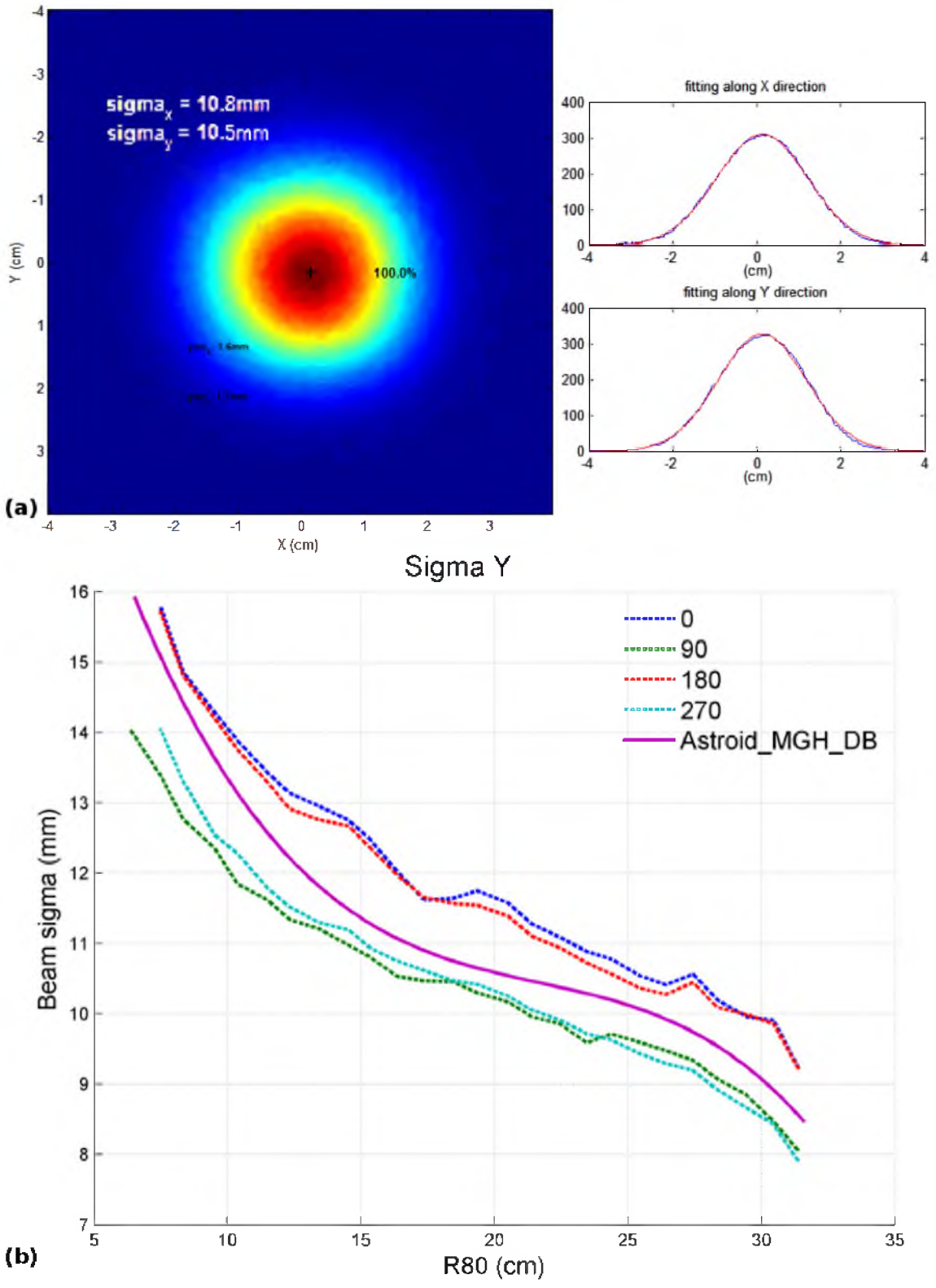

Figure 5.4: *a) Fitting of a single spot size using Gaussian approximations in X and Y directions; b) spot size as a function of energy for the cardinal gantry angles along with the final fit.*

5.3 Challenges in PBS planning

5.3.1 Spot placement

A scanning target volume (STV) is defined as a uniform 6 to 10 mm expansion of a dosimetric target volume (GTV, CTV, or PTV based on physician guidelines). The aforementioned STV is used by the system to geometrically place spots around the target. The spots are placed on a fixed-size grid determined laterally by the spot size (σ) at a given depth, and in depth as a function of the width W_{80} of the distal Bragg peak. The width W_{80} corresponds to the width of the distal 80 % point minus the proximal 80 % point along the Bragg peak curve. These parameters are set by the user, with typically 1 σ between the spots laterally, and 0.8 $\times$ the distal W_{80} in depth. This spot placement methodology is appropriate within the target volume as it results in an adequately homogeneous dose. On the other hand, this approach presents heavy limitations at the edge of the tumor which can potentially result in non-optimal treatment plans. This is true when high density variations are present at the tumor/tissue interface or when organs at risk (OAR) are directly adjacent to the tumor.

A tumor located at the edge of the lungs, for instance, will result in spots which are placed geometrically close to the tumor ($\approx$ 1.05 g/cm^3 density) but within the lungs ($\approx$ 0.4 g/cm^3 density). The large density difference will translate dosimetrically to spots with drastic overshoot in the low density region. This phenomena is illustrated in figure 5.5 where spots within the lungs, such as spot (A), will result in large overshoot and poor contribution to the actual target volume. It then becomes difficult to provide adequate coverage at the tumor interface without allowing unnecessary hot spots inside or outside of the target volume. This issue could be – and will be – solved by considering a spot placement based on water equivalent path length rather than a purely geometrical expansion. The STV would then correspond to a non-uniform expansion of the dosimetric target.

Spots are sometimes non-optimally placed around the tumor edges which is due to the fixed-size grid placement approach. In such instances, the closest spot to a given target's edge might already be far from that edge. Thus, the optimizer will have to put extra dose either inside the target along the edge or in that spot outside the target. The close proximity of an OAR can then be problematic as the OAR sparing could be compromised due to hot spots. One solution to mitigate this issue is to give the user the possibility to manually adjust the

spot placement around the dosimetric target. The optimizer would then be able to produce increased tumor coverage with greater OAR sparing. This solution, however, is not optimal as it would require a more iterative planning process with added computation time in order to optimally adjust the position of the spots. Another solution to this problem has been suggested by *van de Water et al. [117]* using an automated "resampling" process. In their own words, "resampling consisted of repeatedly performing: (1) random selection of candidate pencil beams from a very fine grid, (2) inverse multi-criteria optimization, and (3) exclusion of low-weight pencil beams". At the time of redaction, neither of these solutions has been investigated for Astroid.

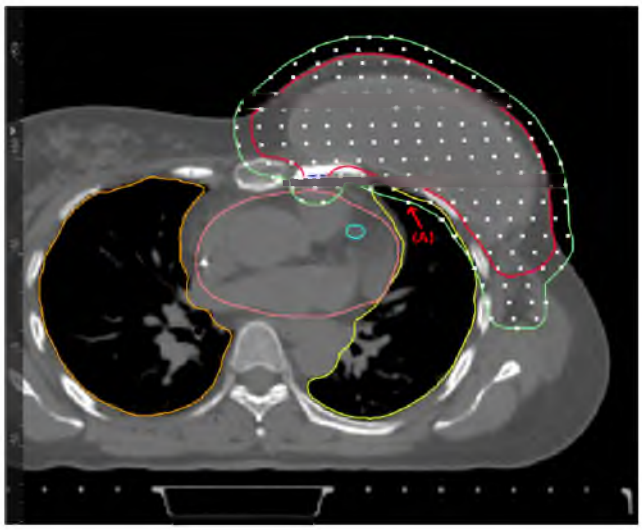

Figure 5.5: *Fictive spot placement along a fixed-size grid based on the geometrical STV expansion. Such fixed-size grid might result in poor optimization capabilities along the edge of the dosimetric target due to large density variations, such as in spot (A).*

5.3.2 Multi criteria optimization

Astroid uses only convex mathematical functions. Thus, the quality of the user-defined MCO parameters is critical as it can significantly affect the quality of the final plan. It is generally admitted that a minimal set of hard constraints should be specified in the MCO as it defines the boundaries of the optimization (hard constraints in convex mathematical functions cannot be violated). Thus, constraints are only specified for "appropriate" target coverage and a few OAR based on the prescription given by the physician. Pareto-optimal plans are then generated based on a more extensive set of objectives. These objectives thus define the optimization space that can be navigated by the user. The number and quality of these Pareto-optimal plans vary greatly as a function of the maximum number of iterations the optimizer is allowed to run (specified by the user). This may further affect the quality of the final plan. These effects are limited in simple cases due to the fact that the optimization is mathematically simple and

every solution is "acceptable". This is true, for instance, when the target is clearly defined within homogeneous tissue with critical OAR located further away from the tumor's edges. In most cases, however, critical OAR abut the target and/or the prescription is specified at multiple dose levels which tremendously increases the mathematical complexity of the optimization. In such cases, the more iterations the optimizer is allowed to run for, the better the balance between OAR sparring and target coverage. The obvious drawback is the drastic difference in computation speed.

In order to obtain better plans, it is also possible to go through a more iterative process using a smaller number of maximum iterations. The plan can quickly be run multiple times using a set of hard constraints which can be adjusted after each iteration, hence using the previous end point as the starting point. In larger problems, however, a set of constraints might become "infeasible" while in reality it is achievable through the multi-criteria optimization process. It is therefore useful to run a final computation with a "feasible" set of constraints for a large number of iterations allowed for the optimizer. This methodology is efficient and permits the user to achieve the most optimal treatment plans. Unfortunately, it comes at a high cost of resources which are limited by the time and computation power available at the time of planning.

5.3.3 Machine related limitations

As previously suggested, the PBS machine parameters are very limited: a set of available energies along with their respective energy spread and beam size at isocenter. Nevertheless, these few parameters have a dramatic influence on the quality of the plan that may be achieved.

The range of available energies determines the range of treatable depths as well as the possible need for range shifters. The use of a range shifter not only reduces the deepest reachable distance within the patient, but it also affects the size of the beam at isocenter due to multiple scattering. Furthermore, its use may be impractical due to the weight and time required for installation. An extensive air gap might also be required in order to avoid collision issues. The air gap will further emphasize the beam size increase due to geometrical considerations. Although the effect of the beam size increase is negligible for a machine with a large spot size (> 10 mm), it results in a poorer plan quality for a machine presenting a small spot size ($\approx$ 5 mm). Additional considerations on the use of a range shifter are the large reduction in the quality of beamline X-ray imaging as well as the potential safety concerns in case of it falling on the

patient during treatment.

The energy spread dictated by the beam transport line affects the width W_{80} of each Bragg peak. A larger energy spread results in slightly poorer homogeneity control between layers, but this issue is negligible as the spread is, by definition, minimal when using the PBS delivery mode.

As already suggested by the issues raised by the use of a range shifter, the beam σ represents the main machine related limitation. The beam size changes as a function of energy because more energetic protons spread significantly less while traveling through the beamline due to their higher velocity. A more energetic beam therefore results in a drastically small σ at isocenter. A smaller beam size results in a greatly improved target conformality and OAR sparing compared to a larger beam σ (*van de Water et al. [118]*). Thus, there has been a race to the smallest proton PBS beam size in order to offer the optimal proton treatment. The question thus becomes: how small is "small"? This is a complicated question to answer. The real issue linked to the beam size arises due the proximity of critical OAR to the target volume. A smaller spot size will result, by definition, in both sharper penumbras and added spot positions along the fixed-size grid. The MGH's spot size, at the time of writing, is quite large ($\approx$ 8 to 16 mm). This results in extraneous dose outside of the target volume. The future machine at MGH will present a significantly smaller spot size (expected $\approx$ 2 to 5 mm), thus offer a much greater control of the dose conformality. At the presently available sizes, a small improvement in the current spot size would result in clinically significant changes in the treatment plan's quality. Conversely, a small increase in the expected future σ would only slightly worsen the quality of the plan as the beam itself is smaller than the MCS spread through the patient. An alternative to improve a treatment plan using a large spot size is to utilize hardware – apertures and range compensators – which then limits the dose distally and laterally, hence improving the dose conformality (*Dowdell et al. [51]*). It should be noted that despite the fact that a smaller spot results in significantly better plans, it also requires drastically more time and computing power to optimize due to the higher problem complexity (many more spots to optimize). There are also a few practical implications from a treatment delivery point of view. Not only do the large number of spots result in a significantly increased treatment time, but the absolute delivery constraints must be significantly tighter in order to ensure the safety of the treatment. In this case, the plan robustness might be more easily affected. Although not yet available, one solution to these issues would be to consider an on-line modulation of the spot

size. Large spots could be delivered within the target while small spots could be delivered around the edges of the tumor. Such a system would ensure optimal quality for the treatment plan (target homogeneity and OAR sparing) as well as optimal treatment delivery speed and convenience.

5.3.4 Treatment robustness

Passively scattered proton fields, or homogeneous PBS fields, deliver a homogeneous dose within the whole target volume; at the exception of patch fields. A perturbation in any direction will result in small variations and is thus mitigated with the use of geometrical margins (beam specific PTV). When considering intensity modulated PBS fields, however, it gets a bit more complicated as beam perturbations will result in local disruptions of the dose homogeneity. The beam perturbations arise from multiple sources such as range uncertainties, setup shifts, and patient motion (especially breathing motion). Setup shifts, for instance, might displace the beam along heterogeneities where a large water equivalent path length difference might occur. This discrepancy could then result in a significant under/overshoot of single pencil beams. Range uncertainties represent the main limitation of proton therapy and many research studies aim at improving this issue. These range uncertainties occur due to setup quality, quality of the CT units' conversion to relative stopping powers, beam degradation, etc.
As a consequence, the "robustness" of each field as well as the overall plan is an important factor which should be taken into consideration for PBS treatment planning. At the time of redaction, however, there has not been an exact set of guidelines or methodologies to ensure the robustness of the treatment. Solutions such as geometrical margins, inter-pencil smearing, or large hot spots within the target volumes have been suggested but not yet fully assessed. For the time being, one can only infer on the treatment's robustness *a posteriori* through recomputations of the nominal plan under different scenarios. An example of this robustness analysis is presented below in a practical case. Such analysis only permits the ability to judge the quality of the plan's robustness but not to improve it. Thus, a plan that is shown not to be robust within clinically acceptable margins will have to be regenerated from the beginning, with its robustness re-assessed.

5.4 A practical example: PMRT

Radiation therapy has been an effective tool in the management of patients with breast cancer. The radio therapeutic treatment has been shown to improve local tumor control and potential survival benefits (*Ragaz et al. [119]*). Over the years, numerous improvements such as heart blocks, CT-based planning, intensity modulation, or breath holding (*Krueger et al., Lu et al., Remouchamps et al. [120, 121, 122]*) have been implemented. These ameliorations have permitted a greater tumor coverage as well as a reduction in the dose to the lung and cardiac structures. Despite these efforts, the heart dose remains an issue for many patients (*Gyenes et al., Darby et al. [123, 124]*). This is true for patients undergoing mastectomy, in which post-mastectomy radiation therapy (PMRT) targets the whole chest wall as well as the potentially involved lymph nodes (axillary, supraclavicular, internal mammary) after mastectomy. Thus, it is necessary to balance tumor coverage and the risks of cardiac failure. Several treatment planning studies have demonstrated significant dosimetric advantages of the use of proton therapy in reducing cardiac and lung doses while improving target coverage (*Ares et al., MacDonald et al. [125, 126]*).

While double-scattering proton therapy achieves these primary goals, certain aspects are less than ideal. The limitation in field size imposes the use of multiple fields which results in hot and cold spots along the matchline. Furthermore, the fixed modulation drives the skin to receive the full prescription dose. As a consequence, the use of PBS for PMRT treatment has been investigated at MGH (*Jimenez et al. [127]*). Two of the most distinctive features of PBS, intensity modulation and larger treatment field size, are critical elements for improving proton PMRT. In this section, we therefore present the treatment planning techniques employed in order to obtain optimal PBS PMRT treatment. It should be noted that only post-mastectomy patient, with or without breast reconstruction with implants, are considered for proton therapy. Indeed, the mobility of an intact breast or of a breast reconstructed with tissue, makes them poor candidates for proton therapy for which position reproducibility is key.

As previously discussed, although the quality of the treatment depends on the planning process, it is also largely affected by the practical considerations of the machine. For this reason, this work also highlights the efforts realized in patient setup and treatment delivery in order to further improve the use of PBS for PMRT treatment. The robustness of the treatment plan was also evaluated *a posteriori*.

5.4.1 Patient setup

PMRT patients are setup on a breast board used for conventional photon/electron treatment. The angle of the breast board is raised at the highest angle possible, limited only by the bore size of the CT scanner. The angle helps the surface imaging system used during patient setup. Various additional steps have been taken in order to improve the patient position reproducibility: the original breast board head rest has been replaced by a head cup generally used for head and neck treatment to better control the neck position; a chin strap and hand grips are provided to further remind the patient of their chin and arm positions. Historically, the patient's arms are generally raised above their head. This is due to the collision issue during treatments with conventional photon tangent fields. Such consideration is not necessary for PBS treatment due to the use of en-face fields. Thus, a new akimbo-like position with the arms down has been evaluated for PBS treatment. Figure 5.6 shows both setup positions for the same patient at the time of CT scan.

This novel akimbo position presents several advantages for PBS treatment:

- Comfort: PMRT patients usually come in for radiation therapy shortly after their mastectomy surgery which leaves them with painful scars around the breast tissue. This makes it particularly difficult, and sometimes unbearable, for them to keep their arms raised above their head.
- Accuracy: as the patient gets tired and/or relaxed during the course of a treatment session, their arms tend to move downwards relative to their bust. This potentially changes both the position and shape of their axillary and suprclavicular nodes which could result in an inaccurate treatment.
- Practicality: not only is the raised-arm position difficult to reproduce, but the elbows and the breast board's arm cups are generally located outside of the CT's reconstruction field of view. This results in potential collision and reproducibility issues of the snout during treatment.

One drawback of using an akimbo-like position is the hardening of the beam through the arms' bony structure, creating artifacts in the CT. However, the conversion curve between CT

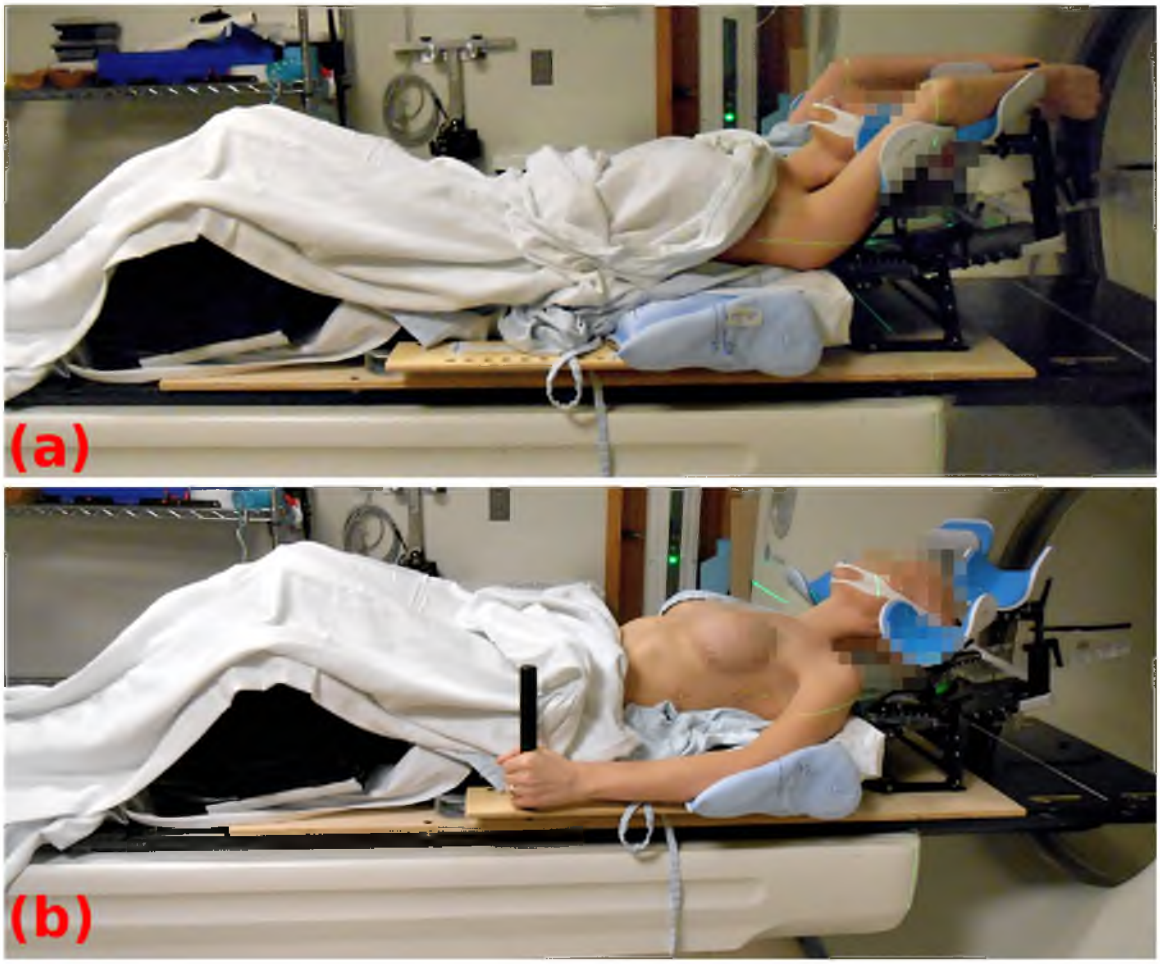

Figure 5.6: *PMRT patient setup at the time of CT scan: (a) conventional arms up setup position, (b) novel arms down setup position; in both cases, a chin strap and hand grips are used to ensure better reproducibility of the setup position.*

HU and the proton relative stopping power ratios (RSP) is adjusted on a patient/scan specific basis. The beam hardening therefore does not affect the quality of the plan nor the dose calculation.

In the case of a larger patient, unwanted underarm skin flaps might be in the beam path. These skin flaps could affect the treatment reproducibility and create areas of hot spots on the skin. For such a patient, the conventional arms-up setup position would be used for treatment.

5.4.2 Treatment planning

The target for PMRT is usually composed of the whole chest wall (CW) and the potentially involved lymph nodes (axillary, supraclavicular, internal mammary).

Planning objectives are generally defined as follow:

- 45 Gy(RBE) to the chest wall and all nodes, followed by a 5.4 Gy(RBE) boost to the chest wall(s) and the internal mammary nodes (IMN) for a total dose of 50.4 Gy(RBE)
- 48 Gy(RBE) max dose to the chest wall's skin ($\approx$ 3 superficial mm)
- 3 Gy(RBE) max dose to the left anterior descending coronary artery (LAD)
- 5 Gy(RBE) max dose to the heart ventricles
- $\leq$ 1 Gy(RBE) max mean dose to the heart
- $V_{20} \leq$ 15 % for each lung
- 42 Gy(RBE) max dose to the thyroid
- 40 Gy(RBE) max dose to the esophagus

Range uncertainties are primordial in proton therapy as they can rapidly result in an under dosing of the target and/or over dosing of the OAR.

For patients without a breast implant, the chestwall target volumes are usually very shallow with a required beam range of 3 cm or less. The associated uncertainty is thus only around a millimeter and can be practically ignored, being comparable to uncertainties in CT scanning, contouring, etc.

For patients that undergo reconstructive surgery, however, the implant will result in a deeper treatment range, hence larger range uncertainties. Measurements were thus performed in order to accurately assess the relative proton stopping power ratio (RSP) of the material inside breast implants. Specifically, a Bragg peak of a known energy/range was irradiated through a water phantom with and without a box containing the material found in breast implants. The range degradation was then evaluated. Based on the conversion curve used for dose computations[70], the Hounsfield units found in breast implants correspond to RSP of 1.02 on average, as evaluated on 10 patients. The range pullback observed during the experiments, on the other hand, yielded a value consistent with a material of 0.92 RSP. During the planning process, the breast implants are therefore contoured and their RSP values homogeneously overridden to 0.92. The omission of this correction would result in Astroid computing each pencil beam with a 10 % pullback error, translating to a 10 % overshoot during treatment delivery. With the contribution from the breast implants entirely eliminated, the resultant range uncertainties consist only of those found in the real chestwall tissue, and can therefore be practically ignored.

PMRT plans are generated with a single geometric en-face field 30° from vertical. This field is first assigned to the 45 Gy(RBE) volume (CW + involved nodes) for 25 fractions, then to the 50.4 Gy(RBE) volume (CW+IMN) for 3 fractions. Pareto-optimal plans are generated through

the optimization of the proton fluence in the individual spots based on the abovementioned set of constraints and objectives. The set of Pareto-optimal plans are then navigated to a desired state. The target coverage and dose to the cardiac structures can then be optimally balanced through intensity modulation. Likewise, it is possible to reduce the skin dose to an acceptable level, especially in the supraclavicular nodal region which is located deeper within the body. Figure 5.7 shows a nominal PBS PMRT plan generated for clinical use at MGH.

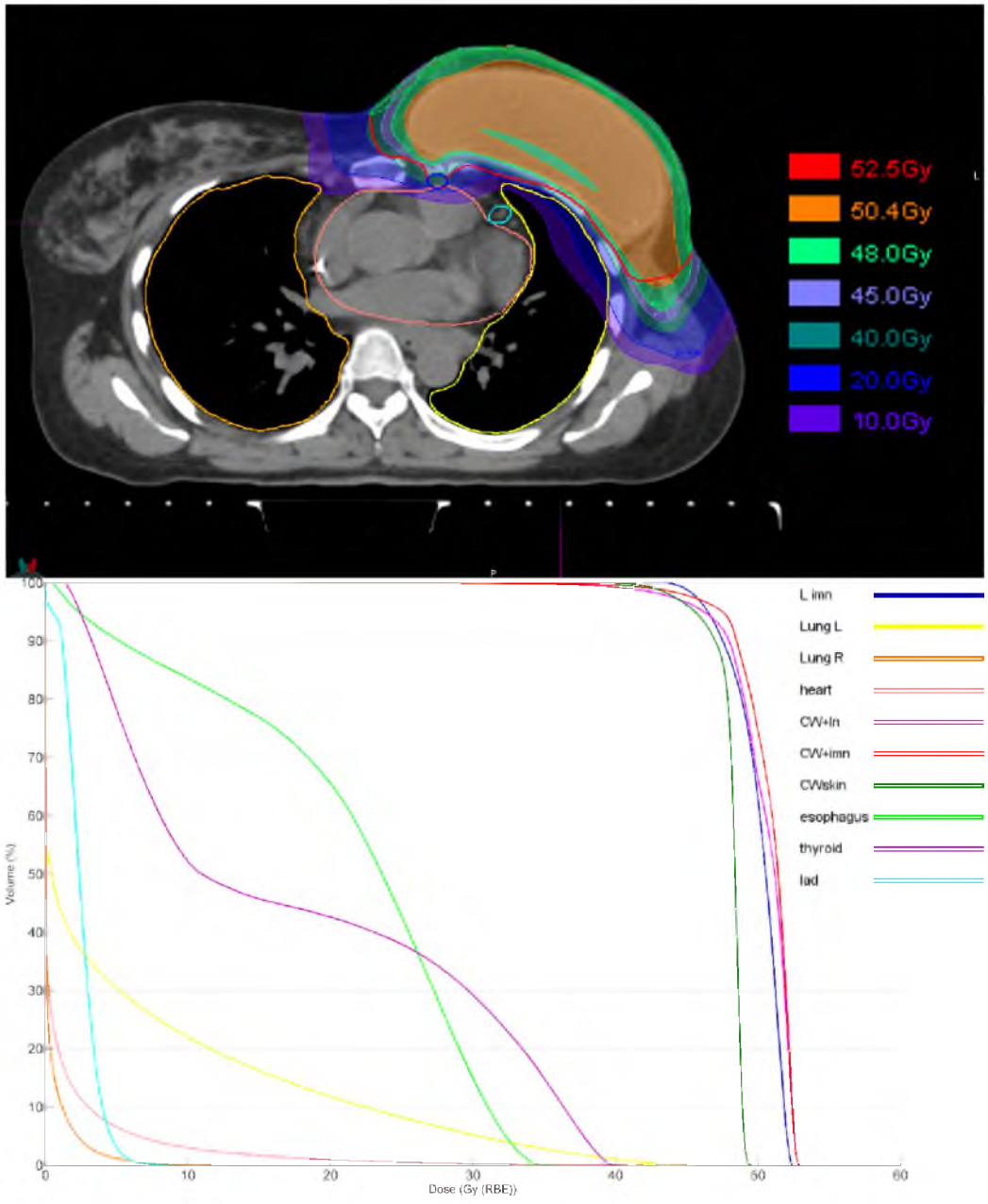

Figure 5.7: *A proton PBS PMRT plan and its associated dose-volume histograms (DVH), as intended for treatment at MGH.*

The treatment plan shown in figure 5.7 was also regenerated using a fictitious machine with a much smaller spot size (2 to 5 mm instead of 9 to 16 mm, as a function of energy). This machine corresponds more or less to a future proton machine that will be installed at MGH. The new plan was optimized and navigated with the exact same set of constraints as the plan intended for treatment. This fictive plan is presented in figure 5.8.

This fictive plan highlights the dramatic effect of the machine parameters on the plan's quality. There is a clear advantage of using a smaller spot size; the IMN coverage is optimal and the only loss in target coverage is fortuitous, due to superficial skin sparing. The drastic reduction in beam penumbra results in higher tumor conformality and far greater OAR sparing with virtually no dose given to the contra-lateral lung.

The PBS PMRT plans generated for clinical treatment at MGH are already considered to represent a great improvement over conventional photon/electron therapy (*Depauw et al. [44]*). The use of a better/newer proton accelerator would therefore help reach the optimal treatment plan.

On the down side, the computation of this plan with such a smaller spot size took approximately five times longer than the clinical plan intended for treatment. The implementation of a much faster dose computation algorithm and/or cloud computing is therefore needed to fully take benefit of the better machine. Additionally, such a treatment plan results in a drastically more complicated treatment delivery. The dramatic increase in the number of spots to be delivered would translate to a significantly longer treatment time. Moreover, the thresholds associated with beam delivery safety would be much tighter due to the smaller spot size, making the delivery much more strenuous on the system.

5.4.3 Plan robustness

As previously discussed, for the moment the robustness of a plan can only be assessed *a posteriori*, and thus only be performed through recomputations of the nominal plan under different scenarios. The robustness of both presented nominal plans (figures 5.7 and 5.8) have then been evaluated against breathing motion and setup shift uncertainties.

The analysis of the setup shift uncertainties was performed as a recomputation of the nominal plans with the introduction of geometrical perturbations. The perturbations were as follow: $\pm$ 3 mm along each translation axis (lateral, longitudinal, vertical), $\pm$ 2 $^\circ$ along each rotation axis (yaw, pitch, roll), and a combination of all aforementioned $\pm$ shifts in all 6 directions simulta-

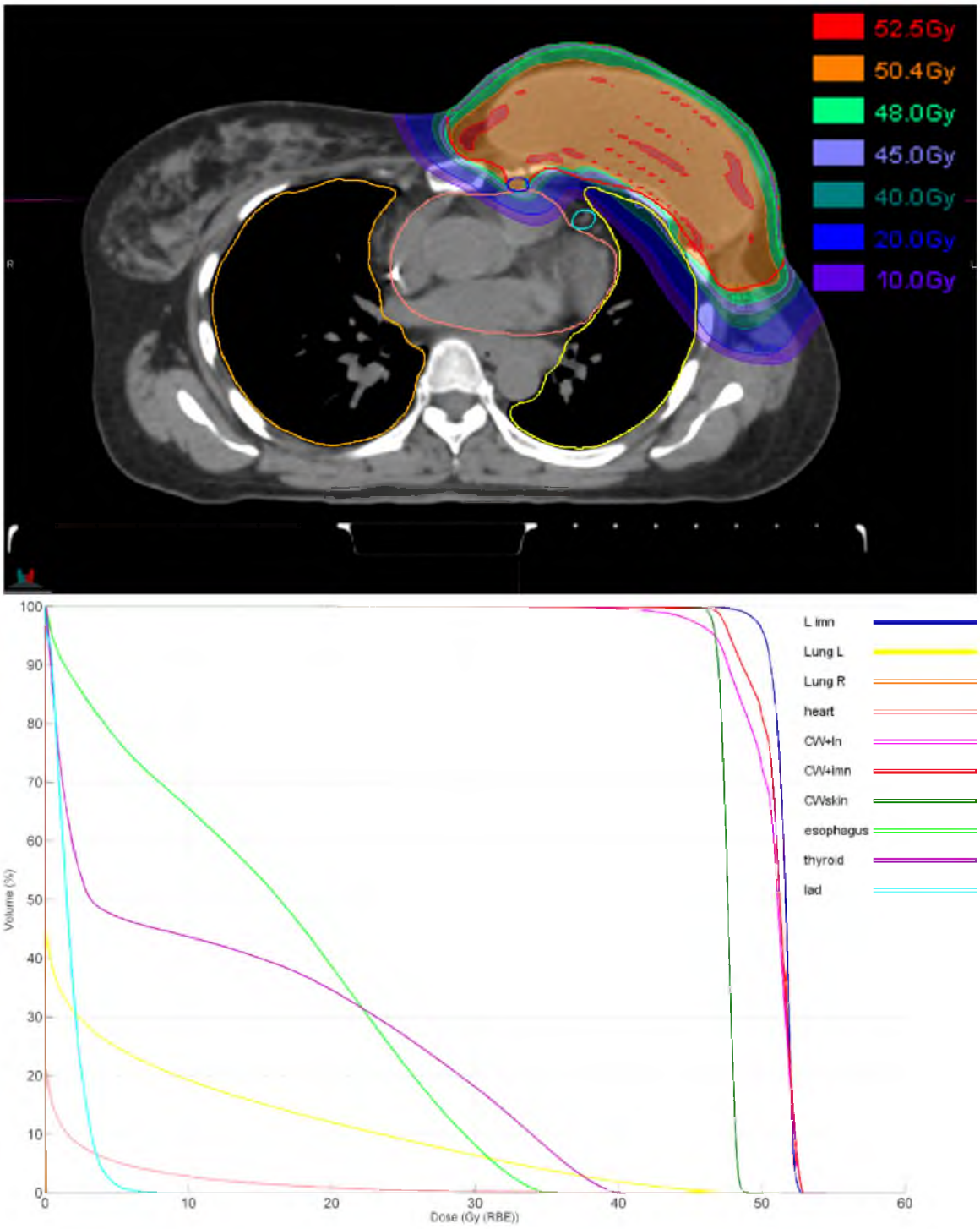

Figure 5.8: *A proton PBS PMRT plan based on the use of a fictitious machine with a small spot size (2-5 mm) and its associated DVH.*

neously. DVH data were then generated for each scenario. The composite dose distribution based on the average of the individual shifts was also computed and its DVH generated. This average dose distribution corresponds to the expected treatment over the course of treatment

due to the statistical randomness of the shifts based on a large fractionation scheme. The result of this analysis is presented in figure 5.9 as DVH envelopes which correspond to the maximum amplitude of the resultant perturbations in the original plan.

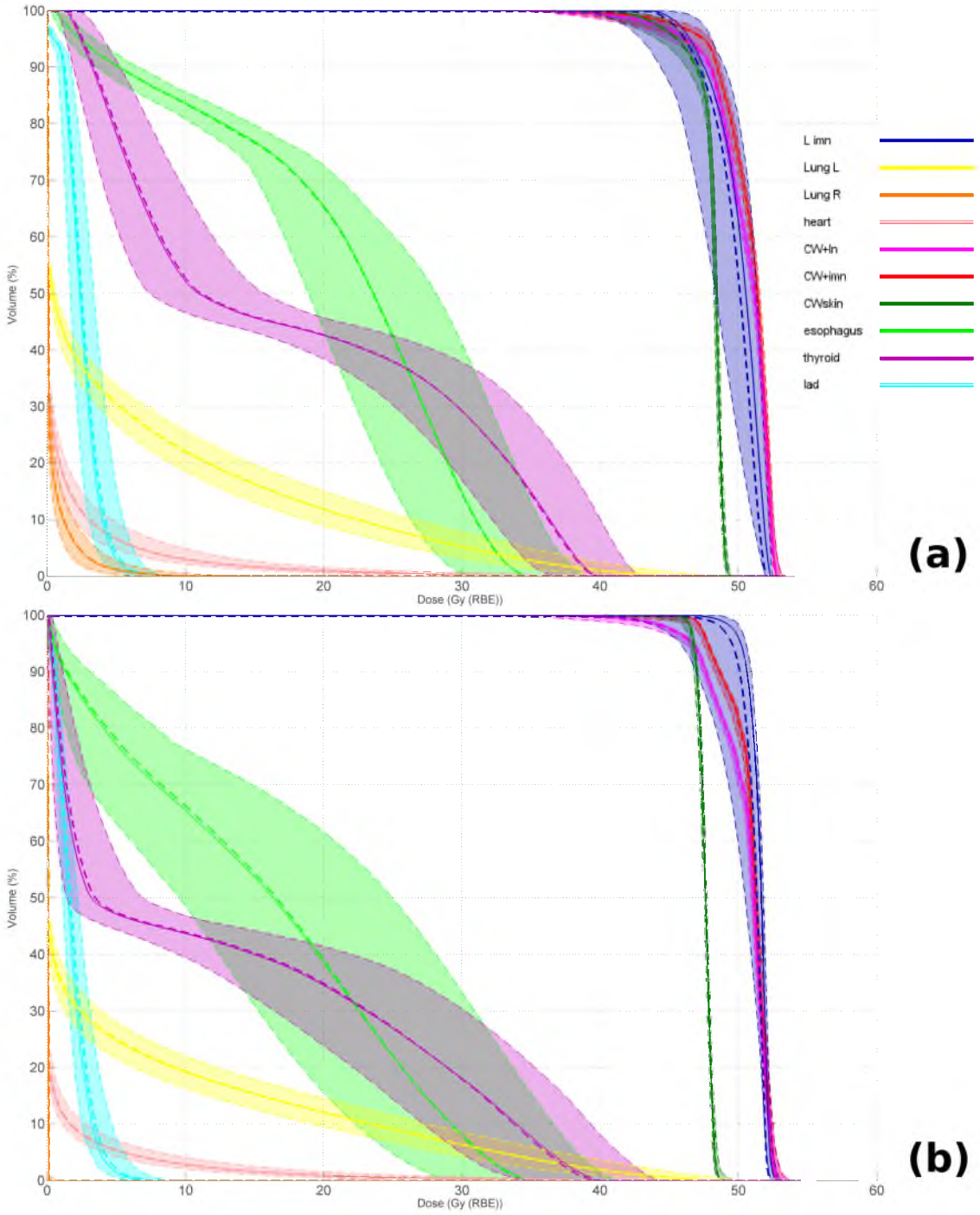

Figure 5.9: *DVH envelopes based on the robustness analysis of the setup shifts (± 3 mm, ± 2 °) performed on previously presented PMRT patient plans (solid line); (a) MGH clinical plan, (b) small spot plan. The thick dotted lines correspond to the composite dose distribution based on the average of the individual shifts' doses.*

The setup robustness analysis considered individual systematic shifts as well as a combination of all these shifts. The combination of all of the shifts is considered a worst case scenario. In reality the worst disturbance would arise from a distinct patient-specific combination of the individual perturbations. This, however, cannot be easily quantified, and the proposed methodology is believed to be a fair representation of the worst case scenario. Consequently, it is admitted that any combination of those shifts ($\leq \pm 3$ mm, $\leq \pm 2$ °) will be contained within those DVH boundaries.

The analysis of the robustness of the setup shifts resulted in appropriate stability of the tumor coverage, hence showing the adequate robustness of such plans. Although the effect on most OAR is small, the IMN, thyroid, and esophagus (which are dosimetricly linked) suffer significantly more from these setup shifts. Nevertheless, the IMN coverage remains higher than with conventional photon/electron therapy.

As expected, these perturbations have a larger effect on a plan based on a smaller spot machine as compared to the current MGH machine. This is explained by the fact that the amplitude of the shifts is comparable to the size of the beam. The nominal dose distribution with the smaller spot size, however, is far better than the intended clinical plan, and the worst case scenario remains similar to the treatment deliverable currently.

In both cases, the composite dose distributions based on the average of the individual shifts' doses are remarkably close to the intended treatment. These DVH deviations are therefore considered clinically acceptable, and the plans reasonably robust. A more consistent set of analyses based on a large cohort of patients will be performed in the future to actually quantify the robustness of the offered PBS PMRT treatment.

For the breathing motion study, a 4D-CT scan of the patient was acquired in addition to the regular planning CT scan performed at quiet respiration. The PBS fields created for the nominal plans were then transferred to each phase of the 4D CT scan and the dose distributions were recomputed. DVH were generated for each of the 10 phases as well as for the total composite dose accumulated through deformable registration, mimicking the actual treatment. Figure 5.10 shows the result of the breathing motion analysis on both the clinical and fictive PBS plans.

The recomputations of the dose distributions onto the 10 phases of the patient's 4D CT scan resulted in little difference for both machine. These deviations, drastically smaller than the

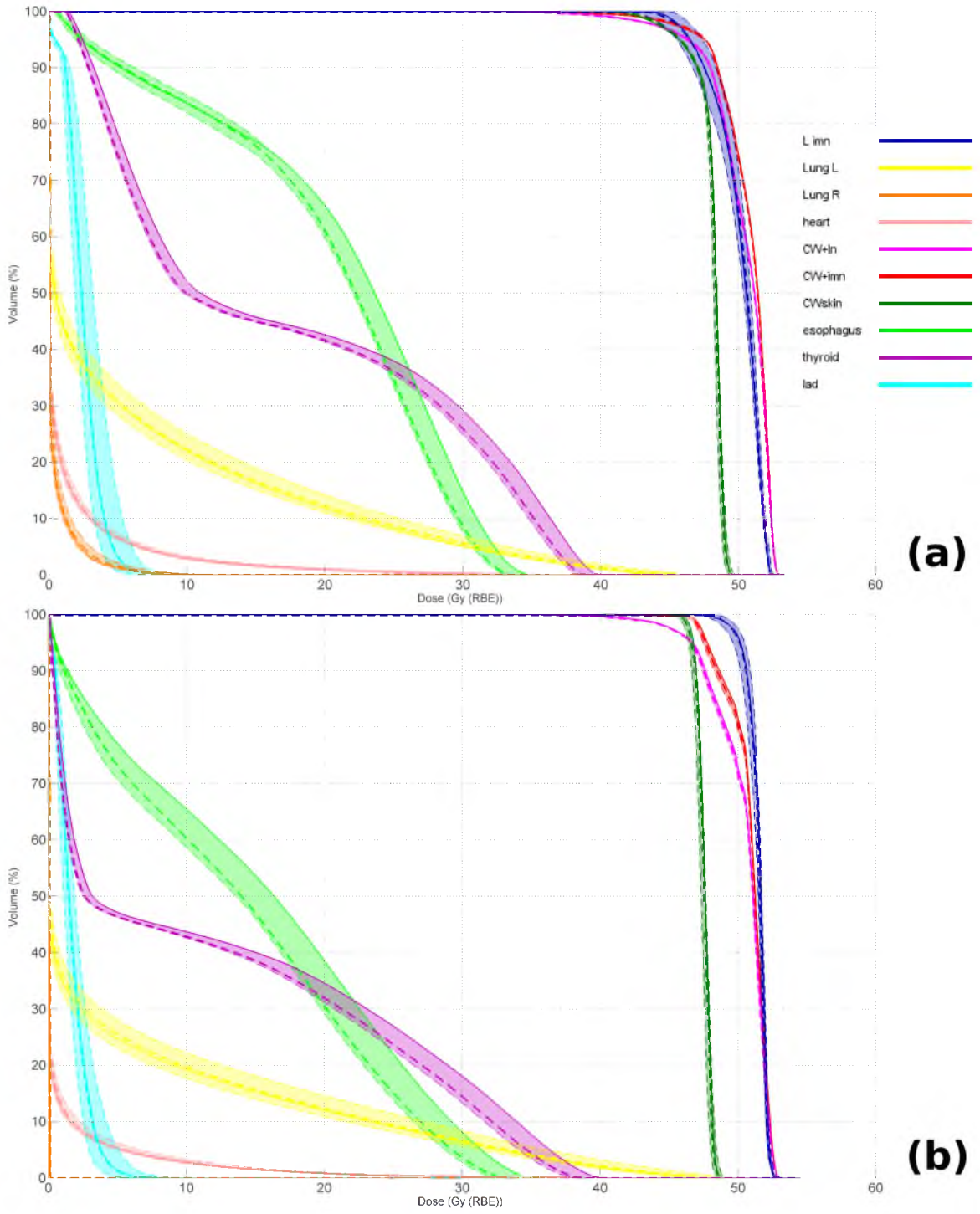

Figure 5.10: *DVH envelopes based on the breathing motion analysis performed on the previously presented PMRT patient plans (solid line); (a) MGH clinical plan, (b) small spot plan. The thick dotted lines correspond to the composite dose distribution based on the average of the 10 breathing phases' doses.*

ones observed in the robustness analysis, are thus believed to be of no clinical concern. Furthermore, the composite dose distribution based on the average of the 10 breathing phases' doses, which statistically correspond to the actual treatment, are remarkably similar to the intended plans.
Ideally, these treatment plan robustness analyses should be performed on every single PBS plan, and should result in specific guidelines for each treatment site at a given institution. Furthermore, being able to predict *a priori* the robustness, or non-robustness, of a given plan, would be of great advantage for PBS treatment planning and delivery. Unfortunately, the current technology does not allow for such heavy recomputations due to limited resources and computing power. The implementation of a much faster dose computation algorithm and/or cloud computing, would once again prove to be very useful in the execution of such a task.

5.4.4 Treatment delivery

The conventional setup process for most proton centers relies on orthogonal X-ray. First, the patient is positioned based on tattoos priorly inked at the time of CT-sim, afterwards orthogonal X-rays are taken at a specified cardinal angle and the patient precisely placed at isocenter; finally, a beamline X-ray is performed at the treatment gantry angle to finalize the setup position. This modality was deemed suboptimal for PMRT patients as it considers bony anatomy as a surrogate for the chest wall position (*Fayad et al. [128]*). Instead, surface imaging is used as the primary tool for patient setup as the target volume is both shallow and superficial (*Gierga et al., Cervino et al. [129, 130]*). The use of surface imaging results in a faster yet more accurate patient positioning along with minimal imaging dose (only the final beamline X-ray is required). An example of a setup surface image is presented in figure 5.11.

Figure 5.12 shows the residual setup errors for 4 patients in all 6 degrees of freedom, based on the use of surface imaging. The boundaries of the aforementioned robustness analysis are highlighted as red dashed lines on these graphs. This emphasizes that the use of surface imaging for patient setup results in treatment position errors largely within the robustness analysis limits. Surface imaging is therefore an appropriate tool for patient positioning. Furthermore, these residual shifts are a combination of both specific positional shifts and breathing motion which, statistically, will average out over the duration of treatment and eliminate most of the undesired dosimetric perturbations.

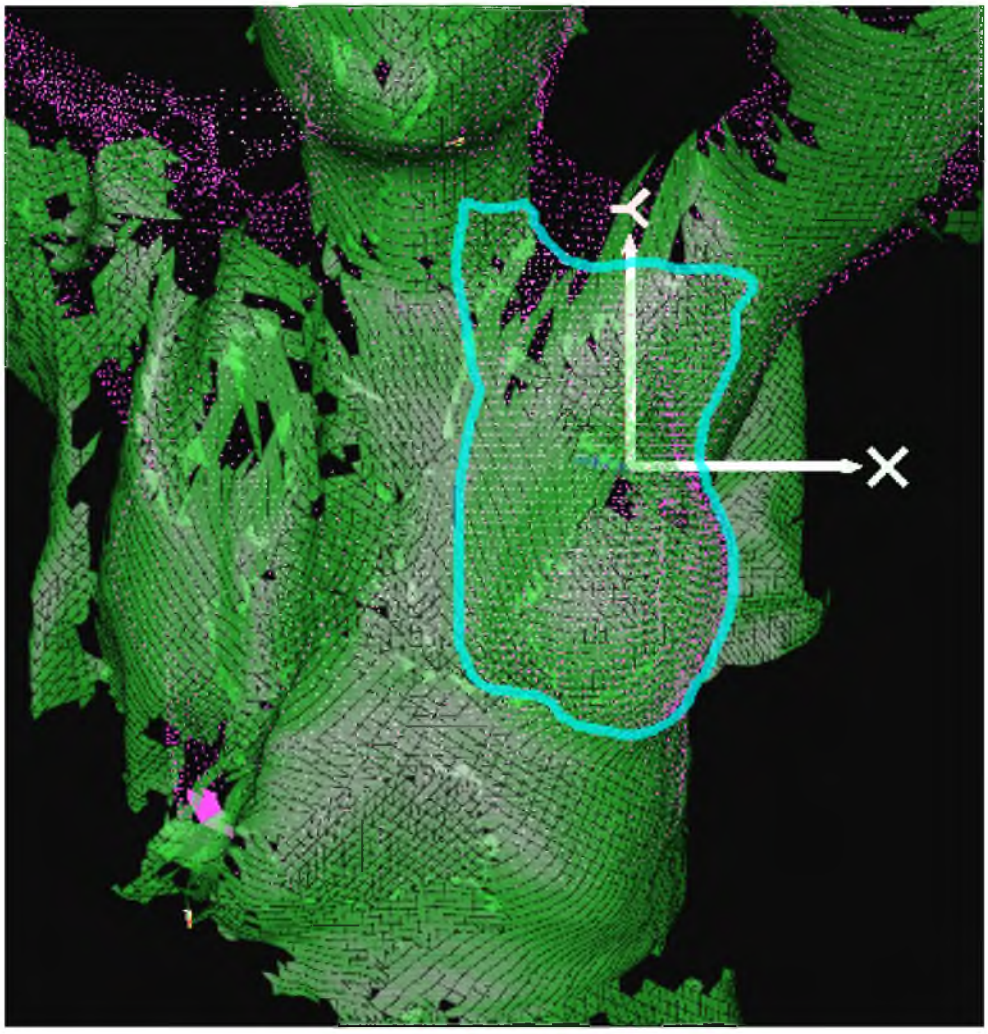

Figure 5.11: *PMRT patient setup at the time of treatment using surface imaging; the finely dotted pink mesh represents the skin contour based on the planning CT while the green area represents a daily setup image that was evaluated for setup registration. The patient could therefore be accurately setup based on the shallow target, virtually represented by the cyan contour, using the skin surface rather than bony anatomy.*

The accuracy of the skin dose calculated by Astroid was also evaluated for PMRT patients due to the shallowness of the target. Two fictional plans were generated in a solid water phantom, one mimicking a non-reconstructed chest wall patient (3 cm Range, full modulation), the other mimicking a patient with a breast implant (11 cm range, full modulation). Measurements were subsequently performed using thermoluminescent dosimeters (TLD) at 0, 1, 3, 5, and 7 mm depth as well as in the center of the fields. Additional measurements were performed at the same positions using a Markus ionization chamber for absolute dosimetry. The results are presented in table 5.1

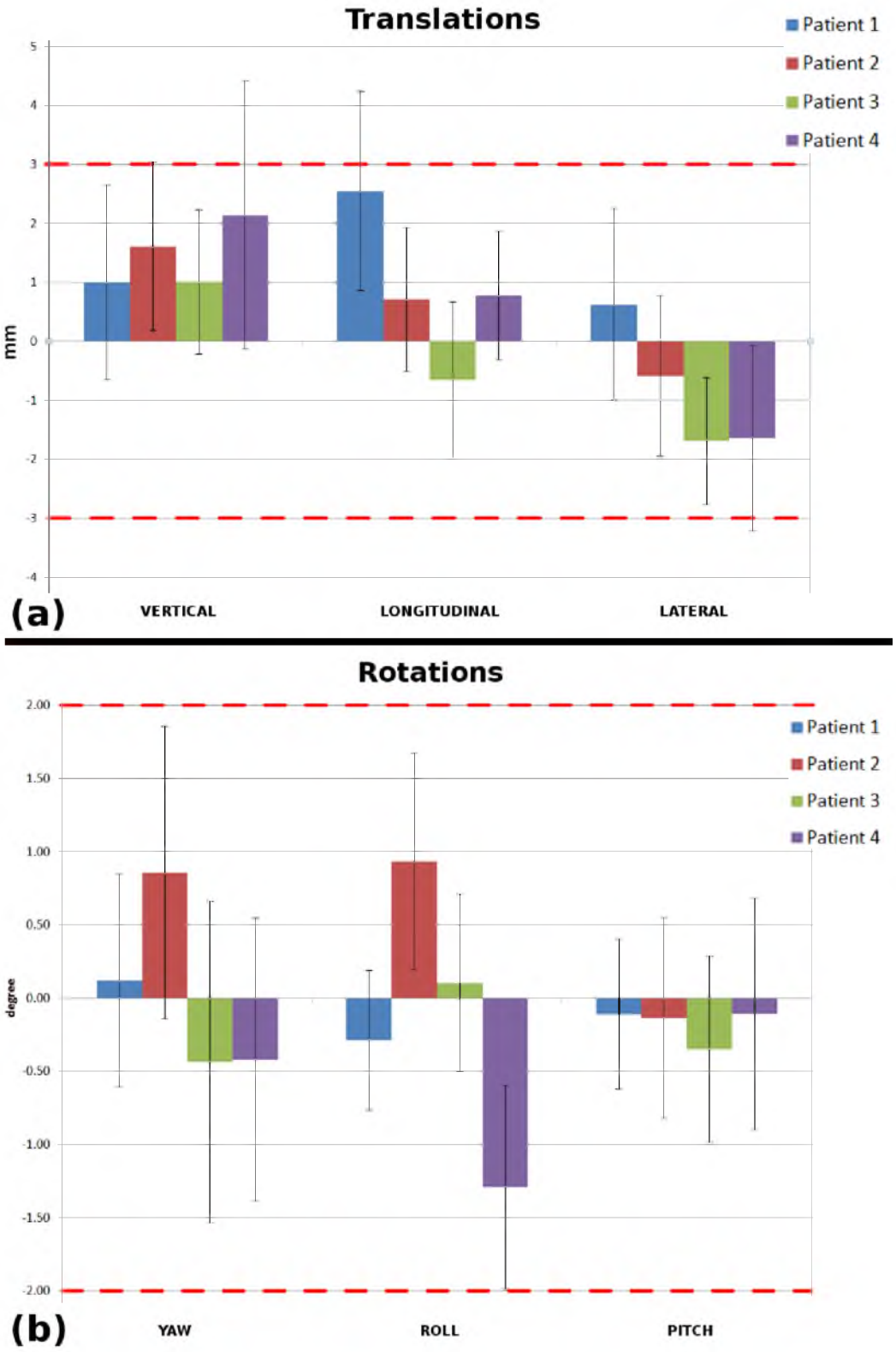

Figure 5.12: *Residual patient setup errors along the 6 degrees of freedom for 4 PMRT patients based on the use of surface imaging. The red dashed lines correspond to the perturbations used in the robustness analysis of the setup shifts.*

(a) 3 cm range, full modulation

Depth mm	Markus chamber cGy(RBE)	TLD cGy(RBE)	TLD error %	Astroid cGy(RBE)	Astroid error %
0	87.6	86.2	-1.5	93	6.2
1	91.0	87.5	-3.9	97	6.7
3.3	99.2	97.4	-1.9	102	2.8
5.4	101.0	98.0	-2.9	102	1.0
7.6	97.5	95.8	-1.7	100	2.6
13	101.5	97.6	-3.9	102	0.4

(b) 11 cm range, full modulation

Depth mm	Markus chamber cGy(RBE)	TLD cGy(RBE)	TLD error %	Astroid cGy(RBE)	Astroid error %
0	88.1	85.6	-2.9	94	6.6
1	90.4	86.5	-4.4	97	7.3
3.3	94.5	92.1	-2.6	97	2.7
5.4	95.4	89.2	-6.5	98	2.8
7.6	93.8	91.2	-2.8	96	2.3
43	99.3	97.2	-2.1	100	0.7

Table 5.1: *Comparison of the skin dose for PBS PMRT treatment between Astroid's predictions, TLD measurements, and Markus chamber measurements for (a) a field mimicking a PMRT treatment without a breast implant (3 cm range, full modulation), and (b) a field mimicking a PMRT treatment with a breast implant (11 cm range, full modulation).*

The TLD and Markus Chamber measurements agree within 5 % of each other, matching expectations (*Zullo et al. [131]*). Those measurements are also in good agreement with the TPS values for depths of 5 mm and beyond. The closer the measurements were from the skin, the larger the TPS's discrepancy, reaching 7 % at the superficial skin. This shows that Astroid slightly overestimates the superficial skin dose for PBS treatments. Although this result is similar to computations performed by photon TPS (*Qi et al. [132]*), the reasons are quite different. In the current version of Astroid, this discrepancy is explained due to the omission of the proton build-up when a range shifter is used, in its current version (*Clasie et al. [11]*). In order to confirm this hypothesis, the two aforementioned plans were re-generated using a fake range shifter burned directly into the CT scan rather than using Astroid's internal range shifter model. These new plans agreed within 2.5 % of the Markus chamber measurements at any depth, as illustrated in figure 5.13.

The current discrepancy introduced by Astroid, however, is not considered an issue from a clinical point of view as it provides further skin sparing, which is desirable. Tangential photon fields commonly deliver ≈ 43-45 Gy(RBE) to the superficial skin through the use of bolus. PBS, on the other hand, is planned with ≈ 48 Gy(RBE) which then translates to ≈ 45.5 Gy(RBE)

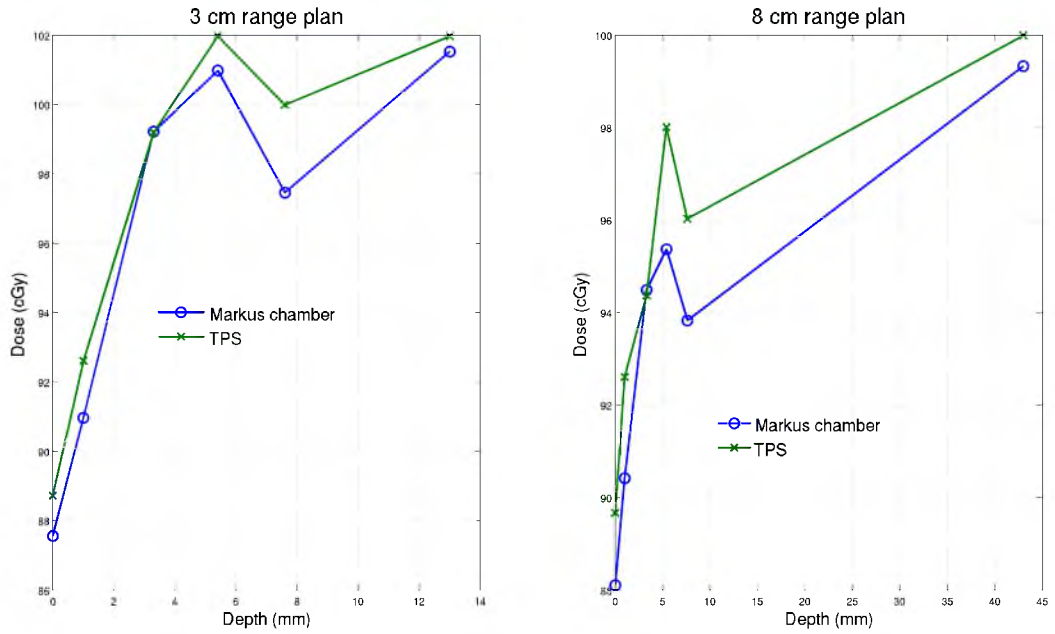

Figure 5.13: *Comparison of the skin dose for PBS PMRT treatment between Markus parallel plate ion chamber measurements and Astroid's prediction based on the use of a fake range shifter rather than the system's internal range shifter algorithm.*

actual dose after a 5 % correction.

5.5 Conclusion

The current treatment planning methodologies for PBS at MGH have been described in this work. Although Astroid's MCO capabilities greatly improve the planning experience and the quality of the treatment plans, it suffers from multiple limitations. From a treatment point of view, the main limitation resides in the machine parameters themselves, especially the size of the beam. It was highlighted that a machine with a smaller spot size results in better tumor coverage along with better OAR sparing. From a technical point of view, however, a smaller spot size results in a significantly longer computation time and computing power needs. The issue of spot placements, due to the fixed-grid size approach, also translates into the need for stronger computing power. With faster computation algorithms, the spot placements could be optimized internally by the system through an iterative process. The robustness of a PBS PMRT plan was evaluated on a single plan only due to the large resource requirements to perform a more systematic study. An institution would greatly benefit from the capability to perform *a priori* robustness analyses for any plan. This, again, translates into the need for a

faster computation algorithm and extended computing power.

Additionally, it was discussed in section 2.4.2 that the pencil beam algorithm commonly used for proton treatment planning was lacking in accuracy in the presence of large heterogeneities. Although, these inaccuracies are generally within the clinically acceptable range (2 %), they can sometimes be far greater for patients with unfavorable geometry, such as in lung cancer patients [24]. In such cases, one must turn toward Monte Carlo dose calculation algorithms which offer single particle tracking models. Thus, these MC algorithms result in appropriate estimations of the dose along large heterogeneities.

With these current limitations in mind, an extremely simplified Monte Carlo algorithm was developed within the Astroid framework. This Monte Carlo engine offers greater accuracy than PBA algorithms as well as faster, more parallelizable computations, which can be used to overcome some of these computing speed needs.

Chapter 6

Fast MC dose algorithm

6.1 Introduction

As previously discussed, proton therapy treatment planning systems (TPS) are currently relying on a pencil peam plgorithm (PBA) for dose computations in patient (*Hong et al. [81]*). PBA, while relatively fast, fails to fully model the effects of heterogeneities which can be critical during delivery, e.g. for lung tumor treatment. It is therefore necessary to turn towards full Monte Carlo (MC) systems such as GEANT4 in order to obtain the most accurate dose representation in patients. However, these systems have a large overhead and generally comes at a high time and resources consumption. For this reason, full MC dose computations are usually reserved as an independent dosimetry check, rather than for actual treatment planning. Thus, there is a real necessity for an improved dose calculation engine in radiation therapy.
We propose a simplified MC algorithm for proton dose calculation. The latter, known as GMC ['glmlk] (*A unique or quirky special feature that makes something "stand out" from its contemporaries.*), was intended to be extremely fast yet accurate against tissue inhomogeneities. GMC's implementation is intended to be at the lowest level of the MGH proton TPS, Astroid, hence simply replacing the current clinical PBA engine. [1]

[1] This work was partially presented at the International Conference on the Use of Computers in Radiation Therapy(*Depauw et al. [55]*), and published in their proceedings(*Depauw et al. [56]*).

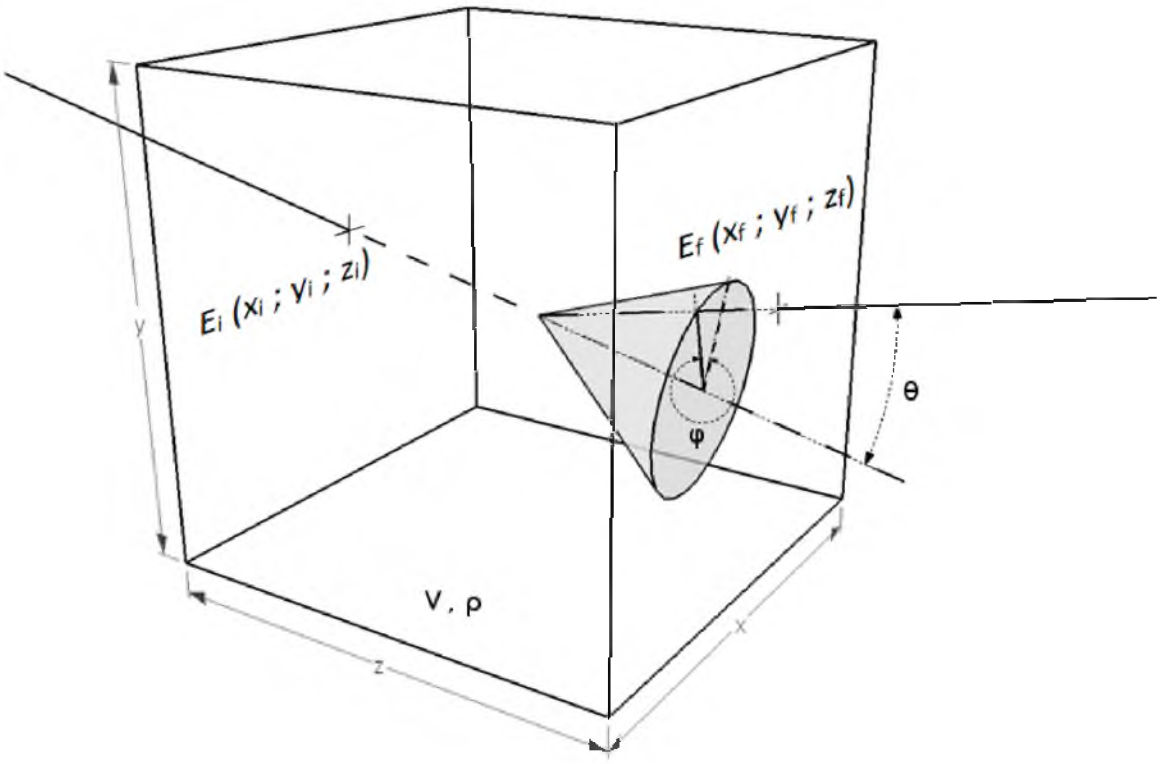

Figure 6.1: *GMC's particle transport model at the voxel level.*

6.2 Algorithm implementation

6.2.1 Specifications

Figure 6.1 shows a representation of the particle transport in GMC at the voxel level. A particle enters a voxel (volume V, density ρ) with certain input parameters: current energy (E_i), relative position (x_i, y_i, z_i) and direction cosines (u_i, v_i, w_i) within the voxel, and initial energy (E_0) (energy at the entrance of the phantom/patient). A cord length (L) is computed from a non-scattered transport of the particle (straight line) through the voxel. For Coulomb scattering, the mean radial scattering angle is subsequently computed from the scattering power described by *Gottschalk [133]*, as shown in equation 6.1, and applied midway through the cord ($\frac{L}{2}$).

$$\langle \theta^2 \rangle = \int_0^L T_{dM} \mathrm{d}x \approx T_{dM_i} \times L \qquad (\mathrm{rad}^2), \tag{6.1}$$

with,

$$T_{dM} = f_{dM}(E_i, E_0) \times \left(\frac{E_s}{E_i}\right)^2 \times \frac{1}{X_s}, \tag{6.2}$$

where,

$$f_{dM} = 0.5244 + 0.1975 \times \log_{10}(1 - \left(\frac{E_i}{E_0}\right)^2) + 0.2320 \times \log_{10}(\frac{E_i}{MeV}) - 0.0098 \times \log_{10}(\frac{E_i}{MeV}) \times \log_{10}(1 - \left(\frac{E_i}{E_0}\right)^2) \quad \text{(MeV)}, \tag{6.3}$$

θ is the average radial scattering angle, x the distance already traveled by the particle along its track in cm, $Es = 15.0$ MeV, and $X_s = 46.88$ cm.

The azimuthal scattering angle is a random variable between 0 and 2π.

The Halo effect, due to the protons' nuclear interactions (inelastic), is evaluated based on a particle's remaining energy E_i. The nuclear interaction probability as a function of particle range in water is described in *Paganetti [12]*. GMC relies on a fit of the probability of interaction per centimeter. This fit, as seen in equation 6.4, is a function of energy based on Janni's energy-range power-law relationship in water (*Janni [66]*). The resulting nuclear interaction probability per centimeter as a function of energy can be seen in figure 6.2. Upon nuclear interaction, the proton will undergo large angle scattering while releasing, on average, half of its kinetic energy to another proton that will scatter with a similarly large angle (see section 2.2.1). For simplicity and computational speed purposes, GMC only halves the energy but doubles the weight of the primary particle deflecting it with a large radial scattering angle only (0.2 radians); the secondary particle itself is not tracked. It is believed that the statistical nature of these nuclear interactions will naturally compensate for the imbalance created by only tracking the primary proton with the additional weight. Similarly to Coulomb scattering processes, the azimuthal angle remains variable between 0 and 2π.

$$\frac{dP}{dR} = 9.297 \times E_i^{-0.509} \quad (\%.\text{cm}^{-1}) \tag{6.4}$$

where, $\frac{dP}{dR}$ is the particle's probability of nuclear interaction per centimeter of range (based on E_0), and E_i the remaining particle energy in MeV.

The mean energy loss ΔE is based on the initial proton energy E_0 and the trapezoidal approximation of the integral under the curve of its corresponding Bragg Peak. The set of Bragg peaks for all energies is given by Astroid's PBS beam data based on *Clasie et al. [11]*, as described in Chapter 5. The local dose deposited ΔD is then computed from equation 6.5, assuming a relative mass stopping power ratio equal to unity. This process is highlighted in figure 6.3 for a 150-MeV proton.

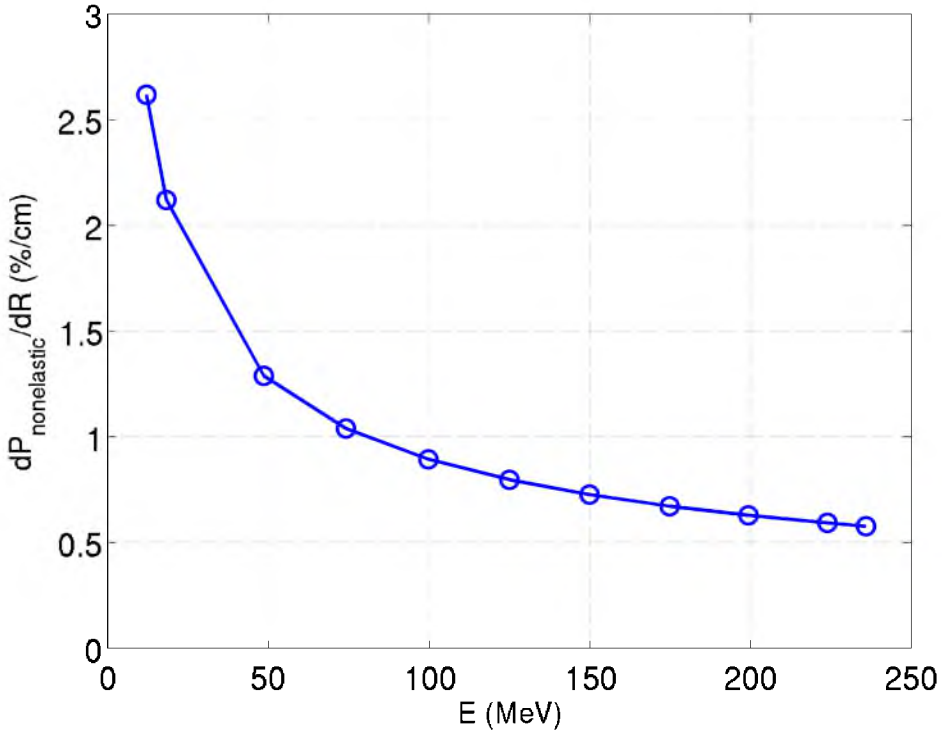

Figure 6.2: *Fit of the nuclear reaction probability per centimeter as a function of remaining energy, based on the data from Paganetti [12].*

$$\Delta D = \frac{\Delta E}{\rho V} \qquad \text{(Gy)}, \tag{6.5}$$

where,

$$\Delta E = S_{medium}^{water} \times L \times \left(\frac{\mathrm{d}E}{\mathrm{d}x}\right)_{water} = \int_{X_1}^{X_2} f(X)\mathrm{d}X \qquad \text{(MeV)}, \tag{6.6}$$

and,

$$\int_{X_1}^{X_2} f(X)\mathrm{d}X \approx \rho L \frac{f(X_2) + f(X_1)}{2} \tag{6.7}$$

where, S_{medium}^{water} is the relative mass stopping power ratio (unitless), and $\int_{X_1}^{X_2} f(X)\mathrm{d}X$ the integral below the Bragg peak curve in which X_1 and X_2 are based on the current particle energy E_i in MeV; $f(X)$ is given in units of Gy.mm^2, and X_1 and X_2 in g/cm^2.

At the TPS level, spot positions for a particular beam are internally selected based on the requested target. The relative dose contribution from each spot j to point i, also known as the D_{ij} matrix, is then computed based on one gigaproton delivered per spot. One D_{ij} matrix is computed per beam. The subsequent optimization/navigation process modulates the number

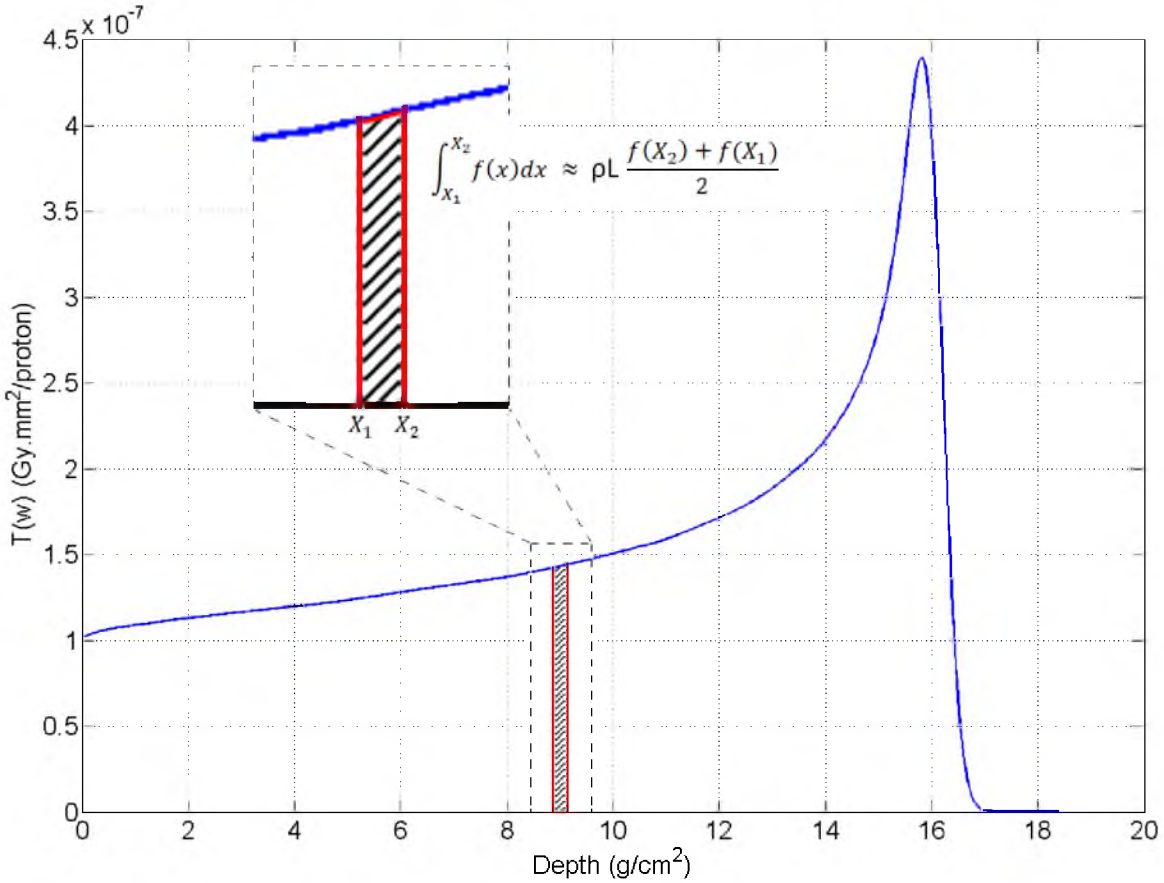

Figure 6.3: *Dose deposition model based on Astroid's PBS beam data(Clasie et al. [11]).*

of protons per spot in each field as a whole in order to attempt to obtain the best compromise between the objectives specified by the user.

GMC is implemented at the lowest level of Astroid within the D_{ij} matrices computation, in lieu of the former PBA engine. It operates at the bixel level, that is, the computation of the dose contribution in patient from each spot based on one gigaproton. This calculation takes into account the machine parameters such as SAD, in order to obtain accurate beam transport, and the initial spread information (beam sigma in air as a function of initial energy). For more details about the higher level hierarchy of Astroid, please refer to *Kooy et al. [45]*.

6.2.2 Double-Scattering algorithm

GMC can also be adapted for proton double-scattering dose computations because a Spread-Out Brag Peak (SOBP) is the combination of multiple pristine Bragg Peaks, as shown in figure 6.4. As such, the initial energy E_0 of the beam could be evaluated from the SOBP range from

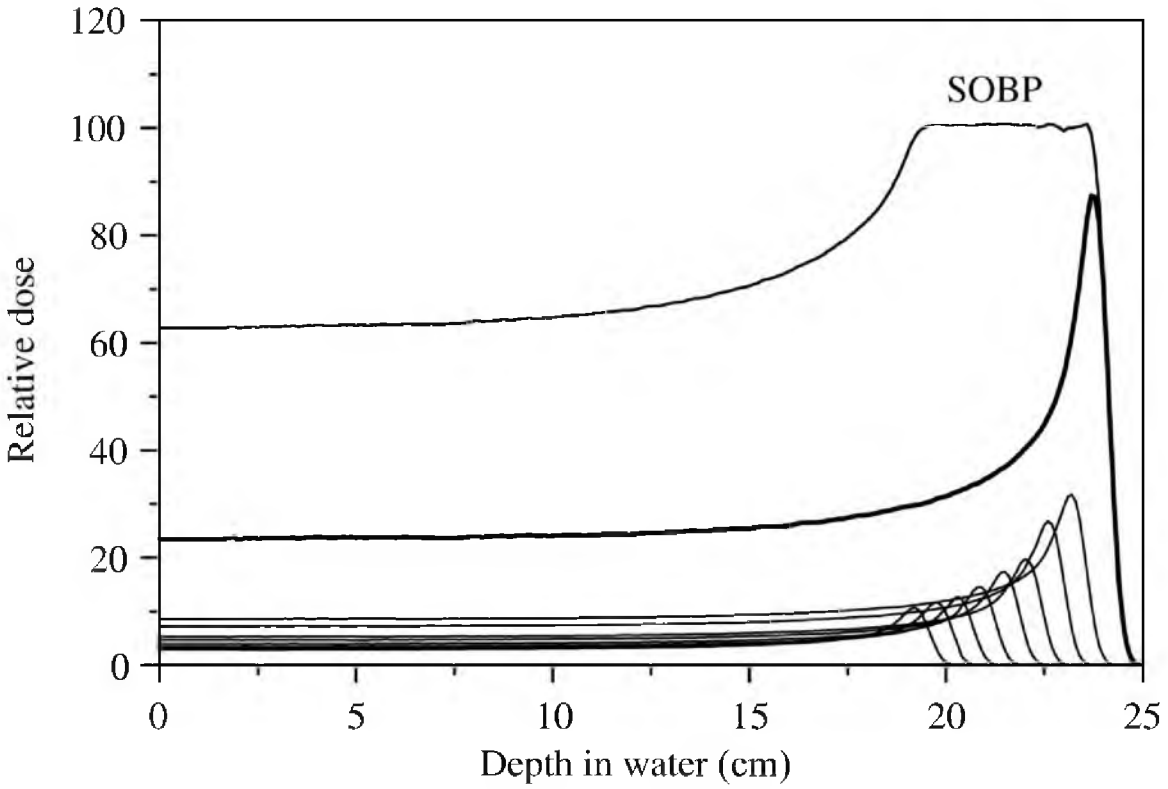

Figure 6.4: *A Spread-Out Bragg Peak (SOBP) based on individual pristine Bragg peaks; this is part of Astroid's DS beam data.*

Janni's energy-range power-law relationship in water as described in equation 6.8 (*Janni [66]*).

$$E_0 \approx 30.486 \times R^{0.576} \qquad \text{(MeV)} \tag{6.8}$$

where, R is the SOBP range in cm, and E_0 the corresponding incident energy of the beam.

Furthermore, in DS mode the dose deposition in the TPS is in relative units only. The field could therefore be computed based on an arbitrarily chosen scale, such as 100 cGy, and then be appropriately normalized according to the plan's prescription.

The energy deposited could be derived from the trapezoidal approximation of the integral under the SOBP curve, similarly to the PBS mode. The remaining energy after each interaction would be based on a fraction of the initial energy E_0.

The scattering power could be computed based on E_0 and the remaining energy, using equation 6.1.

A different approach might have to be implemented concerning nuclear interactions. Some additional specific measurements as a function of equivalent field size would probably be needed.

6.2.3 Portage to GPU

The use of a Graphical Processing Unit (GPU) can drastically improve the performance of any parallelizable algorithm.
For GMC, there is an obvious gain to be performed as each spot is individually computed. There are pitfalls associated with the GPU architecture, such as difficulty of code debugging and non trivial memory considerations. For this work, a so-called "pseudo-code" – a version of the algorithm that is first implemented on a CPU architecture – was generated in order to validate and easily debug the various processes of the algorithm.

6.3 Validation of GMC's algorithm

GMC's dose computation algorithm was tweaked and verified based on the evaluation of the physical observables.

6.3.1 Absolute depth dose distribution

Computation were first performed in a virtual water phantom using a single monochromatic point source. The machine SAD was considered infinite and the incident beam did not present any angular spread in order to match the generation parameters of Astroid's input beam model. The overall depth dose curve was visually inspected and the integral as well as range R_{80} were computed. These depth dose distributions were then compared to the input data from MGH's beam model for all 129 available energies.
The input beam model is expressed in absolute units of Gy(RBE).mm^2.Gp^{-1} in accordance with the convention set by *Pedroni et al. [112]*. These peaks correspond to the integrated depth dose along the beam path. A small discrepancy in range R_{80} was therefore expected in GMC since the cumulative track length of each particle through the phantom would appear slightly shortened due to the added small scattering angles. In order to compensate for this effect, it was necessary to virtually scale the curves from the input model. The range analysis based on the first set of simulated depth dose curves could thus be used to evaluate the correction needed. Rather than stretching the actual input data, GMC slightly decreases the apparent cumulative distance traveled after each interaction/dose deposition. This correction

is performed based on the formula described in equation 6.9.

$$Rtweak_E = 0.9991 - 0.000004 \times E_0 \tag{6.9}$$

where $Rtweak$ is a unitless scaling factor, and E_0 the incident energy of the particle in MeV.

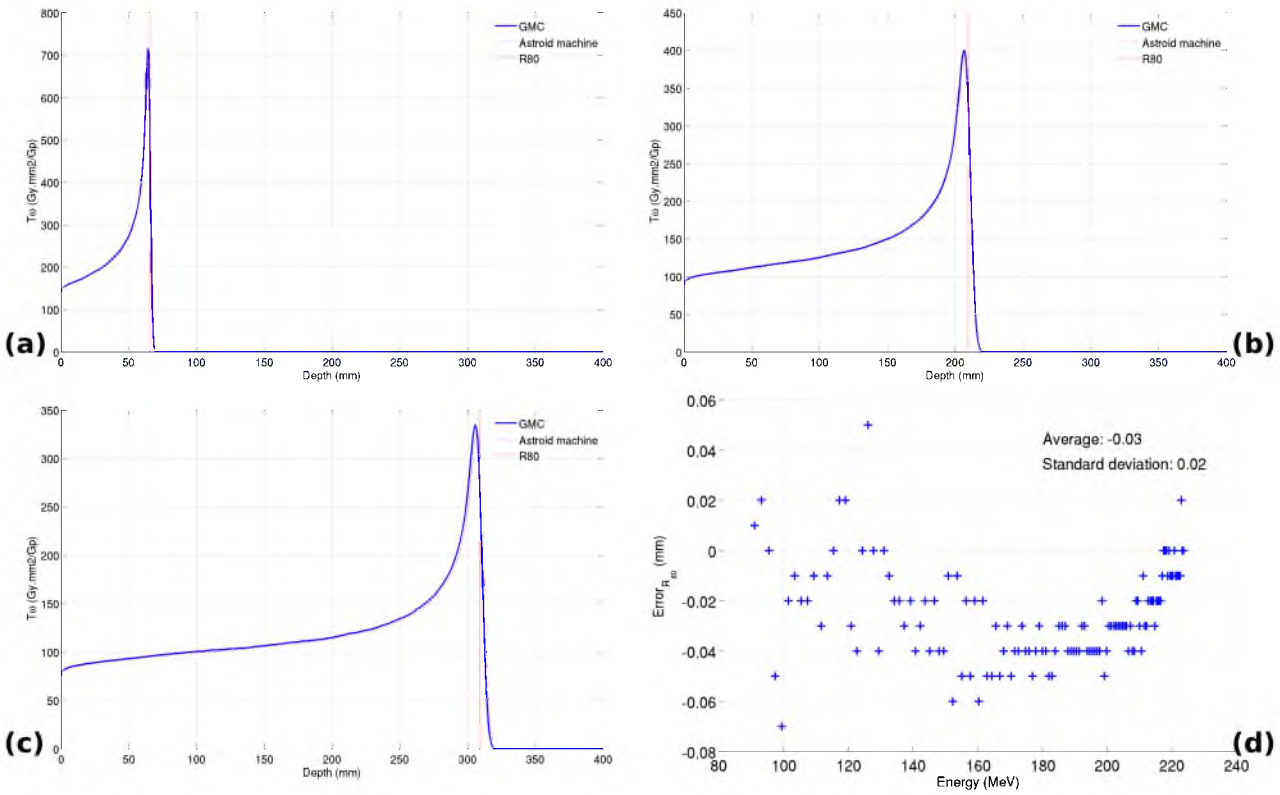

Figure 6.5: *Depth dose comparisons between GMC simulations and Astroid's beam model data for (a) a 91.015 MeV beam, (b) a 175.82 MeV beam, and (c) a 223.25 MeV beam. The simulations were performed in a 2 × 2 × 2 mm voxel geometry with infinite SAD and no initial spread (point source at surface) after path length correction, per equation 6.9; (d) remaining range discrepancy between GMC simulations and Astroid's beam model data after path length correction.*

Figure 6.5(a-c) shows the matching depth dose distributions between the input beam model and GMC's computations for three beam ranges after the range correction. Figure 6.5(d) shows the remaining error in range as a function of beam energy. The curves show extremely good agreement in absolute dose highlighting the proper dose deposition mechanism of GMC's algorithm. The remaining range discrepancy after path length correction is close to null with an average of -0.03 ± 0.02 mm, well beyond clinical expectations.

The proton stopping power ratio (i.e. density) of the virtual water phantom was then altered in order to check that GMC adequately deposits dose as a function of medium stopping power. Figure 6.6 presents three peaks of similar energy but computed with different water densities,

namely 1.0, 1.5, and 0.75. As expected, the height of the peak in absolute dose remains constant as a function of medium density but the range R_{80} is shifted inversely proportional to the medium density.

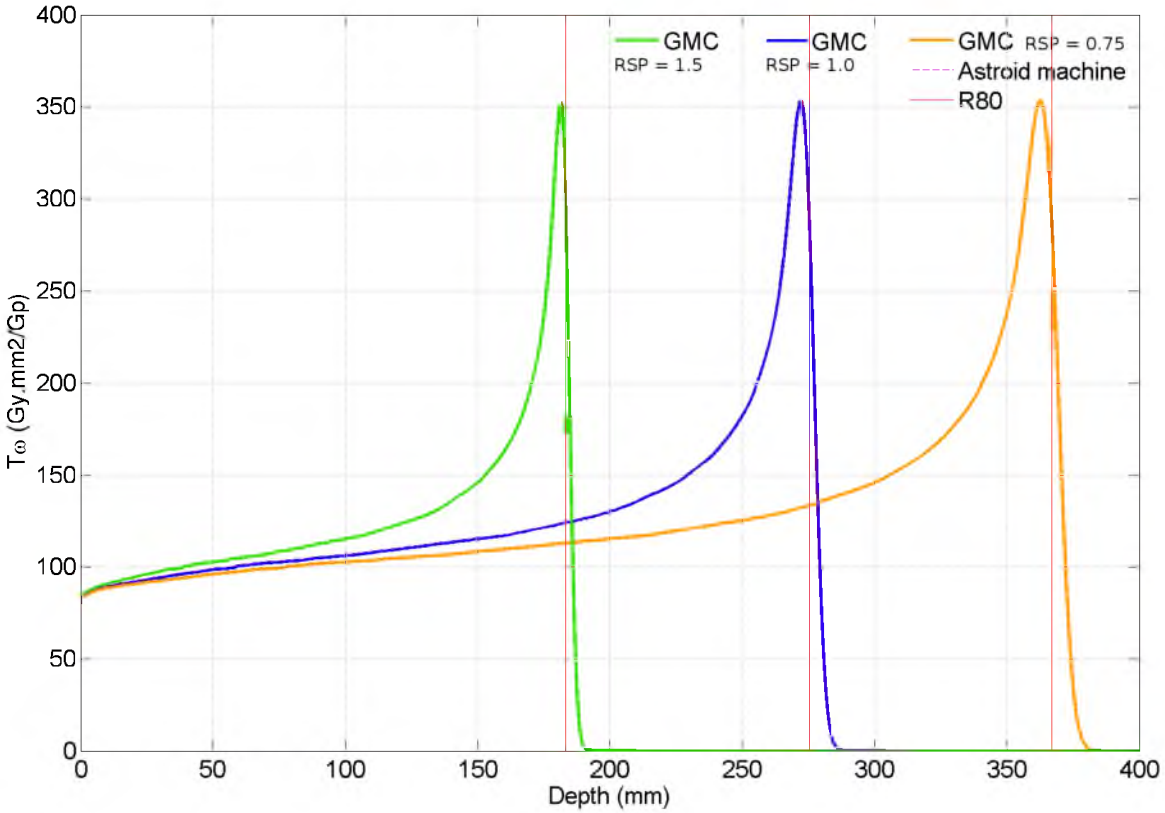

Figure 6.6: *GMC simulations in a water phantom made of three different proton stopping power ratios, namely 1.0 (blue), 1.5 (green), and 0.75 (orange). The height of the curve remains constant while the range is inversely shifted due to the density difference. Astroid's beam model data in water (RSP = 1) is shown for comparison purpose (dashed magenta line).*

6.3.2 Scattering power

The same set of computations could also be analyzed for angular scattering as a function of range. The scattering power, derived from Gottschalk's formula (see equation 6.1, could therefore be evaluated. The sigma of the beam was thus automatically computed along the depth dose curve at every $R_{90}/20$ increments. The average relative angular spread as well as its standard deviation based on all 129 energies are shown in figure 6.7, alongside the theoretical data from *Hong et al. [81]*. The small bump in the entrance region for GMC's computations was believed to arise from the initial absence of spread.This absence of spread resulted in dose deposition in a single voxel laterally, thus affecting the Gaussian fit.

This hypothesis was validated by running the same simulations with a much higher lateral resolution (0.2 mm versus 2 mm) for only a few energies. These results were in perfect agreement with the Hong model, as shown in figure 6.7.

This result highlight the correctness of GMC's scattering power along the depth dose curve as a function of energy.

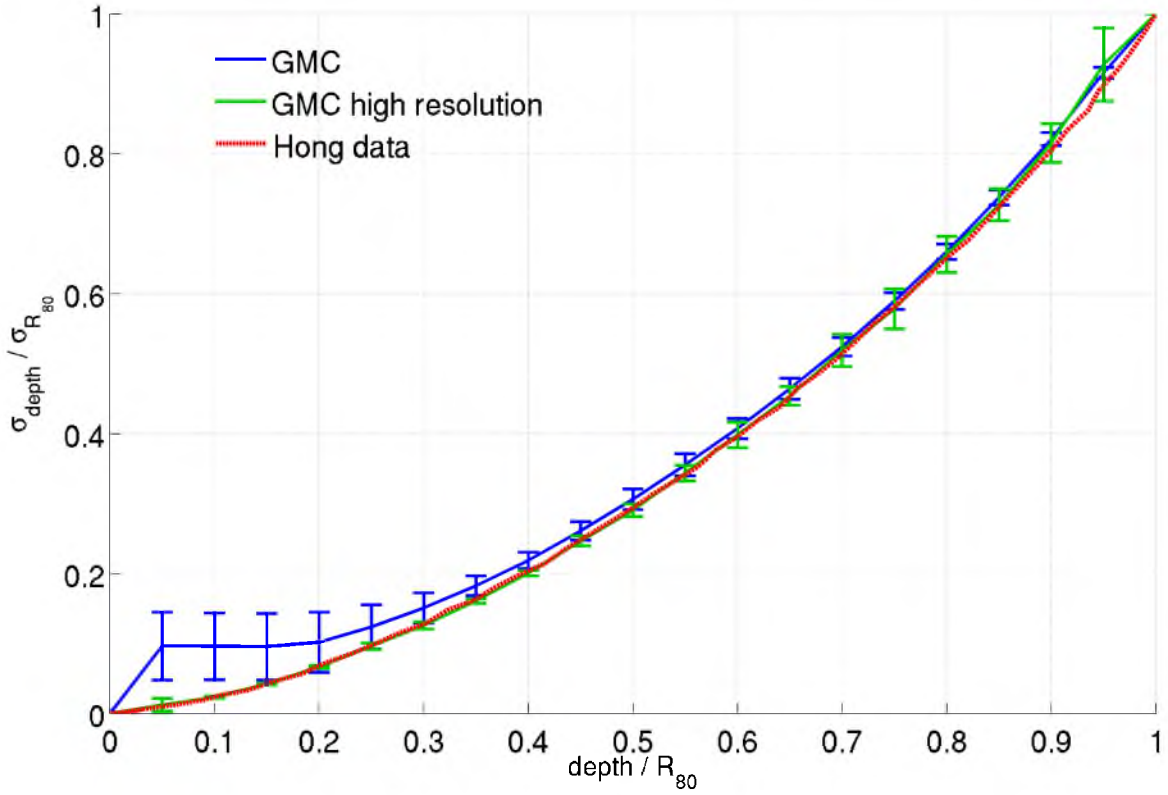

Figure 6.7: *Comparison of the behavior of lateral spread as a function of depth over range for GMC (blue line) versus the Hong model (red line). The inital discrepancy is explained by the coarse simulation resolution in GMC (2 mm cross-section voxels), as proven by the high resolution data (0.2 mm cross-section voxels – green line) based on a few peaks.*

6.3.3 Machine parameters

Subsequent computations were performed with a 6-spot map in order to evaluate the correctness of the machine's geometrical parameters. The geometrical considerations for dose computation are beam size in air at isocenter and SAD. The positions of the six spots at isocenter are known from the input map file (these parameters can be found in table 6.1 as the "expected" values). Thus, these tests further ensured the correctness of the map read-in feature of the code as well as the algorithm's appropriate spot placement. It should be noted that the input map file considered for these analyses is the same map file used clinically to

validate Astroid's proper implementation of new machines.

Figure 6.8 shows the 6-spot map at the surface of the virtual water phantom for three different isocenter positions. The adjusted spot position and size can be appreciated, as well as the different spot size from the distinct incident energies.

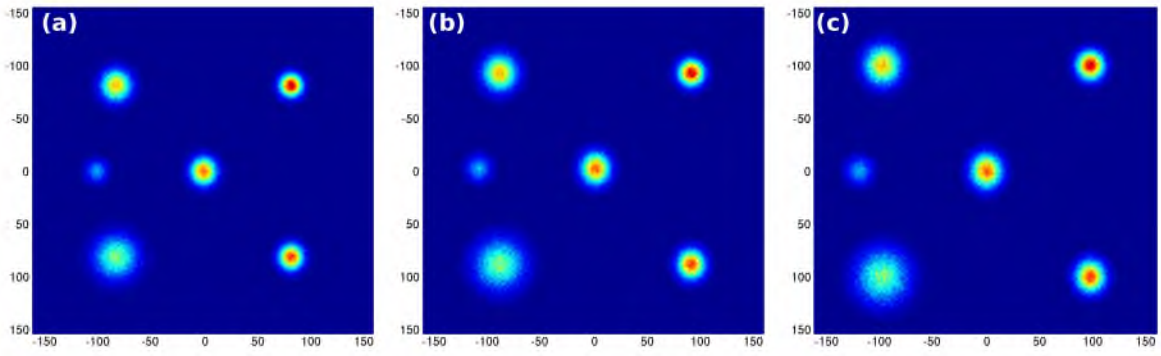

Figure 6.8: *Entrance lateral dose distribution of a 6-spot map simulated in GMC with difference SSD: (a) isocenter at 200 mm depth – SSD of ≈ 1,940 mm; (b) isocenter at the surface – SSD = SAD ≈ 2,140 mm; (c) isocenter 200 mm before the surface – SSD of ≈ 2,340 mm. The initial correction for position and beam size are appreciable.*

Figure 6.9 illustrates the analysis for the machine SAD evaluation, and table 6.1 summarize the overall results of the analyses. The values obtained for SAD as well as spots' sizes and positions agreed well with the expected values, especially given uncertainties in the analysis due to the 2 mm cross-section voxels.

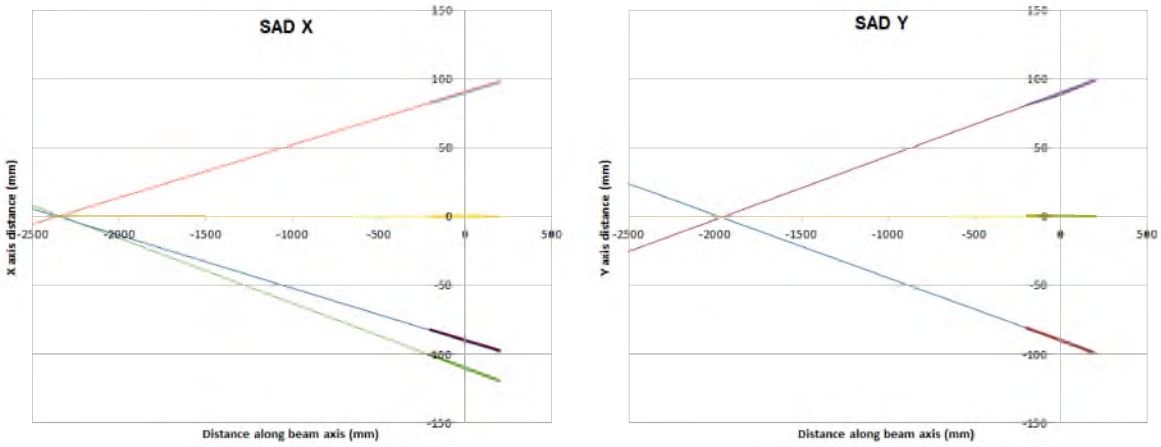

Figure 6.9: *SAD analysis based on the 6-spot map simulations at different SSD. The PBS machine at MGH is a dual SAD system; each SAD corresponds to the center of a bending magnets (X or Y) that are used to steer the pencil beam.*

These results are well within MGH's clinical requirements, and GMC gave slightly better results than the current clinical pencil beam algorithm. This highlights the accuracy of the modeling

(a) Position

Spot #	Energy (MeV)	Expected X position (mm)	Computed X position (mm)	Difference (mm)	Expected Y position (mm)	Computed Y position (mm)	Difference (mm)
1	145.22	-90	-90.05	0.05	-90	-90.01	0.01
2	91.015	-90	-89.78	0.22	90	89.82	0.18
3	223.58	90	-90.07	0.07	-90	-90.22	0.22
4	206.59	90	89.70	0.3	90	89.96	0.04
5	223.58	-110	-110.01	0.01	0	0.10	0.10
6	181.97	0	0.27	0.27	0	0.16	0.16

(b) SAD

Orientation	Expected SAD(mm)	Computed SAD (mm)	Difference (%)
X	2340	2342	0.1
Y	1940	1945	0.3

(c) Sigma

Spot #	Energy (MeV)	Expected σ_X (mm)	Computed σ_X (mm)	Difference (%)	Expected σ_Y (mm)	Computed σ_Y (mm)	Difference (%)
1	145.22	10.36	10.56	1.9	10.36	10.77	3.9
2	91.015	14.82	14.73	0.6	14.68	14.89	1.4
3	223.58	7.70	7.72	0.3	7.99	8.03	0.5
4	206.59	8.25	8.35	1.2	8.97	8.99	0.2
5	223.58	7.70	7.71	0.1	7.99	7.8	2.4
6	181.97	8.86	8.55	3.5	9.75	10.09	3.5

Table 6.1: *Summary of the machine parameter analyses based on the 6-spot map simulation with isocenter at the surface, hence corresponding to beam parameters in air at isocenter: (a) position accuracy analysis, (b) SAD results as presented in figure 6.9, (c) in air spot sigma at isocenter. These highlight the excellent overall agreement between GMC and Astroid's beam model data.*

of machine parameters in GMC. This also shows GMC's proper handling of the input map reading.

6.3.4 Heterogeneities

A simulation was performed using a virtual a water phantom (ρ=1.0 kg.m^3) in which 4 inserts of lung (ρ=0.1 kg.m^3) and bony tissue (ρ=2.0 kg.m^3) material were added.Three spots of equal intensity and σ of 10 mm were placed such that: one spot would go through no heterogeneities, one spot would first travel through the edge of a lung insert then through the edge of a bony tissue insert, one spot would first travel through the edge of a bony tissue insert then through the edge of a lung insert. This setup, as well as the result of the simulation, are illustrated in figure 6.10. The black overlaying box in the figure represents the lung inserts while the bony tissue inserts are represented as white overlaying box. All 4 inserts in this simulation were 6

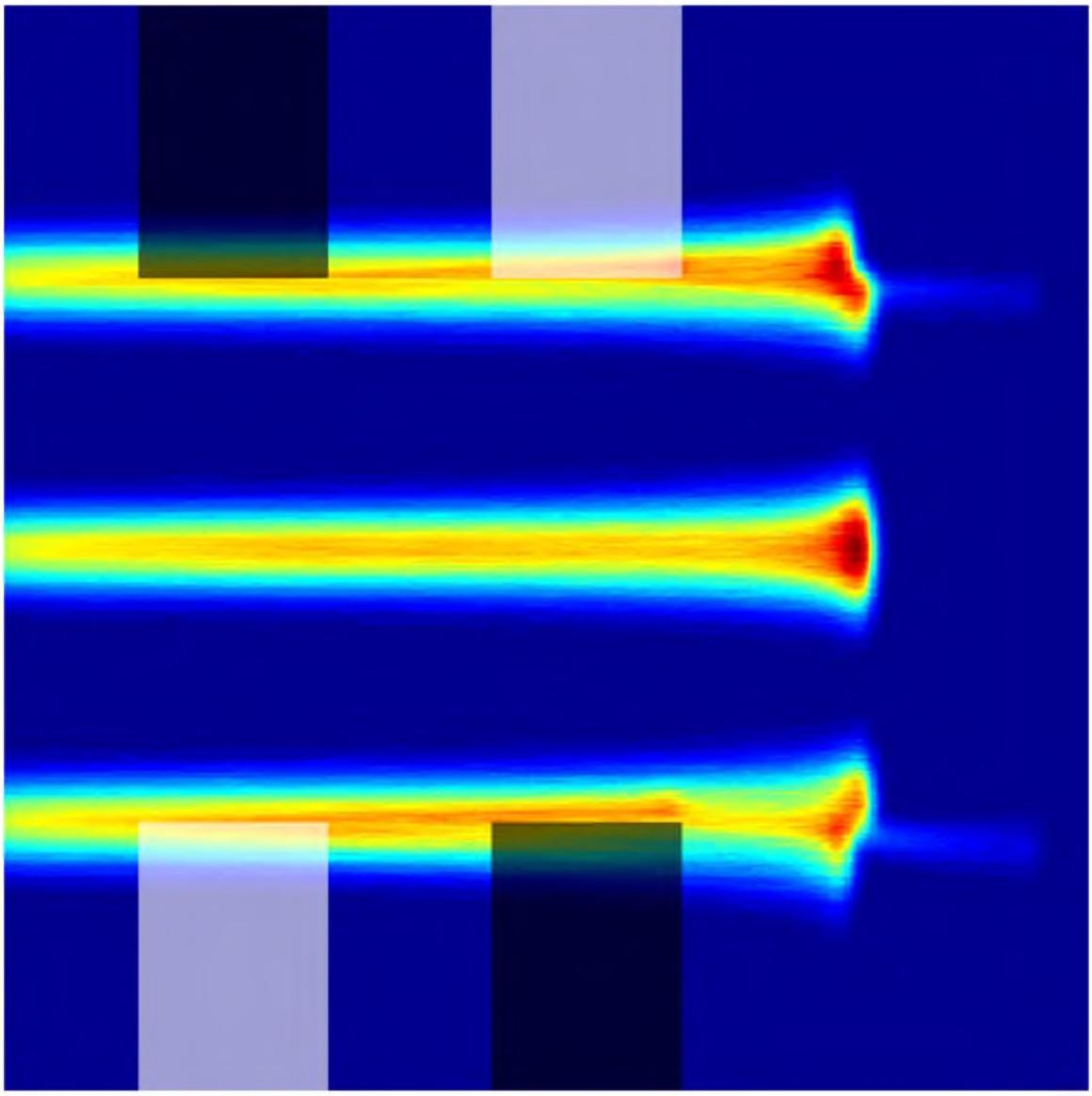

Figure 6.10: *GMC simulation of three 10 mm σ spots in a water phantom with heterogeneities: 4 inserts with either lung tissue (black – RSP =0.1) or bony tissue (white – RSP = 2.0). One spot does not go through any heterogeneities, while the two other spots travel along the edges of the heterogeneous inserts in reverse order. A clear difference in scattering can be observed, as well as tails of protons that interacted more with the lung insert than with the bony tissue insert.*

centimeters thick.

There is an appreciable difference in dose distributions between the two spots traveling along the edges of the heterogeneities in reverse order. This is expected due to the difference in scattering power as a function of remaining energy between the two different inserts. Such a difference in dose distribution would not appear in PBA dose computations. In such an instance, all three spots would look similar as the scattering process is only based on the

equivalent path length along the axis of the spot through ray tracing. This is an important result as it highlights GMC's ability to handle large heterogeneities. This is in direct comparison to Astroid's current PBA.

Although this result corresponds to the theoretical expectations, it is difficult to experimentally demonstrate it. The subsequent dose computations and comparisons in patients (see section 6.4) are considered an appropriate validation step, as data has been clinically approved through QA measurements of the individual patient fields.

A tail of protons can be observed in figure 6.10 beyond the two spots traveling through heterogeneities. These tails correspond to protons which either interacted through lung tissue and scattered off to the side (avoiding the following bone tissue insert), or did not interact much through the bony tissue insert and then scattered inside the lung insert. Such behavior then results in particles with an apparent deeper range. Even though the spots interacted with their respective heterogeneous inserts mirrored one to another, the tails are oriented toward the same direction. This is due to the order of the interactions and the scattering through the inserts. This, in fact, further emphasizes the accuracy of GMC's algorithm to model computations through heterogeneities.

A subsequent setup was simulated with two 2 cm thick inserts of cortical bone (ρ=1.8 g.cm^{-3}) for comparison purposes against the literature. This setup mimics the work performed by *Schaffner et al. [13]*(see Figure 9) in which a 177 MeV beam was simulated with Monte Carlo at the edge of a 2 cm thick cortical bone insert. The insert was then placed at different positions along the beam. The beam parameters were kept similar, i.e. a 177 MeV beam first traversing a 6.8 cm range shifter with a 10 cm air gap. Both the location of the isocenter and the initial spread of the beam were unknown and thus, had to be arbitrarily chosen. The isocenter was placed at the surface of the phantom with the spot size given by MGH's machine parameters, that is $\approx$ 9.0 mm in X and 9.9 mm in Y. Figure 6.11 illustrates the setup as well as the obtained dose distributions.

The range pullback in the region traversing the bone insert is clearly visible. Additionally, a difference in lateral spread can be observed between the two spots as well as the expected small hot and cold areas at the end of range. These results are similar but not identical to the work by *Schaffner et al. [13]*. The overall features are closely related, but their work showed slightly smoother distributions in the pullback region at the end of range. This is believed to have risen from the difference in MC code, the unknown parameters (spot size and isocenter

position), and the lack of advanced validation of the air gap handling in GMC. This result once more illustrates GMC's ability to properly handle heterogeneous media.

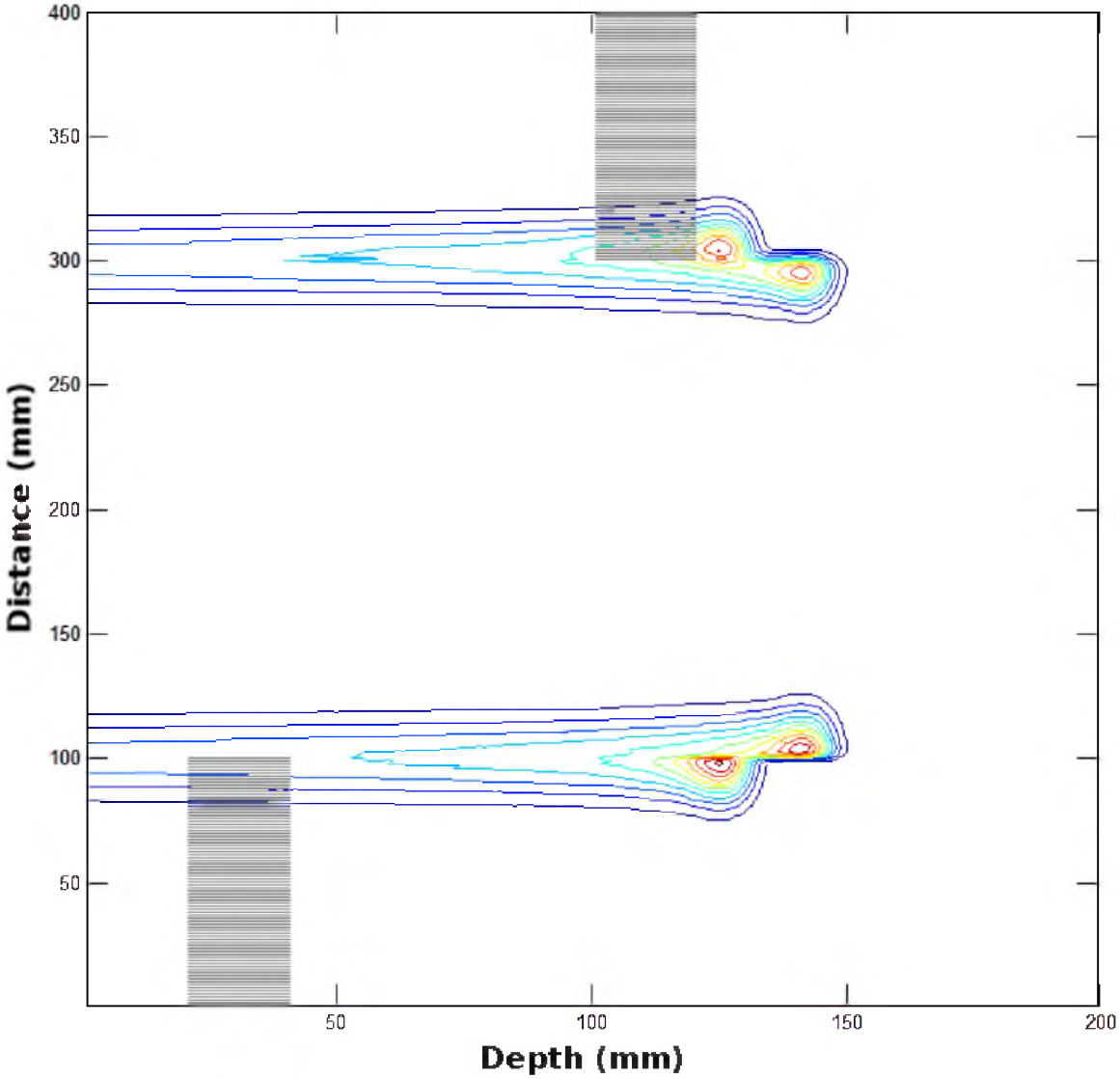

Figure 6.11: *GMC simulation of two 177 MeV spots in a water phantom with 2 cm cortical bone inserts (ρ=1.8 g.cm^{-3}); one insert is located 2 cm from the entrance of the phantom, the other 10 cm. A 6.8 cm range shifter was used with an 8 cm airgap. This setup mimics the work performed by Schaffner et al. [13].*

6.3.5 Halo component

The halo component of a proton beam greatly varies with the equivalent field size of the irradiation. An irradiation larger than 12 cm diameter will result in no discernible effect on the dose distribution due to lateral compensation among the beamlets. For larger cases, it is thus

possible to forgo the halo effect in dose computations altogether. This is the current state of Astroid, in which compensating for the halo effect in the PBA would result in a dramatic reduction of speed performance.

On the other hand, fields smaller than 12 cm may suffer from dose underestimations by a few percents due to the halo effect (*Clasie et al. [11]*). Because of this, it is important to consider these effects at the macro level within GMC to ensure optimal accuracy. Moreover, the addition of the nuclear interactions' modeling presents a highly negligible impact on the performance of a particle-by-particle tracking algorithm such as the one used in GMC.

The intent was for GMC to reproduce our semi-theoretical work described in *Clasie et al. [11]*. As such, the depth dose curves of the beam model were readjusted inside GMC in order to obtain the core of the beam (beam without the halo component). This was performed using equations 5 and 6 from *Clasie et al. [11]* with the given parameters. Figure 6.12 shows the generated core component of a 205.37 MeV beam along with its corresponding Bragg peak from the input beam model. This illustrate the correctness of this work. The core component closely matches the expected core depth dose distribution proposed in *Clasie et al. [11]*, showing the expected dose discrepancy as a function of depth.

The aforementioned methodology for halo handling was employed, halving the primary particle's energy, doubling its weight for dose deposition, and scattering it with a large angle (0.2 rad). Unfortunately, this did not provide the expected result. The amount of energy lost and the amount of weight gained were thus optimized such that the final depth dose curve would match the input beam model. Figure 6.13 presents the status of GMC's halo handling at the time of writing for a 205.37 MeV beam. Although the curve somewhat follows the expected trend, unacceptable over and under-dosing occurs. This result suggests that the use of a mean 0.2-radian scattering angle, along with the semi-theoretical values given in our previous work *Clasie et al. [11]*, are not accurate enough to describe the halo effect from dose computations. The tweaking of the different halo component parameters will be performed in future work.

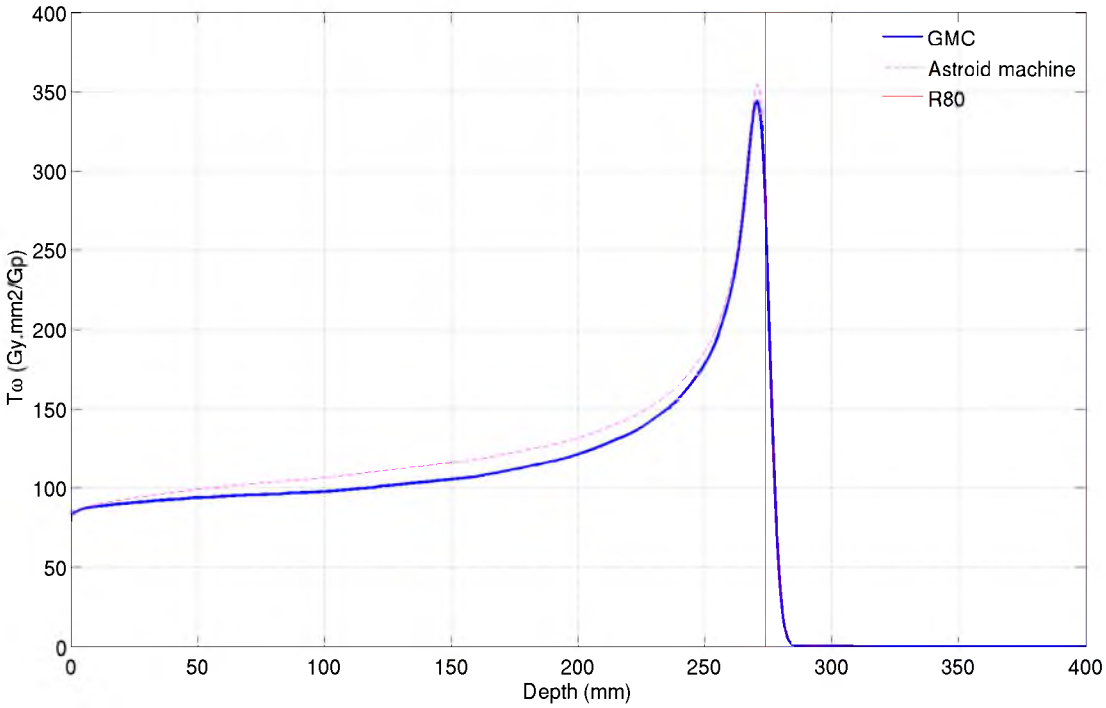

Figure 6.12: *Core component of a 205.37 MeV beam along with its whole depth dose curve from Astroid's beam model. The core component was generated using the equations provided in our work described in Clasie et al. [11].*

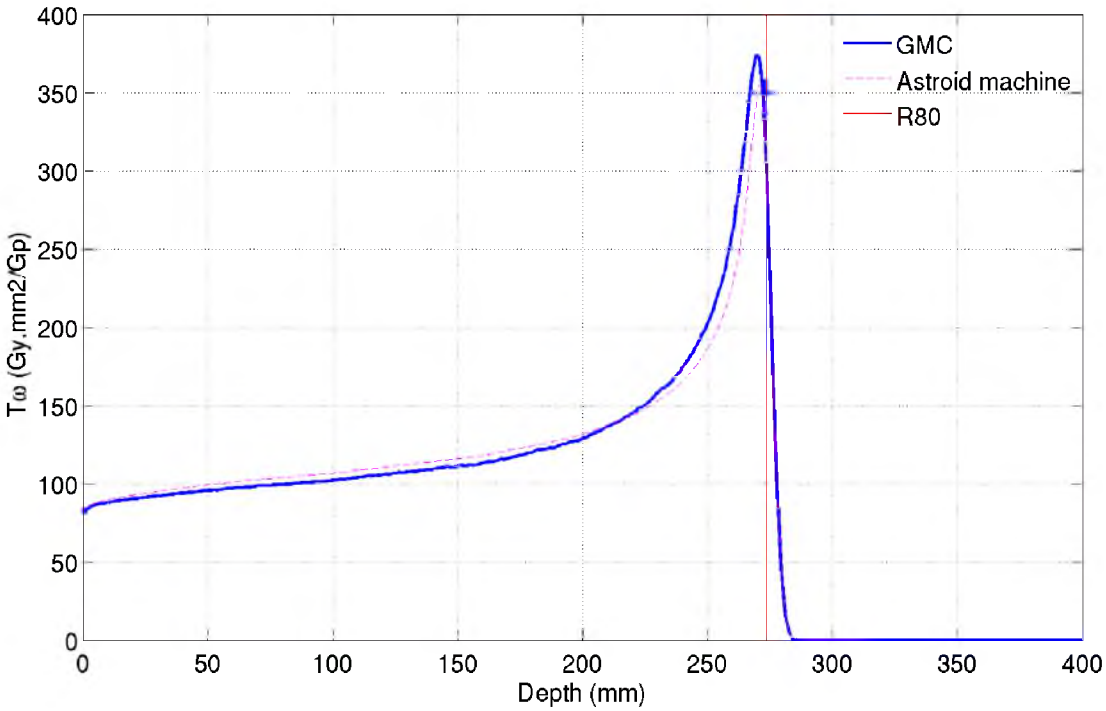

Figure 6.13: *Depth dose curve computed with GMC for a 205.37 MeV beam including the halo component. This represents the status of the halo component in GMC at the time of writing. This shows that it is necessary to tweak the parameters from our previous work (Clasie et al. [11]).*

6.4 Patient calculations and comparisons

6.4.1 Cases

Three distinct patients were considered for validation due to their interesting geometry: one spine sarcoma case with a small homogeneous field, one pericardia & lung sarcoma case presenting large heterogeneities, and one head & neck patient presenting large heterogeneities and planned with two small intensity modulated fields. The CT and delineated contours for these patients are shown in figures 6.14, 6.15, and 6.16, respectively.
The patient's fields were first recomputed in a virtual water phantom, similarly to the process performed at the time of pre-treatment QA. Thus, these computations could be directly compared to the QA data generated prior to patient treatment:

- 3D γ-index evaluations were performed against the QA dose recomputation which was generated using the PBA in water.
- 2D/3D γ-index evaluations were performed against MatriXX™ measurements that were acquired at the time of pre-treatment QA.

Lastly, dose recomputations were performed with GMC in the actual patient's geometry and compared to both the original dose computation from Astroid and a full Monte Carlo dose recomputation (Jan Schuemann, private communication) performed with TOPAS, a framework based on the GEANT4 toolkit [134].
These GMC recomputations were mostly performed with what is considered to be full statistics, that is, 1,000,000 protons generated per requested gigaproton. The grid size was either matching the submillimeter CT grid size (patient dependent), or consisted of a 40 cm^3 cube with 1 mm^3 voxels for the virtual water phantom recomputations. Some discussion on these parameters is provided in section 6.5.

6.4.1.1 Spine sarcoma

Figure 6.14 shows the spine sarcoma patient geometry. This case is of interest due to the small size of the target, approximately 5 × 5 × 7 cm. The small size of the target, along with the highly homogeneous planned dose distribution, represent an optimal configuration to appreciate the full extent of the halo effect. As later illustrated in table 6.3, this hypothesis was further confirmed during patient QA.

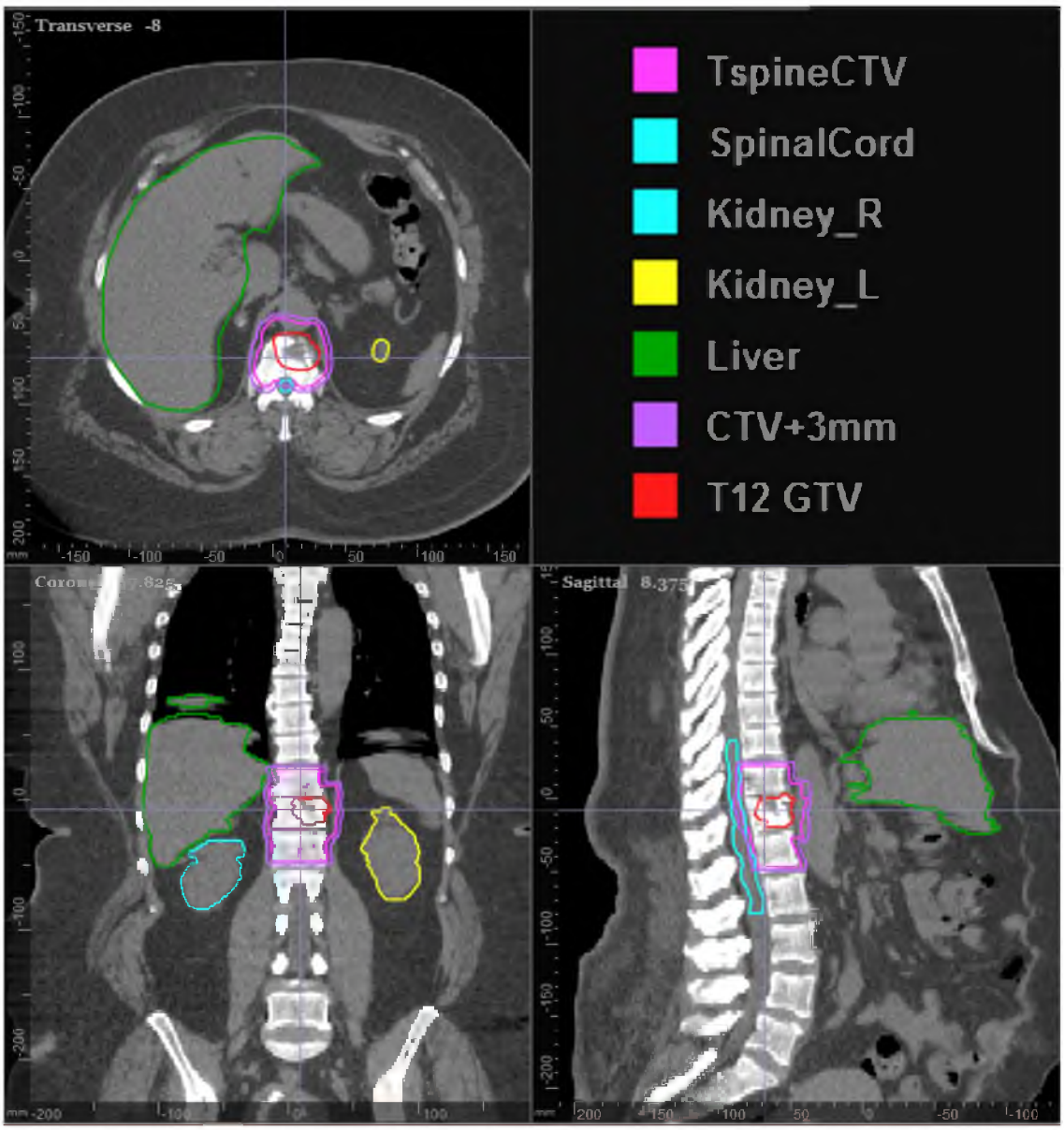

Figure 6.14: *Spine sarcoma patient considered for GMC's computation quality assessment. The target (CTV – magenta contour) is very small, approximately 5 × 5 × 7 cm, for which the PBA dose calculation would suffer from halo effects.*

6.4.1.2 Pericardia & lung sarcoma

Figure 6.15 shows the pericardia & lung sarcoma patient geometry. The large tissue heterogeneities present in this patient push the limit of PBA dose calculations; up to 10 % underdose could have been expected as shown by the work by *Grassberger et al. [24]*.

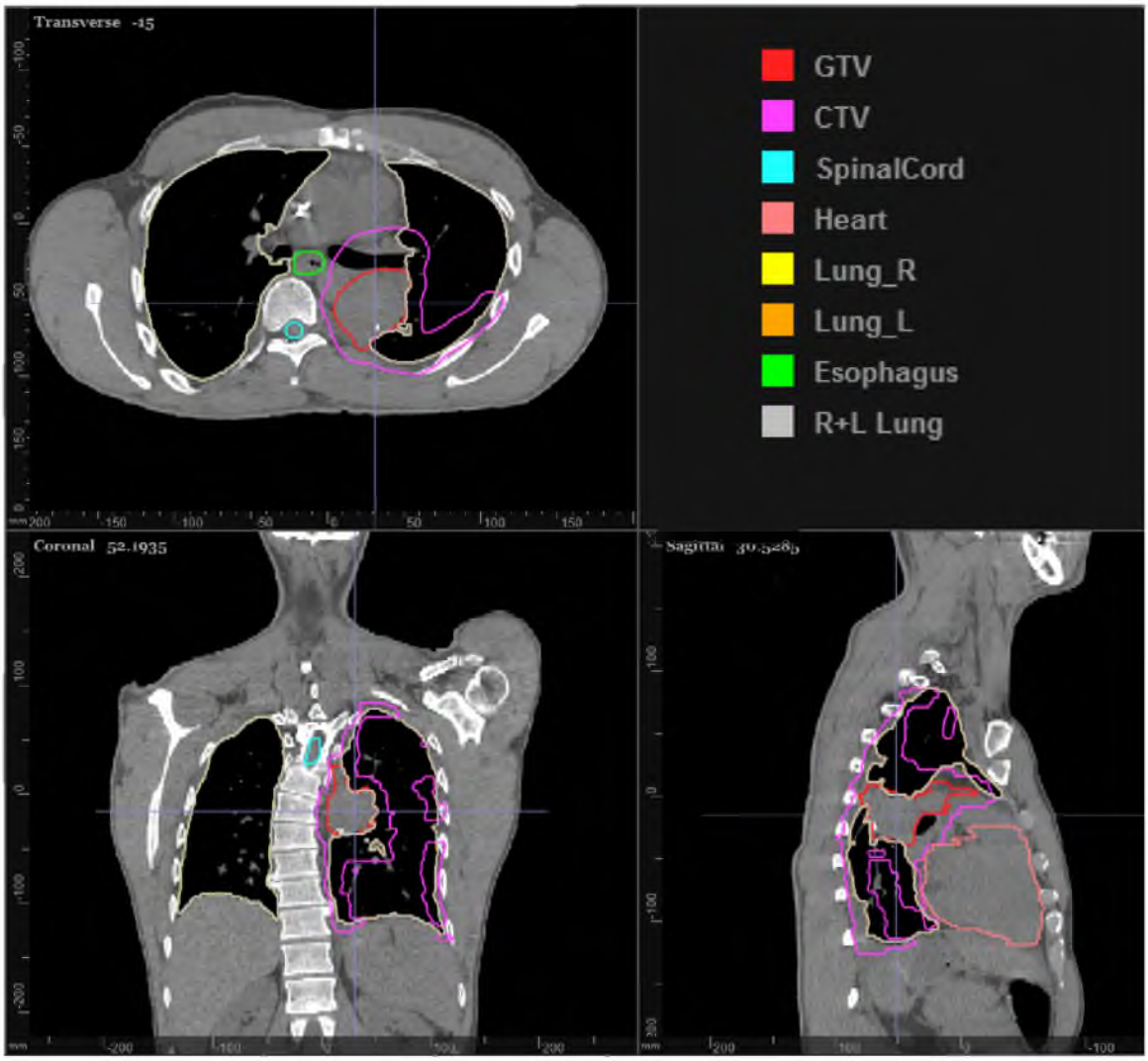

Figure 6.15: *Pericardia & lung sarcoma patient considered for GMC's computation quality assessment. The target (CTV – magenta contour) presents a very irregular shape with large tissue heterogeneities for which the PBA dose calculation would suffer from poor heterogeneity handling.*

6.4.1.3 Head & neck

Figure 6.16 shows the head & neck patient geometry. This case combined all of the worst possible scenarios for PBA dose calculations: small target ($\approx$ 6 cm^3) with large tissue het-

erogeneities, and planned with two intensity modulated beams. As previously discussed, underdosage would be expected from the halo effect as well as from the large inhomogeneities. Additionally, the use of two overlapping IMPT fields can result in serious robustness concerns versus range and geometrical uncertainties. This represents a worst case scenario for PBS in the current clinical context. In fact, these fields were considered inappropriate, and PBS treatment deemed unacceptable for this patient.

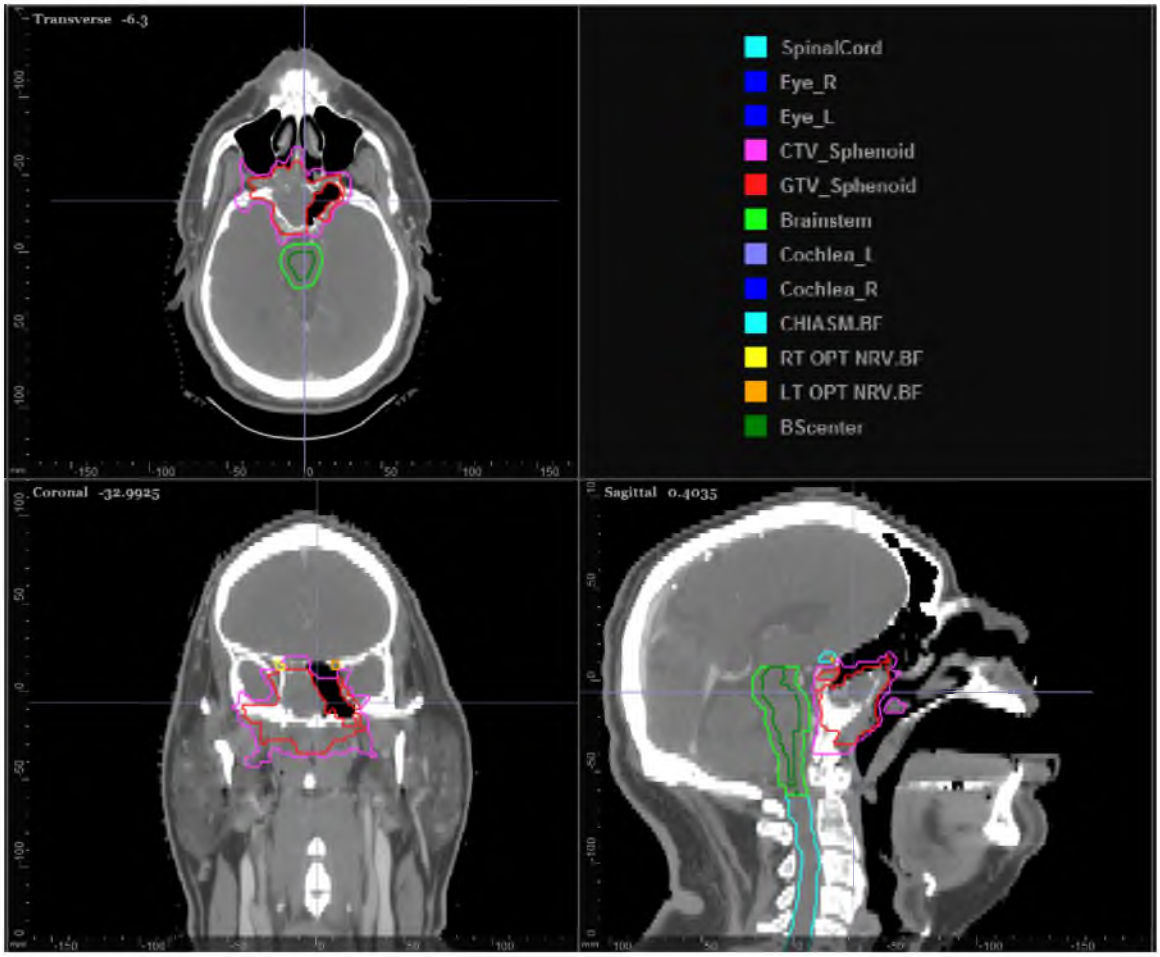

Figure 6.16: *Head & neck patient considered for GMC's computation quality assessment. The target (CTV – magenta contour) is very small (≈ 6 cm^3) and presents large tissue heterogeneities; this is an excellent example of a great combination of feature that reach the limitations of PBA dose calculations.*

6.4.2 Dose recomputations in water

Each of the aforementioned patient's fields, 4 in total, were recomputed in a virtual water phantom corresponding to the dose calculation performed for pre-treatment QA measurements. These dose recomputations were then evaluated against the QA dose computation through

3D γ-analyses based on the work by *Clasie et al. [135]*. Figure 6.17 shows the resulting γ-map for one of these analyses for a 1 mm / 1 % γ-criterion. The overall results of these analyses are presented in table 6.2.

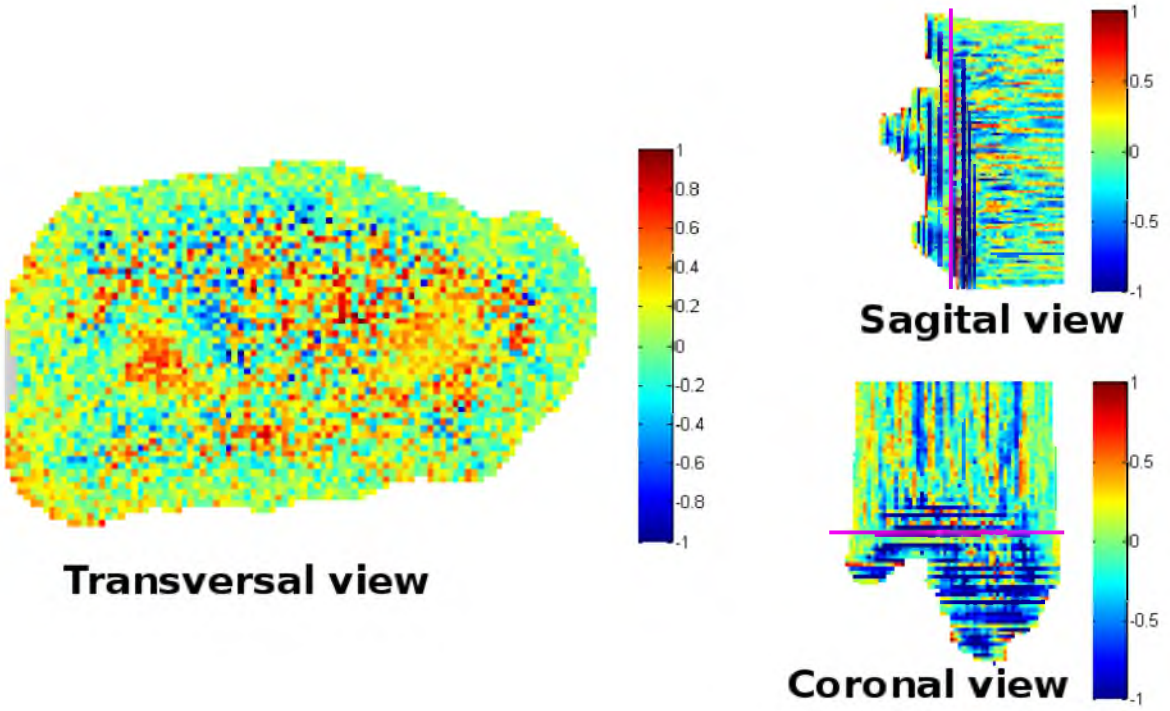

Figure 6.17: *3D γ-map based on a 1 mm / 1 % γ-criterion as evaluated between GMC's water dose recomputation and the original QA dose computation for the pericardia & lung sarcoma field.*

	γ-criterion			
	1 mm / 0.5 %	1 mm / 1 %	2 mm / 0.1 %	2 mm / 0.5 %
Field	Passing rate %			
Spine sarcoma	92.9	93.7	94.9	96.9
pericardia & lung sarcoma	92.7	93.6	95.2	97.3
Head & neck field 1	93.3	94.4	95.1	97.0
Head & neck field 2	92.9	94.0	94.2	96.7

Table 6.2: *3D γ-analyses results between GMC's water dose recomputation and the original QA dose computations. Numerous γ-criteria were used.*

At first glance, the results of the 3D γ-analyses, with an average of 94.7 $\pm$ 1.6 %, were slightly less than expected. A passing rate of 90 % is generally considered acceptable, which is sensible here given the relative tight γ-criteria used. Nevertheless, one would expect better agreement between computer generated dose distributions in water, due to the absence of heterogeneities and measurement uncertainties. One hypothesis was that the QA dose cube, generated with 3 mm^3 voxels, might have degraded the calculation accuracy as compared to

GMC's simulations, which used 1 mm^3 voxels. QA dose cubes were therefore regenerated using a grid with 1 mm^3 voxels for comparison. A 3D γ-analysis using these higher definition cubes yielded very similar results like the one observed in table 6.2, within $\pm$ 1 %.
The subsequent step consisted of 2D/3D γ-analyses between GMC's recomputations in water and actual 2D MatriXX™ measurements that were acquired at the time of pre-treatment QA. Figure 6.18 shows the γ-analysis for the pericardia & lung sarcoma field at a given depth for a 1 mm / 1 % γ-criterion. The head & neck case fields had been considered so small and heterogeneous that treatment was deemed unacceptable using pencil beam scanning. Consequently, no QA measurements were acquired and it was therefore impossible to perform the γ-analysis for those fields.

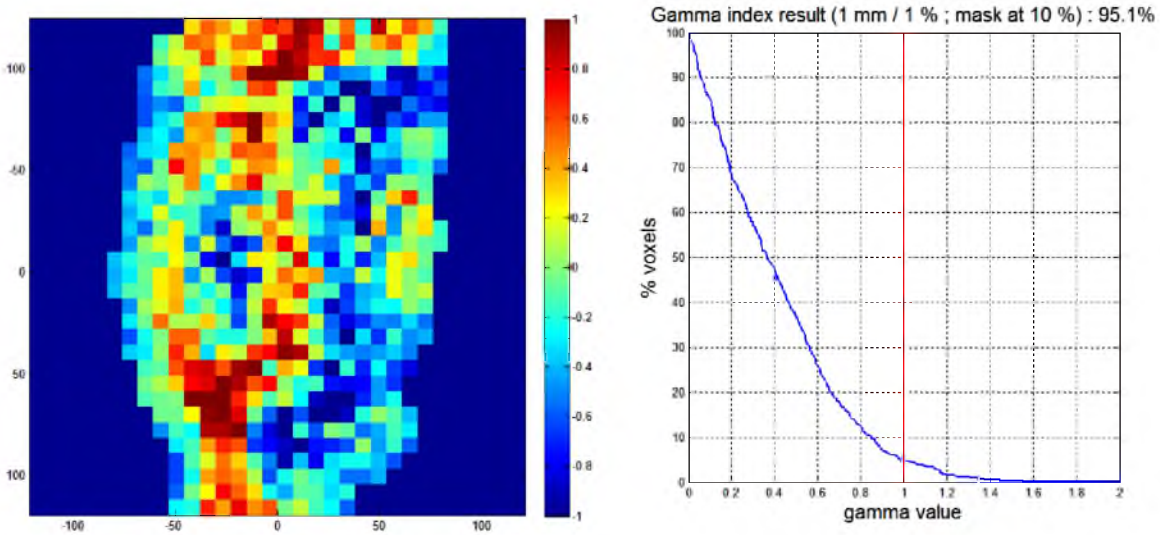

Figure 6.18: *2D/3D γ-analysis result based on a 1 mm / 1 % γ-criterion as evaluated between GMC's water dose recomputation and actual QA MatriXX™ measurement for the pericardia & lung sarcoma field at a depth of 105 mm.*

The results of the 2D/3D γ-analyses for the two other patient cases are presented in table 6.3. It should be noted that in order to obtain the best possible result, the position of the measurement was slightly adjusted ($\pm$ 1 mm) due to slight position uncertainties during the QA acquisition process. This was an appropriate step, as it was not intended to check the delivery but rather the dose computation accuracy. Nevertheless, the 2D/3D γ-analyses for the treated fields – this does not include the non-halo corrected spine fields – all yielded exceptional passing rates, over 95 % for a 1 mm / 1% γ-criterion. This agreement is extremely high, far beyond current clinical expectations. All fields, including the non-halo corrected ones, passed the 3 mm / 3% γ-criterion analysis at 100 %, except for one at 98 %. Conversely,

the actual QA γ-analysis using the current QA dose computations in water resulted in good or acceptable passing rates, except for one field at 76 %. As a comparison point, the γ-analysis for the pericardia & lung sarcoma field at 155 mm depth yielded a passing rate of 69.6 % with a 1 mm / 1% γ-criterion for the current clinical QA dose computation. This is far less than the 99.1 % passing rate obtained using the GMC's dose recalculation.

This is an extremely important result. Not only does it explain the acceptable yet not great results observed in table 6.2, but it also shows the excellent accuracy of GMC's dose computation in water. Conversely, this further highlights the limitations of PBA dose computations, even when performed in a uniform medium.

		γ-criterion		QA measurement
		1 mm / 1 %	3 mm / 3 %	3 mm / 3 %
Field	Depth (mm)	Passing rate %		Passing rate %
Spine sarcoma	105	75.9	100.0	91.9
Spine sarcoma	155	62.1	98.3	76.0
Spine sarcoma (halo corrected)	105	96.6	100.0	99.6
Spine sarcoma (halo corrected)	155	98.6	100.0	99.6
pericardia & lung sarcoma	54	95.1	100.0	99.8
pericardia & lung sarcoma	155	99.1	100.0	94.7

Table 6.3: *2D/3D γ-analyses results between GMC's water dose recomputation and the actual QA MatriXX™ measurements. γ-criteria of 1 mm / 1% and 3 mm / 3% were used. The results of the 2D/3D γ-analyses observed during pre-treatment patient QA are given for informational purposes.*

In order to further assess the quality of GMC's dose recomputations in water, similar simulations were performed in a far less statistically optimal situation. The number of particles was decreased by an order of magnitude (100,000 particles simulated per gigaproton requested), and the voxel size increased from 1 mm^3 to 2 mm^3. The speed considerations associated with such parameters are further discussed in section 6.5.

Table 6.4 gives the results of the 2D/3D γ-analyses between these coarse simulations and actual QA measurements. Although the passing rates of 1 mm / 1 % γ-criterion analyses decreased at the limit of acceptability, the 3 mm / 3 % γ-criterion analyses yielded perfect 100 % passing rates. In fact, similar simulations of the spine sarcoma field using 4 mm^3 voxels resulted in similar passing rates for a 1 mm / 1 % γ-criterion. These results further emphasize the accuracy of GMC's algorithm for dose computations in water, even with far from optimal statistics. This makes GMC very attractive from a clinical use point of view.

It should be noted that the results presented in tables 6.3 and 6.4 are based on γ-analyses

		γ-criterion	
		1 mm / 1 %	3 mm / 3 %
Field	Depth (mm)	Passing rate %	
Spine sarcoma (halo corrected)	105	92.1	100.0
Spine sarcoma (halo corrected)	155	95.2	100.0
pericardia & lung sarcoma	54	86.8	100.0
pericardia & lung sarcoma	155	96.1	100.0

Table 6.4: *2D/3D γ-analyses results between coarse GMC's water dose recomputation (100,000 histories per Gp with 3 mm^3 voxel size) and the actual QA MatriXX™ measurements.*

using spline evaluations. It was discussed in *Clasie et al. [135]* that such evaluations presents limitations when performing γ-analyses on noisy data set. Both the measurements and MC recomputations are, by definition, relatively noisy. The effect is such that an overestimation of the γ-results could occur. The γ-analyses were therefore re-run using a 3 $\times$ 3 median filter on the MC dose distribution along with a simple interpolation evaluation of the γ-indices which, on the other hand, could result in an underestimatation of the γ-results. As expected, the passing rates were reduced but remained superior as compared to the current QA PBA dose calculations for a 3 mm / 3 % γ-criterion, and were mostly acceptable for a 1 mm / 1 % γ-criterion. This, once again, emphasizes the accuracy of GMC's dose recomputation algorithm in water.

6.4.3 Patient dose recomputations

Figure 6.19 shows a comparison of the dose and DVH data for the spine sarcoma case between Astroid's planned dose and GMC's recomputation. Due to a lack of resource, no full MC calculation could be performed. The dose distributions from Astroid's PBA computation and GMC's recalculation appear visually alike, however, GMC's is noisier, as one would expect from a MC simulation. This is also highlighted through the fine agreement in the DVH data, with virtually no tumor coverage difference at V_{95}, and a mean OAR dose discrepancy of 3.5 $\pm$ 2.5 % (driven by the liver and kidneys which received a very low dose). The slight round up in the tumor coverage in GMC's recomputation is explained by the proper handling of lateral scattering. Overall, such a result meets the predicted expectation given the uniformity of the treatment region and the dose, and the fact that the halo component was lacking in this computation. The proper handling of that halo component would be expected to result in an overall uniform drop of the dose within the target volume.

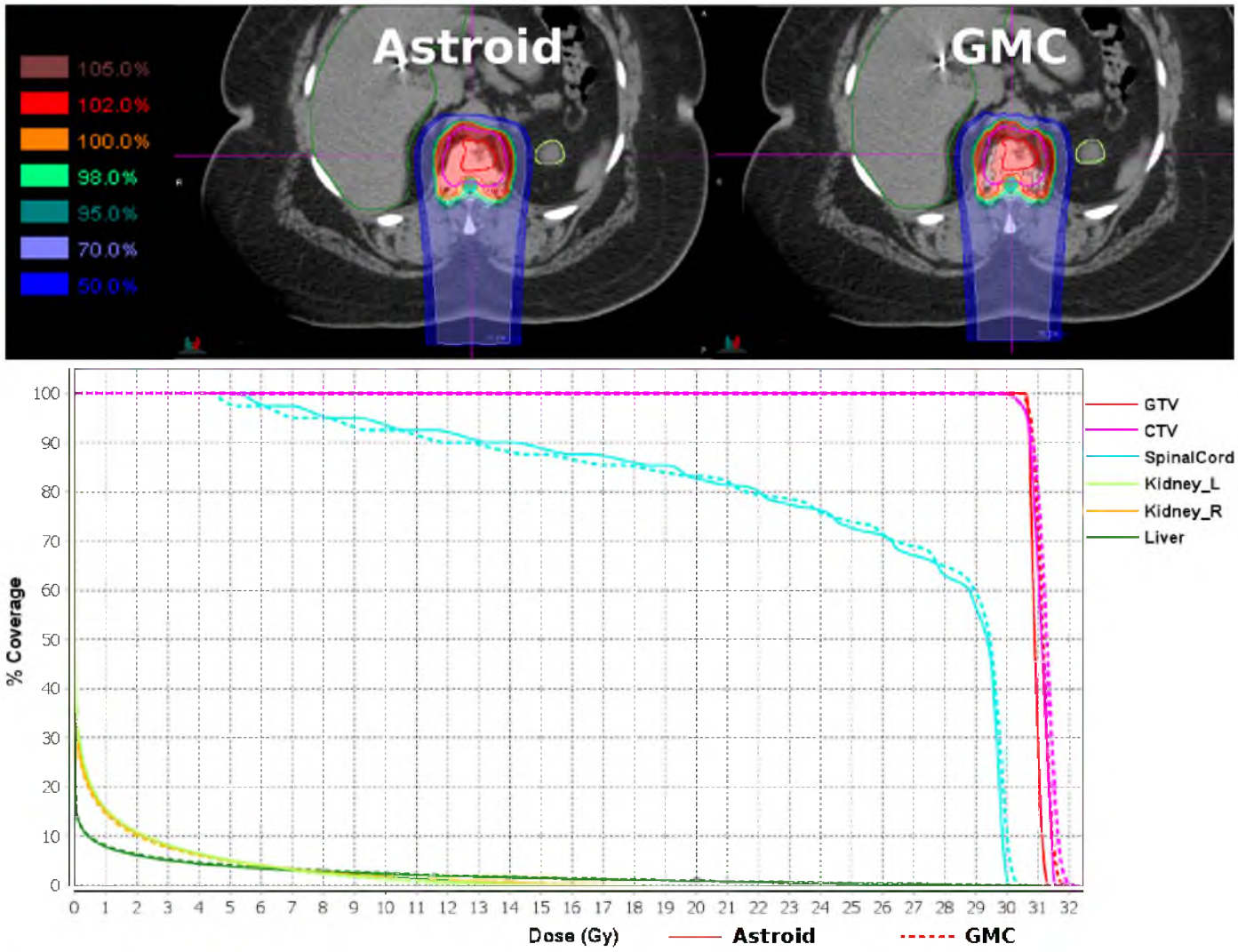

Figure 6.19: *Dose and DVH comparison between the current clinical PBA dose computation (Astroid) and GMC's dose reocmputation (GMC) for the spine sarcoma patient.*

Figures 6.20 and 6.22 show three-way comparisons between the current clinical PBA dose computation (Astroid), GMC's dose recomputation (GMC), and a full MC dose recomputation (TOPAS) for the pericardia & lung sarcoma patient, as well as the head & neck patient. All three of these dose calculations are reasonable, with the TOPAS dose recomputation appearing colder in both cases. The general features, such as penumbra size and slight over or undershooting of the beam, are highly similar between GMC and TOPAS when compared to Astroid. These features arise from the large heterogeneities present in the patient's geometry. Thus, based on these three rather extreme cases, GMC's transport through patient geometries appear accurate. It should be noted that the slight discrepancies in dose level between GMC and TOPAS may be due to the lack of halo component in GMC. This will be evaluated at a later time once the halo component correction has been correctly implemented as discussed in section 6.3.5. Furthermore, it should be noted that TOPAS relies on many tweaks and tricks in order to appropriately match the beam data present in Astroid. As such, there is no true gold standard for dose computations in patients. Only in-vivo measurements can truly assess the dose accuracy.

The DVH comparisons between the current clinical PBA dose computation (Astroid), GMC's dose recomputation (GMC), and a full MC dose recomputation (TOPAS) for the pericardia & lung sarcoma patient and the head & neck patient are presented in figures 6.21 and 6.23. The DVH data confirms the results previously observed in the dose distribution comparisons. TOPAS's recomputations present large target underdosing (3.5 ± 1.1 Gy(RBE) for V_{95}) and differences in OAR dose (11.3 ± 6.7 % mean dose) as compared to Astroid's planned dose. GMC, sensitive to the heterogeneities, presents features similar to that of TOPAS but the effects are not quite as dramatic: target underdosage of 2.1 ± 1.9 Gy(RBE) for V_{95} and OAR mean dose discrepancy of 6.7 ± 5.1 %.

As previously stated, despite the fact that both MC algorithms present similar characteristics against the inhomogeneities, it is difficult to judge their absolute accuracy. It should be noted, however, that GMC relies only on the TPS's beam model with a simple calibration to adjust the range discrepancy due to the scattered nature of the individual proton tracks through interactions. Conversely, systems like TOPAS or any other full MC algorithms must generate their own beam model from square one. This beam model must then be adjusted through numerous tweaks and tricks in order to match the TPS's beam model. This represents a large overhead, and could easily introduce systematic discrepancies in the resulting dose calcula-

tions.

In order to further assess the statistical effects on GMC's dose recomputations, these three patient cases were generated in the low statistical mode (100,000 per Gp requested). An exemplary comparison between the full statistical mode and the low statistical mode for GMC's dose recomputation of the head & neck patient's plan is given in figure 6.24. The dose distribution with low statistics clearly shows a higher noise level than the one with full statistics; this was emphasized in figure 6.24 by using one of the noisiest image slices. On the other hand, the DVH comparison shows very little difference, which fits well within the clinical expectations. Although it is not illustrated here, the two other patient's recomputations yielded similar results. These preliminary examples highlight the possibility to use lower statistics yet obtain appropriate dose computation accuracy, thus highly reduce the required computing power and time.

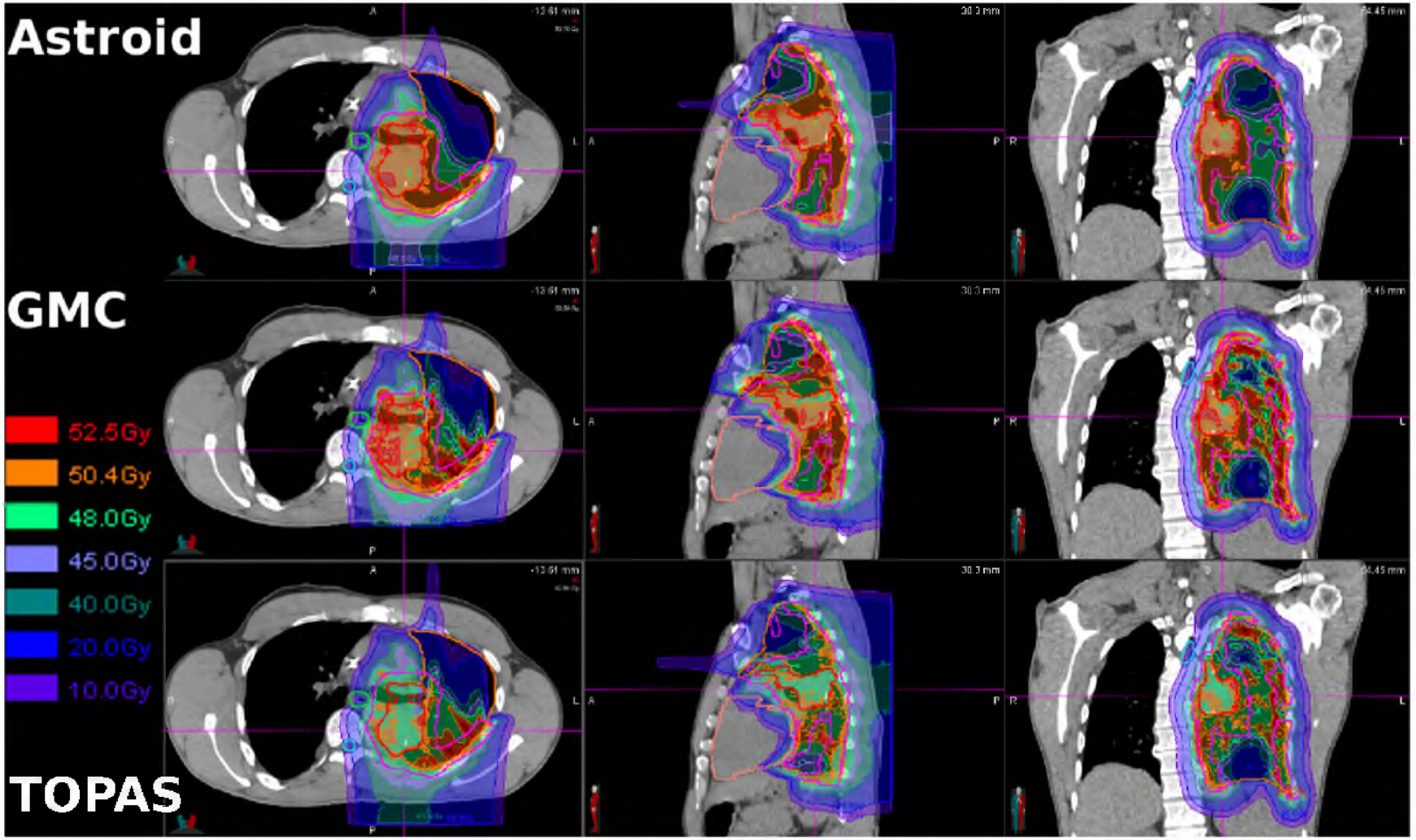

Figure 6.20: *3 way dose comparison for the pericardia & lung sarcoma patient between the current clinical PBA dose computation (Astroid), GMC's dose reocmputation (GMC), and a full MC dose recomputation (TOPAS).*

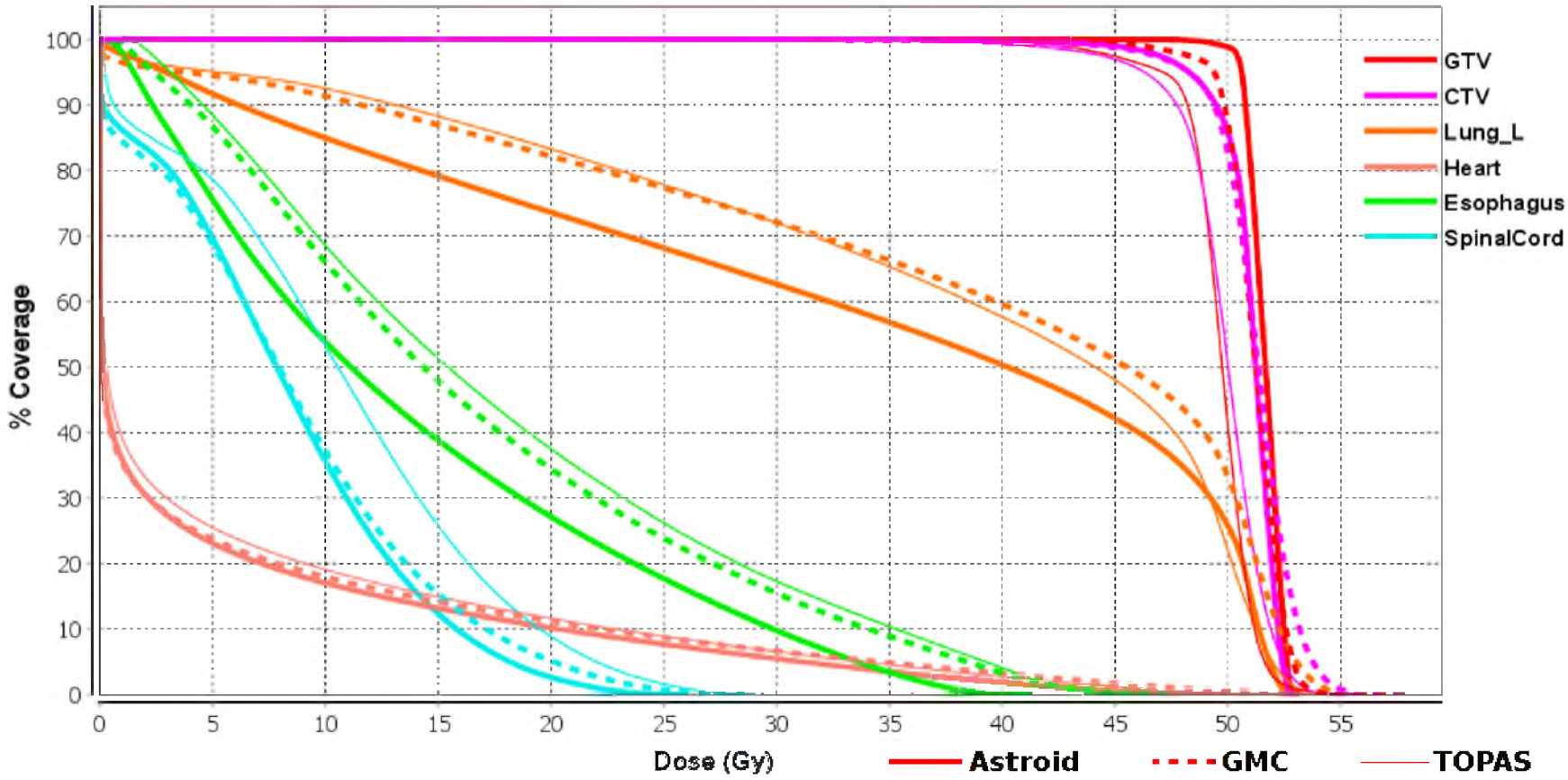

Figure 6.21: *DVH comparison for the pericardia & lung sarcoma patient between the current clinical PBA dose computation (Astroid), GMC's dose recomputation (GMC), and a full MC dose recomputation (TOPAS).*

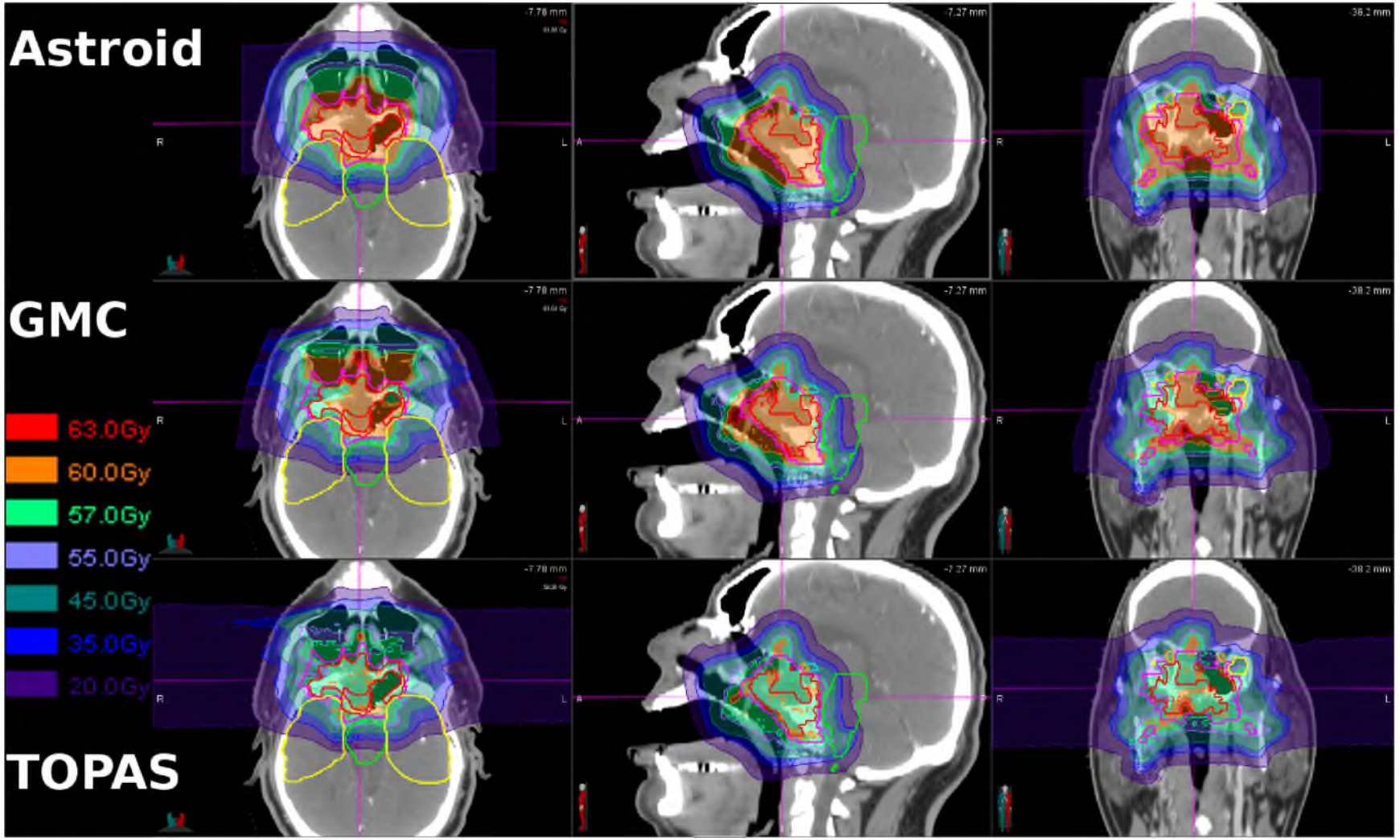

Figure 6.22: *3 way dose comparison for the head & neck patient between the current clinical PBA dose computation (Astroid), GMC's dose recomputation (GMC), and a full MC dose recomputation (TOPAS).*

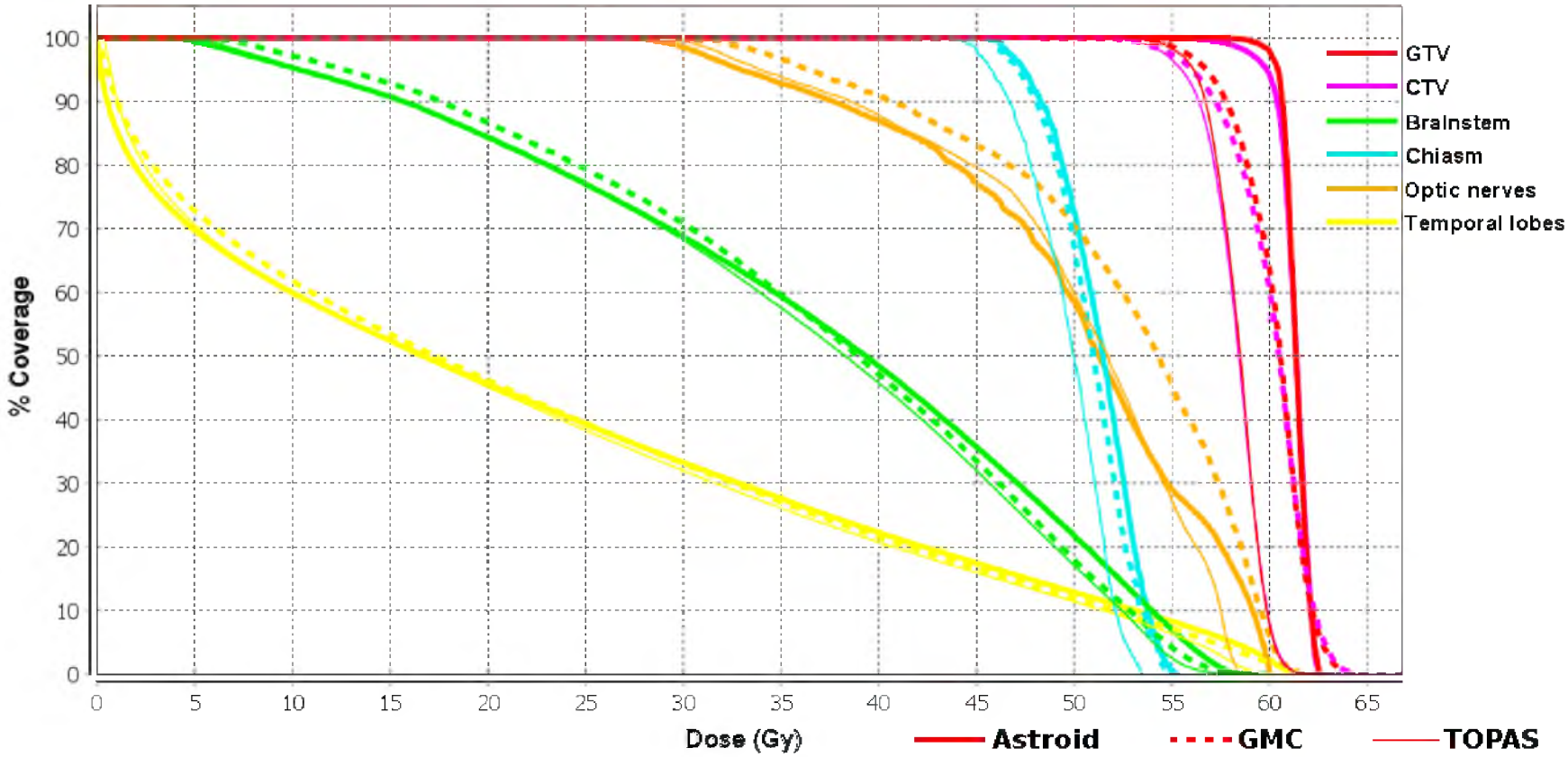

Figure 6.23: *DVH comparison for the head & neck patient between the current clinical PBA dose computation (Astroid), GMC's dose recomputation (GMC), and a full MC dose recomputation (TOPAS).*

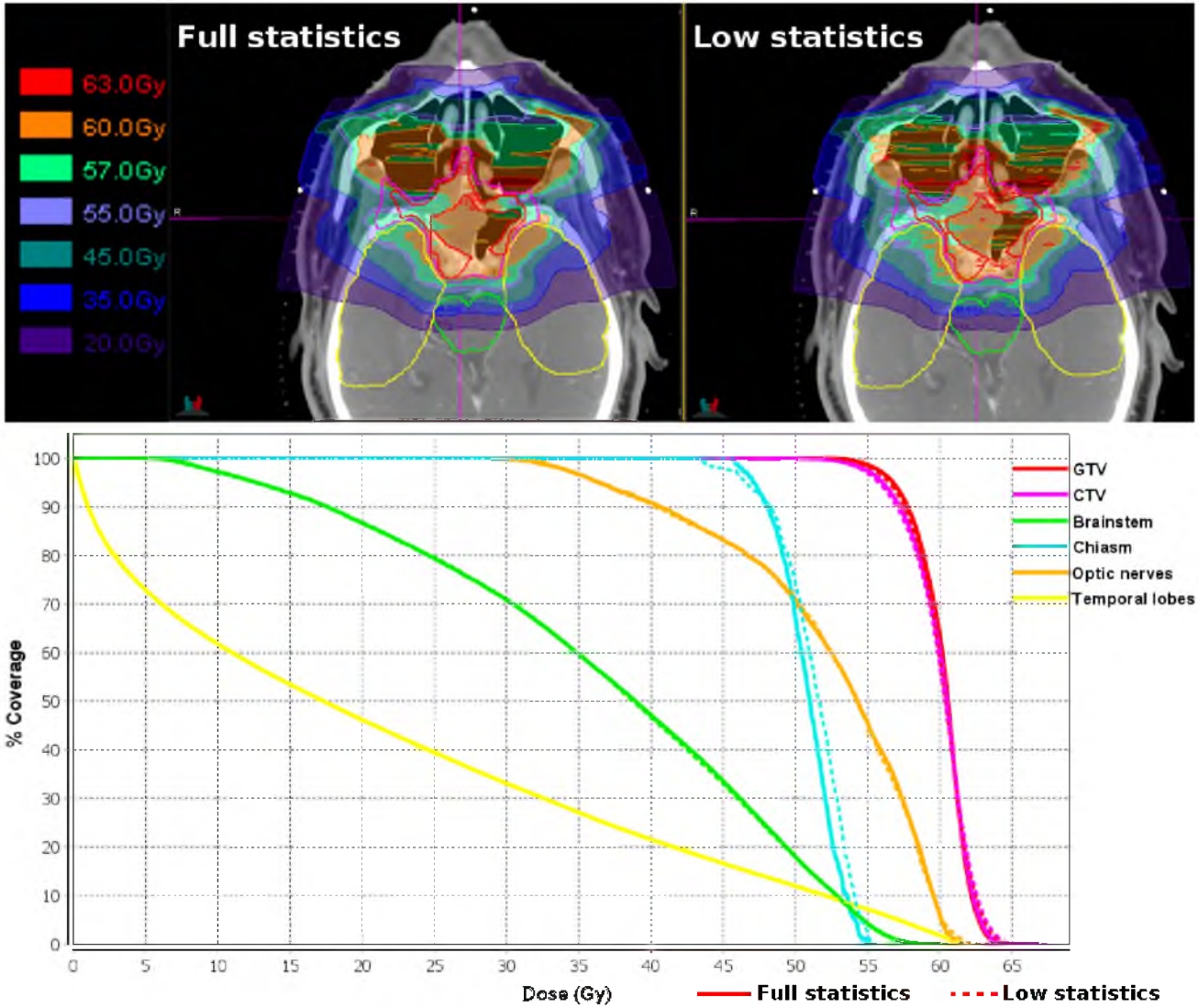

Figure 6.24: *Dose and DVH comparison of GMC's dose recomputations for the head & neck patient with full statistics (1,000,000 particles simulated per requested Gp) versus low statistics (100,000 particles simulated per requested Gp). Although noisier, the low statistics remains accurate from a clinical stand point.*

6.5 Speed considerations

The version of GMC presented in this work was only evaluated for accuracy; the source code was not optimized for speed. Thus, there are multiple opportunities that could help speed up the computation process.

The first aspect consists of the statistics, i.e. how many histories should be simulated and how coarse the dose grid could be in order to ensure acceptable dose computations accuracy. The simulations performed for section 6.4.2 perfectly illustrate these considerations. The "full statistical" computations, considering 1,000,000 histories per gigaproton requested, using a 1 mm^3 voxel geometry, took approximately 315 minutes for the spine sarcoma field and 574 minute for the pericardia & lung field. These numbers are extremely high and unacceptable in clinical practice. On the other hand, the simulations with reduced statistics, 100,000 histories per gigaproton requested, using a 2 mm^3 voxel geometry, took approximately 13 and 26 minutes, respectively. This represents over a 2000 % speedup factor. Albeit the accuracy was diminished when using reduced statistics, it was well within clinical acceptability. Such considerations would need to be taken into account for a finalized algorithm. A more quantitative analysis, however, must be performed in order to optimally balance speed and accuracy.

It is worth noting that GMC's code, in its current form, presents countless mathematical operations and *for loops*. An appropriate profiling of the source code could be performed in order to ensure optimal execution speed throughout the algorithm.

Furthermore, GMC is a perfect candidate for multi-threading. GMC, in its current state, performs dose computations using a single CPU thread. Multiple threads could easily be used for parallel particle tracking, either at the particle or the spot level. The use of "mutex" (locks designed to enforce mutual exclusion for parallel memory access) could easily be implemented on a per dose voxel basis. Such multi-threading implementation would be highly efficient in GMC's algorithm given that two particles are statistically unlikely to have an interaction with the same given voxel at the same time. Currently, a basic desktop computer would offer over 8 threads, while a dedicated workstation could easily offer over 30 threads. Despite the fact that, depending on the code's scalability, the runtime speedup might not linearly increase as a function of available threads, a large speedup should be expected in such environment. Since the simulation of a single particle in GMC currently takes on the order of 3 seconds, such setup should permit us to bring the computation times discussed in section 6.4.2 to

under a minute.

Such speed improvements, however, will not be implemented in the current version of GMC. Only the source code profiling should be performed in order to assess and optimize the functions affecting the computational speed the most. The "pseudo-code" presented in this work was intended for modeling and accuracy validation only. As previously suggested, this algorithm is extremely parallelizable, thus highly suitable for GPU use. The next step will consist of the portage of the source code to the GPU architecture. The simulation of a single particle currently takes about 3 seconds on a "regular" computer. This time is mainly driven by the program's initialization (CT and fluence loading) and finalization (dose cube write-out), as confirmed through the simulation of 1000 particles which occurs in about 4 seconds. In the final layout, these initialization and finalization steps would be independent of GMC, thus the simulation of 1,000 particles would be performed under a second. Once ported to the GPU architecture, one *could* therefore expect to decrease the computation time for an entire field to the level of a second.

6.6 Conclusion

GMC ['gImIk], an extremely simplified MC algorithm for proton dose calculations has been implemented on a CPU architecture. Its basic physics' properties have been validated against the physical observables of a proton beam at the macro level. GMC's dose computation accuracy was then assessed against measurements, with results surpassing clinical expectations. Dose computations in patients were also performed and compared to the current clinical PBA calculation for three patients that presented challenging geometry. These simulations further highlighted the limitations of the current pencil beam algorithm's dose computations.

The current version of the algorithm, running on a single CPU thread, is arguably fast from a Monte Carlo stand point, but undoubtedly slow from a clinical point of view. Although the source code could easily be optimized for computational speed, resulting in a similar calculation time as the current PBA system in place, the aim is to port the algorithm to a GPU architecture. The loading of the patient information, spot placement, etc, will be performed at a higher level by Astroid. GMC's GPU implementation will only perform the dose computation itself based on the provided input. Computation time at the level of a second can then be expected. At such speed, the dose computation is considered "online", and any changes to

the input data, such as range shifter thickness, spots' position and energy, etc, would automatically result in an updated dose distribution.

Online dose calculations open the door to adaptive recomputation. With the proper imaging system, expected daily fractional doses could be instantaneously computed. The position of the spots could further be automatically adapted with the dose instantly recomputed.

Chapter 7

Conclusions and future work

Proton pencil beam scanning radiotherapy is currently at the forefront of the treatment of cancer with a promising future of continuous improvement. For example, the use of proton imaging along with a fast dose computation engine could result in a daily adaptation of the patient's treatment plan based on tumor position. This work has laid a solid foundation to achieving adaptive radiotherapy for PBS. The characteristics and limitations of proton radiography imaging have been evaluated and the design and preliminary experimental work of a small form factor proton radiography system have also been performed. Furthermore, the requisites and limitations of PBS treatment planning were assessed, and a simplified Monte Carlo dose algorithm was implemented.

7.1 Proton imaging

The imaging characteristics and limitations of proton radiography have been evaluated through the use of GEANT4 simulations. These imaging properties were also compared against conventional kV and MV X-ray imaging. In spite of proton radiography's limited spatial resolution (due to multiple Coulomb scattering), it was found that its density resolution was far greater than conventional X-ray radiography. In fact, it was shown that an ROI with a density closely related to the density of its background (up to 0.02 g/cm^3 density difference) could be resolved. This density resolution may be beneficial for certain tumor sites, such as lung cancer. Moreover, the use of the plateau region of the beam's Bragg peak results in a very low imaging dose. The reduced imaging dose is especially attractive for pediatric patients, because even

the smallest dose may be detrimental to the patient. Most importantly, the use of a single beam for both imaging and therapy would ensure a higher treatment accuracy, especially as the technology advances and permits the use of proton imaging for online tumor tracking.
The current design of proton radiography detectors are clinically impracticable. A small form factor proton radiography detector, suitable for clinical use, was therefore designed. Multiple technologies were evaluated: photonic bandgap fibers, a CMOS active pixel sensor, and Bicron scintillating fibers. PBG fibers proved to be unsuitable for proton imaging use as they did not properly react with the beam. Although the CMOS APS yielded inconclusive results due to its integration time, it presented promising aspects which showed the potential for proton imaging. The redesign of a similar CMOS APS system specifically for proton imaging purposes would therefore be worth exploring. It was highlighted that Bicron scintillating fibers were a viable option to be considered for proton radiography purposes. The basic function of the fibers, i.e. acquisition of position and energy information on a particle-by-particle basis, was demonstrated. After calibration, the energy information can be acquired from the amount of signal generated in the fiber through the particle's interaction. The position information can be reconstructed from the coincidental interactions in two sets of parallel fibers set in a 2-dimensional X/Y mesh. This information should be acquired both in front and behind the patient, twice, allowing for the reconstruction of directional information on a particle-by-particle basis through coincidence measurements. This information can then be used to generate radiographs with more advanced image reconstruction algorithms. Nevertheless, a full scale functional system could not be implemented, partly due to the high cost of read-out electronic systems.

7.2 Fast dose computation algorithm

The requisites and limitations of current treatment planning for proton PBS were assessed. The acquisition of the beam model required by the TPS was described. The main limitation of the treatment's quality lies in the machine's spot size. Although the dosimetric benefits of a smaller spot size were highlighted, the downfalls were unfortunately highlighted as well, due to the strict requirements for delivery tolerances and the need for higher computing power. From a TPS point of view, the issues linked to spot placement have been described. Solutions to spot placement issues necessitate heavy computing power, but should be expected to be

performed quickly. The robustness of PBS treatment planning was also discussed through an exemplary case. This type of robustness analysis could be performed routinely in the clinic if the dose computing engine was faster. Lastly, the relative accuracy of the current pencil beam algorithm for dose computation was discussed, as well as the need for more accurate engines, such as Monte Carlo algorithms.

The simplicity of the beam model for PBS facilitates the design of a simplified Monte Carlo algorithm. Thus, GMC, an accurate MC proton dose computation engine, was implemented on the CPU architecture. GMC was then validated against physical observables. The range of the Bragg peak first had to be calibrated in order to match the beam model due to the scattering of the particles. This results in a tortuous path which projects shallower than a straight path. Subsequently, the accuracy of the input position, beam size, and machine SAD was verified. The correctness of the scattering in water was also compared to the theoretical model. The implementation of the halo effect was also evaluated, but it uncovered issues with the theoretical model. Lastly, GMC's behavior against heterogeneities was assessed. Once the implementation was validated, three patient cases were considered for comparisons. GMC's dose recomputations of the patient fields in water were compared to pre-treatment QA dose computation and measurements. The agreement between the QA dose computation and GMC's recomputations was merely acceptable. On the other hand, the comparisons against measurements yielded excellent results. This highlighted the exceptional accuracy of the algorithm used in GMC. The recomputations were ultimately performed in the patient's geometry and compared to both the original Astroid pencil beam algorithm dose computation and the recomputations performed with TOPAS, a full Monte Carlo engine. The general features matched the expectations but, overall, GMC's recomputations displayed a milder discrepancy than TOPAS when compared to Astroid. The evaluation of the accuracy of such computations is difficult however, as there is no ground truth. As GMC is currently implemented on the CPU architecture only, there are numerous opportunities for large speed improvements which are believed to reduce the computational time to a negligible level.

7.3 Future work

The work presented in this thesis lays the foundation for adaptive replanning, which will require both proton imaging and fast dose calculation capabilities in the future. Nevertheless, many

aspects require further investigation and action. These includes:

- Optimize the image reconstruction algorithm for proton radiography based on the patient's diagnostic images.
- Apply the methods learned for proton radiography to a more complex proton CT system.
- Determine proton radiography's capabilities for generating proton range information.
- Assess the real possibilities for a CMOS APS based proton radiography system.
- Build a fully functional prototype of a scintillating fiber device for proton imaging purposes.
- Correct the halo component of GMC's dose computation algorithm.
- Port GMC to the GPU architecture.
- Optimize the accuracy/statistics trade-off for optimal speed performances in GMC.
- Validate GMC against in-vivo measurements.
- Implement a double scattering version of GMC's algorithm.
- Implement relative biological effectiveness (RBE) considerations in GMC.
- Generate a framework combining proton imaging, GMC, and a reoptimization routine.

The immediate future work will specifically focus on GMC's finalization. The parameters of the halo component will first be adjusted so that the core of the depth dose curve is appropriately complimented by the halo component in order to recover the entire pristine peaks of the beam model. Once validated, GMC will be ported from the CPU architecture to the GPU architecture. The computational time on the GPU is expected to be negligible, thus opening the way to online dose recomputations. In parallel, efforts should be put into the design of a full scale proton imaging system. The synergy of the imaging system and GMC's fast algorithm will then pave the way to proton pencil beam scanning adaptive radiation therapy.
The addition of the relative biological effectiveness of protons into GMC's algorithm is another improvement that could be made in the future. Since GMC is implemented based on particle-by-particle tracking, the LET_{∞} information is readily available on a voxel basis. Thus, the

implementation of proton RBE weighted dose computations is not a complicated issue in itself. Proton RBE models, however, present very large uncertainties [136]. Large improvements in RBE models is therefore necessary before such feature could be considered in the clinic.

References

[1] B. Gottschalk, "Bgware," *http://gray.mgh.harvard.edu/index.php?option=com_content&view=article&id* Accessed: July 2014.

[2] H. Paganetti, *Proton therapy physics*. CRC Press, 2011.

[3] U. Schneider, J. Besserer, P. Pemler, M. Dellert, M. Moosburger, E. Pedroni, and B. Kaser-Hotz, "First proton radiography of an animal patient," *Medical physics*, vol. 31, no. 5, pp. 1046–1051, 2004.

[4] P. Pemler, J. Besserer, J. De Boer, M. Dellert, C. Gahn, M. Moosburger, U. Schneider, E. Pedroni, and H. Stäuble, "A detector system for proton radiography on the gantry of the paul-scherrer-institute," *Nuclear Instruments and Methods in Physics Research Section A: Accelerators, Spectrometers, Detectors and Associated Equipment*, vol. 432, no. 2, pp. 483–495, 1999.

[5] T. Li, Z. Liang, J. V. Singanallur, T. J. Satogata, D. C. Williams, and R. W. Schulte, "Reconstruction for proton computed tomography by tracing proton trajectories: A monte carlo study," *Medical physics*, vol. 33, p. 699, 2006.

[6] H. Paganetti, H. Jiang, S.-Y. Lee, and H. Kooy, "Accurate monte carlo simulations for nozzle design, commissioning and quality assurance for a proton radiation therapy facility," *Medical physics*, vol. 31, p. 2107, 2004.

[7] M. Donszelmann, "Wired 4-a generic event display plugin for jas 3," Stanford Linear Accelerator Center (SLAC), Menlo Park, CA, Tech. Rep., 2004.

[8] G. GIMP, "Image manipulation program," *User Manual, Edge-Detect Filters, Sobel, The GIMP Documentation Team*, 2008.

[9] W. S. Rasband, "Imagej, us national institutes of health, bethesda, maryland, usa," 1997.

[10] A. Allisy, A. Kelleler, R. Caswell *et al.*, "Stopping powers and ranges for protons and alpha particles," *ICRU Report*, vol. 49, 1993.

[11] B. Clasie, N. Depauw, M. Fransen, C. Gomà, H. R. Panahandeh, J. Seco, J. B. Flanz, and H. M. Kooy, "Golden beam data for proton pencil-beam scanning," *Physics in medicine and biology*, vol. 57, no. 5, p. 1147, 2012.

[12] H. Paganetti, *Proton Therapy Physics*. CRC Press, 2012.

[13] B. Schaffner, E. Pedroni, and A. Lomax, "Dose calculation models for proton treatment planning using a dynamic beam delivery system: an attempt to include density heterogeneity effects in the analytical dose calculation," *Physics in medicine and biology*, vol. 44, no. 1, p. 27, 1999.

[14] W. St Clair, J. Adams, M. Bues, B. Fullerton, S. La Shell, H. Kooy, J. Loeffler, and N. Tarbell, "Advantage of protons compared to conventional x-ray or imrt in the treatment of a pediatric patient with medulloblastoma," *International Journal of Radiation Oncology* Biology* Physics*, vol. 58, no. 3, pp. 727–734, 2004.

[15] U. Mock, D. Georg, J. Bogner, T. Auberger, and R. Pötter, "Treatment planning comparison of conventional, 3d conformal, and intensity-modulated photon (imrt) and proton therapy for paranasal sinus carcinoma," *International Journal of Radiation Oncology* Biology* Physics*, vol. 58, no. 1, pp. 147–154, 2004.

[16] A. Trofimov, P. L. Nguyen, J. J. Coen, K. P. Doppke, R. J. Schneider, J. A. Adams, T. R. Bortfeld, A. L. Zietman, T. F. DeLaney, and W. U. Shipley, "Radiotherapy treatment of early-stage prostate cancer with imrt and protons: a treatment planning comparison," *International Journal of Radiation Oncology* Biology* Physics*, vol. 69, no. 2, pp. 444–453, 2007.

[17] D. L. Miglioretti, E. Johnson, A. Williams, R. T. Greenlee, S. Weinmann, L. I. Solberg, H. S. Feigelson, D. Roblin, M. J. Flynn, N. Vanneman *et al.*, "The use of computed tomography in pediatrics and the associated radiation exposure and estimated cancer risk," *JAMA pediatrics*, vol. 167, no. 8, pp. 700–707, 2013.

[18] U. Schneider and E. Pedroni, "Multiple coulomb scattering and spatial resolution in proton radiography," *Medical physics*, vol. 21, no. 11, pp. 1657–1663, 1994.

[19] U. Schneider and E. Pedroni, "Proton radiography as a tool for quality control in proton therapy," *Medical physics*, vol. 22, no. 4, pp. 353–363, 1995.

[20] F. Sauli, "Gem: A new concept for electron amplification in gas detectors," *Nuclear Instruments and Methods in Physics Research Section A: Accelerators, Spectrometers, Detectors and Associated Equipment*, vol. 386, no. 2, pp. 531–534, 1997.

[21] L. Johnson, B. Keeney, G. Ross, H.-W. Sadrozinski, A. Seiden, D. Williams, L. Zhang, V. Bashkirov, R. Schulte, and K. Shahnazi, "Initial studies on proton computed tomography using a silicon strip detector telescope," *Nuclear Instruments and Methods in Physics Research Section A: Accelerators, Spectrometers, Detectors and Associated Equipment*, vol. 514, no. 1, pp. 215–223, 2003.

[22] C. Talamonti, V. Reggioli, M. Bruzzi, M. Bucciolini, C. Civinini, L. Marrazzo, D. Menichelli, S. Pallotta, N. Randazzo, V. Sipala *et al.*, "Proton radiography for clinical applications," *Nuclear Instruments and Methods in Physics Research Section A: Accelerators, Spectrometers, Detectors and Associated Equipment*, vol. 612, no. 3, pp. 571–575, 2010.

[23] V. Sipala, M. Bruzzi, M. Bucciolini, G. Candiano, L. Capineri, G. P Cirrone, C. Civinini, G. Cuttone, D. Lo Presti, L. Marrazzo *et al.*, "A proton imaging device: Design and status of realization," *Nuclear Instruments and Methods in Physics Research Section A: Accelerators, Spectrometers, Detectors and Associated Equipment*, vol. 612, no. 3, pp. 566–570, 2010.

[24] C. Grassberger, J. Daartz, S. Dowdell, T. Ruggieri, G. Sharp, and H. Paganetti, "Quantification of proton dose calculation accuracy in the lung," *International Journal of Radiation Oncology* Biology* Physics*, vol. 89, no. 2, pp. 424–430, 2014.

[25] N. Depauw, S. Danto, B. Bednarz, H. Paganetti, Y. Fink, and J. Seco, "Preliminary study of proton radiography imaging qualities using GEANT4 monte carlo simulations," *Nuclear technology*, vol. 175, no. 1, pp. 6–10, 2011.

[26] N. Depauw and J. Seco, "Sensitivity study of proton radiography and comparison with kV and MV x-ray imaging using GEANT4 monte carlo simulations," *Physics in Medicine*

and Biology, vol. 56, no. 8, p. 2407, 2011.

[27] N. Depauw, M. Dias, A. Rosenfeld, and J. Seco, "Ion radiography as a tool for patient set-up and image guided particle therapy: A monte carlo study." *Technology in cancer research & treatment*, 2013.

[28] N. Depauw, V. Taranenko, S. Danto, F. Sorin, Y. Fink, and J. Seco, "TH-D-201B-03: A comparison of protons versus gamma x-rays in producing patient radiographs: A monte carlo study," *Medical Physics*, vol. 37, p. 3472, 2010.

[29] N. Depauw, M. Dias, and J. Seco, "TH-E-220-04: IGPT using proton radiography: A monte carlo study," *Medical Physics*, vol. 38, p. 3879, 2011.

[30] J. Seco and N. Depauw, "Proof of principle study of the use of a CMOS active pixel sensor for proton radiography," *Medical Physics*, vol. 38, p. 622, 2011.

[31] J. Seco, N. Depauw, S. Danto, H. Paganeti, and Y. Fink, "Qualitative evaluation of proton radiography for viewing density differences in lung tumors: A monte carlo study," *Nuclear technology*, vol. 175, no. 1, pp. 27–31, 2011.

[32] J. C. Polf, N. Depauw, and J. Seco, "Monte carlo studies of prompt gamma emission and of proton radiography/proton-CT," in *Monte Carlo Techniques in Radiation Therapy*, J. Seco and F. Verhaegen, Eds. CRC Press, 2013, pp. 263–272.

[33] J. Seco and N. Depauw, "WE-E-201C-04: Development of the first MGH proton range telescope (PRaT) prototype using scintillating fibers," *Medical Physics*, vol. 37, p. 3440, 2010.

[34] M. Dias, N. Depauw, and J. Seco, "TU-C-214-02: Proton radiography gui interface, PR-Creator, for in-room patient setup and real-time tumor tracking in proton beam therapy," *Medical Physics*, vol. 38, p. 3756, 2011.

[35] J. Seco, M. Dias, N. Depauw, and S. MacDonald, "SU-EJ-168: Proton radiography for pediatric, t-spine and lung malignancies; development and enhancement of a proton imaging technique," *Medical Physics*, vol. 38, p. 3482, 2011.

[36] J. Seco, M. Oumano, N. Depauw, M. Dias, and R. Teixeira, "SU-EI-97: Characterizing the modulation transfer function (MTF) of proton radiography." *Medical physics*, vol. 39,

no. 6, p. 3647, 2012.

[37] M. Spadea, A. Fassi, N. Depauw, M. Riboldi, G. Baroni, and J. Seco, "Contrast enhanced proton radiography for in-room soft tissue-based setup," *International Journal of Radiation Oncology* Biology* Physics*, vol. 84, no. 3, p. S53, 2012.

[38] M. Spadea, A. Fassi, N. Depauw, M. Riboldi, G. Baroni, and J. Seco, "TH-E-BRA-05: Improving the contrast of proton and carbon radiography by using CT prior knowledge." *Medical physics*, vol. 39, no. 6, p. 4012, 2012.

[39] N. Depauw and J. Seco, "TH-A-213CD-09: The use of scintillating fibers for proton imaging purposes." *Medical physics*, vol. 39, no. 6, p. 3988, 2012.

[40] N. Depauw and J. Seco, "Preliminary results of a scintillating fibers detector for proton radiography," 2012.

[41] M. Goulet, L. Gingras, N. Depauw, L. Archambault, J. Seco, and L. Beaulieu, "WE-G-BRB-06: Real-time radiation field tracking using long scintillating fibers." *Medical physics*, vol. 39, no. 6, p. 3968, 2012.

[42] O. Koybasi, M. Goulet, N. Depauw, L. Gingras, L. Archambault, L. Beaulieu, and J. Seco, "Development of a 2D scintillating fiber detector for proton radiography," in *Nuclear Science Symposium and Medical Imaging Conference (NSS/MIC), 2012 IEEE*. IEEE, 2012, pp. 4318–4323.

[43] N. Depauw, "Proton radiography and fast mc dose algorithm." *Geant4 Australian School and User Workshop*, 2013.

[44] N. Depauw, J. Daartz, E. Batin, A. Rosenfeld, H. Kooy, S. MacDonald, and H. Lu, "A novel approach to post-mastectomy radiation therapy using scanned proton beam." *International Journal of Radiation Oncology* Biology* Physics*, vol. 91, no. 2, pp. 427–434, 2015.

[45] H. M. Kooy, B. M. Clasie, H.-M. Lu, T. M. Madden, H. Bentefour, N. Depauw, J. A. Adams, A. V. Trofimov, D. Demaret, T. F. Delaney *et al.*, "A case study in proton pencil-beam scanning delivery," *International Journal of Radiation Oncology* Biology* Physics*, vol. 76, no. 2, pp. 624–630, 2010.

[46] S. J. Dowdell, B. Clasie, N. Depauw, P. Metcalfe, A. B. Rosenfeld, H. M. Kooy, J. B. Flanz, and H. Paganetti, "Monte carlo study of the potential reduction in out-of-field dose using a patient-specific aperture in pencil beam scanning proton therapy," *Physics in Medicine and Biology*, vol. 57, no. 10, p. 2829, 2012.

[47] A. Carabe, M. Moteabbed, N. Depauw, J. Schuemann, and H. Paganetti, "Range uncertainty in proton therapy due to variable biological effectiveness," *Physics in Medicine and Biology*, vol. 57, no. 5, p. 1159, 2012.

[48] K. T. Butterworth, C. K. McGarry, B. Clasie, A. Carabe-Fernandez, J. Schuemann, N. Depauw, S. Tang, S. J. McMahon, G. Schettino, J. M. O'Sullivan *et al.*, "Relative biological effectiveness (RBE) and out-of-field cell survival responses to passive scattering and pencil beam scanning proton beam deliveries," *Physics in Medicine and Biology*, vol. 57, no. 20, p. 6671, 2012.

[49] B. Clasie, H. Bentefour, P. Boisseau, Y. Claereboudt, D. Demaret, N. Depauw, D. Herrup, H. Lu, W. Nett, H. Kooy *et al.*, "TH-C-BRD-01: Technical and practical considerations in implementing proton pencil beam scanning," *Medical Physics*, vol. 36, p. 2794, 2009.

[50] B. Clasie, H. Kooy, N. Depauw, C. Goma, A. Carabe-Fernandez, H. Panahandeh, J. Seco, S. Tang, and J. Flanz, "SU-ET-723: Pencil beam depth-dose distributions in the astroid TPS," *Medical Physics*, vol. 38, p. 3657, 2011.

[51] S. Dowdell, B. Clasie, N. Depauw, P. Metcalfe, A. Rosenfeld, H. Kooy, J. Flanz, and H. Paganetti, "MO-F-213AB-03: Potential reduction in out-of-field dose in pencil beam scanning proton therapy through use of a patient-specific aperture." *Medical physics*, vol. 39, no. 6, p. 3872, 2012.

[52] N. Rochet, E. Batin, N. Depauw, K. Jee, H. Kooy, F. Khan, P. Paetzold, A. Russell, T. Bortfeld, and D. Craft, "Advances in whole abdominal irradiation: What protons, VMAT, and IMRT using multicriteria optimization can offer," *International Journal of Radiation Oncology* Biology* Physics*, vol. 87, no. 2, pp. S748–S749, 2013.

[53] A. Carabe-Fernandez, M. Moteabbed, N. Depauw, and H. Paganetti, "SU-E-T-648: Range uncertainty in proton therapy due to variable biological effectiveness," *Medical Physics*, vol. 38, p. 3639, 2011.

[54] C. McGarry, K. Butterworth, B. Clasie, S. A. Carabe-Fernandez, N. Depauw, H. Kooy, H. Ming, S. Tang, J. O'Sullivan, G. Schettino *et al.*, "EP-1587 cell survival responses to modulated proton beams delivered by passive scattering and pencil beam scanning," *Radiotherapy and Oncology*, vol. 103, pp. S608–S609, 2012.

[55] N. Depauw, B. Clasie, T. Madden, A. Rosenfeld, and H. Kooy, "GMC ['gimik]: a one-variable monte carlo dose algorithm for proton therapy," 2013.

[56] N. Depauw, B. Clasie, T. Madden, A. Rosenfeld, and H. Kooy, "GMC ['gimik]: algorithm for proton therapy." *Journal of Physics: Conference Series*, vol. 489, p. 012010, 2014.

[57] R. Wilson, "Radiobiological use of fast protons." *Radiobiology*, vol. 47, pp. 487–491, 1946.

[58] J. Lawrence, "Proton irradiation of the pituitary." *Cancer*, vol. 10, no. 4, pp. 795–798, 1957.

[59] J. Lawrence, "Proton irradiation of the pituitary." *Cancer*, vol. 10, no. 4, pp. 795–798, 1957.

[60] J. M. Slater, J. O. Archambeau, D. W. Miller, M. I. Notarus, W. Preston, and J. D. Slater, "The proton treatment center at loma linda university medical center: rationale for and description of its development," *International Journal of Radiation Oncology* Biology* Physics*, vol. 22, no. 2, pp. 383–389, 1992.

[61] Particle Therapy Co-Operative Group, "Facilities in operation," *http://www.ptcog.ch/index.php/facilities-in-operation*, Accessed: April 2014.

[62] Particle Therapy Co-Operative Group, "Facilities under construction," *http://www.ptcog.ch/index.php/facilities-under-construction*, Accessed: April 2014.

[63] T. F. De Laney and H. M. Kooy, *Proton and charged particle radiotherapy*. Lippincott Williams & Wilkins, 2008.

[64] F. H. Attix, *Introduction to radiological physics and radiation dosimetry*. John Wiley & Sons, 2008.

[65] T. Bortfeld, "An analytical approximation of the bragg curve for therapeutic proton beams," *Medical physics*, vol. 24, no. 12, pp. 2024–2033, 1997.

[66] J. F. Janni, "Proton range-energy tables, 1 kev-10 gev, energy loss, range, path length, time-of-flight, straggling, multiple scattering, and nuclear interaction probability. part i. for 63 compounds," *Atomic data and nuclear data tables*, vol. 27, p. 147, 1982.

[67] J. A. Purdy, "Dose to normal tissues outside the radiation therapy patient's treated volume: a review of different radiation therapy techniques," *Health physics*, vol. 95, no. 5, pp. 666–676, 2008.

[68] X. Zhang, Y. Li, X. Pan, L. Xiaoqiang, R. Mohan, R. Komaki, J. D. Cox, and J. Y. Chang, "Intensity-modulated proton therapy reduces the dose to normal tissue compared with intensity-modulated radiation therapy or passive scattering proton therapy and enables individualized radical radiotherapy for extensive stage iiib non-small-cell lung cancer: a virtual clinical study," *International Journal of Radiation Oncology* Biology* Physics*, vol. 77, no. 2, pp. 357–366, 2010.

[69] T. A. Van de Water, A. J. Lomax, H. P. Bijl, M. E. de Jong, C. Schilstra, E. B. Hug, and J. A. Langendijk, "Potential benefits of scanned intensity-modulated proton therapy versus advanced photon therapy with regard to sparing of the salivary glands in oropharyngeal cancer," *International Journal of Radiation Oncology* Biology* Physics*, vol. 79, no. 4, pp. 1216–1224, 2011.

[70] U. Schneider, E. Pedroni, and A. Lomax, "The calibration of ct hounsfield units for radiotherapy treatment planning," *Physics in medicine and biology*, vol. 41, no. 1, p. 111, 1996.

[71] S. España and H. Paganetti, "The impact of uncertainties in the ct conversion algorithm when predicting proton beam ranges in patients from dose and pet-activity distributions," *Physics in medicine and biology*, vol. 55, no. 24, p. 7557, 2010.

[72] H. Paganetti, "Range uncertainties in proton therapy and the role of monte carlo simulations," *Physics in medicine and biology*, vol. 57, no. 11, p. R99, 2012.

[73] K. M. Hanson, "Development of a proton radiographic system for diagnosis and localization of soft-tissue abnormalities. final report," Los Alamos Scientific Lab., N. Mex.(USA), Tech. Rep., 1978.

[74] K. M. Hanson, "Proton computed tomography," *Nuclear Science, IEEE Transactions on*, vol. 26, no. 1, pp. 1635–1640, 1979.

[75] V. Steward, "Are x-rays the ultimate?: Proton (heavy ion) radiography in neurologic diagnosis," *Journal of the neurological sciences*, vol. 39, no. 2, pp. 261–293, 1978.

[76] S. L. Kramer, D. R. Moffett, R. L. Martin, E. P. Colton, and V. W. Steward, "Proton imaging for medical applications." *Radiology*, vol. 135, no. 2, pp. 485–494, 1980.

[77] R. W. Schulte, V. Bashkirov, M. C. L. Klock, T. Li, A. J. Wroe, I. Evseev, D. C. Williams, and T. Satogata, "Density resolution of proton computed tomography," *Medical physics*, vol. 32, no. 4, pp. 1035–1046, 2005.

[78] G. Coutrakon, V. Rykalin, V. Bashkirov, F. Hurley, R. Schulte, R. Johnson, and H. Sadrozinski, "Design and construction of the first proton ct scanner," in *AIP Conference Proceedings*, vol. 1525, no. 1, 2013.

[79] R. Schulte, S. Penfold, J. Tafas, and K. Schubert, "A maximum likelihood proton path formalism for application in proton computed tomography," *Medical physics*, vol. 35, p. 4849, 2008.

[80] H. Ryu, E. Song, J. Lee, and J. Kim, "Density and spatial resolutions of proton radiography using a range modulation technique," *Physics in medicine and biology*, vol. 53, no. 19, p. 5461, 2008.

[81] L. Hong, M. Goitein, M. Bucciolini, R. Comiskey, B. Gottschalk, S. Rosenthal, C. Serago, and M. Urie, "A pencil beam algorithm for proton dose calculations," *Physics in medicine and biology*, vol. 41, no. 8, p. 1305, 1996.

[82] S. Agostinelli, J. Allison, K. e. Amako, J. Apostolakis, H. Araujo, P. Arce, M. Asai, D. Axen, S. Banerjee, G. Barrand *et al.*, "Geant4—a simulation toolkit," *Nuclear instruments and methods in physics research section A: Accelerators, Spectrometers, Detectors and Associated Equipment*, vol. 506, no. 3, pp. 250–303, 2003.

[83] J. Allison, K. Amako, J. Apostolakis, H. Araujo, P. A. Dubois, M. Asai, G. Barrand, R. Capra, S. Chauvie, R. Chytracek *et al.*, "Geant4 developments and applications," *Nuclear Science, IEEE Transactions on*, vol. 53, no. 1, pp. 270–278, 2006.

[84] H. Paganetti, H. Jiang, K. Parodi, R. Slopsema, and M. Engelsman, "Clinical implementation of full monte carlo dose calculation in proton beam therapy," *Physics in medicine and biology*, vol. 53, no. 17, p. 4825, 2008.

[85] V. Steward and A. Koehler, "Proton beam radiography in tumor detection," *Science*, vol. 179, no. 4076, pp. 913–914, 1973.

[86] K. Hanson, J. Bradbury, R. Koeppe, R. Macek, D. Machen, R. Morgado, M. Paciotti, S. Sandford, and V. Steward, "Proton computed tomography of human specimens," *Physics in medicine and biology*, vol. 27, no. 1, p. 25, 1982.

[87] C. Z. Jarlskog and H. Paganetti, "Physics settings for using the geant4 toolkit in proton therapy," *Nuclear Science, IEEE Transactions on*, vol. 55, no. 3, pp. 1018–1025, 2008.

[88] M. Berger, "Estar, pstar, and astar: computer programs for calculating stopping-power and range tables for electrons, protons, and helium ions," *Unknown*, vol. 1, 1992.

[89] I. Kawrakow and D. Rogers, "The egsnrc code system: Monte carlo simulation of electron and photon transport," 2000.

[90] M. U. G. MathWorks, "the mathworks," *Inc., Natick, MA*, 2008.

[91] H. P. Society, "Radiation exposure from medical diagnostic imaging procedures," *https://www.hps.org/documents/meddiagimaging.pdf*, Accessed: February 2014.

[92] C. Walter, J. Boda-Heggemann, H. Wertz, I. Loeb, A. Rahn, F. Lohr, and F. Wenz, "Phantom and in-vivo measurements of dose exposure by image-guided radiotherapy (igrt): Mv portal images vs. kv portal images vs. cone-beam ct," *Radiotherapy and Oncology*, vol. 85, no. 3, pp. 418–423, 2007.

[93] K. Kuriki, O. Shapira, S. Hart, G. Benoit, Y. Kuriki, J. Viens, M. Bayindir, J. Joannopoulos, and Y. Fink, "Hollow multilayer photonic bandgap fibers for nir applications," *Optics Express*, vol. 12, no. 8, pp. 1510–1517, 2004.

[94] P. Yeh, A. Yariv, and E. Marom, "Theory of bragg fiber," *JOSA*, vol. 68, no. 9, pp. 1196–1201, 1978.

[95] R. Cregan, B. Mangan, J. Knight, T. Birks, P. S. J. Russell, P. Roberts, and D. Allan, "Single-mode photonic band gap guidance of light in air," *science*, vol. 285, no. 5433, pp. 1537–1539, 1999.

[96] D. C. Allan, J. A. West, J. C. Fajardo, M. T. Gallagher, K. W. Koch, and N. F. Borrelli, "Photonic crystal fibers: effective-index and band-gap guidance," in *Photonic crystals*

and Light Localization in the 21st Century. Springer, 2001, pp. 305–320.

[97] B. Eggleton, C. Kerbage, P. Westbrook, R. Windeler, and A. Hale, "Microstructured optical fiber devices," *Optics Express*, vol. 9, no. 13, pp. 698–713, 2001.

[98] M. Bayindir, O. Shapira, D. Saygin-Hinczewski, J. Viens, A. F. Abouraddy, J. D. Joannopoulos, and Y. Fink, "Integrated fibres for self-monitored optical transport," *Nature Materials*, vol. 4, no. 11, pp. 820–825, 2005.

[99] F. Sorin, A. F. Abouraddy, N. Orf, O. Shapira, J. Viens, J. Arnold, J. D. Joannopoulos, and Y. Fink, "Multimaterial photodetecting fibers: a geometric and structural study," *Advanced Materials*, vol. 19, no. 22, pp. 3872–3877, 2007.

[100] LabVIEW, "Vi reference manual," *National Instruments*, 1998.

[101] Saint-Gobain Crystals™, "Plastic scintillators brochure," *http://www.crystals.saint-gobain.com/uploadedFiles/SG-Crystals/Documents/SGC%20Organics%20Brochure.pdf*, Accessed: March 2014.

[102] XiA™, "Pixie-16 specifications," *http://www.xia.com/DGF_Pixie-16.html*, Accessed: March 2014.

[103] Struck™, "Sis3305 specifications," *http://www.struck.de/sis3305.html*, Accessed: March 2014.

[104] A. Sipos, E. Grusell, A. Kerek, W. Klamra, J. Molnár, L.-O. Norlin, D. Novák, A. Sanchez-Crespo, J. Van der Marel, and J. Végh, "Visualization of neutron and proton induced particle production in a cmos image sensor," *Nuclear Instruments and Methods in Physics Research Section A: Accelerators, Spectrometers, Detectors and Associated Equipment*, vol. 509, no. 1, pp. 328–332, 2003.

[105] A. Sanchez-Crespo, A. Kerek, W. Klamra, J. Molnár, L.-O. Norlin, B. Skatt, E. Grusell, D. Novák, A. Sipos, J. Van der Marel *et al.*, "Proton therapy beam dosimetry with silicon cmos image sensors," *Nuclear Instruments and Methods in Physics Research Section A: Accelerators, Spectrometers, Detectors and Associated Equipment*, vol. 525, no. 1, pp. 289–293, 2004.

[106] J. Yorkston, "Recent developments in digital radiography detectors," *Nuclear Instru-*

ments and Methods in Physics Research Section A: Accelerators, Spectrometers, Detectors and Associated Equipment, vol. 580, no. 2, pp. 974–985, 2007.

[107] N. Allinson, T. Anaxagoras, J. Aveyard, C. Arvanitis, R. Bates, A. Blue, S. Bohndiek, J. Cabello, L. Chen, S. Chen *et al.*, "The multidimensional integrated intelligent imaging project (mi-3)," *Nuclear Instruments and Methods in Physics Research Section A: Accelerators, spectrometers, Detectors and Associated Equipment*, vol. 604, no. 1, pp. 196–198, 2009.

[108] R. Turchetta, A. Fant, P. Gasiorek, C. Esbrand, J. Griffiths, M. Metaxas, G. Royle, R. Speller, C. Venanzi, P. van der Stelt *et al.*, "Cmos monolithic active pixel sensors (maps): developments and future outlook," *Nuclear Instruments and Methods in Physics Research Section A: Accelerators, Spectrometers, Detectors and Associated Equipment*, vol. 582, no. 3, pp. 866–870, 2007.

[109] J. Osmond, E. Harris, A. Clark, R. Ott, A. Holland, and P. Evans, "An investigation into the use of cmos active pixel technology in image-guided radiotherapy," *Physics in medicine and biology*, vol. 53, no. 12, p. 3159, 2008.

[110] R. R. Schaller, "Moore's law: past, present and future," *Spectrum, IEEE*, vol. 34, no. 6, pp. 52–59, 1997.

[111] I. J. Das, C.-W. Cheng, R. J. Watts, A. Ahnesjö, J. Gibbons, X. A. Li, J. Lowenstein, R. K. Mitra, W. E. Simon, and T. C. Zhu, "Accelerator beam data commissioning equipment and procedures: Report of the tg-106 of the therapy physics committee of the aapm," *Medical physics*, vol. 35, no. 9, pp. 4186–4215, 2008.

[112] E. Pedroni, S. Scheib, T. Böhringer, A. Coray, M. Grossmann, S. Lin, and A. Lomax, "Experimental characterization and physical modelling of the dose distribution of scanned proton pencil beams," *Physics in medicine and biology*, vol. 50, no. 3, p. 541, 2005.

[113] E. W. Cascio, J. M. Sisterson, B. Gottschalk, and S. Sarkar, "Measurements of the energy spectrum of degraded proton beams at nptc," in *IEEE radiation effects data workshop*, 2004, pp. 151–155.

[114] D. Craft, T. Halabi, and T. Bortfeld, "Exploration of tradeoffs in intensity-modulated radiotherapy," *Physics in medicine and biology*, vol. 50, no. 24, p. 5857, 2005.

[115] D. L. Craft, T. F. Halabi, H. A. Shih, and T. R. Bortfeld, "Approximating convex pareto surfaces in multiobjective radiotherapy planning," *Medical physics*, vol. 33, no. 9, pp. 3399–3407, 2006.

[116] W. Chen, J. Unkelbach, A. Trofimov, T. Madden, H. Kooy, T. Bortfeld, and D. Craft, "Including robustness in multi-criteria optimization for intensity-modulated proton therapy," *Physics in medicine and biology*, vol. 57, no. 3, p. 591, 2012.

[117] S. van de Water, A. Kraan, S. Breedveld, W. Schillemans, D. Teguh, H. Kooy, T. Madden, B. Heijmen, and M. Hoogeman, "Improved efficiency of multi-criteria impt treatment planning using iterative resampling of randomly placed pencil beams," *Physics in medicine and biology*, vol. 58, no. 19, p. 6969, 2013.

[118] T. A. van de Water, A. J. Lomax, H. P. Bijl, C. Schilstra, E. B. Hug, and J. A. Langendijk, "Using a reduced spot size for intensity-modulated proton therapy potentially improves salivary gland-sparing in oropharyngeal cancer," *International Journal of Radiation Oncology* Biology* Physics*, vol. 82, no. 2, pp. e313–e319, 2012.

[119] J. Ragaz, I. Olivotto, J. Spinelli, N. Phillips, S. Jackson, K. Wilson, M. Knowling, C. Coppin, L. Weir, and K. Gelmon, "Locoregional radiation therapy in patients with high-risk breast cancer receiving adjuvant chemotherapy: 20-year results of the british columbia randomized trial," *J Natl Cancer Inst*, vol. 97, pp. 116–126, 2005.

[120] E. A. Krueger, B. A. Fraass, D. L. McShan, R. Marsh, and L. J. Pierce, "Potential gains for irradiation of chest wall and regional nodes with intensity modulated radiotherapy," *International Journal of Radiation Oncology* Biology* Physics*, vol. 56, no. 4, pp. 1023–1037, 2003.

[121] H.-M. Lu, E. Cash, M. H. Chen, L. Chin, W. J. Manning, J. Harris, and B. Bornstein, "Reduction of cardiac volume in left-breast treatment fields by respiratory maneuvers: a ct study," *International Journal of Radiation Oncology* Biology* Physics*, vol. 47, no. 4, pp. 895–904, 2000.

[122] V. M. Remouchamps, F. A. Vicini, M. B. Sharpe, L. L. Kestin, A. A. Martinez, and J. W. Wong, "Significant reductions in heart and lung doses using deep inspiration breath hold with active breathing control and intensity-modulated radiation therapy for patients

treated with locoregional breast irradiation," *International Journal of Radiation Oncology* Biology* Physics*, vol. 55, no. 2, pp. 392–406, 2003.

[123] G. Gyenes, G. Gagliardi, I. Lax, T. Fornander, and L. E. Rutqvist, "Evaluation of irradiated heart volumes in stage i breast cancer patients treated with postoperative adjuvant radiotherapy." *Journal of clinical oncology*, vol. 15, no. 4, pp. 1348–1353, 1997.

[124] S. C. Darby, M. Ewertz, P. McGale, A. M. Bennet, U. Blom-Goldman, D. Brønnum, C. Correa, D. Cutter, G. Gagliardi, B. Gigante *et al.*, "Risk of ischemic heart disease in women after radiotherapy for breast cancer," *New England Journal of Medicine*, vol. 368, no. 11, pp. 987–998, 2013.

[125] C. Ares, S. Khan, A. Macartain, J. Heuberger, G. Goitein, G. Gruber, G. Lutters, E. Hug, S. Bodis, and A. Lomax, "Postoperative proton radiotherapy for localized and locoregional breast cancer: potential for clinically relevant improvements?" *Int J Radiat Oncol Biol Phys*, vol. 76, pp. 685–697, 2010.

[126] S. M. MacDonald, R. Jimenez, P. Paetzold, J. Adams, J. Beatty, T. F. DeLaney, H. Kooy, A. G. Taghian, H.-M. Lu *et al.*, "Proton radiotherapy for chest wall and regional lymphatic radiation; dose comparisons and treatment delivery," *Radiation Oncology*, vol. 8, no. 1, p. 71, 2013.

[127] R. B. Jimenez, C. Goma, J. Nyamwanda, H. M. Kooy, T. Halabi, B. N. Napolitano, S. M. McBride, A. G. Taghian, H.-M. Lu, and S. M. MacDonald, "Intensity modulated proton therapy for postmastectomy radiation of bilateral implant reconstructed breasts: A treatment planning study," *Radiotherapy and Oncology*, vol. 107, no. 2, pp. 213–217, 2013.

[128] H. Fayad, T. Pan, J. F. Clement, and D. Visvikis, "Technical note: Correlation of respiratory motion between external patient surface and internal anatomical landmarks," *Medical physics*, vol. 38, p. 3157, 2011.

[129] D. P. Gierga, M. Riboldi, J. C. Turcotte, G. C. Sharp, S. B. Jiang, A. G. Taghian, and G. T. Chen, "Comparison of target registration errors for multiple image-guided techniques in accelerated partial breast irradiation," *International Journal of Radiation Oncology* Biology* Physics*, vol. 70, no. 4, pp. 1239–1246, 2008.

[130] L. I. Cervino, S. Gupta, M. A. Rose, C. Yashar, and S. B. Jiang, "Using surface imaging and visual coaching to improve the reproducibility and stability of deep-inspiration breath hold for left-breast-cancer radiotherapy," *Physics in medicine and biology*, vol. 54, no. 22, p. 6853, 2009.

[131] J. R. Zullo, R. J. Kudchadker, X. R. Zhu, N. Sahoo, and M. T. Gillin, "Lif tld-100 as a dosimeter in high energy proton beam therapy—can it yield accurate results?" *Medical Dosimetry*, vol. 35, no. 1, pp. 63–66, 2010.

[132] Z.-Y. Qi, X.-W. Deng, S.-M. Huang, L. Zhang, Z.-C. He, X. A. Li, I. Kwan, M. Lerch, D. Cutajar, P. Metcalfe *et al.*, "In vivo verification of superficial dose for head and neck treatments using intensity-modulated techniques," *Medical physics*, vol. 36, no. 1, pp. 59–70, 2008.

[133] B. Gottschalk, "On the scattering power of radiotherapy protons," *Medical physics*, vol. 37, p. 352, 2010.

[134] J. Perl, J. Shin, J. Schümann, B. Faddegon, and H. Paganetti, "Topas: An innovative proton monte carlo platform for research and clinical applications," *Medical physics*, vol. 39, no. 11, pp. 6818–6837, 2012.

[135] B. M. Clasie, G. C. Sharp, J. Seco, J. B. Flanz, and H. M. Kooy, "Numerical solutions of the γ-index in two and three dimensions," *Physics in medicine and biology*, vol. 57, no. 21, p. 6981, 2012.

[136] H. Paganetti, A. Niemierko, M. Ancukiewicz, L. E. Gerweck, M. Goitein, J. S. Loeffler, and H. D. Suit, "Relative biological effectiveness (rbe) values for proton beam therapy," *International Journal of Radiation Oncology* Biology* Physics*, vol. 53, no. 2, pp. 407–421, 2002.